



Améliorations de la cartographie des mouvements myocardiques basée sur la résonance magnétique

Ezgi Berberoğlu

► To cite this version:

Ezgi Berberoğlu. Améliorations de la cartographie des mouvements myocardiques basée sur la résonance magnétique. Medical Imaging. ETH Zurich (Suisse), 2022. English. NNT : . tel-03694663

HAL Id: tel-03694663

<https://theses.hal.science/tel-03694663>

Submitted on 20 Jun 2022

HAL is a multi-disciplinary open access archive for the deposit and dissemination of scientific research documents, whether they are published or not. The documents may come from teaching and research institutions in France or abroad, or from public or private research centers.

L'archive ouverte pluridisciplinaire **HAL**, est destinée au dépôt et à la diffusion de documents scientifiques de niveau recherche, publiés ou non, émanant des établissements d'enseignement et de recherche français ou étrangers, des laboratoires publics ou privés.

DISS. ETH NO. 28292

Improvements of Magnetic Resonance Based Myocardial Motion Mapping

A thesis submitted to attain the degree of

DOCTOR OF SCIENCES of ETH ZURICH

(Dr. sc. ETH Zurich)

presented by

Ezgi Berberoğlu

MSc, Middle East Technical University

born on 23.08.1987

citizen of Turkey

accepted on the recommendation of

Prof. Dr. Sebastian Kozerke

Prof. Dr. Martin Genet

Prof. Dr. Julius Guccione

09-03-2022

Abstract

Cardiovascular diseases (CVDs) remain the leading cause of death and disability worldwide. Moreover, the life quality of patients is severely decreased by the long-term care required, causing a significant increase in healthcare costs. Although several advancements have been made for CVD management in terms of diagnostic, prognostic and therapeutic techniques, the development of novel and more effective approaches is still required to decrease the prevalence of cardiac-related diseases. Early and accurate diagnosis of cardiac dysfunction plays a significant role to reduce or stop disease progression. In this respect, efforts have been mainly focused on non-invasive characterization of functional measures of myocardium that can increase the diagnostic accuracy of traditional techniques.

In clinical cardiology, cardiac performance is mostly assessed based on global functional parameters, e.g., ventricular volume, ventricular mass and ejection fraction (EF). Although EF has been the key parameter for disease diagnosis and management, it has been shown to be in normal ranges despite specific dysfunctional cases, e.g. in heart failure with preserved ejection fraction. Strain, strain rate and torsion, however, have allowed for a deeper insight into myocardial function, providing additional diagnostic and prognostic characterization on the regional level in addition to the conventional functional measures. Global longitudinal and circumferential strains are commonly used in clinical setting for assessing myocardial contractility. Although several research studies have reported left-ventricular radial strain and torsion to be early indicators of impaired myocardial contractility, they are rarely utilized in the clinical setting.

Computational models have become a powerful tool to characterize cardiac physiology in health and disease and to extract functional parameters, e.g., stress and contractility, that cannot be obtained directly by any in vivo techniques. Recent cardiac models account for many aspects of cardiac behavior, spanning from electrophysiology, fluid mechanics and material behavior. Several computational models have been proposed to study dysfunctional cases, including myocardial infarction and ischemia, valvular disease and cardiomyopathies. Moreover, incorporation of patient-specific cardiac geometries and functional parameters has

brought a novel perspective to cardiac research. Given the recent improvements in medical imaging technology, the generation of more detailed individualized cardiac models is a critical step towards bringing translational computational models into clinic.

Several imaging modalities are utilized for diagnostic purposes in the clinics. Among them, cardiovascular magnetic resonance (CMR) is accepted as the gold standard to assess myocardial function. In the context of this thesis, the focus lies on two magnetic resonance (MR) sequences: cine and tagged CMR, having their own advantageous features. Cine CMR provides excellent tissue contrast to visualize cardiac anatomy for the characterization of global functional measures, e.g., left-ventricular mass, volumes and EF. Tagged CMR allows for the assessment of local deformation, e.g. strain, strain rate and torsion. Although global circumferential and longitudinal strains have a good reproducibility across image post-processing techniques both on cine and tagged CMR, radial strain is mostly underestimated on tagged CMR and varies significantly among different techniques regardless of the image type utilized.

To investigate the accuracy and precision of strain quantification, we performed a detailed analysis using synthetic 3D tagged CMR, generated from a biomechanical model of the left ventricle. Several image characteristics were varied including image resolution, tag line distance and the signal-to-noise ratio (SNR). A finite element-based image registration technique was employed to track tissue motion over time. The resulting displacement and strain fields are compared to ground truth to assess the contribution of each image characteristic to tracking errors. Radial strain is shown to be sensitive to changes in image resolution and SNR while circumferential and longitudinal components are relatively robust with respect to changes in image characteristics. This study stands as a systematic investigation of image requirements for myocardial deformation quantification.

To address the shortcoming of individual cine and tagged CMR data analysis, we proposed a combined image analysis technique of tagged and cine CMR to improve radial strain and twist quantification. For this purpose, tracking is first performed on cine images and the resulting displacement field is utilized to mask the tagged images; tracking is then performed on the masked tagged images. The performance of the combined technique is shown both on human and porcine datasets in terms of strain and twist quantification. The analysis results reveal the

superiority of combined image registration over tagged-only analysis in terms of radial strain quantification while more physiological twist is achieved compared to cine-only registration.

Zusammenfassung

Herz-Kreislauf-Erkrankungen (CVDs) sind nach wie vor weltweit die Hauptursache für Tod und Invalidität. Darüber hinaus wird die Lebensqualität der Patienten durch die erforderliche Langzeitpflege stark beeinträchtigt, was zu einem erheblichen Anstieg der Gesundheitskosten führt. Obwohl beim CVD-Management in Bezug auf diagnostische, prognostische und therapeutische Techniken mehrere Fortschritte erzielt wurden, ist die Entwicklung neuer und effektiverer Ansätze immer noch erforderlich, um die Prävalenz von Herzerkrankungen zu verringern. Eine frühzeitige und genaue Diagnose von Herzfunktionsstörungen spielt eine wichtige Rolle, um das Fortschreiten der Krankheit zu reduzieren oder zu stoppen. In dieser Hinsicht konzentrierten sich die Bemühungen auch auf die nicht-invasive Charakterisierung funktioneller Messungen des Myokards, die die diagnostische Genauigkeit herkömmlicher Techniken erhöhen können.

In der klinischen Kardiologie wird die Herzleistung meist anhand globaler funktioneller Parameter beurteilt, z. B. Ventrikelvolumen und -masse sowie Auswurffraktion (EF). Obwohl EF der Schlüsselparameter für die Krankheitsdiagnose und -behandlung ist, wurde gezeigt, dass sie trotz spezifischer dysfunktionaler Fälle, z.B. Herzinsuffizienz mit erhaltener Auswurffraktion, in normalen Bereichen liegen kann. Dehnung, Dehnungsrate und Torsion haben einen tieferen Einblick in die Myokardfunktion ermöglicht und im Vergleich zu den herkömmlichen funktionellen Massen eine zusätzliche diagnostische und prognostische Charakterisierung auf regionaler Ebene bereitgestellt. Globale Längs- und Umfangsdehnungen werden im klinischen Umfeld häufig zur Beurteilung der myokardialen Kontraktilität verwendet. Obwohl mehrere Forschungsstudien berichtet haben, dass radiale Dehnung und Torsion des LV Frühindikatoren für eine beeinträchtigte myokardiale Kontraktilität sind, werden sie im klinischen Umfeld selten verwendet.

Computermodelle sind zu einem leistungsstarken Werkzeug geworden, um die Herzphysiologie bei Gesundheit und Krankheit zu charakterisieren und auch funktionelle Parameter, z.B. neuere Herzmodelle berücksichtigen mehrere Aspekte des Herzverhaltens, die von

Elektrophysiologie, Strömungsmechanik und Materialverhalten reichen. Es wurden mehrere Rechenmodelle vorgeschlagen, um dysfunktionale Fälle zu untersuchen, darunter Myokardinfarkt und Ischämie, Herzklappenerkrankungen und Kardiomyopathien. Darüber hinaus hat die Einbeziehung patientenspezifischer Herzgeometrien und funktioneller Parameter eine neue Perspektive in die Herzforschung gebracht. Angesichts der jüngsten Verbesserungen in der medizinischen Bildgebungstechnologie ist die Generierung detaillierterer individualisierter Herzmodelle ein entscheidender Schritt, um translationale Computermodelle in die Klinik zu bringen.

Mehrere bildgebende Verfahren werden für diagnostische Zwecke in den Kliniken verwendet. Unter ihnen gilt die kardiovaskuläre Magnetresonanz (CMR) als Goldstandard zur Beurteilung der Myokardfunktion. Im Zusammenhang mit dieser Arbeit sind zwei Magnetresonanz (MR)-Sequenzen erwähnenswert; cine und tagged CMR, die je ihre eigenen vorteilhaften Eigenschaften haben. Cine CMR bietet einen hervorragenden Gewebekontrast und damit eine Visualisierung der Herzanatomie zur Charakterisierung globaler Funktionsmasse, z.B. linksventrikuläre Masse, Volumen und EF. Das tagging CMR ermöglicht die Beurteilung lokaler Verformungen, z.B. Dehnung, Dehnungsrate und Torsion, was mit cine CMR aufgrund fehlender Merkmale in der Myokardwand nicht möglich ist. Obwohl globale Umfangs und Längsdehnungen eine gute Reproduzierbarkeit sowohl bei der cine als auch beim tagging CMR aufweisen, wird die radiale Dehnung beim tagging CMR unterschätzt und variiert erheblich zwischen den verschiedenen Techniken, unabhängig vom verwendeten Bildtyp.

Um die Genauigkeit und Präzision der Dehnungsquantifizierung zu untersuchen, haben wir in eine detaillierte Analyse mit synthetischem 3D-getaggttem CMR durchgeführt, das aus einem biomechanischen Modell des linken Ventrikels generiert wurde. Mehrere Bildeigenschaften wurden variiert, darunter die Bildauflösung, der Taglinienabstand und das Signal-zu-Rausch-Verhältnis (SNR). Eine Finite-Elemente-basierte Bildregistrierungstechnik wird verwendet, um die Gewebebewegung über die Zeit zu verfolgen. Die resultierenden Verschiebungs und Dehnungsfelder werden mit der bekannten Referenz verglichen, um den Beitrag jedes Bildmerkmals in Hinblick Verfolgungsfehlern zu bewerten. Die radiale Dehnung reagiert empfindlich auf Änderungen der Bildauflösung und des SNR, während Umfangs und Längskomponenten

relativ robust gegenüber Änderungen der Bildeigenschaften sind. Diese Studie steht als systematische Untersuchung der Bildanforderungen für die Quantifizierung der myokardialen Deformation.

Um die radiale Dehnungs und Verdrehungsquantifizierung der getaggtten CMR-Datenanalyse zu verbessern, schlagen wir eine kombinierte Bildanalysetechnik aus getaggttem und cine-CMR vor. Zu diesem Zweck wird zuerst eine Bildregistrierung an Cine-Bildern durchgeführt und das resultierende Verschiebungsfeld wird verwendet, um die getaggtten Bilder zu maskieren; die Verfolgung wird dann an den maskierten Taging-Bildern durchgeführt. Die Leistung der kombinierten Technik wird sowohl an Human als auch an Schweinedatensätzen im Bezug auf die Dehnungs und Verdrehungsquantifizierung gezeigt. Die Analyseergebnisse zeigen die Überlegenheit der kombinierten Bildregistrierung gegenüber der nur getaggtten Analyse im Bezug auf die Quantifizierung der radialen Dehnung, während im Vergleich zur reinen Cine-Registrierung eine größere physiologische Verdrehung erreicht wird.

Table of Contents

Abstract	2
Zusammenfassung	5
Table of Contents	8
Chapter 1 Introduction	10
1.1. Motivation.....	10
1.2. Outline	12
Chapter 2 Cardiac Physiology and Mechanical Modeling	13
2.1. The Heart.....	13
2.1.1. Cardiac Anatomy.....	13
2.1.2. Cardiac Microstructure.....	14
2.1.3. Cardiac Cycle.....	18
2.2. Fundamentals of Continuum Mechanics	20
2.2.1. Kinematics	20
2.2.2. Concept of Stress and Fundamental Stress Measures	23
2.2.3. Balance Principles	25
2.3. Cardiac Mechanical Modeling.....	28
2.3.1. Overview	28
2.3.2. Computational Modeling of the Heart.....	29
Chapter 3 Imaging Cardiac Function and Myocardial Motion Analysis.....	35
3.1. Global and Regional Measures of Cardiac Function.....	35
3.1.1. Myocardial Strain and Strain Rate	36
3.1.2. Left Ventricular Rotation (Twist).....	36
3.2. Imaging Cardiac Function	38
3.2.1. Overview	38
3.2.2. Cardiovascular Magnetic Resonance.....	39
3.3. Myocardial Motion Analysis	45
3.3.1. Tagged CMR.....	45
3.3.2. Cine CMR.....	48
3.3.3. Combined Approaches	49
3.3.4. Machine Learning Based Methods.....	49
Chapter 4 Clinical Utility and Future Applications of CMR Imaging.....	51
4.1. Overview	51
4.2. Diagnostic Applications	52
4.2.1. Congenital Heart Disease	52
4.2.2. Ischemic Heart Disease	54
4.2.3. Non-Ischemic Cardiomyopathies	56
4.3. Therapy Management	58
4.4. Emerging Applications.....	60

Chapter 5 In-silico Study of Accuracy and Precision of Left-Ventricular Strain Quantification from 3D Tagged MRI	63
5.1. Introduction	63
5.2. Methods	65
5.2.1. Cardiac Biomechanical Model and Reference Left-Ventricular Motion	65
5.2.2. Synthetic Image Generation	66
5.2.3. FE-based Image Registration	68
5.2.4. Performance Metrics for Cardiac Strain Quantification	70
5.3. Results	72
5.3.1. Isotropic Images.....	72
5.3.2. Anisotropic Images.....	75
5.4. Discussion	79
5.5. Conclusion	81
5.6. Supporting Information	82
Chapter 6 Quantification of Left Ventricular Strain and Torsion by Joint Analysis of 3D Tagging and Cine MR Images	86
6.1. Introduction	86
6.2. Materials and Methods	88
6.2.1. Image Acquisition and Preprocessing	88
6.2.2. FEM-based Image Registration	89
6.2.3. Coupling SSFP and 3DTAG Images	91
6.2.4. Metrics Used to Assess m3DTAG Image Registration Performance.....	92
6.3. Results	94
6.3.1. Analysis of Method Parameters.....	94
6.3.2. Method Validation	96
6.3.3. Left Ventricular Strain and Twist Quantification.....	97
6.4. Discussion	101
6.5. Conclusion	105
Chapter 7 Discussion and Outlook.....	106
7.1. Discussion	106
7.2. Outlook	108
Abbreviations	110
Bibliography	112
List of Publications.....	142
Acknowledgements	143
Curriculum Vitae.....	145

Chapter 1

Introduction

This chapter introduces the basic motivation and the brief outline of the thesis.

1.1. Motivation

Despite remarkable progress in diagnostic and therapeutic techniques, cardiovascular diseases (CVDs) remain the leading cause of death worldwide [Timmis et al., 2020; Virani et al., 2021]. According to the European Cardiovascular Disease Statistics 2019 [Timmis et al., 2020], around 9.6 million people lose their life due to a cardiac-related disease in the member countries of the European Union. Moreover, CVDs significantly contribute to healthcare expenditures, which are expected to increase exponentially in the near future [Timmis et al., 2020]. Early detection of cardiac dysfunction is crucial to allow for early treatment and to increase the life expectancy of patients. It is foreseeable that novel cardiac biomarkers integrated with modern imaging modalities will provide greater insight into cardiac physiology and pathology, supporting early diagnosis and development of more robust treatment strategies.

The assessment of regional left-ventricular (LV) function is crucial for the diagnosis and management of CVDs [Abraham et al., 2002]. Compared to LV global metrics, e.g., ventricular volume and ejection fraction, regional contractile properties are more sensitive to e.g. ischemic events, which relate to imbalances in oxygen supply and demand in myocardial tissue [Ross, 1999]. Among the clinical metrics, quantitative evaluation of wall thickness is known to yield accurate results [Castillo et al., 2003]. Myocardial strain, however, allows for a comprehensive analysis of cardiac motion accounting for deformation in the circumferential, longitudinal, and radial directions [Smiseth et al., 2016]. Moreover, LV strain rate and rotation are clinically significant metrics on the regional performance of the LV myocardium [Götte et al., 2006; Smiseth et al., 2016].

Several cardiovascular magnetic resonance (CMR) techniques have been introduced to image and quantify myocardial deformation. Among them, cine CMR has been considered the reference method for imaging cardiac anatomy and ventricular volumes [La Gerche et al., 2013]. The advantages of cine CMR, e.g., excellent tissue contrast and absence of ionizing radiation, have enabled its wide usage in clinical practice for the routine evaluation of variety of cardiac diseases [Pennell et al., 2004]. Although cine CMR yields robust estimates of global functional parameters, it is limited in assessing the regional heterogeneity of myocardial deformation due to the lack of features to be tracked on the myocardial wall. Tagged CMR allows for regional motion quantification based on line or grid pattern modulation on the LV [Zerhouni et al., 1988]. It yields estimates of deformation in the circumferential and longitudinal directions. However, tag lines generated on the myocardial wall do not allow for an accurate segmentation of endocardial and myocardial borders, compromising ventricular functional analysis. As a consequence, radial strain is consistently underestimated by any motion tracking algorithm on tagged data [Tobon-Gomez et al., 2013]. However, there is no systematic study to date devoted to the investigation of possible causes of such an underestimation.

The first part of the thesis aims to clarify resolution and signal-to-noise ratio (SNR) dependencies of strain analysis from tagged CMR by a detailed study on motion quantification from synthetic three-dimensional (3D) tagged CMR data generated using a biomechanical model of the LV. It is shown that radial strain estimation is sensitive to image resolution and SNR, implying the need for higher resolution and SNR to estimate radial strain accurately.

In view of the analysis results, the second part of the thesis presents a joint image registration technique of tagged and cine CMR for an improved LV strain and twist quantification. It is demonstrated that the combined approach provides more physiological LV strain and twist compared to each data source alone. Similar to the image combination techniques proposed in the literature [Shi et al., 2012; Schrauben et al., 2018], the aim is to utilize the advantageous features of each imaging modality; acquiring global shape information from cine CMR and local deformation from tagged CMR.

This thesis presents a systematic study on LV deformation quantification from cine and tagged CMR using a finite element-based image registration method. The research proposes improvements for enhanced radial strain estimation from tagged CMR. Moreover, the combined image analysis technique stands as a promising alternative, yielding more physiological estimates of LV radial strain and twist. Thereby, in addition to the clinically accepted deformation measures, LV radial strain and twist can be used for a more comprehensive assessment of myocardial function to detect early alterations in the myocardium before global impairment occurs.

1.2. Outline

This thesis is organized as follows. Chapter 2 lays out the basics of cardiac physiology and the current state of modeling approaches for cardiac mechanics with the fundamentals of continuum mechanics summarized. Chapter 3 introduces the cardiac imaging modalities and myocardial motion analysis techniques with an emphasis on CMR. In Chapter 4, the clinical utility of CMR tracking is introduced with a brief summary of future applications. Chapter 5 presents a detailed analysis of LV myocardial motion quantification using finite element-based image registration, that allows assessing the accuracy of current metrics while revealing possible improvements to acquire more robust estimates. To this end, Chapter 6 introduces a combined image analysis technique of cine and tagged CMR to address the limitations of each imaging modality, aiming to improve myocardial deformation assessment. Chapter 7 concludes the thesis with a discussion and outlook of improvements.

Chapter 2

Cardiac Physiology and Mechanical Modeling

The aim of this chapter is to introduce the basic concepts of cardiac anatomy and physiology, mainly focusing on the electrical and mechanical functions of the heart. A brief overview of the fundamental concepts of continuum mechanics is introduced before the current state of the art on cardiac mechanical modeling.

2.1. The Heart

This section outlines the basics of cardiac anatomy, describing the main components and their role in cardiac function. The myocardial architecture is later introduced, and the cardiac cycle is briefly summarized in terms of the electrical and mechanical activity of the heart.

2.1.1. Cardiac Anatomy

The heart is the main organ in the cardiovascular system, responsible for pumping blood throughout the body to provide the central and peripheral tissues and organs with oxygen and nutrients. Moreover, it regulates the distribution of hormones and the removal of metabolic wastes vital for the living organism. A healthy human heart is about the size of a closed fist and weighs between 200 to 425 grams.

The human heart consists of four chambers, see Figure 2.1. The right and left atria are the upper chambers, divided by the interatrial septum. The right atrium receives the venous blood through the superior and inferior venae cavae, which transport deoxygenated blood. The left atrium receives the oxygenated blood from the lungs through the pulmonary vein. The right and left ventricles, divided by the interventricular septum, constitute the lower chambers, with the LV having the largest volume among all chambers. Compared to other chambers, the

LV has a relatively thicker wall so that it can generate higher pressure to pump blood to the entire body through the aorta.

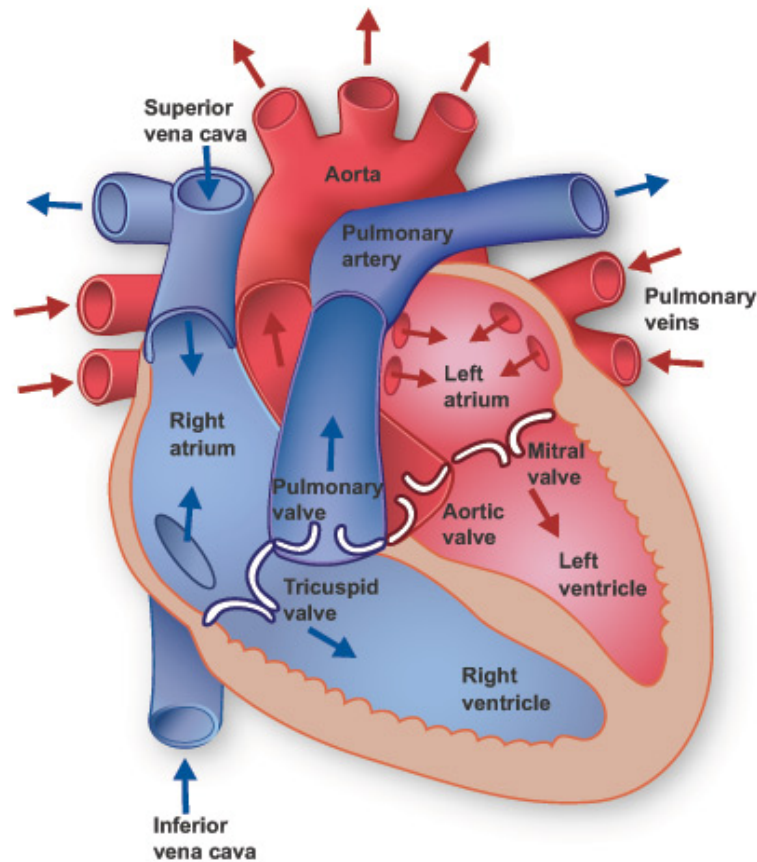


Figure 2.1. Anatomy of the human heart representing the atria, ventricles, major blood vessels, and valves. The arrows represent the direction of blood flow; red for oxygenated and blue for deoxygenated blood. Adapted from www.texasheart.org.

One-way regulation of blood flow through the heart is maintained by the atrioventricular and semilunar valves. The two AV valves, the mitral and tricuspid valves, prevent blood flow from the ventricles to the atria. The mitral valve allows blood flow from the LA to the LV while the tricuspid valve is responsible for controlling the flow from the right atrium to the RV. The semilunar valves, i.e., the pulmonary and aortic valves, prevent the backflow of blood into the ventricles.

2.1.2. Cardiac Microstructure

Covered by a double-walled sac, called the pericardium, the heart wall is composed of three distinctive layers; epicardium, myocardium, and endocardium, see Figure 2.2.

The endocardium, the innermost layer, lines the cardiac chambers. It is approximately 100 μm in thickness and primarily composed of endothelial cells. The outermost layer, the epicardium, functions as the protective layer with a thickness of 2 mm with the main constituent of epimysial collagen. The pericardial cavity, layered by the parietal pericardium outside and visceral pericardium inside, contains the pericardial fluid that helps decrease the friction between layers as the heart pumps blood.

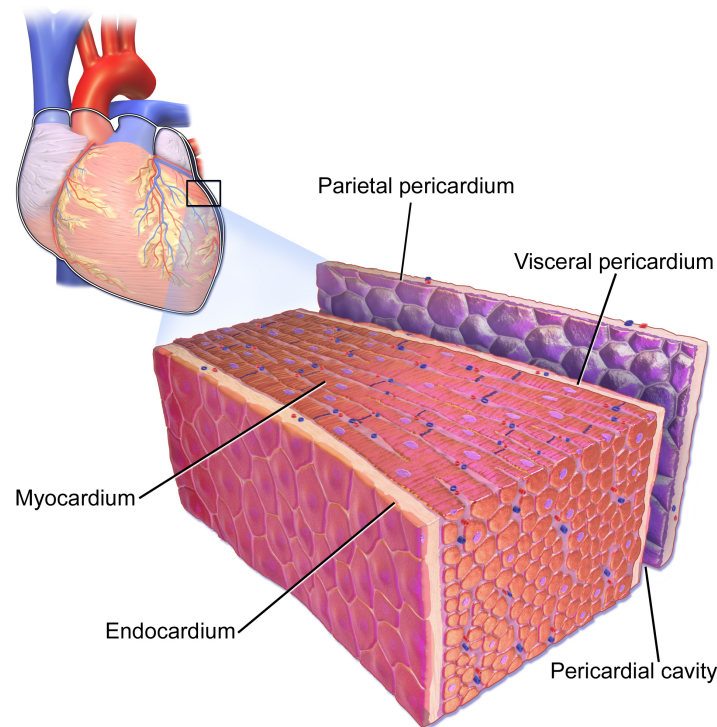


Figure 2.2. Representation of the layers of the human heart wall; endocardium (inner layer), myocardium (middle layer), and epicardium (outer layer). Illustration by BruceBlaus, licensed under CC BY 3.0.

The myocardium lies between the epicardium and endocardium and constitutes the thickest layer of the heart wall. It is the main functional unit being responsible for the pumping action. The myocardium has unique cellular and physiological characteristics that allow repeated contraction of the heart and provide an efficient mechanism to distribute blood through the whole body. It is composed of specialized collections of cells organized in a highly hierarchical structure, see Figure 2.3.

At the tissue level, the myocardium is layered into sheetlets, a small group of cardiomyocytes (muscle fibers) [Sands et al., 2005; Hales et al., 2012], composed of four to six cells with 100-

200 μm in thickness. These structures are bound by the perimysium, a collagenous connective tissue [Le Grice et al., 1997] mainly composed of type I, III, and V collagen [Light & Champion, 1984]. The laminar organization of sheetlets [Smaill & Hunter, 1991; Le Grice, Smaill, et al., 1995], which are coupled by the extracellular collagen fibers, has been associated with ventricular wall thickening at the macroscopic level during contraction of the heart [Le Grice, Takayama, et al., 1995; Costa et al., 1999]. The local arrangement of sheetlets can be determined based on the sheetlet angle that serves as a biomarker for the assessment of cardiac function [Tueni et al., 2020].

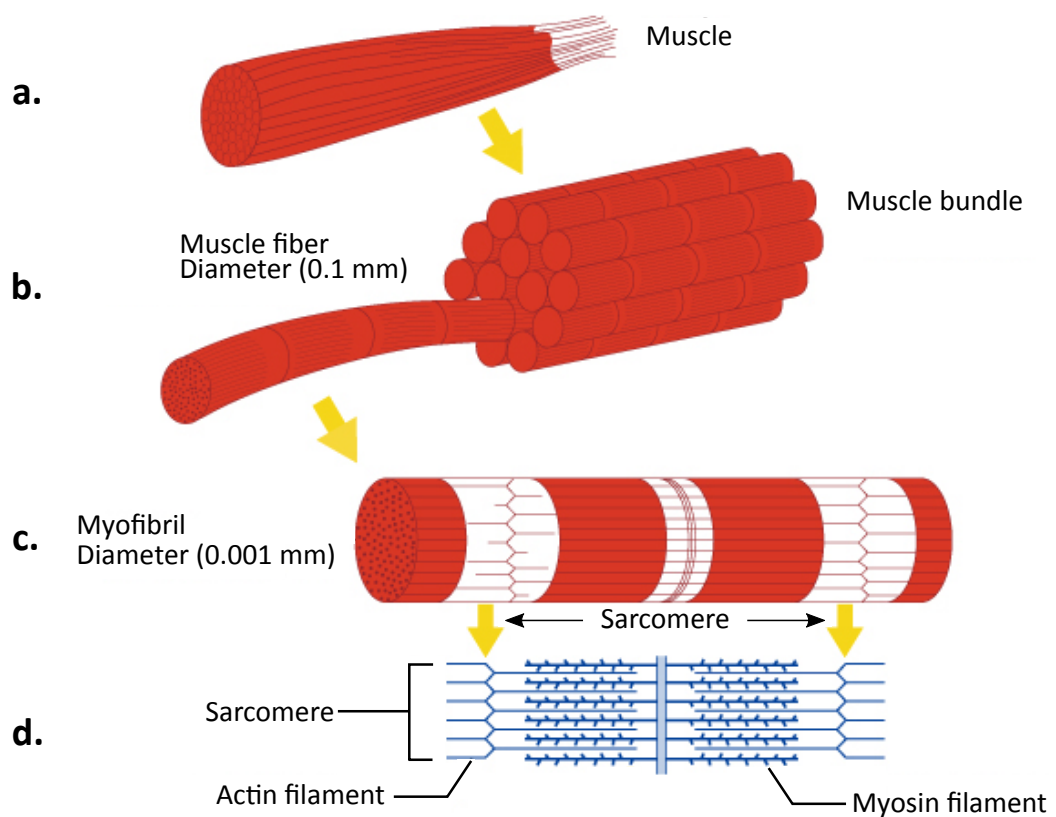


Figure 2.3. The hierarchical organization of the skeletal muscle, (a) from tissue level down to (b) muscle fiber (muscle cells) and (c) myofibrils. (d) At the lowest scale, myofibrils are made of sarcomeres with the contractile proteins actin and myosin. Adapted from www.spring8.or.jp.

The components of sheetlets, cardiomyocytes (Figure 2.3b), are the basic contractile units of the heart with a cylindrical shape and a length of around 100-150 μm and a diameter ranging between 10–25 μm . The cardiomyocytes are surrounded by cardiac collagen matrix and connected to each other through intercalated discs at their ends [Kanzaki et al., 2010] and

known to change their form and function due to the growth and remodeling of the heart. These contractile units follow a right-handed spiral-like arrangement in the endocardium to a left-handed one in the epicardium, with a smooth transition across the wall [Rohmer et al., 2007], as for example imaged by diffusion tensor imaging, see Figure 2.4. The special arrangement of fibers has been shown to play a decisive role in determining electrical and mechanical properties of the heart [Fleming et al., 2008; Lekadir et al., 2014; Palit et al., 2015; Qin & Fei, 2015].

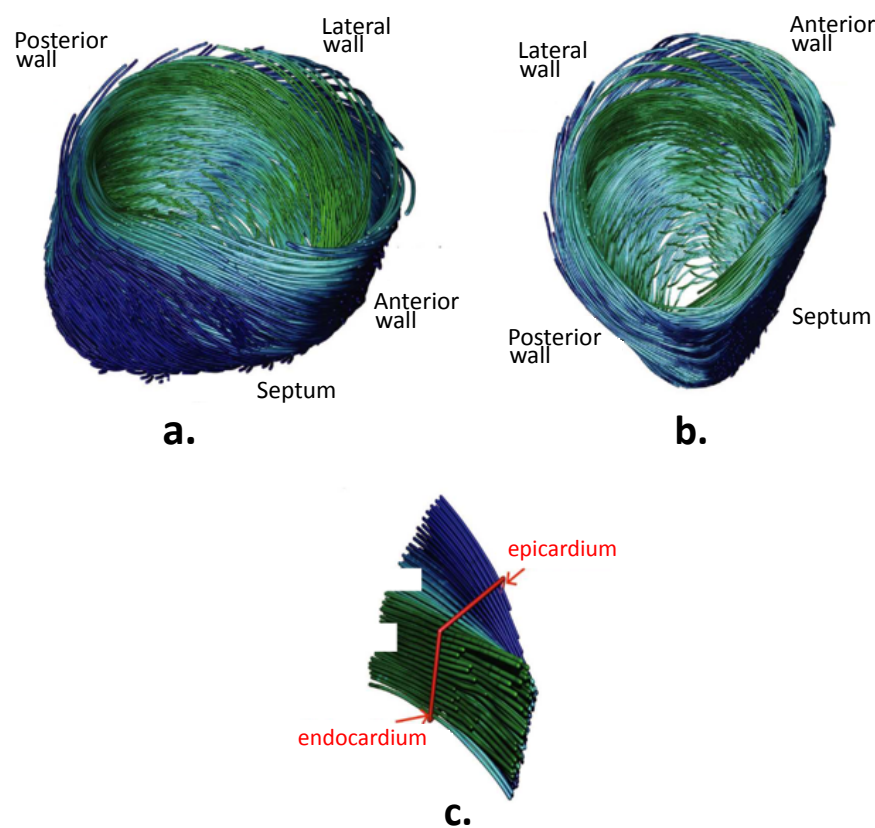


Figure 2.4. Cardiac myofiber distribution imaged by diffusion tensor imaging. The smooth transition across the wall from a right-handed spiral-like pattern in the endocardium to a left-handed one in the epicardium is represented on different views. Adapted from [Rohmer et al., 2007].

The cardiomyocytes are made up of myofibrils (Figure 2.3c), which are composed of long bundles of sarcomeres (Figure 2.3d), which are the main contractile units of the myocardium. They have an approximate length of $2\ \mu\text{m}$ and are composed of two major proteins aligned in parallel; thin actin filaments and thick myosin filaments anchored to z-lines (Figure 2.3d). These proteins generate tension, sliding over each other, thereby pulling the z-lines closer, as described in the sliding filament theory [H. E. Huxley, 1963]. Based on the complex ion

dynamics at the cellular level, this theory explains how the cross bridges are formed, and the sarcomeres change length due to contraction, which is reflected as the change of length of the muscle at the tissue level [Quarteroni, Lassila, et al., 2017].

On the cellular level, the structural changes caused by maladaptive cardiac growth can be explained by the way the sarcomeres are added to each other (Figure 2.5). In case of volume overload (e.g., due to aortic regurgitation), the sarcomeres are added in series (eccentric hypertrophy), causing ventricular dilation at the organ level. If the driving factor is volume overload (e.g., due to mitral regurgitation), the sarcomeres are arranged in parallel (concentric hypertrophy) causing ventricular wall thickening.

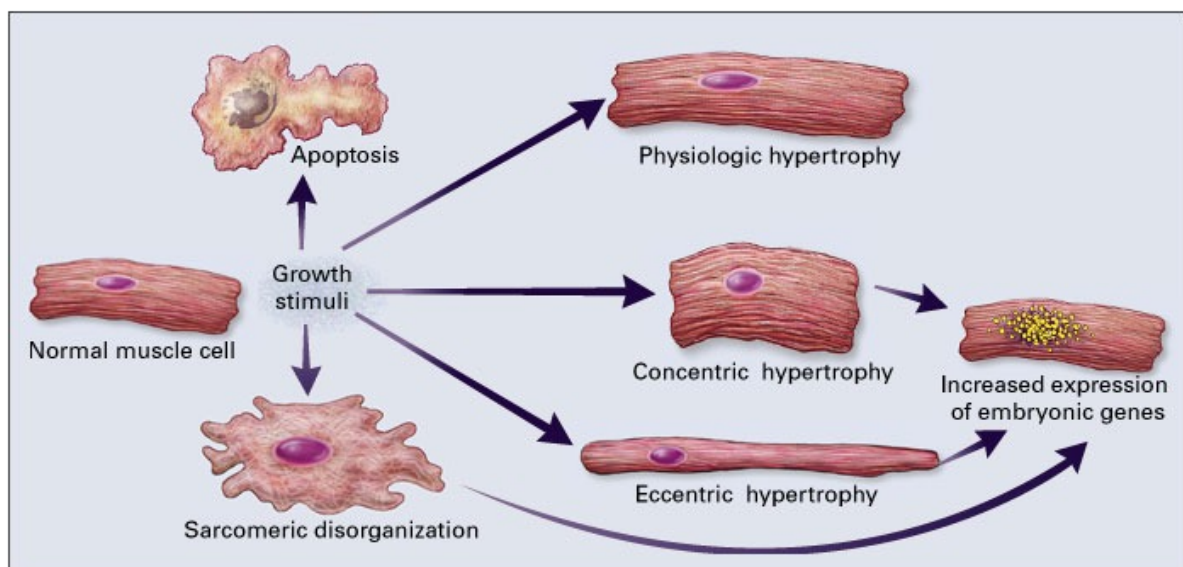


Figure 2.5. Maladaptive morphological changes in myocytes in response to different growth stimuli. In case of pressure overload, sarcomeres are added in parallel at the cellular level while they are added in series if the driving factor is the volume overload. Extracted from [Hunter et al., 1999].

2.1.3. Cardiac Cycle

A complete cardiac cycle refers to the coordinated contraction and relaxation of atria and ventricles during a heartbeat. In terms of mechanical changes, it can be divided into four phases: isovolumetric contraction, ejection, isovolumetric relaxation, and filling. Figure 2.6 represents the change in aortic pressure, atrial pressure, LV pressure, LV volume, and electrocardiogram (ECG) during a cardiac cycle. The activation is initiated by the spontaneous action potentials generated in the sinoatrial node, causing the depolarization of the atria, which is shown by the P wave on ECG. The contraction of the atria due to depolarization

causes an increase in the atrial pressure. The left ventricular volume just after the atrial contraction is called the end-diastolic (ED) volume, which is around 120 ml for a healthy human heart.

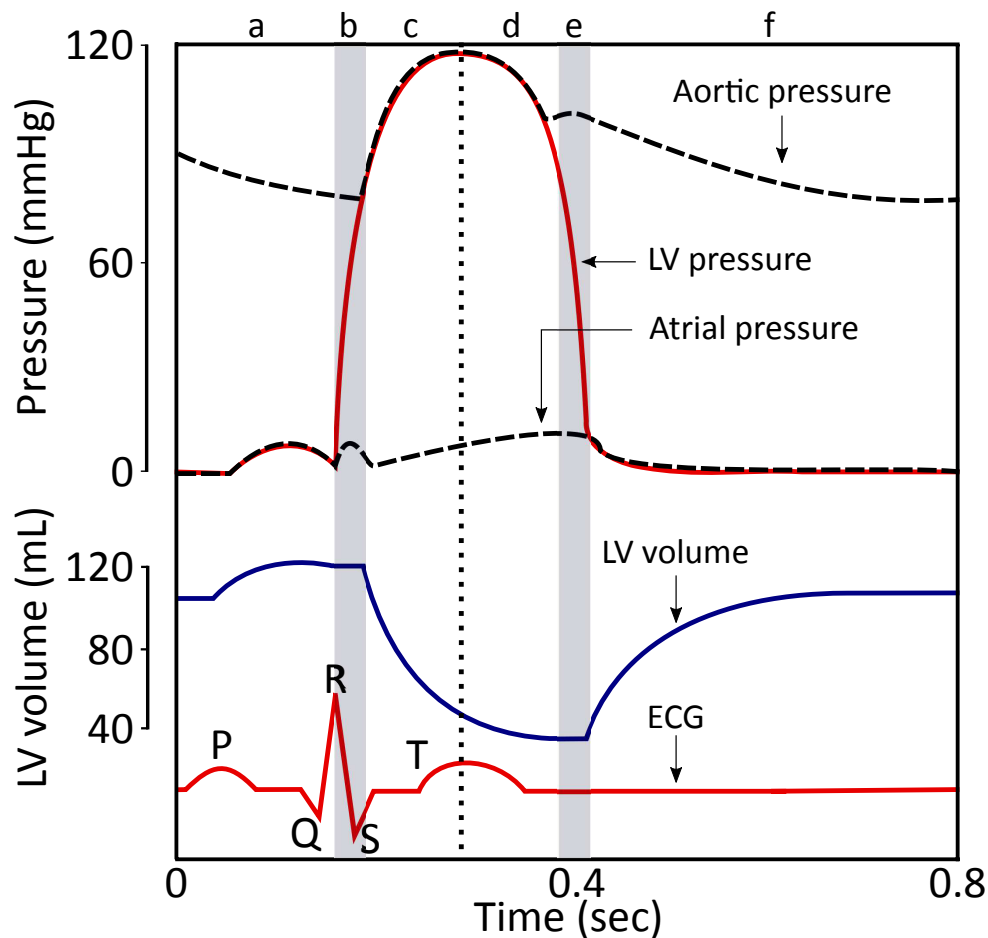


Figure 2.6. Cardiac cycle diagram showing the electrical and mechanical changes during a heartbeat. Changes in aortic pressure, LV pressure, atrial pressure, LV volume, and electrocardiogram (ECG) are depicted with respect to time. Adapted from [Klabunde, 2005].

The electrical waves are transmitted to the ventricles through the atrioventricular node, causing the ventricles to depolarize, shown by the QRS complex of the ECG. Explained by electromechanical coupling, electrical activation causes the contraction of the ventricles, followed by an increase in intraventricular pressure. As the pressure in the right and left ventricles exceeds the atrial pressure, the AV valves are closed, increasing the ventricular pressure without a change in volume while the chambers keep contracting. This phase is known as the isovolumetric contraction phase and is represented in Figure 2.6b. The interventricular pressure increases until it exceeds the aortic pressure, which causes the semilunar valves to open, and ejection begins, as shown in Figure 2.6c. During this phase, the rate of ejection decreases, which is followed by the repolarization of the ventricle, depicted

by the T wave in the ECG and a decrease in the LV pressure (Figure 2.6d). The decrease in LV pressure below the aortic pressure causes the closure of aortic and pulmonic valves, hence, the ventricular volume is kept constant while the LV pressure is still decreasing. This phase is called the isovolumetric relaxation phase (Figure 2.6e). The LV volume at the end of this phase is called the end-systolic (ES) volume, which is around 50 ml. The increase in atrial pressure during this phase is observed due to venous return. When the LV pressure falls below the atrial pressure, the AV valves open, and ventricular filling starts (Figure 2.6f).

2.2. Fundamentals of Continuum Mechanics

Continuum mechanics deals with the mathematical description of the material motion and deformation, relating the strains with the resulting stresses assuming a continuous distribution of the mass. This section outlines the fundamentals of non-linear continuum mechanics and the key quantities which form the basics of this thesis, i.e., the kinematics of deformation, stress measures, and the balance equations.

2.2.1. Kinematics

Kinematics is concerned with the mathematical representation of the motion of objects. A continuous description of the matter is assumed, represented by the body \mathcal{B} , which is composed of an infinite number of points, $\mathbf{P} \in \mathcal{B}$. The motion of a solid body can be considered as a family of configurations parameterized by time t . It is convenient to describe the configuration of a solid body at time t_0 as reference state (Lagrangian/material configuration), occupying the region Ω_0 . Likewise, the deformed state (Eulerian/spatial configuration) of the body \mathcal{B} at any time $t \neq t_0$ is denoted by the region Ω . The position vectors at reference and the spatial configurations of material point P are labeled by $\mathbf{X} \in \Omega_0$ and $\mathbf{x} \in \Omega$, respectively, see Figure 2.7.

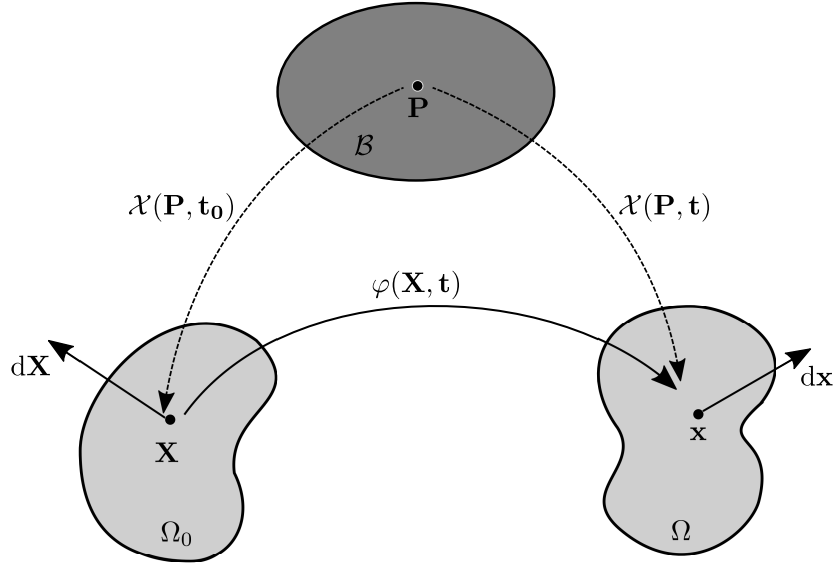


Figure 2.7. Motion of a continuous body in time.

We can relate a particle $\mathbf{P} \in \mathcal{B}$ to points $\mathbf{X} \in \Omega_0$ and $\mathbf{x} \in \Omega$ through the map χ ; $\mathbf{X} = \chi(\mathbf{P}, t_0)$ and $\mathbf{x} = \chi(\mathbf{P}, t)$, respectively, yielding the following relation:

$$\mathbf{x} = \chi[\chi_0^{-1}(\mathbf{X}, t)] = \varphi(\mathbf{X}, t), \quad (2.1)$$

φ , which is the deformation map, describing the motion of the body between the reference and the spatial configurations, which can also be uniquely inverted to represent the inverse motion; $\mathbf{X} = \varphi^{-1}(\mathbf{x}, t)$.

2.2.1.1. Fundamental Geometric Maps

Deformation gradient, $\mathbf{F}(\mathbf{X}, t) = \frac{\partial \varphi(\mathbf{X}, t)}{\partial \mathbf{X}}$, can be considered as the primary deformation measure in continuum mechanics and serves as a mapping between the referential tangent vector $d\mathbf{X}$ and its spatial counterpart $d\mathbf{x}$ through the following relation:

$$d\mathbf{x} = \mathbf{F}(\mathbf{X}, t)d\mathbf{X}. \quad (2.2)$$

Based on \mathbf{F} , the volume elements in the reference and current configurations are related by:

$$dv = J(\mathbf{X}, t)dV, \quad (2.3)$$

where J represents the determinant of \mathbf{F} , $J = \det \mathbf{F}$. The impenetrability of the material body induces $J(\mathbf{X}, t) > 0$ for $\mathbf{X} \in \Omega_0$ at any time t . For incompressible materials, J satisfies the condition

$$J = \det \mathbf{F} = 1. \quad (2.4)$$

Another geometric map represents the relationship between the normals in the reference and current configurations, denoted by \mathbf{n} and \mathbf{N} , respectively. We start by defining the volume map as follows:

$$d\mathbf{s} \cdot d\mathbf{x} = J(d\mathbf{S} \cdot d\mathbf{X}), \quad (2.5)$$

where $d\mathbf{S} = d\mathbf{S}\mathbf{N}$ and $d\mathbf{s} = d\mathbf{s}\mathbf{n}$ stand for the infinitesimal area elements in the reference and current configurations. Inserting Equation 2.2, we obtain the area (normal) map as follows:

$$\begin{aligned} d\mathbf{s} \cdot (\mathbf{F}d\mathbf{X}) &= J(d\mathbf{S} \cdot d\mathbf{X}), \\ d\mathbf{s} &= J\mathbf{F}^{-T}d\mathbf{S}. \end{aligned} \quad (2.6)$$

2.2.1.2. Strain Measures

Right and Left Cauchy-Green Strain Tensor. Cauchy-Green strain tensors are used to represent the deformation of the tangential vectors between the reference and current configurations. We assume that $d\mathbf{X}^{(1)}$ and $d\mathbf{X}^{(2)}$ are the two tangent vectors defined in the reference configuration while $d\mathbf{x}^{(1)}$ and $d\mathbf{x}^{(2)}$ represent their spatial counterparts. The dot products of the referential and spatial vectors are related by:

$$\begin{aligned} d\mathbf{x}^{(1)} \cdot d\mathbf{x}^{(2)} &= (\mathbf{F}d\mathbf{X}^{(1)}) \cdot (\mathbf{F}d\mathbf{X}^{(2)}) \\ &= d\mathbf{X}^{(1)} (\mathbf{F}^T \mathbf{F}) d\mathbf{X}^{(2)} \\ &= d\mathbf{X}^{(1)} \mathbf{C} d\mathbf{X}^{(2)}, \end{aligned} \quad (2.7)$$

where \mathbf{C} is the Right Cauchy-Green Tensor, defined in the reference configuration. In order to define its spatial counterpart, Equation 2.7 is reformulated in terms of the inverse deformation gradient, \mathbf{F}^{-1} , as follows:

$$\begin{aligned} d\mathbf{X}^{(1)} \cdot d\mathbf{X}^{(2)} &= (\mathbf{F}^{-1}d\mathbf{x}^{(1)}) \cdot (\mathbf{F}^{-1}d\mathbf{x}^{(2)}) \\ &= d\mathbf{x}^{(1)} (\mathbf{F}^{-T} \mathbf{F}^{-1}) d\mathbf{x}^{(2)} \\ &= d\mathbf{x}^{(1)} \mathbf{b}^{-1} d\mathbf{x}^{(2)}, \end{aligned} \quad (2.8)$$

where \mathbf{b} is the Left Cauchy-Green tensor. Both Cauchy-Green tensors are symmetric and positive definite, and contain strain information excluding the rigid body rotation. The principal scalar invariants of \mathbf{C} and \mathbf{b} are equal and given as:

$$I_1 = \text{tr } \mathbf{C}, \quad (2.9)$$

$$I_2 = \frac{1}{2} [I_1^2 - \text{tr}(\mathbf{C}^2)], \quad (2.10)$$

$$I_3 = \det \mathbf{C}, \quad (2.11)$$

where $I_3 = 1$ for incompressible materials in relation to Equation 2.4.

Green-Lagrange and Euler-Almansi Strain Tensor. In order to define the change in squared length of the tangents, we further introduce two more strain tensors. First, the Green-Lagrange strain tensor, \mathbf{E} , is obtained through the relation:

$$\begin{aligned} \frac{1}{2} (|\mathbf{d}\mathbf{x}|^2 - |\mathbf{d}\mathbf{X}|^2) &= \frac{1}{2} (\mathbf{d}\mathbf{X}\mathbf{C}\mathbf{d}\mathbf{X} - \mathbf{d}\mathbf{X} \cdot \mathbf{d}\mathbf{X}) \\ &= \frac{1}{2} (\mathbf{d}\mathbf{X}(\mathbf{C} - \mathbf{I})\mathbf{d}\mathbf{X}) \\ &= \mathbf{d}\mathbf{X}\mathbf{E}\mathbf{d}\mathbf{X}, \end{aligned} \quad (2.12)$$

where $\mathbf{E} = \frac{1}{2}(\mathbf{C} - \mathbf{I})$. Reformulating Equation 2.12 in terms of the Left Cauchy-Green tensor, one can obtain the Euler-Almansi strain tensor as $\mathbf{e} = \frac{1}{2}(\mathbf{I} - \mathbf{b}^{-1})$.

2.2.2. Concept of Stress and Fundamental Stress Measures

Consider a cut-out part $\mathcal{B}_p \subset \Omega_0$ and its spatial counterpart $\mathcal{S}_p \subset \Omega$, whose boundaries are represented by $\partial\mathcal{B}_p$ and $\partial\mathcal{S}_p$, respectively, see Figure 2.8. A traction force \mathbf{T} occurs on the surface of the reference subdomain \mathcal{B}_p due to the rest of the body. Similarly, \mathbf{t} , defined on the surface \mathcal{S}_p , represents the action of the rest of the body and called as Cauchy (true) traction vector. These two traction vectors can be related through the Cauchy stress tensor, $\boldsymbol{\sigma}$, according to the Cauchy's theorem:

$$\mathbf{t} := \boldsymbol{\sigma}\mathbf{n}. \quad (2.13)$$

Geometrically, $\boldsymbol{\sigma}$ is a second order tensor field mapping of the normal vector \mathbf{n} onto the tangent vector \mathbf{t} . The Kirchhoff stress tensor, is derived by multiplying the Cauchy stress tensor, $\boldsymbol{\sigma}$, with the Jacobian J

$$\boldsymbol{\tau} := J\boldsymbol{\sigma}. \quad (2.14)$$

The Lagrangian counterpart of Eulerian Cauchy's theorem can be formulated as

$$\mathbf{T} := \mathbf{P} \cdot \mathbf{N}, \quad (2.15)$$

where \mathbf{P} is the first Piola-Kirchhoff stress tensor, mapping the reference normal to \mathbf{N} to the reference traction vector \mathbf{T} defined on the deformed area and parallel with \mathbf{t} , (Figure 2.8), satisfying

$$\mathbf{T}dA = \mathbf{t}da. \quad (2.16)$$

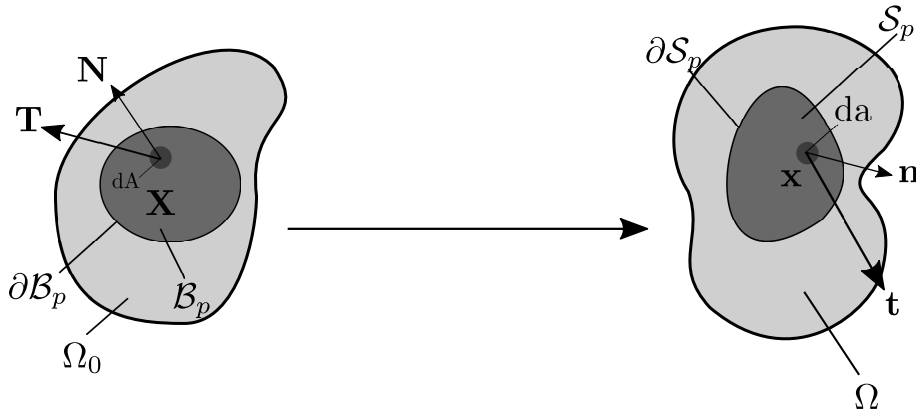


Figure 2.8. Traction vectors and the unit outward normals represented on the cut-out parts of the body for the reference and spatial configurations.

Combining these two, the first Piola-Kirchhoff stress tensor is determined as

$$\begin{aligned} \mathbf{P}N dA &= \boldsymbol{\sigma}n da, \\ \mathbf{P} &= J\boldsymbol{\sigma}\mathbf{F}^{-T}, \\ &= \boldsymbol{\tau}\mathbf{F}^{-T}. \end{aligned} \quad (2.17)$$

The last stress measure, the second Piola-Kirchhoff stress tensor \mathbf{S} , is defined as a mapping from the reference normal \mathbf{N} to the reference traction vector \mathbf{T} , through $\mathbf{T} = \mathbf{S}\mathbf{N}$.

2.2.3. Balance Principles

The balance laws of continuum mechanics are a set of differential equations that are valid for any particular material and must be satisfied for all time frames. The balance principles are based on the conservation of mass, linear momentum, angular momentum and first and second laws of thermodynamics.

Balance of mass. The fundamental principle states that mass, M , of a deformable body \mathcal{B} is assumed to be a conserved material property that is independent of time and deformation. If $\rho_0(\mathbf{X})$ and $\rho(\mathbf{x}, t)$ are the mass densities in the reference and current configurations, respectively, following relation must be satisfied:

$$\frac{d}{dt} \int_{\Omega_0} \rho_0(\mathbf{X}) dV = \frac{d}{dt} \int_{\Omega} \rho(\mathbf{x}, t) dv = 0. \quad (2.18)$$

Recalling Equation 2.1 and Equation 2.3, mass densities in the reference and current configurations can be related as follows:

$$\int_{\Omega_0} [\rho_0(\mathbf{X}) - \rho(\varphi(\mathbf{X}, t), t) J(\mathbf{X}, t)] dV = 0. \quad (2.19)$$

resulting in the continuity mass equation $\rho(\varphi(\mathbf{X}, t), t) = J(\mathbf{X}, t) \cdot \rho_0(\mathbf{X})$.

Balance of linear momentum. The momentum balance equations are obtained by adopting Newton's first and second principles of motion on the continuum level. Assuming that $\mathbf{V}(\mathbf{X}, t)$ and $\mathbf{v}(\mathbf{x}, t)$ represent the reference and current velocity fields, the total linear momentum is:

$$\mathbf{I}(t) = \int_{\Omega_0} \rho_0(\mathbf{X}) \mathbf{V}(\mathbf{X}, t) dV = \int_{\Omega} \rho(\mathbf{x}, t) \mathbf{v}(\mathbf{x}, t) dv. \quad (2.20)$$

In large deformation theory, the time derivative of the total linear momentum equals the summation of the forces acting on the body, stated by the equation:

$$\frac{d}{dt} \int_{\Omega} \rho(\mathbf{x}, t) \mathbf{v}(\mathbf{x}, t) dv = \int_{\Omega} \rho \mathbf{b} dv + \int_{\partial\Omega} \mathbf{t} da, \quad (2.21)$$

in terms of the traction force and body force, \mathbf{t} and \mathbf{b} , respectively. Inserting Equation 2.13 and using the divergence theorem and mass conservation principle, we obtain:

$$\int_{\Omega} (\text{div}(\boldsymbol{\sigma}) + \rho \mathbf{b} - \rho \dot{\mathbf{v}}) dv = 0, \quad (2.22)$$

which is valid for any domain Ω , yielding the local spatial form of the balance of linear momentum:

$$\rho \dot{\mathbf{v}} = \text{div}(\boldsymbol{\sigma}) + \rho \mathbf{b}, \quad (2.23)$$

which can be written in the reference configuration as $\rho_0 \dot{\mathbf{V}} = \text{DIV}(\mathbf{P}) + \rho_0 \mathbf{B}$.

Balance of angular momentum. Following the same approach, the total angular momentum in the reference and current configurations is formulated as the cross product of the position vector and the linear momentum:

$$\mathbf{J}(t) = \int_{\Omega_0} \mathbf{X} \times \rho_0(\mathbf{X}, t) \mathbf{V}(\mathbf{X}, t) dV = \int_{\Omega} \mathbf{x} \times \rho(\mathbf{x}, t) \mathbf{v}(\mathbf{x}, t) dv. \quad (2.24)$$

The balance principle for the angular momentum requires that the time derivative of the angular momentum should be equal to the sum of the moments acting on the body, written in equation form as:

$$\frac{d}{dt} \int_{\Omega} \mathbf{x} \times \rho \mathbf{v} dv = \int_{\Omega} \mathbf{x} \times \rho \mathbf{b} dv + \int_{\partial\Omega} \mathbf{x} \times \mathbf{t} da. \quad (2.25)$$

Recalling Equation 2.13, Cauchy and divergence theorems,

$$\int_{\Omega} \mathbf{x} \times (\rho \dot{\mathbf{v}} - \rho \mathbf{b} - \text{div}(\boldsymbol{\sigma})) dv = 0. \quad (2.26)$$

This relation holds only when the Cauchy stress tensor, $\boldsymbol{\sigma}$, is symmetric, providing the following symmetry relations

$$\boldsymbol{\sigma} = \boldsymbol{\sigma}^T, \boldsymbol{\tau} = \boldsymbol{\tau}^T, \mathbf{P}\mathbf{F}^T = \mathbf{F}\mathbf{P}^T, \mathbf{S} = \mathbf{S}^T. \quad (2.27)$$

First and second laws of thermodynamics. From the perspective of constitutive modeling, the first and second laws of thermodynamics can be used to express the “Clausius-Duhem

inequality" which is crucial while describing the consistent material behavior. For this purpose, we introduce the first principle which is concerned with the conservation of energy:

$$\mathbf{P} : \dot{\mathbf{F}} - \text{DIV}(\mathbf{Q}) + R = \dot{e}, \quad (2.28)$$

in terms of $\mathbf{P} : \dot{\mathbf{F}}$, \mathbf{Q} , R , and e that are the stress power in the current configuration, the heat flux, heat production, and the internal energy in the reference configuration, respectively.

The second law of thermodynamics explains the energy transfer between systems, introducing the variable, called entropy, \mathbf{S} , which is a measure of disorder. Based on the principle that the entropy production is a non-negative quantity, the balance equation is

$$\dot{s} + \text{DIV}\left(\frac{\mathbf{Q}}{\theta}\right) - \frac{R}{\theta} \geq 0, \quad (2.29)$$

in terms of s , and θ , that are specific internal entropy and temperature in the reference configuration, respectively. The Clausius-Duhem inequality is obtained by combining Equation 2.28 and Equation 2.29:

$$\dot{s} + \text{DIV}\left(\frac{\mathbf{Q}}{\theta}\right) - \frac{1}{\theta}(\dot{e} - \mathbf{P} : \dot{\mathbf{F}} + \text{DIV}(\mathbf{Q})) \geq 0. \quad (2.30)$$

Expanding the divergence operator and introducing the specific free energy $\Psi = \Psi(\mathbf{F}, \theta) = e - \theta s$, and its time derivative as $\dot{\Psi} = \dot{e} - \dot{\theta}s - \theta\dot{s}$,

$$\begin{aligned} \dot{\Psi} + s\dot{\theta} - \mathbf{P} : \dot{\mathbf{F}} + \frac{1}{\theta}\mathbf{Q} \cdot \nabla_x \theta &\geq 0, \\ \left(\frac{\partial \Psi}{\partial \mathbf{F}} - \mathbf{P}\right) : \dot{\mathbf{F}} - \dot{\theta}\left(\frac{\partial \Psi}{\partial \theta} + s\right) + \frac{1}{\theta}\mathbf{Q} \cdot \nabla_x \theta &\geq 0. \end{aligned} \quad (2.31)$$

The free energy function is expressed in terms of the stress tensors based on the fact that Equation 2.31 must be valid for any $\dot{\mathbf{F}}$ and $\dot{\theta}$. Hence,

$$\mathbf{P} = \frac{\partial \Psi}{\partial \mathbf{F}}, \quad (2.32)$$

where Ψ must also satisfy the material objectivity, which is a fundamental concept in continuum mechanics stating that the material properties are independent of the rigid body motions, which can be naturally enforced by using the following variant of Equation 2.31:

$$\mathbf{S} = \frac{\partial \Psi(\mathbf{C}, \theta)}{\partial \mathbf{C}}. \quad (2.33)$$

Thus, choosing an appropriate stress-strain relationship, i.e. a material behavior, amounts to specify a free energy potential. This section presents the fundamentals for the mechanical modeling approaches presented in the next section.

2.3. Cardiac Mechanical Modeling

This section outlines an overview of the current state of the art on computational modeling approaches to the cardiovascular system, with an emphasis on LV mechanical models.

2.3.1. Overview

Several mathematical models have been developed to simulate cardiac function [Noble, 2002; Hunter et al., 2003]. Due to its composite and complex nature, the first models assumed a modular framework, representing the individual components, e.g., the microvasculature [Quarteroni et al., 2000, 2009; Nichols et al., 2011], electrical [Plonsey & Barr, 1987; Gulrajani, 1988; Alonso et al., 2016] or mechanical activity of the heart [Hunter et al., 1998], systemic or pulmonary circulation [Sharp & Dharmalingam, 1999; Kheifets et al., 2013]. The ultimate goal of these computational models is to develop robust and reliable in-silico models representing the whole cardiovascular system to explain the physiological processes, using appropriate coupling conditions and advanced numerical techniques [Quarteroni, Manzoni, et al., 2017]. Advances in cardiac imaging modalities have recently provided anatomically-detailed ventricular geometries, allowing for a deeper understanding of cardiac function through more realistic models [Gurev et al., 2011]. Moreover, the cardiac models integrated with image-based individual geometries serve as a validation of image registration techniques for the assessment of myocardial contractility [Phatak et al., 2009; Genet et al., 2018; Berberoğlu et al., 2019] and to improve the current image acquisition techniques [Berberoğlu et al., 2021].

2.3.2. Computational Modeling of the Heart

Computational cardiac modeling requires linking the behavior on the molecular, cellular, and organ level simultaneously. Recent advances in computational methods provide robust and realistic cardiac models where the interaction between different functional levels can be simulated [Noble, 2002; Bovendeerd, 2012]. Such models have emerged as a promising tool to investigate different pathologies [L. C. Lee et al., 2014], e.g., aortic aneurysms, coronary stenosis, and cardiac valvular disease, and also for the optimization of existing therapeutic techniques, e.g., LV assist devices, cardiac resynchronization therapy (CRT), ablation therapy, and risk stratification. Compared to atrial [Gonzales et al., 2013] and four-chamber [Trayanova, 2011] models, research has been mostly focused on the ventricular modeling [Aguado-Sierra et al., 2011; Berberoglu et al., 2014; Genet et al., 2014; Rossi et al., 2014].

Ventricular geometry. Cardiac models have benefitted significantly from the advances in cardiac imaging [Trayanova, 2011]. The previous models of the heart were developed using idealized geometries, e.g., spherical, cylindrical, or elliptical ventricular models [Arts et al., 1979; Guccione et al., 1991, 1993; Bovendeerd et al., 1992]. Gradually, more accurate ventricular geometries were developed using histological techniques on animal hearts, e.g., rabbits and dogs [Hunter et al., 1992; Vetter et al., 1998], accounting for the anisotropic properties of the myocardium. Guccione et al. [Guccione et al., 1995] utilized an LV geometry of the canine heart to demonstrate the regional changes in LV deformation and its relation to the spatial position and fiber angle. Recently, magnetic resonance (MR) and diffusion tensor imaging provide high spatial resolution images of the heart; at the scale of the fiber and sheet structure [Helm et al., 2005; Gurev et al., 2011] that allow for a structurally-motivated strain/stress distribution for the healthy myocardium and simulation of several pathologies affecting cardiac geometry, e.g., remodeling of the heart and myocardial infarction (MI) [Vadakkumpadan et al., 2010].

Passive behavior. Cardiac mechanics simulation is based on solving a set of nonlinear differential equations, requiring the incorporation of accurate material models and boundary conditions. Several studies have been conducted to understand the highly nonlinear structure of the myocardium [Young et al., 1998; Sands et al., 2005], and models have been proposed

to understand the behavior of cardiac structure [Gilbert et al., 2007]. Today, it is known that the LV myocardium is composed of bundles of myofibers that have a transmural distribution across the ventricular wall [Le Grice, Smaill, et al., 1995], which is the basis for both the electrical and mechanical behavior of the heart. Referring to the characteristic fibrous structure of the myocardium, previous models were based on a transversely isotropic architecture, which assumes that the material properties are symmetric about the myofiber axis only [Humphrey & Yin, 1987; Humphrey et al., 1990; Guccione et al., 1991; Kerckhoffs et al., 2003]. The myocardium has later been shown to be an orthotropic microstructure through shear experiments [Dokos et al., 2002; Tueni, 2021], and several models have been developed which can model the distinct behavior of the myocardium in mutually orthogonal planes [Costa et al., 1996; Schmid et al., 2006]. In a recent model proposed by Holzapfel and Ogden [Holzapfel & Ogden, 2009], the myocardium is assumed to be a non-homogeneous, thick-walled, non-linearly elastic and incompressible material, accounting for structural properties of the myocardium, depicted in Figure 2.9.

The proposed strain energy function is formulated in terms of the unit vectors \mathbf{f}_0 , \mathbf{s}_0 and \mathbf{n}_0 representing the muscle fiber, myocardial sheet, and the normal directions, respectively:

$$\begin{aligned}\Psi(\mathbf{C}, p) &= W(I_C) + W_{ff}(I_{ff}) + W_{ss}(I_{ss}) + W_{fs}(I_{fs}) + p(J - 1), \\ \Psi &= \frac{a}{2b} \{\exp[b(I_C - 3)] - 1\} + \frac{a_{ij}}{2b_{ij}} \left\{ \exp \left[b_{ij} (I_{ij} - \delta_{ij})^2 \right] - 1 \right\} + p(J - 1).\end{aligned}\quad (2.34)$$

$I_C = \text{tr}(\mathbf{C})$ and $I_{ij} = \mathbf{C} : \mathbf{i}_0 \otimes \mathbf{j}_0$ are the invariants, δ_{ij} is the Kronecker delta and a , b , a_{ij} and b_{ij} represent the material parameters.

Recalling Equation 2.32 and Equation 2.33, the explicit forms of stress tensors can be derived from the strain energy function. The isotropic and transversely isotropic strain energy functions can be written by setting $a_{ff} = b_{ff} = 0$ and $a_{ss} = a_{ss} = a_{fs} = b_{fs}$, respectively. The HO model is advantageous over the others in the sense that in addition to biaxial data, it accounts for the shear data to model the orthotropic behavior accurately [Holzapfel & Ogden, 2009].

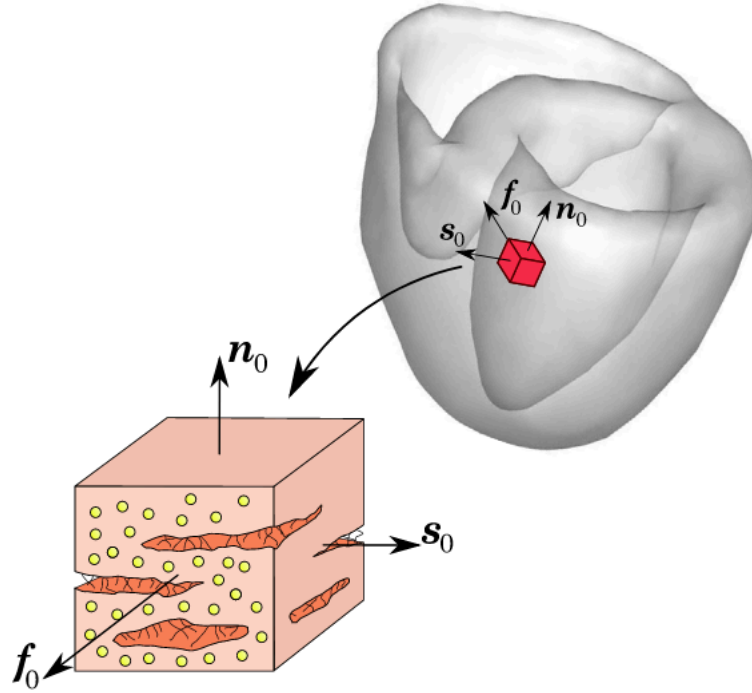


Figure 2.9. The orthotropic microstructure of the myocardium. f_0 and s_0 are the unit vectors representing the fiber and sheet directions, respectively, while n_0 denotes the unit vector in the direction orthogonal to f_0 and s_0 . Adapted from [Berberoglu et al., 2014].

Electrical models. Apart from the purely passive mechanical behavior, LV models are further enhanced with the mathematical descriptions of active muscle contraction, which can be explained by the complex ion mechanisms at the cellular level [Ter Keurs et al., 1980, 1988]. Numerous quantitative descriptions have been proposed to simulate the action potential generation in the cardiac cell [Hodgkin & Huxley, 1952]. Derived from [Hodgkin & Huxley, 1952], the Fitz Hugh-Nagumo model [FitzHugh, 1961; Nagumo et al., 1962] is one of the simplest phenomenological approaches to simulate the action potential of the excitable media, which was later tailored to cardiac cells by the Aliev-Panfilov model [Aliev & Panfilov, 1996]. More detailed models representing the mechanics of ion channels were introduced [Ten Tusscher et al., 2004; Corrado & Niederer, 2016]. These models have been incorporated into finite-element models of LV to couple the cellular level mechanisms with organ-level models [Hunter et al., 1998; Ambrosi et al., 2011; Land et al., 2012; Göktepe et al., 2014] in order to predict global cardiac function.

Active contraction. A physiologically relevant constitutive material model should account for the active contraction of the myocardium in order to accurately simulate the cardiac behavior both in health and disease. Originating from the classical Hill model [Hill, 1938, 1949] on modeling skeletal muscle tissue, simple mathematical models were developed to simulate the contraction mechanism of the myocardium. With the inclusion of the actin-myosin bridging to simulate the active muscle response [A. F. Huxley, 1957], first detailed models have been proposed [Wong, 1971, 1972], motivated by the mechanisms and structure at the molecular level. Further models accounted for the fiber orientation, muscle length, and kinetic properties [Tözeren, 1985]. A deactivation model of cardiac contraction was implemented to quantify active fiber stress, predicting transmural ES strain distribution in good agreement with experiments [Guccione et al., 1993]. In another study, Guccione et al. [Guccione et al., 1995] implemented a microstructurally based 3D ventricular contraction model using an axially symmetric LV geometry of a canine heart. The in-plane strains estimated from the model were shown to be in good agreement with the measurements while the transverse shear strains are not estimated at all. Several other models have been proposed to account for the cellular dynamics [Hunter et al., 1998; Bestel et al., 2001; Niederer et al., 2006]. Recent work by Chapelle et al. [Chapelle et al., 2012] extended an earlier model [Bestel et al., 2001] incorporating the energy input for accurate modeling of mechanical work.

Boundary conditions. For the heart models, determination and handling of realistic boundary conditions remain a key challenge. The lack of surrounding structures in cardiac models needs to be compensated by imposing adequate boundary conditions to match the expected physiological response. The literature on cardiac models considers two main approaches for the determination of boundary conditions; one is the hemodynamics of blood flow and its mechanical interaction with the inner layer of the atrial and ventricular cavities and another is the mechanical interaction between the heart and the pericardium. Several models have been developed to represent the blood flow dynamics [Doost et al., 2016] from zero-dimensional (0D) to multidimensional models. For the purpose of simulating ventricular mechanics, however, 0D models have been shown to be accurate enough to represent the circulatory system [Kerckhoffs et al., 2007]. Among many aspects of computational cardiac models, simulating the blood flow provides an understanding of the hemodynamics in the cardiovascular system. The most basic form of 0D models was introduced by Otto Frank

[Sagawa et al., 1990] as a two-element Windkessel model, which aims to predict the cardiac output as a function of pressure in the aorta. The modeling of blood flow is formulated analogously to electrical conduction in a circuit, where electrical current, potential, capacitance, and resistance represent the blood flow, blood pressure, arterial compliance, and resistance, respectively. Due to the shortcomings of two-element models, especially in simulating the resistance of the valves, a three-element Windkessel model was proposed with an additional resistive element [Westerhof et al., 1971]. The model can be further improved with the addition of an inductor for the incorporation of inertia of blood [Stergiopulos et al., 1999]. 0D models are sufficient to model the contribution of global arterial parameters, however, distributed models are required to simulate the pressure and flow locally. 1D models are well suited to analyze the flow and pressure wave, accounting for the geometry and the material properties of arteries. Moreover, they are computationally advantageous over multi-scale models as they are formulated in only one spatial dimension and time. Several 1D models have been proposed in the literature to simulate the hemodynamics of both parts and the entire cardiovascular system [Van De Vosse & Stergiopulos, 2011]. Recently, 1D models have been used in 3D fluid-structure interaction models to provide the boundary conditions and also for patient-specific models due to their greatly reduced computational expense compared to multi-scale models [Van De Vosse & Stergiopulos, 2011]. Due to their complexity and the computational expense, 3D models are generally applied to model the local phenomena of the system in case a more detailed description of local flow-field details is required. These models are based on computational fluid dynamics and yield the properties that cannot be derived from 1D models, e.g., wall shear stress or vorticity fields [Van De Vosse & Stergiopulos, 2011]. Depending on the objective, combinations of the models can be employed.

In addition to modeling the hemodynamics, another boundary condition is imposed by the mechanical interaction between the heart and the pericardium. Although pericardial fluid was previously thought to provide the mechanical interaction with the heart [Holt, 1970], it was later shown that the fluid only helps decrease the friction while the pericardium slides over the endocardium [Hills & Butler, 1985]. Several models have been proposed to impose the effect of the pericardium as a diastolic constraint [Jöbsis et al., 2007] although the systolic effect has been studied mostly on animals [Sudak, 1965; Holt, 1970]. The biventricular heart

models include constraints either as viscoelastic boundary conditions [Chabiniok et al., 2012] or by defining a fixed pericardium warping the myocardium to satisfy the no penetration condition [Marchesseau et al., 2013]. The effect was also formulated partially by applying pericardial boundary conditions on the apex [Sainte-Marie et al., 2006] or apex and valve annuli [Sermesant et al., 2012; Tobon-Gomez et al., 2013]. Four-chamber models [Augustin et al., 2016; Land & Niederer, 2018], however, are more complex to simulate especially in applying the boundary conditions, and none of them is sufficient to represent physiological behavior. The most detailed model has been proposed by [Fritz et al., 2014], which requires solving multiple contact problems, hence, becomes computationally expensive. The reader is referred to [Peirlinck et al., 2019; Pfaller et al., 2019] for more information about the application of boundary conditions.

Chapter 3

Imaging Cardiac Function and Myocardial Motion Analysis

This chapter outlines the fundamentals of cardiac imaging and motion analysis. Section 3.1 introduces the global and regional metrics used to assess cardiac performance and their clinical relevance. The imaging techniques used to measure these metrics are later introduced in Section 3.2, and the related motion analysis techniques are summarized in Section 3.3 with an emphasis on MR-based imaging.

3.1. Global and Regional Measures of Cardiac Function

Quantification of cardiac function on the global basis is widely performed by examining myocardial mass, cavity volume, and ejection fraction, defined as the percentage of the blood volume leaving the heart during each cardiac cycle [Frangi et al., 2001]. Despite its common clinical use for the assessment of cardiac performance, EF is limited in assessing the contractile properties of the heart [Earls et al., 2002]. In contrast, regional changes are shown to allow for proper diagnosis and early intervention for many cardiac diseases [Sutherland et al., 1994; Nagueh et al., 2001; Ibrahim, 2011; Ng et al., 2011]. Among them, ischemic heart disease (IHD) is known to cause local dysfunctions of the heart wall, and most of the time, global functional measures show limited sensitivity to detect the location and severity of infarction [Friedberg & Mertens, 2009; Collins, 2015]. Moreover, regional changes in cardiac function are found to be a strong indicator of both hypertrophic cardiomyopathy (HCM) [Runqing et al., 2006; Serri et al., 2006; Smiseth et al., 2016; Huang et al., 2017] and heart failure with preserved ejection fraction [Hasselberg et al., 2015; Smiseth et al., 2016].

To this end, the current research has been focused mostly on the determination of regional metrics to quantify local cardiac function. Several metrics have been defined to quantify the

regional function of the heart. Among them, myocardial wall thickening, strain, and strain rate are the most commonly used regional measures. Myocardial wall thickening is computed as the percentage change in ventricular wall thickness between the ES and ED phases, and are known to be a sensitive marker to detect pathological tissue, e.g., infarcted myocardium in IHD patients [Engblom et al., 2009].

3.1.1. Myocardial Strain and Strain Rate

Myocardial strain and strain rate are known to allow for the early detection of regional dysfunctions before the onset of global abnormalities [Smiseth et al., 2016]. The strain has been shown to be more accurate in determining the regional properties of the myocardium compared to wall thickness [Götte et al., 2001], which has also been confirmed in animal studies [Azhari et al., 1995]. It also helps to understand the normal function of the heart by revealing physiologic heterogeneities [Moore et al., 2000; Kuijer et al., 2002; Jeung et al., 2012]. Owing to the ventricular geometry, myocardial strain is best represented in the local coordinate system as shown in Figure 3.1. Radial strain represents the thickening of the ventricle and has positive values during systole ranging between 30%-40% on average for a healthy human heart [Kuijer et al., 2002] (Figure 3.1b, top). Circumferential (Figure 3.1b, middle) and longitudinal (Figure 3.1b, bottom) strains remain negative as they represent the shortening and compression of the ventricle, respectively [Hui Wang & Amini, 2012], and range between -15% to -20% [Jeung et al., 2012]. Regional strain analysis is usually performed segment-wise, using the 16 or 17 segment models published by the American Heart Association [Cerqueira et al., 2002] (Figure 3.2). Accordingly, the 3D ventricle is divided into three longitudinal layers, which are further divided into 4-6 circumferential sectors.

3.1.2. Left Ventricular Rotation (Twist)

The LV performs a wringing motion during contraction. In a healthy heart, when viewed from base to apex, the heart contracts counterclockwise at the basal and clockwise at the apical regions (Figure 3.3), which is explained by the helical arrangement of the myofibers. The angle of rotation is calculated for all points in LV around a pre-determined axis of rotation for each heart phase with respect to the ED configuration. The left ventricular twist is defined as the

difference in average rotation in apical and basal regions of the LV. Torsion can consequently be computed by dividing the twist by the length in the long-axis direction.

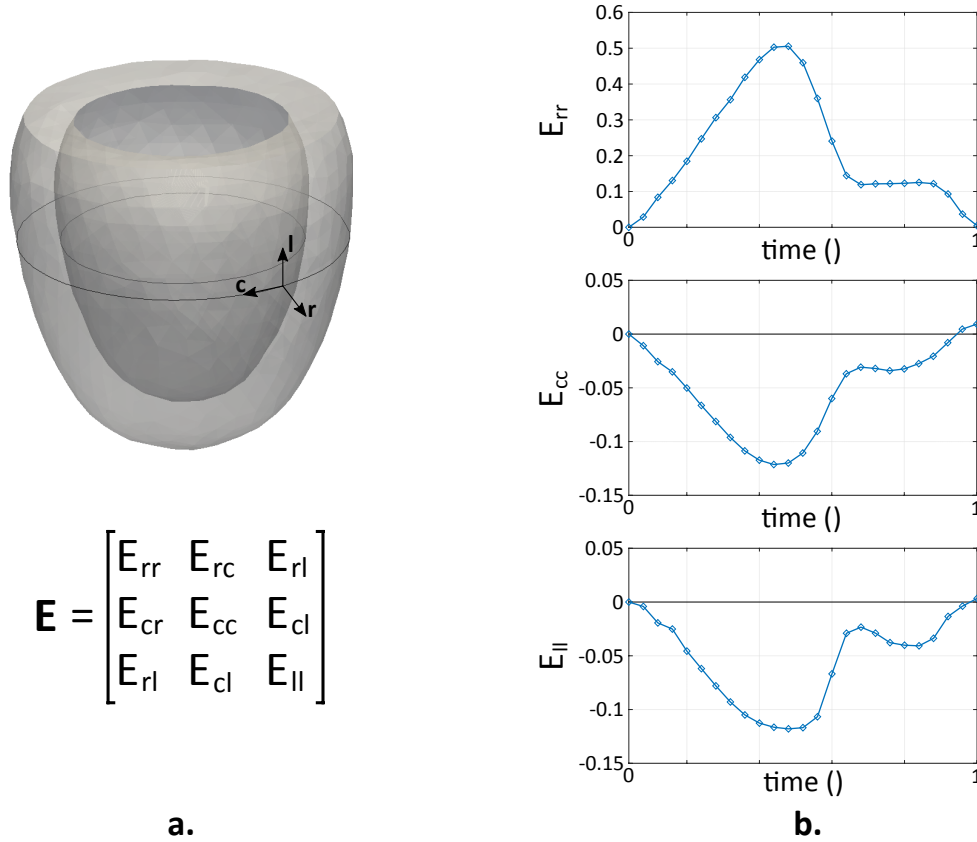


Figure 3.1. Left ventricular strain components. (a) E_{rr} , E_{cc} , and E_{ll} represent the principal components: radial, circumferential and longitudinal strains, respectively. The shear components are also in matrix representation. (b) Radial strain (top) represents the wall thickening and ranges between 30%-40% during systole for a healthy human heart [Kuijjer et al., 2002]. Circumferential (middle) and longitudinal (bottom) components have their peak systolic values at around -15% [Jeung et al., 2012] and represent the shortening and compression of the ventricle, respectively.

The rotation is heterogeneous from sub-epicardium to sub-endocardium, and the twist ranges between -10° and -15° for a healthy human heart [Sengupta et al., 2008]. It has been shown that LV twist is a robust parameter in determining myocardial function [Götte et al., 2006] and is an efficient biomarker to assess ventricular ejection during contraction [Ibrahim, 2011]. It can also have increased values in the early stages of HCM [Imbalzano et al., 2011].

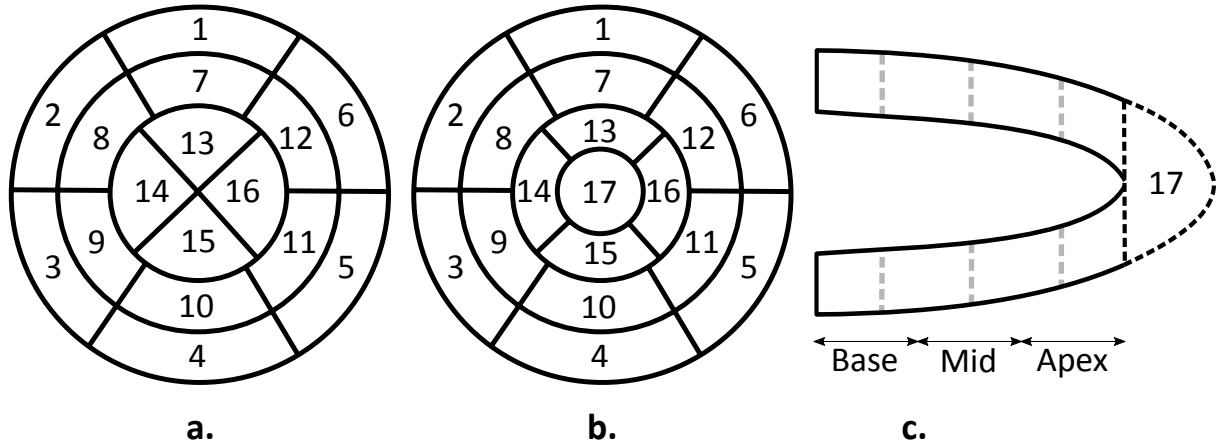


Figure 3.2. Left-ventricular segmentation proposed by the AHA model. Polar plots representing (a) 16-segment and (b) 17-segment models. (c) The 17-segment model has one more sector in the apex, which is also shown by the dashed lines in the longitudinal view. Both models have six basal and six mid-cavity sectors.

3.2. Imaging Cardiac Function

3.2.1. Overview

Several imaging modalities have been developed to investigate the structural and functional properties of the heart. The first technique used to measure the regional function was placing physical markers such as radiopaque materials [Brower et al., 1978; Ingels et al., 1980; Reneman et al., 2011; Meier et al., 2017], or ultrasound crystals [Rankin et al., 1976; Myers et al., 1986; Villarreal et al., 1988] in the heart muscle tissue, allowing for tracking material points on the ventricular wall. Although it is possible to measure regional deformation using these markers, the technique is limited by its invasiveness and the finite number of markers that can be implanted. Moreover, there is a high risk that the implanted markers may add bias by altering the normal deformation pattern of the tissue.

Later, several imaging techniques have been introduced for the quantitative assessment of regional function using non-invasive and more accurate measurements [Ibrahim, 2011]. Among them, the most widely accepted ones are echocardiography, cardiac computed tomography, and MRI. Echocardiography is commonly used in the clinical setting as it is advantageous in terms of availability and portability while offering a low-cost option to image the heart with a sufficient temporal resolution. It allows for an accurate representation of

cardiac function through 3D echo and contrast-enhanced echo, while Doppler echo is available to measure blood flow velocity. Tissue Doppler imaging [Miyatake et al., 1995; Abraham et al., 2007] and speckle tracking [Amundsen et al., 2006; Geyer et al., 2010] have been introduced for the measurement of myocardial strain. Despite many advantageous features, echocardiography is limited by its operator dependency and low SNR. Computed tomography offers superior spatial resolution, which allows for imaging of fine features such as the coronaries [Earls et al., 2002]. On the downside, CT requires the use of iodinated contrast agents, and the patient is exposed to ionizing radiation during imaging.

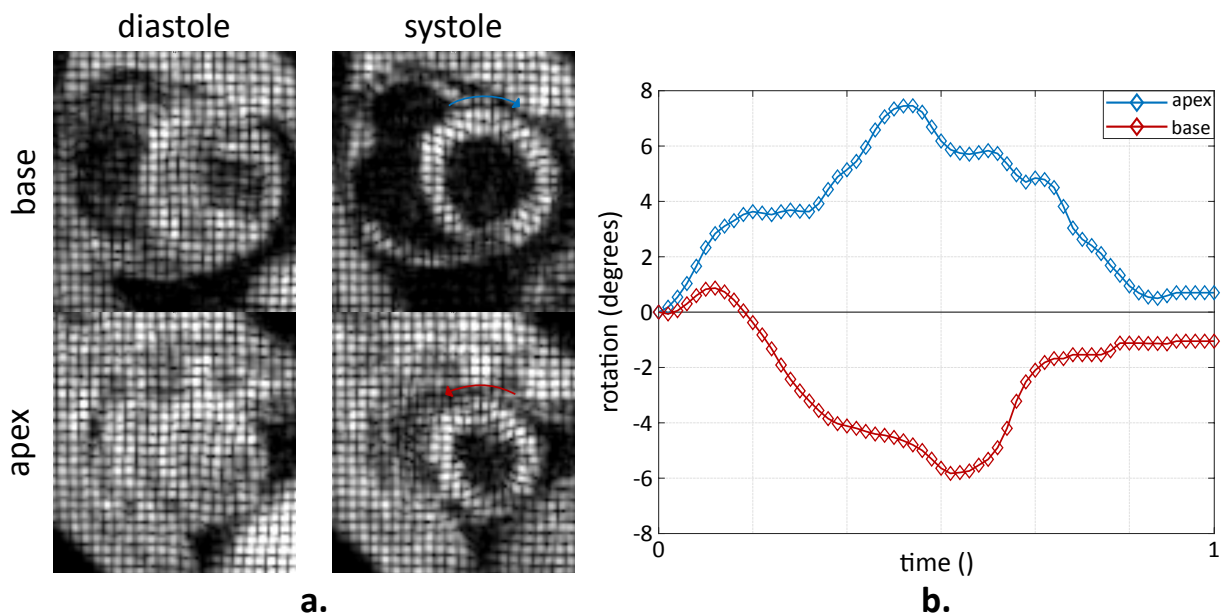


Figure 3.3. Left-ventricular rotation. (a) Tagged MR images showing the deformation pattern in the basal and apical slices for diastole and systole in a porcine heart. Shown by the arrows on the images in the systolic time frame are the LV rotation directions, which are also represented by the curves in (b). The difference in rotation between apical and basal regions for each time frame yields the twist.

3.2.2. Cardiovascular Magnetic Resonance

CMR is a non-invasive imaging technique widely used for the diagnosis and management of CVDs [Earls et al., 2002]. It is accepted to be the gold standard for the assessment of cardiac function, volumes, and also tissue perfusion as well as valve motion. In addition to global functional measures, it enables assessing regional metrics, e.g., strain, strain rate, and torsion [Götte et al., 2006]. The main advantageous feature of CMR is the variety of measurements possible, e.g., myocardial function, flow, stress perfusion, viability, angiography, making it a

key imaging modality for the diagnosis of myocardial ischemia, congenital heart disease, assessment of ventricular volumes for both LV and RV. Recent progress in CMR imaging also allows for the acquisition of high-resolution [Ortega et al., 2011; Kutty et al., 2013] images and provides 3D and 4D imaging options at user-defined orientations. Moreover, it is known to have advantages over echocardiography in terms of the image artifacts and contrast [Peng et al., 2016] and allows for the assessment of tissue viability through delayed-enhancement CMR. There has been extensive research in clinical MRI [Ibrahim, 2017] to reduce scan time, improve image quality (increasing temporal and spatial resolution), and develop new sequences directly aiming at determining specific disease characteristics.

3.2.2.1. CMR Tagging

CMR tagging permits quantifying regional myocardial deformation and has evolved since it was first introduced by Zerhouni et al. [Zerhouni et al., 1988] in the late 1980s. This technique allows labeling myocardial tissue and tracking these labels to quantify the deforming heart. To this end, radiofrequency pulses, including interspersed magnetic field gradients, are applied at end-diastole to spatially modulate tissue magnetization [Zerhouni et al., 1988]. The contrast in the tagged images is affected by the time span between the tagging preparation and image acquisition, which is explained by the longitudinal relaxation of tagged magnetization [Fischer et al., 1993]. The tagging pattern degrades toward the end of the cardiac cycle, compromising the performance of myocardial motion analysis, which is also known as tag fading. In order to increase the spatial frequency of taglines, DANTE was introduced by Mosher and Smith [Mosher & Smith, 1990], providing flexibility to control the width and spacing of the taglines.

Spatial modulation of magnetization (SPAMM) has been introduced by Axel and Dougherty [Axel & Dougherty, 1989b] as a fast and efficient alternative to the original technique [Zerhouni et al., 1988]. The grid tag pattern generated by SPAMM is achieved by a pair of nonselective radiofrequency pulses playing out at either side of a magnetic field gradient. Here the single gradient introduces a spatially-dependent sinusoidal phase. Since its invention, SPAMM has been validated in several studies [Young et al., 1993; Moore et al., 1994] to assess myocardial contractility in the clinical setting [Yeon et al., 2001]. In order to address tag

fading of SPAMM, Fischer et al. [Fischer et al., 1993] introduced complementary SPAMM (CSPAMM). The CSPAMM images are acquired by subtracting two SPAMM images with phase-shifted, i.e., inverted tag line patterns, thereby removing the signal that does not contain motion information. This technique was further improved by slice-following CSPAMM [Fischer et al., 1994], which accounts for the through-slice motion of the heart. Several other techniques have been proposed to acquire 3D myocardial motion pattern. For this purpose, Kuijer et al. [Kuijer et al., 1999] combined in-plane motion from tagged images with the through-plane motion measured from phase-contrast based velocity maps. In another study, tagged CMR of orthogonal LV planes were combined for 3D strain analysis of the LV myocardium [Kuijer et al., 2000]. Based on the CSPAMM technique, accelerated whole-heart 3D tagging technique was developed to address the misalignment problems observed in multi-slice image acquisitions [Ryf et al., 2002]. Further improvements have allowed for a reduction of scan time enabling imaging in three [Rutz et al., 2008] or even in a single breath-hold [Stoeck et al., 2012].

While CMR tagging is a powerful technique, providing detailed information of myocardial motion, it still needs to be improved for the quantification of radial strain, which is relatively inaccurate due to the finite number of tag lines on the myocardial wall [Moore, McVeigh, et al., 2000]. Since its development, several attempts have been made to develop more effective pulse sequences and image acquisition techniques [Nguyen et al., 2003; Pai & Axel, 2006]. Special tagging patterns have been proposed by matching the cardiac geometry and tagging pattern. Among them, radial and polar tagging [Bosmans et al., 1996; Nasiraei-Moghaddam & Paul Finn, 2014] yield tagging patterns compatible with the pseudo-cylindrical coordinate system of the heart while localized tagging allowed for customizing the tagline spacing [McVeigh & Bolster, 1998].

3.2.2.2. Cine Imaging

Cine CMR has become the gold standard in clinical applications to assess the global functional parameters such as ventricular volumes, EF, and mass [Castillo et al., 2003]. It provides excellent temporal [Barkhausen et al., 2001; Plein et al., 2001] and spatial resolution, with a high SNR and tissue contrast [Barkhausen et al., 2001; Pereles et al., 2001]. The most fundamental contrast generating mechanism in cine CMR is the difference in relaxation times

of tissues [Ibrahim, 2017]. Cine CMR depicts morphologic and functional abnormalities with great precision and provides better diagnostic confidence compared to other techniques [Pereles et al., 2001]. Owing to the relative homogeneity of relaxation times in the myocardial wall, cine CMR provides limited information about the transmural variation of cardiac motion pattern, e.g., on the relative rotation of the endocardial layer relative to the epicardial layer (transmural shear) or of basal with respect to apical slices (torsion) [Ubbink et al., 2006]. CMR imaging provides a set of parallel short-axis images and two-chamber, three-chamber, and four-chamber long-axis images (Figure 3.4). Most of the cardiac motion tracking algorithms on cine CMR require an accurate delineation of epicardial and endocardial borders (shown in Figure 3.5) either by manual or automated segmentation.

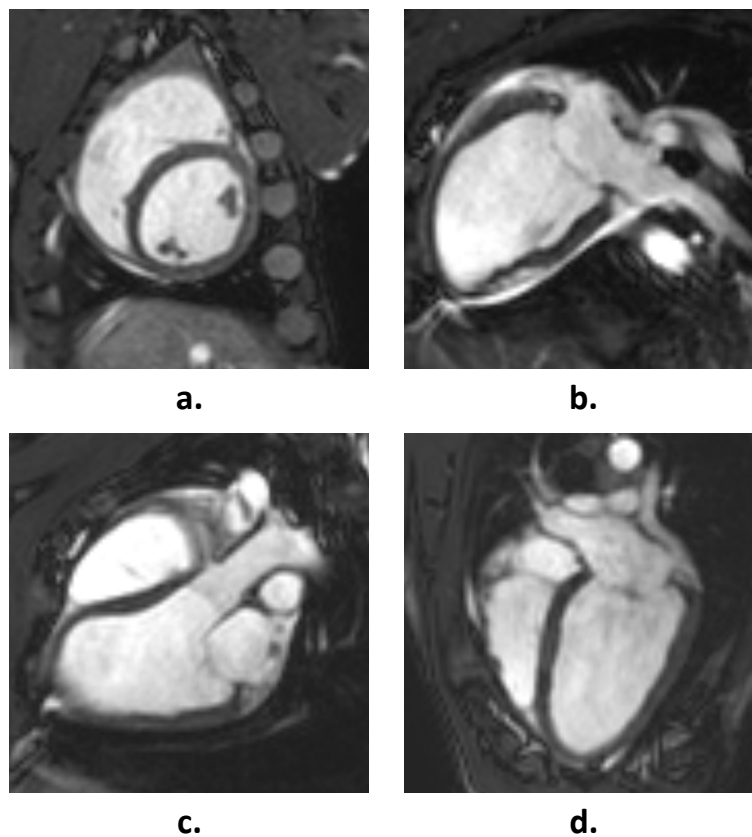


Figure 3.4. Cine MR images of the pig heart showing (a) short-axis, (b) two-chamber, (c) three-chamber, and (d) four-chamber views.

Conventional cine CMR is performed using a slice-based approach, acquiring 2D short-axis images that require multiple breath-holds [Leiner & Strijkers, 2018]. In addition to patient discomfort, this technique is susceptible to respiratory motion artifacts. Moreover, the technique relies on the operator's experience to accurately plan the short-axis slices. Therefore, several improvements have been proposed to overcome these limitations in the

clinical setting. Compressed sensing CMR acquisition now yields full coverage of the LV with high temporal and spatial resolution in a single breath-hold [Vincenti et al., 2014]. The method provides reliable LV mass, volume, and EF in the clinical setting.

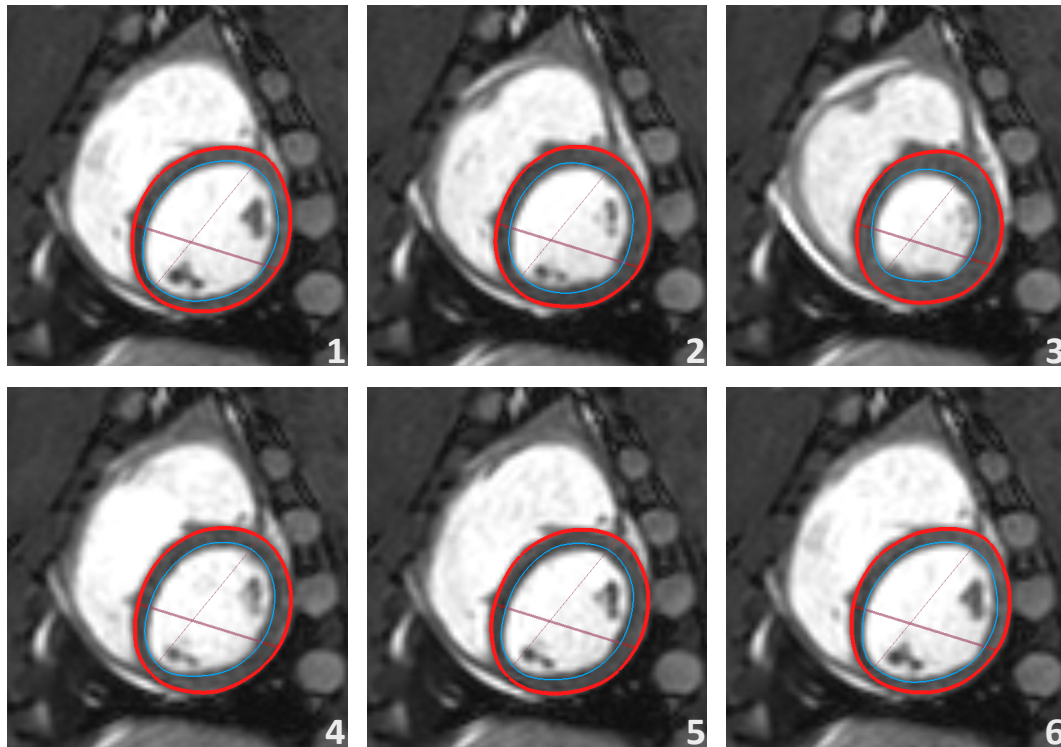


Figure 3.5. Cine CMR images of the pig heart showing the short-axis view for different time frames. Starting from the top-left corner (end diastole), endocardial and epicardial borders are represented by the blue and red contours, respectively. The thickening of the ventricular wall is clearly observed at the end-systolic time frame (slice number 3) compared to the reference configuration.

3.2.2.3. Alternative CMR Techniques

Cine and tagged CMR have their own limitations for myocardial deformation quantification. To take advantage of both imaging techniques, the patient undergoes both cine and tagged CMR in consecutive scans. To reduce the number of scans, recent studies have focused on the improvement of current techniques to allow for the quantification of regional and global ventricular properties in a single scan, making the process more feasible for clinical use [Schrauben et al., 2018]. Subtly-tagged steady state free precession (SSFP) (SubTag SSFP) imaging, as proposed by Schrauben et al., allows for the acquisition of cine CMR with tag pattern superimposed, thereby combining the evaluation of both ventricular function and more accurate regional strain assessment in a single scan.

Displacement encoding with stimulated echoes (DENSE) has been introduced as an alternative to tagged CMR to improve the spatial resolution. It was first applied by Aletras et al. [Aletras, Ding, et al., 1999] for myocardial strain quantification. Different from the tagging techniques, DENSE directly encodes tissue displacement into image phase. Based on the stimulated echo acquisition mode pulse sequence [Frahm et al., 1985], it provides a simplified technique to acquire myocardial motion without the need for tag line detection. DENSE has been validated against other tagging methods [Feng et al., 2009] and has been shown to require minimum user interaction compared to conventional tagging techniques [Aletras, Balaban, et al., 1999].

Strain encoding is a CMR technique first introduced by Osman et al. [Osman et al., 2001] to quantify myocardial strains from magnitude images. Different from conventional CMR tagging, SENC applies tagging in through-plane direction. While short-axis images are utilized to compute longitudinal strains with SENC, circumferential strain is measured from long-axis images. SENC has been used to estimate myocardial strain both in the left and right ventricles [Youssef et al., 2008; Neizel et al., 2009] and demonstrated to be comparable to 3D tagging in terms of peak circumferential and longitudinal strain values. 2D and 3D strain maps have been obtained by combining SENC with other techniques [Hess et al., 2009; Sampath et al., 2009]. Pan et al. [Pan et al., 2006] reduced the image acquisition time by introducing fast-SENC, which is an accelerated imaging sequence based on SENC. It utilizes a combination of spiral acquisition and localized SENC excitation, providing a reduced field-of-view avoiding fold-over artifacts. Low-frequency and high-frequency data, called low-tuning and high-tuning images, respectively, are acquired in an interleaved fashion, reducing the scan time to a single heartbeat. Slice-following SENC was developed to account for the through-plane motion of the heart [Fahmy et al., 2006]. Combining these two, Ibrahim et al. [Ibrahim et al., 2007] introduced slice-following fast-SENC.

Finally, CMR phase-contrast imaging, or tissue phase mapping, allows for a pixel-wise analysis of myocardial velocity with high temporal and spatial resolution [Jung et al., 2006]. It allows for the assessment of myocardial strain [Espe et al., 2013] and strain rate [Delfino et al., 2008]. A common drawback associated with this imaging method is the long scan time required [Wymer et al., 2020].

3.3. Myocardial Motion Analysis

The ultimate objective of cardiac motion quantification is to acquire useful clinical metrics that provide early diagnosis and aid improved treatment. Numerous cardiac motion analysis algorithms have been developed and applied both for research purposes and in the clinical setting. Although the complex deformation pattern of the heart is well captured with today's imaging technology, the wide-spread use of cardiac motion analysis algorithms is still limited due to the lack of validation and the time-consuming post-processing required. This chapter offers an overview of CMR-based myocardial motion analysis. After introducing the motivation behind motion quantification, motion analysis techniques are summarized.

3.3.1. Tagged CMR

Cardiac motion tracking algorithms on tagged CMR can be grouped into two classes, direct and indirect methods. Direct methods are based on measuring deformations by detecting dedicated image features, e.g., tag lines or tag intersections. The performance of direct methods is hence affected by the distribution of tag lines or tag intersections [Tobon-Gomez et al., 2013] and image quality. To improve the robustness of direct methods, tag intersections have been approximated by thin-plate splines from which tag surfaces can be reconstructed [Kerwin & Prince, 1998]. In another study, tracking is performed by using B-splines to reconstruct tag planes, yielding 3D positions of each feature in the deforming myocardium in time [Amini et al., 2001].

Among all the methods working directly on tagged CMR data, phase-based techniques allow for a rapid and more automatic quantification of displacement field by removing the need for detecting and tracking tag lines [Arts et al., 2010]. The motion analysis algorithms in this group are based on the Fourier shift property. HARmonic-Phase (HARP) analysis is currently the most popular technique for the analysis of tagged CMR images due to its simplicity and performance [Osman et al., 1999, 2000] (Figure 3.6). It utilizes a band-pass filter for the extraction of a single spectral peak of the Fourier-transformed tagged CMR data (Figure 3.6b). The harmonic magnitude (Figure 3.6c) and phase (Figure 3.6d) images are obtained by the inverse Fourier

transforming of the extracted harmonic peak. The magnitude image represents the ventricular geometry while the phase image provides information on myocardial deformation. This process is repeated for each tag direction such that motion information in 2D or 3D can be reconstructed. Material point tracking over time is then accomplished by utilizing the harmonic phase data (Figure 3.6d) [Pan et al., 2005].

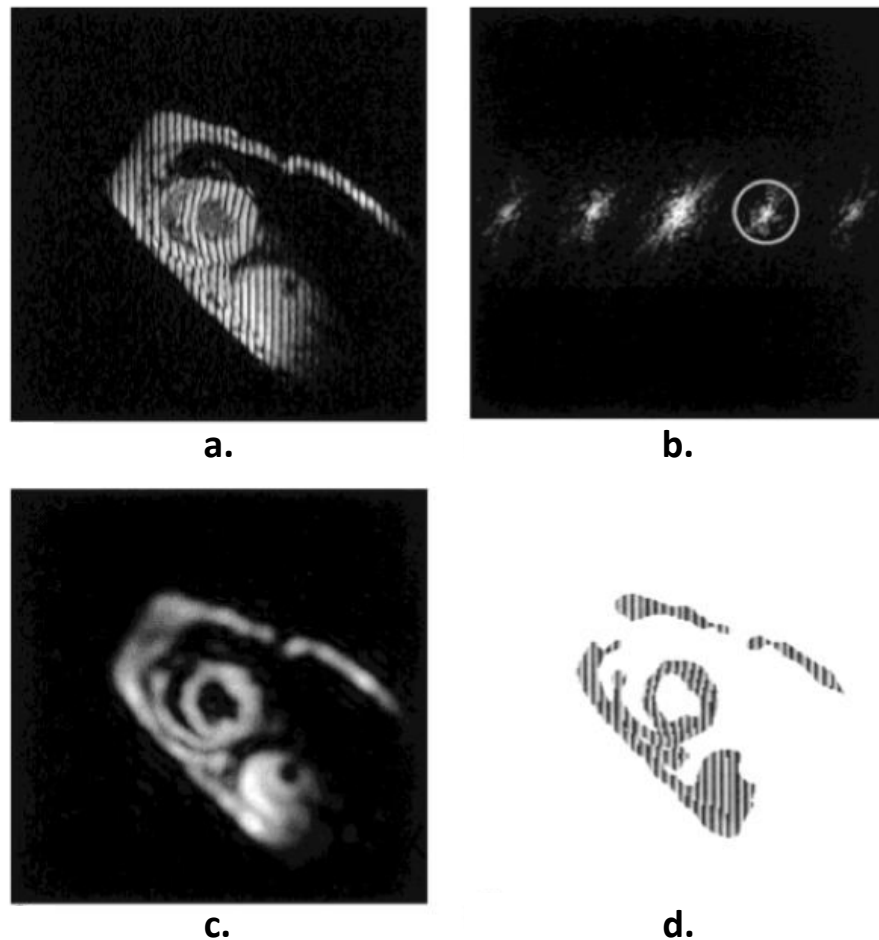


Figure 3.6. Harmonic phase (HARP) analysis. (a) The original CMR tagged image showing SPAMM tag pattern. (b) Fourier transform of the original image. One of the spectral peaks is marked with a circle and used to generate the harmonic magnitude image in (c) and the phase image in (d). Extracted from [Osman et al., 1999].

The fast-HARP technique was proposed to decrease the acquisition time drastically [Sampath et al., 2003]. The technique was further enhanced to accommodate for 3D motion analysis [Pan et al., 2003] by combining short-axis and long-axis image sets. zHARP, developed by Abd-Elmoniem et al. [Abd-Elmoniem et al., 2007], allowed for the quantification of in-plane and through-plane motion. Fast-HARP was further used for strain analysis in combination with SENC [Sampath et al., 2009] to include the through-plane component. The method's accuracy

in quantifying myocardial strain was demonstrated on post-infarct patients [Garot et al., 2000]. Despite its fairly easy use, the HARP method is limited by the SNR [Liu et al., 2004] and phase aliasing [Arts et al., 2010]. As an alternative post-processing method, sine-wave modeling (SinMod) was developed [Arts et al., 2010] to account for the noise sensitivity problem of HARP, and has been shown to perform similarly compared to HARP in terms of speed, but better in terms of accuracy of the displacement fields [Arts et al., 2010]. This technique is further demonstrated to perform well in the 3D domain for the extraction of 3D cardiac deformations [Pan et al., 2005; Hui Wang et al., 2013]. However, SinMod is built to process consecutive images and relies on the fact that the displacements between temporal frames are small.

Other than phase-based techniques, Gabor filters, deformable contours and optical flow methods have been used for tagged CMR post-processing. Gabor filters [Ting Chen et al., 2010] are band-pass filters to locally filter CMR tagged images for deformation quantification. The Gabor filter has been applied both on 2D [Montillo et al., 2004] and 3D images [Qian et al., 2006]. Among the deformable contours, Base-splines [Tustison et al., 2003] are used to quantify myocardial deformation through an energy minimization problem. The main advantage of the technique is that it offers flexibility in determining the spline shape, providing a more accurate approximation than global polynomial fitting [Huang et al., 1999]. B-spline models have been extended to enable 3D analysis [Radeva et al., 1997; Huang et al., 1999] also based on a cylindrical coordinate system [Deng & Denney, 2004, 2005]. Deformable models are advantageous as they also allow for the construction of statistical models of the heart and combining tagged CMR with functional information [Hui Wang & Amini, 2012]. Moreover, these models are superior to model-free approaches in terms of providing prior information on the expected object shape, yielding better accuracy in case of low SNR [Xu et al., 2000]. Optical flow methods have been used in tracking tagged CMR data [Qian et al., 2006; Florack & Van Assen, 2010]. One of the fundamental assumptions in this technique is the constant image intensity along a motion trajectory [Hui Wang & Amini, 2012], which is, however, not fulfilled in tagged CMR due to the relaxation of longitudinal magnetization.

3.3.2. Cine CMR

One of the techniques to extract motion information from cine CMR is feature tracking (FT), based on detecting certain landmarks on the cavity-tissue boundary [Maret et al., 2009]. CMR-FT has been validated against harmonic phase analysis for strain calculation [Hor et al., 2010] and shown to allow for the quantification of myocardial motion both on the healthy volunteers [Schuster et al., 2011] and also on the patients suffering from ischemic cardiomyopathy [Schuster et al., 2013]. It has been proven to be successful in classifying many cardiac disorders, including dilated cardiomyopathy [Romano et al., 2018], ischemic cardiomyopathy [Schuster et al., 2013], and congenital heart diseases [Steinmetz et al., 2018], mostly based on global LV circumferential and global LV longitudinal strain quantification. Moreover, it has been utilized in several studies for the assessment of mechanical dyssynchrony [Taylor et al., 2014; Kowallick et al., 2017]. However, similar to all other 2D-based techniques, CMR-FT is unable to assess through-plane strain [Schuster et al., 2011] and CMR-FT derived radial strain is not satisfying [Padiyath et al., 2013] showing high variability [Schuster et al., 2013]. The most apparent problem of this technique is its dependence on the user to delineate the endocardial and epicardial contours manually, which is demonstrated through studies on inter-study reproducibility [Morton et al., 2012] and intra-observer reproducibility [Schuster et al., 2013] of CMR-FT strain assessment. Moreover, strain measurements reported from CMR-FT analysis are performed only on the global level, revealing that regional differences in strain are underestimated with this method. Among the other strain components, only the circumferential strain agrees with CMR tagging results globally. However, the segmental differences cannot be characterized unless tagging is utilized [Augustine et al., 2013; Cowan et al., 2015].

Accounting for the incompressibility of myocardium, several deformable models have been proposed to assess the motion of both the LV [Bistoquet et al., 2007] and both ventricles [Bistoquet et al., 2008] using cine CMR. Among them, finite element (FE) based models have the advantage of providing prior information on the heart structure and the material properties [Young, 1999; Hu et al., 2003]. Veress et al. [Veress et al., 2001] utilized hyperelastic warping in combination with a FE model on cine CMR. LV motion analysis with hyperelastic warping was validated against HARP for the quantification of radial and circumferential strains [Phatak et al., 2009].

3.3.3. Combined Approaches

Cine and tagged CMR images have their relative advantages and disadvantages. In terms of global strain characterization, feature tracking on cine images has yielded good results while, concurrently, providing ventricular volume, mass, and EF. However, the detection of regional motion remains challenging due to the lack of contrast within the myocardial wall. While tagged CMR seems promising for material point tracking within the wall, it remains difficult to detect the endocardial and epicardial borders due to the poor definition of tissue interfaces. In order to combine the advantageous features of the two imaging modes, combined image analysis techniques have been introduced. A finite element model of the LV [Young et al., 2012] was constructed to quantify myocardial deformation on SubTag SSFP data [Schrauben et al., 2018] (see Section 3.2.2.3). Moreover, non-rigid image registration techniques have been utilized to simultaneously register tagged and cine CMR images based on similarity metrics that balance the contribution of these two image types [Shi et al., 2012]. The error in motion tracking decreased compared to cine or tagged CMR registration alone. In another study based on spatial adaptive weighting for the combined analysis, a valve plane constraint was introduced for more accurate cardiac motion analysis [Haiyan Wang et al., 2012]. Chitiboi et al. [Chitiboi et al., 2020] combined cine CMR with three-chamber tagged CMR using a non-rigid registration algorithm [Knutsson & Andersson, 2005] to improve the local strain analysis in HCM patients.

3.3.4. Machine Learning Based Methods

Recently, machine-learning (ML) approaches have gained popularity in cardiac motion quantification, drastically reducing the analysis time. One of the ML-based techniques, convolutional neural networks, has been demonstrated to be applicable for the automated analysis of myocardial deformation [Ferdian et al., 2020]. A fully convolutional neural network has been used to analyze LV characteristics using short-axis and long-axis views of cine CMR images [Bai et al., 2018]. The technique was shown to have human-level performance on the UK Biobank¹ dataset for the quantification of ventricular mass and volume. A fully automated

¹ <http://imaging.ukbiobank.ac.uk>

framework has been proposed to estimate circumferential strain for HCM and healthy control subjects, using CMR-FT on cine image sequences [Vigneault et al., 2017]. For this purpose, a deep learning approach was utilized to automatize feature extraction, decreasing the processing time and dependency on the manual delineation of contours. In another study, a convolutional network has been integrated to CMR-FT to estimate radial, longitudinal, and circumferential strain components on a group of healthy volunteers and ischemic patients [Puyol-Anton et al., 2018]. Another deep-learning approach was implemented to characterize segmental myocardial deformation from cine CMR [Hammouda et al., 2020]. Ferdian et al. implemented two neural networks for the quantification of radial and circumferential deformation of the LV [Ferdian et al., 2020]. In a recent study by Loecher et al. [Loecher et al., 2021], an ML-based tag tracking technique, which was trained on synthetic tagged images of the heart, has been utilized. The technique has its novelty in tracking arbitrary points of the LV wall, removing the need for points anchored to tagging pattern or its intersections only. Therefore, compared to conventional analysis techniques, a denser deformation map of the myocardium is achieved, allowing for a more accurate strain quantification from tagged CMR. However, the method still needs to be validated for assessing regional dysfunctions. Ghadimi et al. [Ghadimi et al., 2021] has proposed a deep learning-based approach for strain quantification using DENSE images. Both global and regional circumferential strains have been shown to be in good agreement with the conventional techniques on healthy and diseased hearts.

Chapter 4

Clinical Utility and Future Applications of CMR Imaging

This chapter aims to summarize the clinical utility and future applications of CMR-based image tracking techniques. Section 4.1 addresses the motivation to integrate CMR imaging techniques into routine clinical workflow. Section 4.2 presents CMR solutions for the commonly observed cardiac diseases, which is followed by CMR-based therapy management in Section 4.3. After summarizing emerging applications of CMR in Section 4.4, the chapter is finalized with mentioning the limitations in Section 4.5.

4.1. Overview

Advances in medical imaging technology have facilitated the integration of imaging modalities with routine clinical practice. MRI has been utilized to quantify cardiac function since the 1980s [Matthaei et al., 1985]. It has since then evolved from being a research tool to being used for clinical purposes. Today, CMR stands as an accurate and highly versatile imaging modality in the clinical setting, offering a safe way to quantify the functional, anatomical, and metabolic function of the cardiovascular system. It has been one of the routine clinical examinations for the assessment of myocardial viability and function, suspected cases of cardiomyopathies, myocarditis, valvular and pericardial disease, and congenital heart disease. The use of contrast agents for CMR has provided improved image quality that allows for a more accurate assessment of anatomical and functional changes. Moreover, the excellent results for interstudy reproducibility of CMR [Grothues et al., 2002] have provided proof for it to be used for follow-up examinations to assess ventricular function after therapeutic interventions.

4.2. Diagnostic Applications

In order to comply with the context of the thesis, this section introduces the diagnostic utility of CMR-based techniques with an emphasis on LV functional assessment. CMR-based diagnostic techniques for the assessment of the most commonly observed CVDs; congenital heart disease, coronary heart or IHD, and non-ischemic cardiomyopathies are briefly portrayed.

4.2.1. Congenital Heart Disease

Congenital heart disease stands as the most common type of major congenital abnormalities [Dolk et al., 2011]. 1.5 million children are born with a type of congenital heart disease every year, corresponding to almost 8 per 1000 live births [Rebergen & De Roos, 2000]. Congenital heart diseases often require surgical intervention to improve the survival rate and alleviate the symptoms [Brickner et al., 2000]. The common types of congenital heart disease affecting LV performance and anatomical features are the ventricular septal defects, transposition of great arteries, and Tetralogy of Fallot. Ventricular septal defects are a common type of congenital heart disease that is caused by an abnormality while the interventricular septum is being formed. The extra blood flow from the LV to the right ventricle is observed through the defect in the septal wall, which is characterized by the size, thereby, determining the amount of interventricular flow. In case of transposition of the great arteries, oxygenated blood is transferred to the lungs as the pulmonary artery arises from the LV while the aorta is connected to the RV, pumping deoxygenated blood to the body [Partington & Valente, 2013]. Most of the time, the patient needs a series of surgeries and follow-up medications and may have serious long-term health problems [Warnes, 2006]. Tetralogy of Fallot is the most commonly observed cyanotic congenital heart disease [Reller et al., 2008] that is a combination of various defects observed in other types of congenital heart disease; ventricular septal defect, pulmonary stenosis, ventricular hypertrophy, and aortic valve enlargement, resulting in a decrease in the blood oxygen content supplied to the body, see Figure 4.1. Tetralogy of Fallot can be diagnosed during pregnancy or after birth and requires surgical operations at different time points during lifetime.

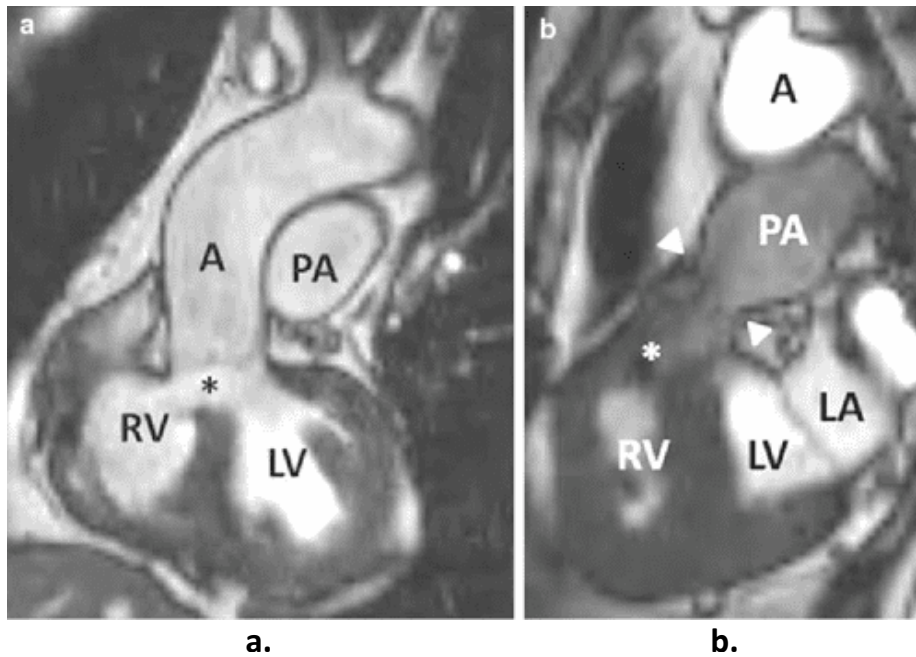


Figure 4.1. CMR images of Tetralogy of Fallot. (a) The most commonly observed congenital heart defects, e.g., ventricular septal defect (indicated by the asterisk), overriding aorta (shown by A), and right ventricular thickening are shown. PA denotes the pulmonary artery. (b) Cine SSFP image parallel to the PA showing the dephasing jet (asterisk) and the level of the pulmonic valve (arrowheads) (right). Extracted from [Hughes & Siegel, 2010].

The long-term follow-up of the cardiovascular status of these patients is costly and preferably requires noninvasive imaging techniques with low to no dose of ionizing radiation. Morphological and anatomical assessment of cardiac structures are of high importance for the diagnosis of congenital heart disease [Scholtz et al., 2014]. CMR can provide clinical metrics for an accurate diagnosis of uncertain cases, especially when the patient has malformations of the chest wall or post-operative scars, resulting in suboptimal echocardiographic window [Pennell et al., 2004]. Owing to its precision in quantifying ventricular anatomy and function, CMR plays a pivotal role in the management of congenital heart disease [Marcu et al., 2006; Assomull et al., 2007].

The assessment of right ventricular properties is difficult compared to the LV in congenital heart disease patients due to its geometry and location [Schuster et al., 2016], therefore, the studies have been mostly focused on the LV. Cine CMR is the principal sequence to evaluate the anatomical features of the heart and extracardiac structures, e.g., intracardiac pathways, systemic and pulmonary veins, and ventricular outflow tracts [Geva et al., 2003; Gutiérrez et al., 2008]. EF is the common metric to describe the ventricular function in addition to wall

thickening and stroke volume [Gutiérrez et al., 2008], whose difference between left and right ventricles allows for the assessment of shunt fractions and valvular regurgitation [Lorenz et al., 2000]. Shunt fraction, which is defined as the ratio between pulmonary and systemic flow, is another diagnostic metric in cases of intracardiac and extracardiac shunting [Gutiérrez et al., 2008]. In addition to anatomical information, the measurement of hemodynamic parameters is vital to assess the flow distribution and pressure gradients, which requires both the velocity- and magnitude-encoded images [Gutiérrez et al., 2008].

4.2.2. Ischemic Heart Disease

Ischemic heart disease, also called coronary heart disease, is a type of CVD caused by the impaired blood supply to the heart due to structural or functional changes in the blood vessels [Klabunde, 2005]. According to the statistics of the WHO [World Health Organization, 2020], IHD is the number one cause of death worldwide. Common techniques for the diagnosis of IHD are based on ECG findings, cardiac imaging modalities, and biomarkers [Thygesen et al., 2012]. Early detection of IHD is of paramount importance to prevent disease progression.

Early signs of IHD are observed on regional properties, especially wall motion abnormalities, commonly assessed by echocardiography [Sudarshan et al., 2015]. Although it is the first choice in the routine evaluation of coronary heart disease patients, interpretation of echocardiographic findings relies on visual assessment, hence, they are operator-dependent [Dandel et al., 2009]. Moreover, the assessment of myocardial damage is performed based on LV ejection fraction (LVEF), which is not reliable due to the distorted chamber geometry or motion pattern [Salvo et al., 2015]. It also does not account for the change in regional contractile properties of the heart, which is commonly observed in coronary heart disease patients [Abraham et al., 2001]. The diagnostic value of strain imaging has been shown to perform better for the early identification of coronary heart disease compared to LVEF [Shimoni et al., 2011]. Moreover, IHD is mostly related to the impaired contraction in the endocardium as the first signs of IHD are observed in the subendocardial layer [Sarvari et al., 2013]. Speckle tracking echocardiography is an established technique for the assessment of infarcted region during stress echocardiography and allows to determine the early changes [Uusitalo et al., 2016]. Unlike cine CMR, tagged CMR has not made the transition into clinical routine for the

assessment of coronary heart disease patients due to the lack of fast motion analysis techniques for myocardial strain quantification [Garot et al., 2000].

CMR has been clinically used for stress imaging, e.g., dobutamine stress MR and myocardial perfusion imaging [Kelle & Nagel, 2008]. Dobutamine stress MR was first introduced in the beginning of 1990s [Pennell et al., 1992] and shown to perform as well as dobutamine echocardiography in determining coronary heart disease [Pennell et al., 1992]. The assessment is performed based on the detection of impairment of contractile properties of the heart. Owing to its high spatial resolution and low inter-observer variability [Paetsch et al., 2006], dobutamine stress MR is superior to ECG testing [Nagel et al., 1999] and echocardiography. Dobutamine stress MR utilizes graded doses of dobutamine infusion for the assessment of viable myocardium [Kelle & Nagel, 2008; Arai, 2011]. Such an inotropic stimulation enhances the contractility of the myocardium while providing coronary vasodilation [Charoenpanichkit & Hundley, 2010]. The assessment of myocardial viability is performed based on wall motion changes after dobutamine infusion; while myocardial dysfunction at high level of stress occurs in viable myocardium, scarred myocardium is not able to respond [Sandstede, 2003]. Another technique used for diagnosing IHD, myocardial perfusion, allows for the detection of perfusion abnormalities in the subendocardial layer [Kelle & Nagel, 2008]. The use of gadolinium delayed enhancement techniques to detect the infarcted region is one of the cornerstones in the clinical adaptation of CMR [Simonetti et al., 2001]. The use of contrast agents allows for a clear distinction of the infarcted tissue and detection of acute and chronic MI, see Figure 4.2.

Strain and strain rate are the most commonly used clinical metrics for the assessment of coronary heart disease, and shown to be reduced in case of MI [Heimdal et al., 1998; Voigt et al., 2000]. The characterization of ischemic regions was successfully performed using strain mapping [Croisille et al., 1999; Gotte et al., 1999]. The infarcted zone was subjected to strain analysis using SENC [Neizel et al., 2009], and later by several researchers to understand the behavior around the infarcted zone [Bogaert et al., 2000; Inoue et al., 2010]. Götte et al. [Götte et al., 2001] showed that the functional assessment of the myocardium is more accurately performed based on strain rather than using wall thickness as metric.

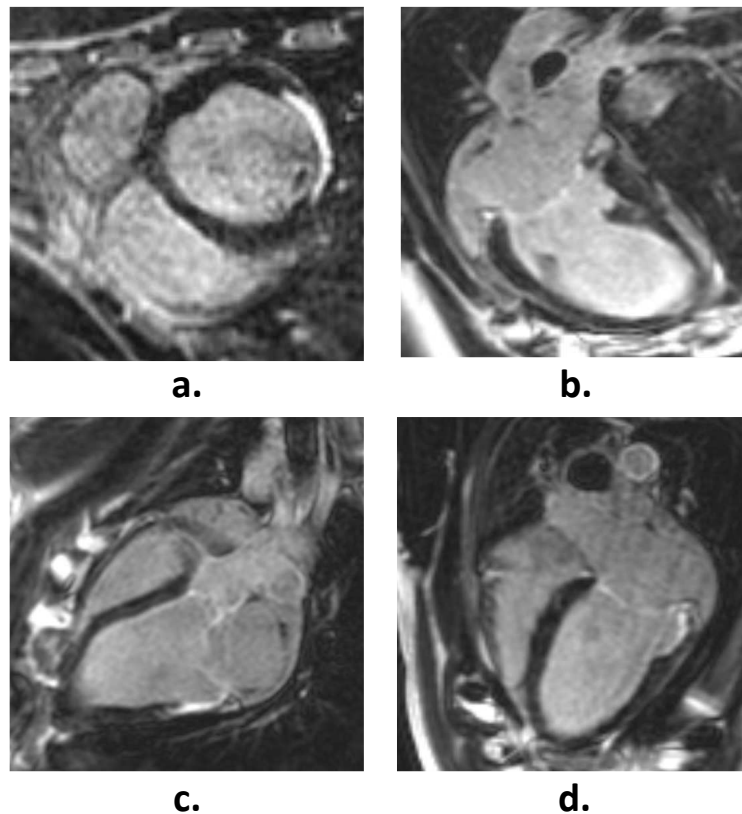


Figure 4.2. MR late-gadolinium enhancement images of the pig heart showing (a) short-axis, (b) two-chamber, (c) three-chamber, and (d) four-chamber views. The infarcted region is seen as bright pixels on the anterior LV wall in (a, c, d).

The performance assessment of functional LV metrics derived from CMR-FT was performed for scar detection using LGE imaging as the reference for scar localization [Maret et al., 2009]. The regional analysis on the LV wall revealed impaired functional measurements, e.g., displacement, velocity, and strain in the radial and longitudinal directions, from the segments with scarred tissue. CMR tagging has also been used for the detection of IHD [Rogers et al., 1999; Rosen et al., 2006; Korosoglou et al., 2009, 2010].

4.2.3. Non-Ischemic Cardiomyopathies

Depending on the driving mechanisms and alterations on the functional, structural, and molecular level, cardiomyopathies can be either physiologic or pathologic. Physiological growth is the normal response of the heart to compensate for the changes in tissue due to stimulating factors such as extreme physical activity, pregnancy, or biological signals [Rubler et al., 1977; Pelliccia et al., 2002]. Pathological cardiac growth, however, generally occurs due to a

functional loss in the cardiac muscle tissue caused by a CVD. Among the non-ischemic cardiomyopathies, the most common ones are dilated cardiomyopathy and HCM (Figure 4.3). Originating from abnormal re-structuring of the cardiomyocytes and the extracellular matrix, remodeling is irreversible. In case of dilated cardiomyopathy, the ventricle stretches (Figure 4.3b), resulting in weakening of the ventricular walls and a decrease in pumping efficiency. Hypertrophied cardiomyopathy, in contrast, relates to the thickening of the heart walls (Figure 4.3c) with an accompanying decrease in the ventricular cavity volume. Both dilated cardiomyopathy and hypertrophied cardiomyopathy decrease the pumping efficiency of the heart progressively.

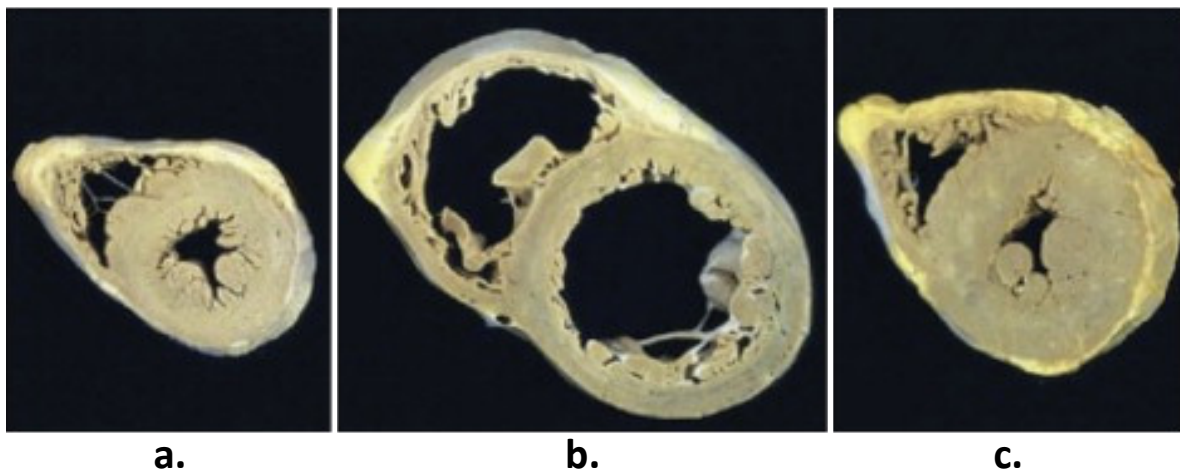


Figure 4.3. (a) Transverse section showing the healthy heart. (b) Eccentric hypertrophy due to ventricular volume overload and (c) concentric hypertrophy due to pressure overload. Adapted from [Kumar et al., 2005; Allen et al., 2013].

The diagnosis is mainly performed based on deformation metrics, e.g., strain, strain rate, and twist, and clinical utility of these parameters in assessment of dilated cardiomyopathy and hypertrophied cardiomyopathy has been shown in many studies [Yip et al., 2003; Nesbitt et al., 2009]. CMR provides an efficient characterization of myocardial properties for the assessment of cardiomyopathies [Assomull et al., 2006; O'Hanlon et al., 2007]. It performs as an accurate alternative to assess the location and severity of hypertrophy when echocardiographic techniques are suboptimal [Rickers et al., 2005], e.g., in the apical region [Moon et al., 2004]. CMR-FT was utilized in a group of patients with HCM to assess LV rotational dynamics and its relation to the extent of LGE [Nucifora et al., 2014]. Peak LV twist was found to increase while the untwisting rate was delayed in these patients. Moreover, LGE properties that might be observed due to hypertrophy were demonstrated to have significant effects on LV rotation.

Myocardial tagging techniques have been extensively used for understanding LV functional and structural changes in dilated cardiomyopathy [Nelson et al., 2000; Young et al., 2001] and hypertrophied cardiomyopathy [Maier et al., 1992; Mishiro et al., 1999; Edvardsen et al., 2006; Soler et al., 2006]. Young et al. [Young et al., 2001] utilized a FE model to quantify regional myocardial displacement and strain in a group of patients with dilated cardiomyopathy. They could successfully show the consistent pattern of regional deformation in dilated hearts as it is reported by some other imaging modalities [Fujita et al., 1993; Bach et al., 1995; Uematsu et al., 1995]. Myocardial tagging has also been used to study the rotation pattern in case of dilated cardiomyopathy. Setser et al. [Setser et al., 2003] demonstrated impaired ventricular rotation in terms of both the spatial distribution and magnitude. The region-specific rotational patterns and displacement changes have been compared between healthy volunteers and HCM patients [Maier et al., 1992]. In case of hypertrophied hearts, cardiac rotation and radial displacement were reported to decrease mainly in the posterior region and inferior septal zone, respectively. Early-diastolic strain rates have been shown to reduce significantly in HCM [Ennis et al., 2003; Edvardsen et al., 2006].

4.3. Therapy Management

With the advancements in cardiovascular imaging and treatment techniques, the survival rate of patients with CVDs has increased, generating a new patient population [Van Der Linde et al., 2011]. Owing to its superior interstudy reproducibility, CMR has recently gained popularity in the assessment of ventricular morphology and function after therapeutic intervention [Marcu et al., 2006].

Cardiac resynchronization therapy. CRT is a technique to reduce the intraventricular and interventricular dyssynchrony [Heydari et al., 2012]. Recent studies have revealed that CRT decreases patient hospitalization and improves LV systolic function, providing an increased quality of life [Higgins et al., 2003]. CRT requires invasive procedures during the patient's lifetime for device implantation and exchange, and continuous monitoring [Heydari et al., 2012]. Despite all the efforts, the response rate of patients to CRT therapy is 30% - 40% [Bristow et al., 2004; Cleland et al., 2008], requiring an optimal patient selection strategy to improve CRT

outcome. Myocardial strain allows for a comprehensive assessment of wall motion, providing differentiation between the active and passive deformation of the myocardium [Dandel et al., 2009]. It has been used in several studies for guiding and evaluating CRT [Becker et al., 2007; Pouleur et al., 2011]. Moreover, recent studies based on speckle-tracking reveal that compared to longitudinal strain, circumferential and radial components are better estimates of CRT response [Suffoletto et al., 2006], which is not possible to quantify with most echocardiographic techniques [Heydari et al., 2012].

Despite its common usage, cine CMR is not the best imaging mode to assess regional dyssynchrony, while DENSE, SENC, phase-contrast CMR, and myocardial tagging yield more robust estimates [Reichek, 1999; Heydari et al., 2012]. White et al. [White et al., 2006] successfully related the infarction size based on delayed enhancement CMR with the CRT response in a group of patients with interventricular dyssynchrony. To this end, CMR combined with LGE imaging has become an integral part of guiding CRT, especially to guide the lead placement [Heydari et al., 2012]. In another study utilizing LGE-CMR, Chalil et al. [Chalil et al., 2007] reported quantitative measure of scar size, transmural, and the pacing location for optimal response to CRT. Mechanical indexes derived from tagged images proved to be a good estimator of functional recovery upon CRT [Bilchick et al., 2008]. Rutz et al. [Rutz et al., 2009] combined viability and dyssynchrony maps based on accelerated 3D tagging CMR in a group of patients with left bundle branch block and patients after MI and successfully quantified global and segmental dyssynchrony parameters.

Coronary revascularization. Coronary revascularization is one of the most common treatment techniques to reopen narrowed or severely blocked arteries [Fitchett et al., 2014]. It has been shown that, if not revascularized, metabolically active dysfunctional myocardium has the risk of developing into scar tissue [K. S. Lee et al., 1994]. To guide patient selection for revascularization, CMR plays an important role [Morton et al., 2010]. The conventional approaches for guidance utilize anatomical information acquired from coronary angiography that might not accurately assess myocardial viability and ischemia, which are the main indicators of coronary heart disease. Therefore, coronary heart disease patients should have functional assessments before revascularization to optimize the benefit from the treatment [Silber et al., 2005]. CMR offers techniques for the ischemia and viability assessment that are summarized in Section

4.2.2. Thereby, the clinician can decide if revascularization is required depending on the viability of the myocardium and also the appropriate vessels to be revascularized.

4.4. Emerging Applications

Molecular imaging has provided visualization of physiological processes at the molecular level [Herschman, 2003; Jaffer & Weissleder, 2004; Choudhury et al., 2004], and shown to be promising in cardiovascular medicine for the early detection of dysfunctions before the onset of clinical events [Naghavi et al., 2003; Jaffer et al., 2005]. The molecular imaging techniques are mainly focused on visualizing atherosclerosis [Naghavi et al., 2003; Libby, 2012], macrophages [Choudhury et al., 2004; Jaffer et al., 2006; Libby, 2012] and thrombosis [Badimon & Fuster, 2002], which are related to the IHD and sudden cardiac failure. Molecular imaging techniques have also been applied to image disease progression after MI and also used to guide therapies for myocardial regeneration, e.g., stem cell therapy [Jaffer et al., 2007]. Stem cells derived from bone marrow were first administrated in the beginning of the 2000s with the aim to the myocardium after IHD [Hamano et al., 2001], followed by clinical trials [Wollert et al., 2004; Bartunek et al., 2005; Janssens et al., 2006; Kraitchman & Bulte, 2008]. However, cardiac stem cell therapy of the human heart has not been successful so far [Sürder et al., 2013, 2016].

There has been a growing interest in integrating clinical data with computational models for a better understanding of the cardiovascular system, not only for research purposes but also in the clinical setting. Translational cardiac modeling promises to guide the search for more robust biomarkers to improve diagnosis and therapy planning [Chabiniok et al., 2016]. Considering the medical and economical concerns in developing cardiac devices, computational heart models could play a significant role in the development, testing, and validation phases until the device is ready to be used in the clinics. Computational models are a promising part of the performance assessment, especially of artificial heart valves [Yoganathan et al., 2004] and LV assist devices [Fraser et al., 2011; Lim et al., 2012; McCormick et al., 2014]. Moreover, a quantitative understanding of myocardial properties contributes to a better diagnosis of cardiac dysfunction with the help of biomarkers which are not possible to acquire without patient-specific cardiac models [Vicky Y. Wang et al., 2009; Sermesant et al., 2012; Genet et al., 2015; Chabiniok et al., 2016].

Computational cardiac models may also be used to guide and improve current therapeutic techniques, reducing the need for invasive data [Chabiniok et al., 2016]. These models are commonly preferred in the optimization of lead placement for CRT and also to better assess the relation between mechanical and electrical activation [Kerckhoffs et al., 2008; Kayvanpour et al., 2015]. In one of their studies, Sermesant et al. [Sermesant et al., 2012] has compared in vivo measurements and predicted values of isochrones and pressure curves for different pacing modes of CRT, including atrial, right ventricular, left ventricular endocardial, and biven-tricular pacing with simultaneous endocardial left ventricular pacing, see Figure 4.4. For each pacing, the measured and the predicted endocardial isochrones are compared and shown to be in good agreement. The comparison for biventricular pacing with simultaneous endocardial left ventricular pacing is shown in Figure 4.4a. The simulated pressure curves are also demon-strated to correlate with the measurements for each pacing protocol, see Figure 4.4b.

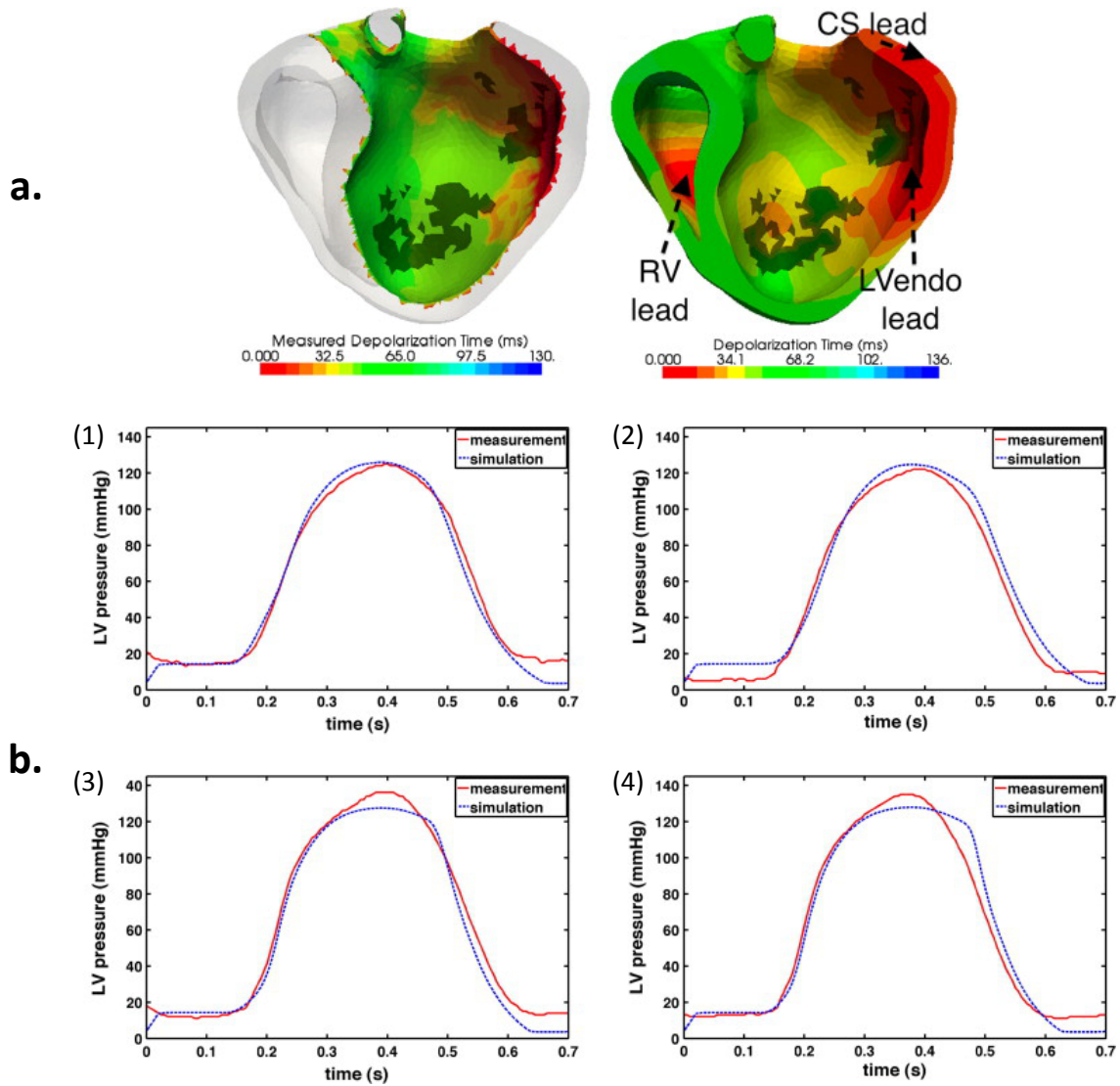


Figure 4.4. Comparison of in vivo measurements and model prediction for different pacing protocols for CRT. (a) The measured isochrones for left ventricular pacing are projected on the endocardium (left). Coronary sinus and endocardial pacing catheters are shown. The corresponding prediction results are represented (right). (b) The pacing effect on the pressure development comparing the simulation results and the measurements for (1) atrial, (2) right ventricular, (3) left ventricular endocardial (4) biventricular pacing with simultaneous endocardial left ventricular pacing protocols. Adapted from [Sermesant et al., 2012].

Chapter 5

In-silico Study of Accuracy and Precision of Left-Ventricular Strain Quantification from 3D Tagged MRI²

5.1. Introduction

The noninvasive assessment of myocardial function represents an important diagnostic tool in the clinic. Beyond cine Magnetic Resonance Imaging (MRI), a number of dedicated approaches to quantify ventricular tissue motion and strains have been proposed, including phase contrast [Bryant et al., 1984], tissue tagging [Zerhouni et al., 1988], displacement encoding [Aletras, Ding, et al., 1999] and strain encoding [Osman et al., 2001].

In the present paper, we focus on 3D tagged MRI [Axel & Dougherty, 1989a], which is based on the principle of SPAMM [Zerhouni et al., 1988; Fischer et al., 1993]. Since its inception, a number of improvements have been proposed [Axel & Dougherty, 1989a; Ryf et al., 2002; Rutz et al., 2008; Shehata et al., 2009; Stoeck et al., 2012] and the method has been shown to reveal alterations in myocardial function for a variety of pathologies including IHD [Kramer et al., 1993; Marcus et al., 1997], aortic stenosis [Stuber et al., 1999], cardiac hypertrophy [Young et al., 1994], left bundle branch block [Rutz et al., 2009], cardiomyopathy [Young et al., 2001] and coronary artery disease [Kraitchman et al., 2003], among others.

Processing techniques for tagged data can be divided into three main categories: direct, Fourier-based, and tracking-based approaches [Tobon-Gomez et al., 2013]. While direct methods aim to extract tag features using image filtering and segmentation approaches [Kraitchman et

² Published in: Berberoğlu, E., Stoeck, C. T., Moireau, P., Kozerke, S., & Genet, M. (2021). In-silico study of accuracy and precision of left-ventricular strain quantification from 3D tagged MRI. *PLoS One*, 16(11), e0258965. doi:10.1371/journal.pone.0258965.

al., 1995], Fourier-based methods exploit the Fourier-shift theorem by band-pass filtering a single tagging peak in k-space yielding a material point-specific image phase which can be tracked (HARP [Osman et al., 1999, 2000]). Limitations include a reduction of spatial resolution due to band-pass filtering [Liu et al., 2004], as well as potential phase aliasing [Arts et al., 2010]. Using SinMod, the noise sensitivity of HARP is partly addressed by providing improved accuracy of the displacement fields in low SNR scenarios [Arts et al., 2010]. SinMod was also demonstrated to perform well in 3D [Hui Wang et al., 2013]. However, SinMod, like HARP and other phase-based approaches, requires sufficiently small displacements in-between temporal frames. Tracking-based approaches aim to find a deformation field to register any two images, typically involving also some form of regularization [Hui Wang & Amini, 2012; Tobon-Gomez et al., 2013]. Compared to Fourier-based approaches, which are applicable to tagged images only, tracking-based methods have a wider range of applications, including cine, tagged [Tobon-Gomez et al., 2013; Genet et al., 2018] or ultrasound images [L. C. Lee & Genet, 2019]. Among the tracking-based approaches, Finite-Element (FE)-based methods offer a convenient way to constrain the solution displacement field, with a proper discretization independent of the image discretization, thus naturally providing geometrical regularization [Mansi et al., 2011; McLeod et al., 2012; Zou et al., 2018]. Moreover, it allows the incorporation of mechanical regularization, either based on basic mechanical principles, or using mechanical models [Genet et al., 2018]. These models require the prescription of appropriate boundary conditions and a material model to characterize the cardiac constitutive behavior.

Studies using MRI tagging have revealed regional differences in strain distribution [Young et al., 1994; Moore, Lugo-Olivieri, et al., 2000; Bogaert & Rademakers, 2001]. While circumferential and longitudinal strains are reported frequently for both healthy subjects and patients, radial strain is often omitted due to limited accuracy and precision [Simpson et al., 2013]. At the same time, radial strain is a decisive metric for assessing contractility of the heart [Fallah-Rad et al., 2011].

It is the objective of the present work to analyze the dependency of radial, circumferential and longitudinal strain quantification from 3D tagged MRI with regard to tag distance, image resolution, and SNR. To do so, synthetic tagged images are generated using a reference biomechanical LV model [Sainte-Marie et al., 2006; Imperiale et al., 2011] as input. Strain is then

quantified from the synthetic images using a recently proposed FE-based method with mechanical regularization referred to as equilibrated warping [Genet et al., 2018].

5.2. Methods

Figure 5.1 summarizes the pipeline of this study, which includes the reference LV model (Figure 5.1a), rasterization, resampling and convolution (Figure 5.1b), image processing (Figure 5.1c), and image registration (Figure 5.1d).

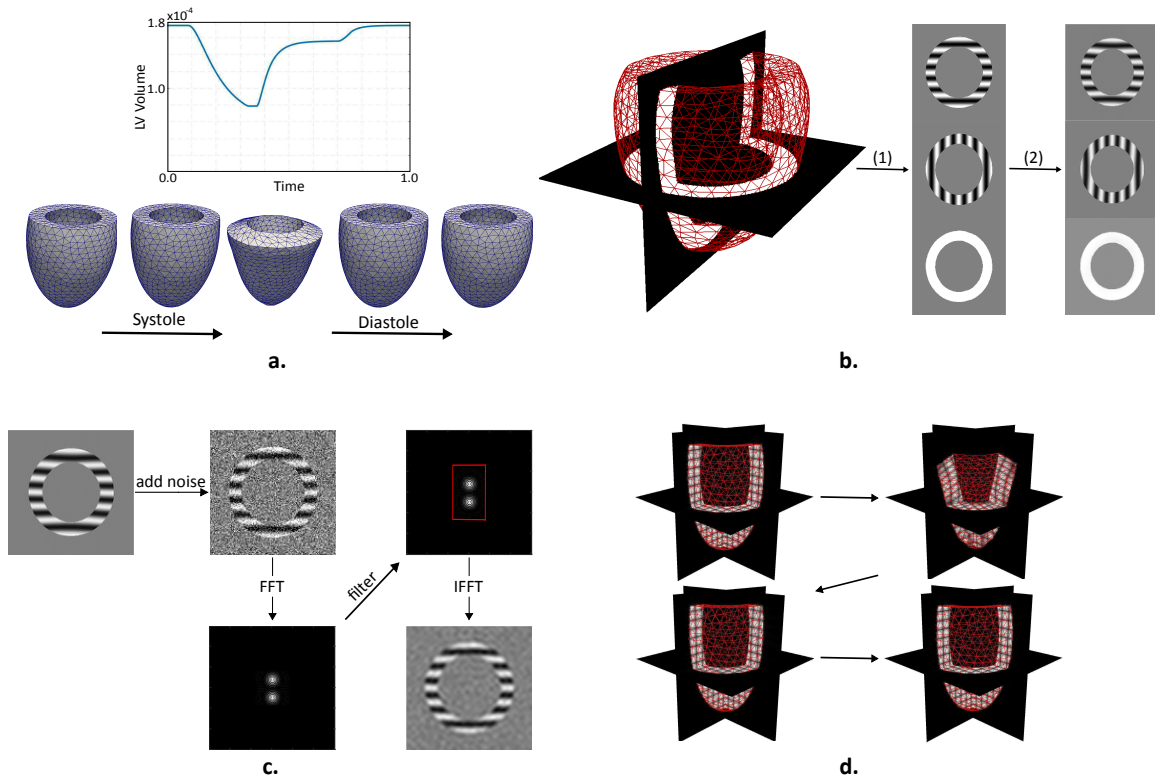


Figure 5.1. Study design. (a) Reference biomechanical LV model simulating the full cardiac cycle. (b) Synthetic image generation using the model. Three different image stacks with tag lines in orthogonal directions are generated by rasterization (1) and then resampled by cropping in k-space and convolved in time (2). (c) Adding noise and changing image resolution by filtering in k-space. (d) Image registration showing 3D tagged images superimposed with the warped mesh for different time frames.

5.2.1. Cardiac Biomechanical Model and Reference Left-Ventricular Motion

In this study, we utilize a generic anatomical model of the LV represented by a truncated ellipsoid with an approximate ED volume of 202 ml, decreasing down to 62 ml at ES. The

ventricular wall thickness is almost constant across the ventricle with approximate values of 15 mm and 22 mm at end-diastole and end-systole, respectively. We consider a reference biomechanical model of the LV [Sainte-Marie et al., 2006; Chapelle et al., 2012], which combines a passive visco-hyperelastic behavior with a micro-macro model of the active muscle contraction [Chapelle et al., 2012], and is coupled to a lumped cardiovascular circulation model [Sainte-Marie et al., 2006]. FE resolution of the model provides the displacement field over the LV (from which one can compute any deformation metric, e.g., strain, strain rate, etc.) with 1000 time steps throughout the cardiac cycle. The model is used as ground truth in the study. To ensure a physiological behavior and prevent unrealistically large displacement velocities at the base of the LV [Kozerke et al., 1999], the displacement was interpolated in time, capping the maximum velocity to 0.1mm/ms (Figure 5.1a).

5.2.2. Synthetic Image Generation

The modified LV model is further utilized to generate synthetic 3D-tagged images as follows. First, tagged images with 0.5 mm pixel size are generated from the time-resolved LV meshes through rasterization [Sermesant et al., 2003], and using a simplified complementary spatial modulation model [Ryf et al., 2002] for 3D tagging without tag-line fading (Figure 5.1b-1). We assume a standard image generating function used in CSPAMM to create the tagged image stacks:

$$I = \sin\left(\frac{\pi X_i}{s}\right), \quad (5.1)$$

where X_i corresponds to the spatial coordinate of the image voxel in the i^{th} direction, and s is the tagging distance, ranging from 3 mm to 7 mm (Figure 5.2a). Compared to other tagging techniques, in which the tagging pattern is approximated by higher order functions, (e.g., SPAMM) [Ryf et al., 2002], here we assume the standard modulation pattern for CSPAMM as a “worst case” scenario in terms of tag line contrast. Considering the approximate ventricular wall thickness at ED, the synthetic images have between ca. 2 (for 7 mm tagging) and 5 (for 3 mm tagging) tag lines within the thickness of the myocardium.

Three stacks are generated, with $i = 1, 2, 3$ for each tagging direction. Thereafter, images are resampled to 1 mm pixel size using zero-filling after cropping in k-space and convolution in

time (Figure 5.1b-2) using a convolution window size of 40 ms [Axel & Dougherty, 1989a]. Then, the images are resampled in time to yield 100 time steps throughout the cardiac cycle. These three series of images are then combined using:

$$I_0(\mathbf{X}) = \sqrt[3]{\left| \sin\left(\frac{\pi X_1}{s}\right) \right| \cdot \left| \sin\left(\frac{\pi X_2}{s}\right) \right| \cdot \left| \sin\left(\frac{\pi X_3}{s}\right) \right|}. \quad (5.2)$$

to generate the reference dataset used for 3D validation of the FE-based image registration technique (Figure 5.1d).

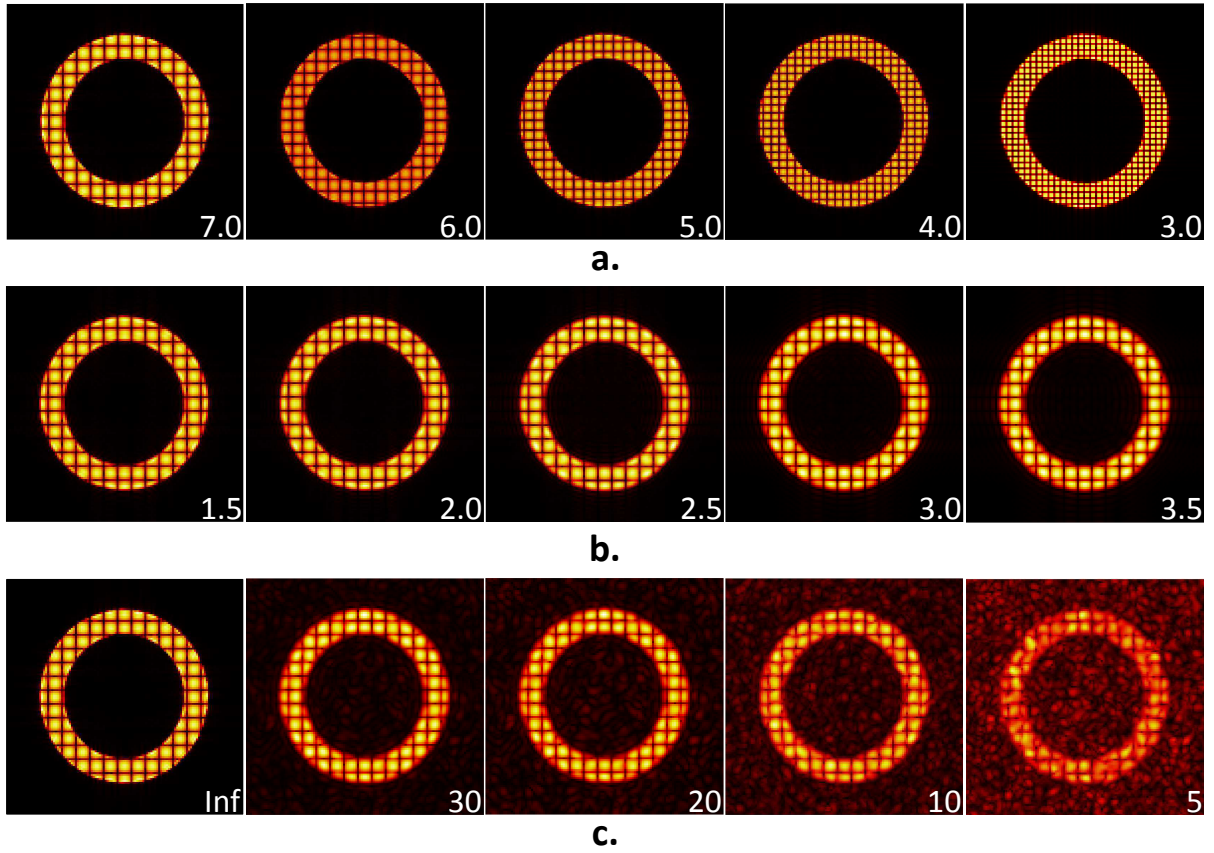


Figure 5.2. Isotropic synthetic images to analyze the effect of image properties. Images with (a) varying tag distances (in mm), (b) pixel sizes (in mm), and (c) SNRs (values are written at the bottom right corner for each case). Images shown in (a) are noiseless and have 1 mm pixel size. Images in (b) are noiseless and have 7 mm tag distance. For the ones in (c), pixel size and tag distance are 3.5 mm and 7 mm, respectively. Images represent the configuration at end-diastolic time frame.

In addition to the reference images, datasets with varying image properties are generated (Figure 5.1c). First, different levels of Gaussian noise with zero mean are added to generate

sets of images with varying SNR, which is defined as the ratio of the magnitude of the signal to standard deviation of the noise:

$$\text{SNR} = \frac{\text{Max}_{\text{signal}}}{\text{Std}_{\text{noise}}}. \quad (5.3)$$

Then, image spatial resolution is changed by filtering the reference dataset in k-space using a box filter with different bandwidth (Figure 5.1c). We generated image sets varying in tag distance (Figure 5.2a), pixel size (Figure 5.2b), and SNR (Figure 5.2c).

5.2.3. FE-based Image Registration

FE-based image registration is then performed on the synthetic datasets to investigate the effect of image properties on deformation quantification (Figure 5.1d). A continuum formulation of the image registration problem is introduced and later discretized using the FE method. Considering the reference and current configurations of the object represented by the images, Ω_0 and Ω_t , related image intensity fields are denoted by I_0 and I_t . A deformation map $\Phi(\mathbf{X})$ is defined between these two configurations to map the reference points $\mathbf{X} \in \Omega_0$ onto their spatial counterparts $\mathbf{x} = \Phi(\mathbf{X}) = \mathbf{X} + \mathbf{U}(\mathbf{X}) \in \Omega_t$, where \mathbf{U} is the displacement field. In the presence of image noise, this problem is ill-posed and requires to be formulated as a minimization problem. Hence, the problem of finding the displacement field can be formulated as

$$\text{find } \mathbf{U} = \underset{\{\mathbf{U}\}}{\text{argmin}} = \{h(\mathbf{U}) = (1 - \beta)\Psi^{\text{im}}(\mathbf{U}) + \beta\Psi^{\text{reg}}(\mathbf{U})\}. \quad (5.4)$$

which aims to minimize the functional h expressed in terms of regularization strength β . The image similarity metric, Ψ^{im} ,

$$\Psi^{\text{im}}(\mathbf{U}) = \frac{1}{2} \|I_t \circ \Phi - I_0\|_{L^2(\Omega_0)}^2, \quad (5.5)$$

and the regularization energy, Ψ^{reg} ,

$$\Psi^{\text{reg}} = \sum_K \frac{1}{2} \|\text{Div}(\mathbf{F} \cdot \mathbf{S})\|_{L^2(K)}^2 + \sum_F \frac{1}{2h} \llbracket \mathbf{F} \cdot \mathbf{S} \cdot \mathbf{N} \rrbracket_{L^2(F)}^2, \quad (5.6)$$

are weighted by factors $(1 - \beta)$ and β , respectively, to rescale the regularization strength to stay in the range $[0,1]$. K , F and \mathbf{N} represent the set of finite elements, the set of interior

facets, and the facets normal, respectively. \mathbf{S} and \mathbf{F} are the second Piola-Kirchhoff stress tensor and transformation gradients, respectively, and h is a characteristic length of the elements; see [Genet et al., 2018] for more details. The novelty in the method is the regularization technique which is a continuum finite strain formulation of the equilibrium gap principle introduced in [Claire et al., 2004], readily discretizable with standard finite elements. Compared to other mechanical regularization techniques, equilibrated warping enforces only the basic principle of mechanical equilibrium, but does not constrain strain magnitude in any way. Moreover, the registration problem is geometrically regularized by the FE mesh. In addition to the equations specified above, Equation 5.6 requires the specification of a constitutive model, chosen here as Neo-Hookean compressible hyperelastic potential with Ciarlet-Geymonat [Ciarlet, 1982]:

$$\rho_0 \psi = \frac{\kappa}{2} (J^2 - 1 - \ln(J)) + \frac{\mu}{2} (I_C - 3 - 2\ln(J)), \quad (5.7)$$

in terms of bulk and shear modulus, κ and μ , volume map, $J = \text{Det}(\mathbf{F})$, and $I_C = \text{Tr}(\mathbf{C})$. Here, $\mathbf{F} = \mathbf{Grad}(\Phi)$ and $\mathbf{C} = \mathbf{F}^T \mathbf{F}$ are the deformation gradient and right Cauchy-Green deformation tensor, respectively. Following the general FE procedure, the variational form of Equation 5.4 is obtained by derivation. It is then linearized, and discretized using standard continuous Lagrange elements. More details on the formulation and solution procedure can be found in [Genet et al., 2018]. The method implementation is freely available as a python library³ implemented based on FEniCS [Alnæs et al., 2015] and VTK⁴ libraries.

The impact of the regularization parameter and the mechanical model utilized are further discussed in [Genet et al., 2016, 2018]. In this study, for each image set, we run the registration algorithm for a range of regularization strength β and use the best performing value (i.e. estimated motion closest to ground truth) in the analysis. The reader is referred to [Genet et al., 2018] for a more detailed discussion on the choice of β in case the ground truth is unknown. By designing this “optimal” registration technique, we focus the study on the image content itself, not the image processing approach.

³ https://gitlab.inria.fr/mgenet/dolphin_warp

⁴ <http://www.vtk.org>

5.2.4. Performance Metrics for Cardiac Strain Quantification

Strain quantification performance is assessed through computing the normalized mean and standard deviation of the norm of the displacement error given by:

$$d_i = \frac{\|\mathbf{u}_{\text{reg}}^i - \mathbf{u}_{\text{ref}}^i\|}{\max\|\mathbf{u}_{\text{ref}}\|}, \quad (5.8)$$

$$d_{\text{avg}} = \frac{1}{N_n} \sum_{i=1}^{N_n} d_i \times 100 (\%), \quad (5.9)$$

$$d_{\text{std}} = \frac{1}{N_n} \sum_{i=1}^{N_n} (d_i - d_{\text{avg}})^2 \times 100 (\%), \quad (5.10)$$

where d_{avg} and d_{std} are the normalized mean and standard deviation in displacement error norm. $\mathbf{u}_{\text{reg}}^i$ and $\mathbf{u}_{\text{ref}}^i$ are the displacement vectors at node i at ES time frame, for the registered case and ground truth, respectively. Moreover, N_n is the total number of nodes.

In addition to the displacement error, we investigate the component-wise sensitivity of the strain to a change in image characteristics by computing the mean and standard deviation according to:

$$e_i = \mathbf{s}_{\text{reg}}^i - \mathbf{s}_{\text{ref}}^i, \quad (5.11)$$

$$e_{\text{avg}} = \frac{1}{N_{\text{el}}} \sum_{i=1}^{N_{\text{el}}} e_i, \quad (5.12)$$

$$e_{\text{std}} = \frac{1}{N_{\text{el}}} \sum_{i=1}^{N_{\text{el}}} (e_i - e_{\text{avg}})^2, \quad (5.13)$$

where e_{avg} and e_{std} are the mean and standard deviation in strain error for component s , which is a scalar field, while s_{reg}^i and s_{ref}^i are the strain values at element i at ES time frame for the registered case and the ground truth, respectively.

In this study, we investigate both the individual and combined effects of two image characteristics, Tag distance to Pixel size Ratio (TPR) and SNR on images with isotropic (Figure 5.2) and

anisotropic (Figure 5.3) spatial resolution. The first part, analysis on isotropic images, includes noiseless images with TPR ranging from 2.8 to 7.0 (Figure 5.2a, b), and images with varying levels of SNR (from 5 to 30) (Figure 5.2c), keeping the tag distance and pixel size constant: 7 mm and 1 mm, respectively. The combined effect of TPR and SNR is investigated on the image set with isotropic pixel size ranging from 1.5 mm to 3.5 mm having different SNRs (from 5 to 30) and a tag distance of 7 mm.

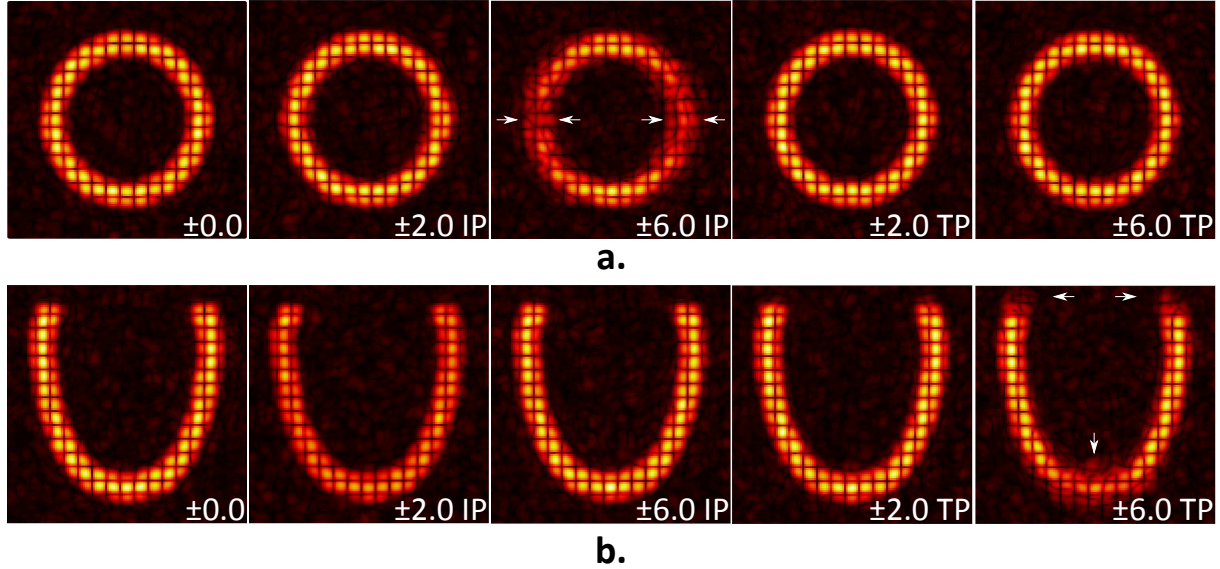


Figure 5.3. Anisotropically resolved synthetic images to analyze the effect of geometrical inconsistencies. Images with 7 mm tag distance, SNR 20, and $3.5 \times 7.0 \times 7.0 \text{ mm}^3$ pixel size for varying amounts of shift increasing from left to right (values are written at the bottom right corner for each case) on (a) short-axis and (b) long-axis views. IP and TP stand for the direction of shift, in-plane and through-plane, respectively. Images represent the configuration at end-diastolic time frame. The arrows indicate the regions with the largest amount of error due to shift for IP (± 6 IP) and TP (± 6 TP).

The second part is focused on the analysis of anisotropic image resolutions. Similarly, individual effects of resolution and SNR are analyzed first. For this purpose, we generated noiseless images with 7 mm tag distance and pixel size ranging from 1.5 mm to 3.5 mm in the tagging direction, while the transverse directions are assigned to a larger pixel size ranging from 3.5 mm to 7 mm. For the SNR analysis, three datasets are chosen to represent different levels of pixel size ($2.0 \times 4.0 \times 4.0 \text{ mm}^3$, $3.0 \times 6.0 \times 6.0 \text{ mm}^3$, and $3.5 \times 7.0 \times 7.0 \text{ mm}^3$) with varying noise levels in the same interval as used for the isotropic case. The anisotropic image analysis is enriched by going beyond random errors and considering a source of systematic error (Figure 5.3). Since in vivo 3D tagged images are acquired in three successive breath-holds, individual image

stacks may not be perfectly aligned [Stoeck et al., 2012]. Hence, we introduce shifts between individual image stacks to better reproduce the in vivo image acquisition, and understand the effect on deformation analysis. In this study, we simulated in-plane (IP) and through-plane (TP) shifts of image stacks with $3.5 \times 7.0 \times 7.0 \text{ mm}^3$ pixel size and SNR 20. For this purpose, the image stack tagged in Z is kept constant for both cases while the two other stacks are shifted in the respective planes by the same amount (Figure 5.3).

5.3. Results

5.3.1. Isotropic Images

5.3.1.1. Impact of TPR. Figure 5.4 presents the error analysis as a function of TPR, where the black curves represent change in pixel size for a constant tag distance of 7 mm while the red curves stand for constant pixel size of 1 mm as tag distance varies. Normalized mean \pm standard deviation of the displacement error norm (defined Equations 5.9 and 5.10, reported Figure 5.4) and mean \pm standard deviation in Green-Lagrange strain component errors (defined Equations 5.12 and 5.13, reported Figure 5.4b-d) are used as the metrics to assess strain estimation accuracy. As shown in Figure 5.4a, the tracking algorithm performs well in comparison to ground truth with a displacement error of $1.1 \pm 0.8\%$ relative to the reference image set. Moreover, it still performs well for TPR higher than 4.0. The largest strain error is observed in the radial component, which is 0.1 ± 0.2 for 1 mm pixel size and 3 mm tag distance (Figure 5.4b).

5.3.1.2. Impact of SNR. Figure 5.5 presents the effect of SNR on strain measurement. For all plots, black curves stand for the best performing regularization β while the red ones represent error in the displacement field when no regularization is applied. For the best case (Inf SNR), error in the displacement field is $1.1 \pm 0.8\%$ (Figure 5.5a). For SNR 5, regularization decreases the error from $3.5 \pm 2.6\%$ (for $\beta = 0$) to $1.6 \pm 1.1\%$ (for best $\beta = 0.05$). A similar trend is found in Figure 5.5b-d in terms of mean \pm standard deviations in Green-Lagrange strain component errors. For SNR 5, errors in radial, circumferential, and longitudinal components are 0.0 ± 0.3 , 0.0 ± 0.1 , and 0.0 ± 0.1 when no regularization is applied. For optimal regularization, errors in these components vanishes for all components.

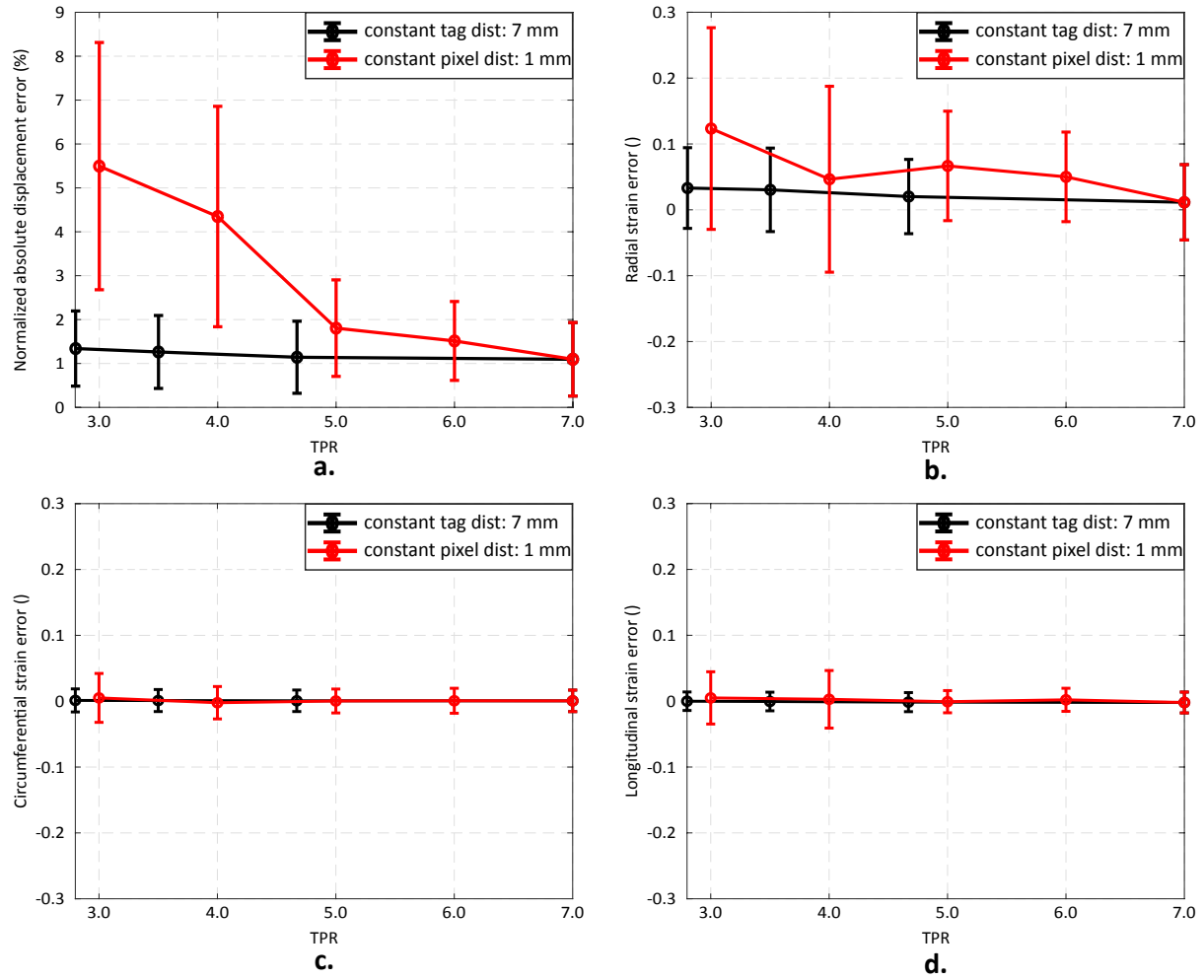


Figure 5.4. Effect of Tag distance to Pixel size Ratio (TPR) on noiseless isotropic image analysis. (a) Normalized mean \pm standard deviations in displacement error norm (%) plotted as a function of TPR. Black curve stands for the errors computed for the images with different pixel sizes keeping the tag distance constant at 7 mm while the red one represents the analysis results with different tag distances where the pixel size is 1 mm. (b-d) Mean \pm standard deviations in component-wise Green-Lagrange strain error as a function of TPR for the best performing regularization strength. Radial strain component is more sensitive to a change in TPR while the (c) circumferential and the (d) longitudinal components are more accurately measured.

5.3.1.3. Combined Impact of TPR and SNR. Figure 5.6 presents the results for the images with different isotropic resolutions varying in SNR at a fixed tag distance of 7 mm. Error in displacement field significantly increases as pixel size and SNR change from 1.0 mm to 3.5 mm and Inf to 5, respectively (Figure 5.6a). While the error in displacement field is $1.1 \pm 0.8\%$ for 1 mm pixel size and Inf SNR, it increases to $3.1 \pm 1.8\%$ when pixel size is 3.5 mm and SNR 5 (worst case). Radial strain error (Figure 5.6b) is larger compared to other components (Figure 5.6c, d) and 0.01 ± 0.14 for the worst case. The reader is referred to Figure 5.10 in Supporting

Information for the choice of optimal β values for varying image resolution and SNR. The two-way ANOVA analysis on SNR and image resolution shows that SNR is the main source of error in displacement field, radial and circumferential strain errors with 56%, 69% and 39%, respectively, while the corresponding contributions from image resolution are 39%, 20% and 37%. The longitudinal strain error, however, is 17% due to SNR and 72% due to image resolution ($p < 0.0001$).

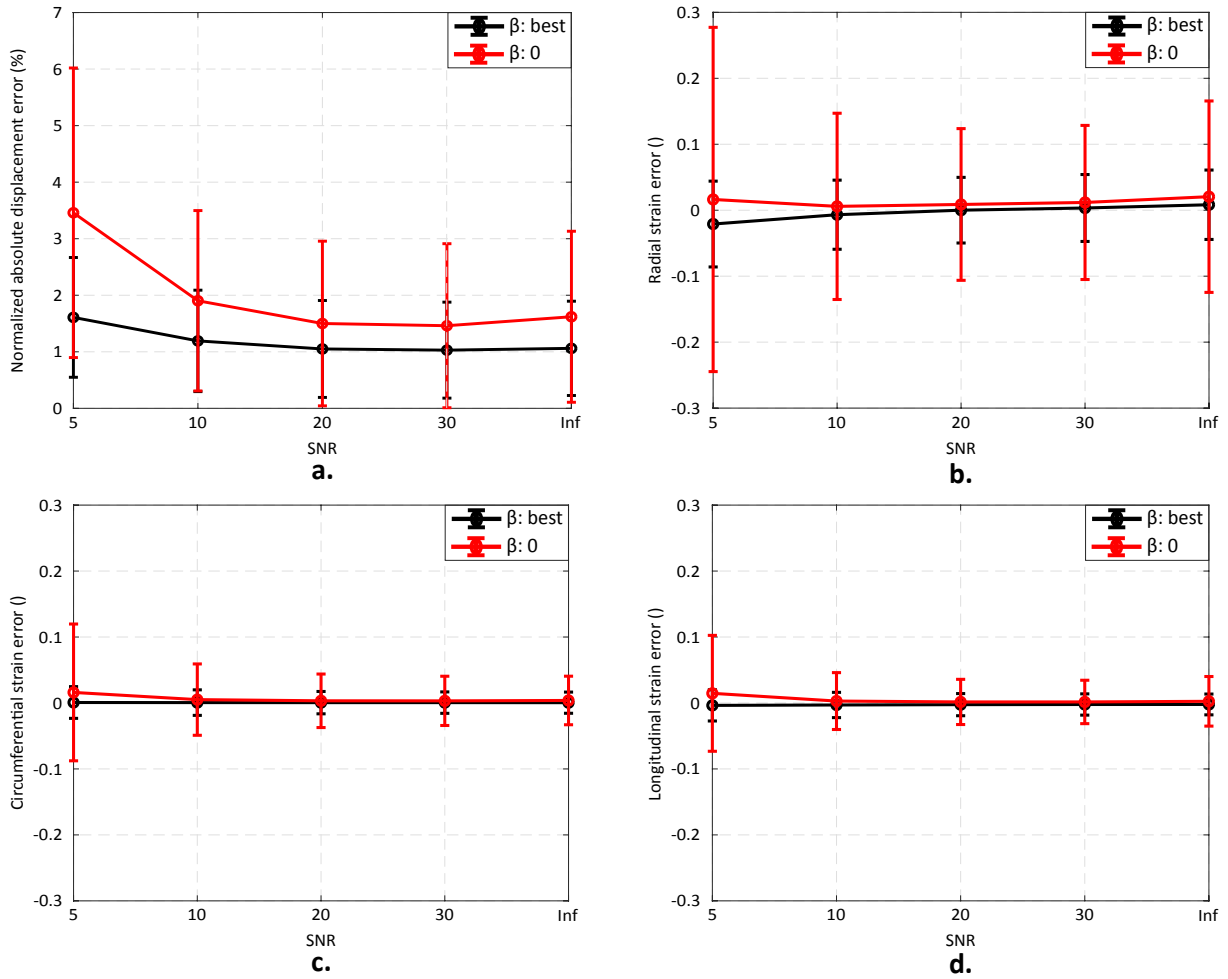


Figure 5.5. Effect of SNR on isotropic image analysis. Results on images with 1 mm pixel size and 7 mm tag distance. (a) Normalized mean \pm standard deviations in displacement error norm (%) without regularization (red curve) and with optimal regularization (black curve). Regularization helps decreasing the registration error significantly. (b-d) Mean \pm standard deviations in component-wise Green-Lagrange strain error as a function of SNR which is independent of regularization strength for $\text{SNR} \geq 20$.

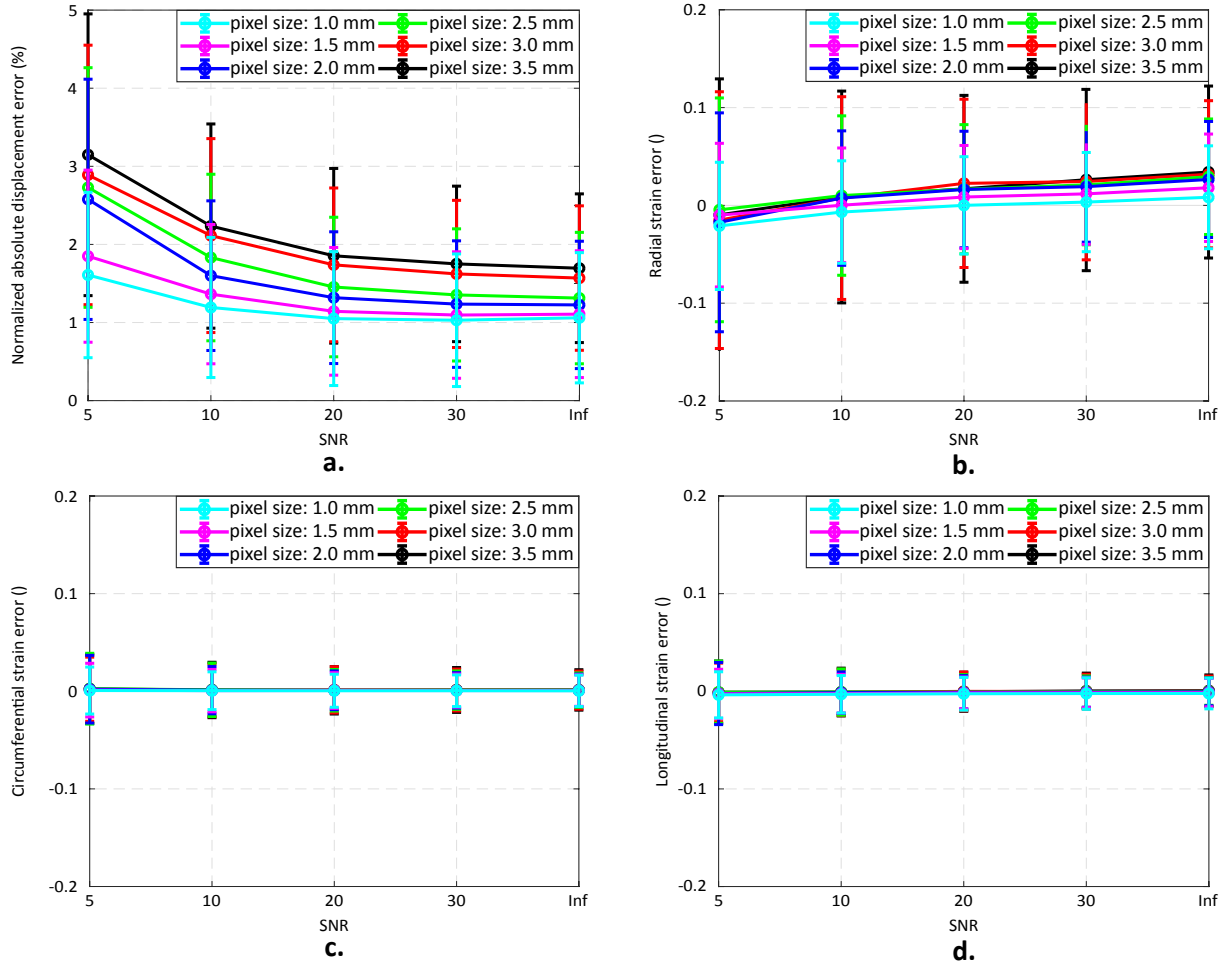


Figure 5.6. Combined effect of image resolution and SNR on isotropic image analysis. Results on images with 7 mm tag distance. (a) Normalized mean \pm standard deviations in displacement error norm (%) plotted as a function of SNR for different pixel sizes. (b-d) Mean \pm standard deviations in component-wise Green-Lagrange strain error as a function of SNR and pixel size. Combined effect of pixel size and SNR is more pronounced on the (b) radial strain component while there is almost no change in the (c) circumferential and (d) longitudinal components. Legends show the pixel size in mm.

5.3.2. Anisotropic Images

5.3.2.1. Impact of Image Resolution. Figure 5.7 summarizes the analysis results on noiseless anisotropically resolved images. For each plot, the x axis represents the pixel size in tagging direction which is finer compared to the orthogonal (transverse) directions represented by the y axis. Figure 5.7a shows the normalized mean \pm standard deviation (%) of the displacement error norm which increases from 1.5% to 2.6% as the pixel size increases from $1.5 \times 3.5 \times 3.5 \text{ mm}^3$ to $3.5 \times 7.0 \times 7.0 \text{ mm}^3$. The error in radial strain increases up to 0.06 when the

pixel size in orthogonal direction is larger than 5 mm (Figure 5.7b). Moreover, circumferential (Figure 5.7c) and longitudinal (Figure 5.7d) components are less sensitive to change in image resolution.

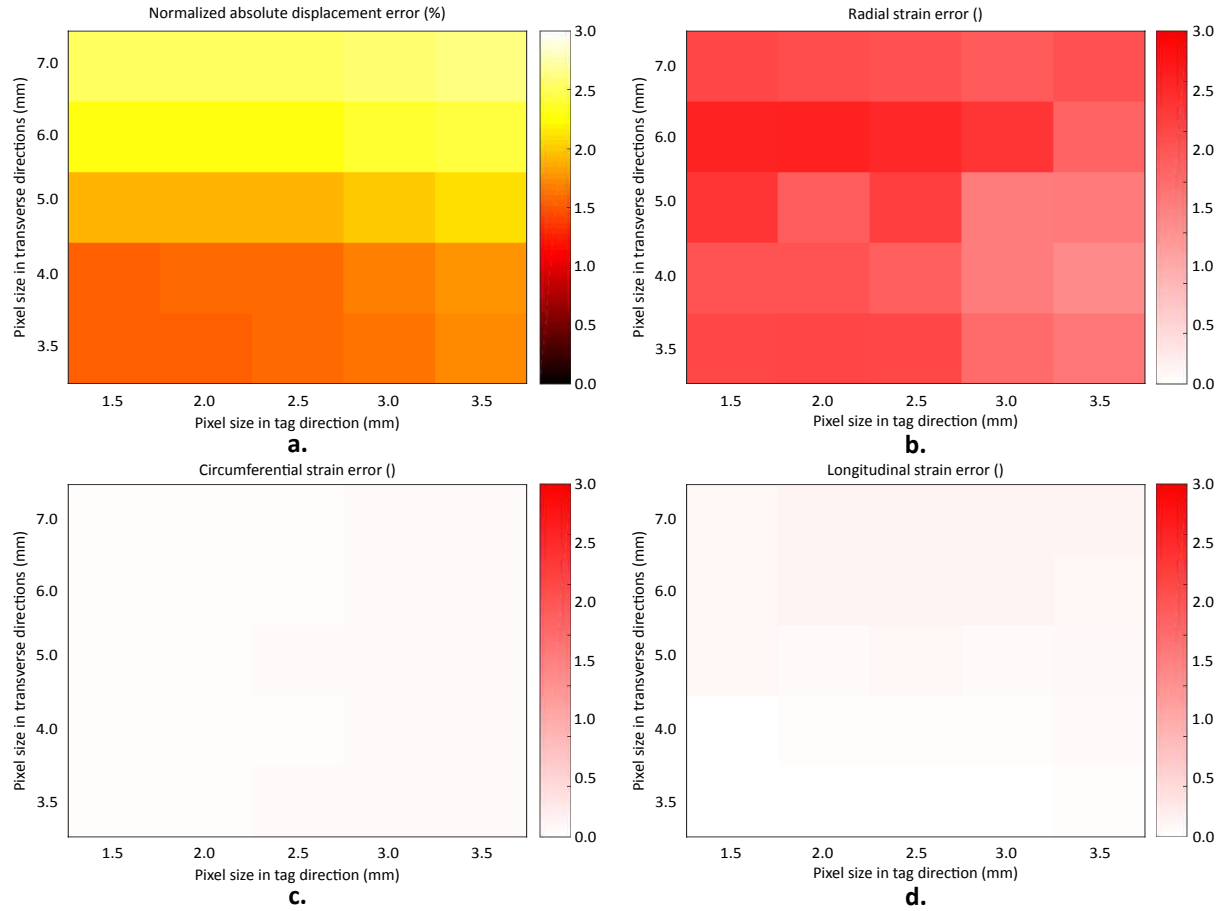


Figure 5.7. Effect of image resolution on anisotropically resolved image analysis. Results on noiseless images with 7 mm tag distance. (a) Normalized mean \pm standard deviations in displacement error norm (%) as a function of pixel size. (b-d) Signed averages in Green-Lagrange strain component errors as a function of pixel size. Radial strain component is the most sensitive to an increase in pixel size, while (c) circumferential and the (d) longitudinal components are not affected at all.

5.3.2.2. Combined Impact of Image Resolution and SNR. We observe an increase in error both in displacement field (Figure 5.8a) and strain components (Figure 5.8b-d) for anisotropic images as SNR decreases and pixel size increases. The lowest error was found for the smallest pixel size and highest SNR: the error in displacement field is $1.5 \pm 1.0\%$ while it increases to $4.4 \pm 2.8\%$ for the worst case ($3.5 \times 7.0 \times 7.0 \text{ mm}^3$ pixel size & SNR 5) (Figure 5.8a) The reader is referred to Figure 5.10b in Supporting Information for the choice of optimal β values for anisotropic image resolutions ($2.0 \times 4.0 \times 4.0 \text{ mm}^3$, $3.0 \times 6.0 \times 6.0 \text{ mm}^3$ and $3.5 \times 7.0 \times 7.0 \text{ mm}^3$) and varying SNR. ANOVA analysis shows that SNR is the main source of error in displacement and

radial, circumferential and longitudinal strain errors with values of 62%, 78%, 64%, and 46%, respectively while image resolution contributes with 36%, 1%, 16%, and 24% to each field ($p < 0.0001$).

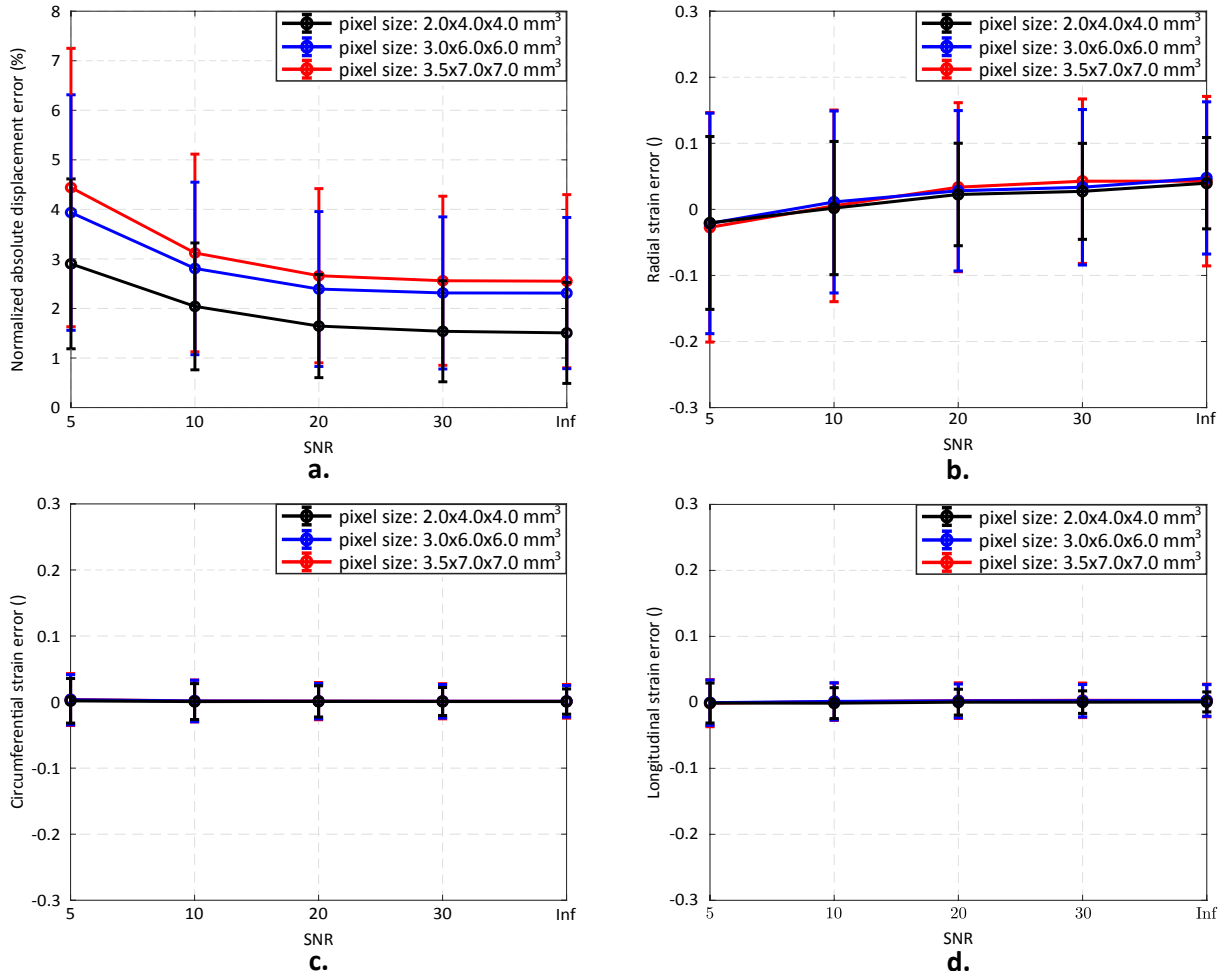


Figure 5.8. Combined effect of image resolution and SNR on anisotropically resolved image analysis. Results on images with 7 mm tag distance. (a) Normalized mean \pm standard deviations in displacement error norm (%) plotted as a function of SNR for different pixel sizes. (b-d) Mean \pm standard deviations in component-wise Green-Lagrange strain error as a function of SNR and pixel size. Combined effect of increased pixel size and decreased SNR is more pronounced on the (b) radial strain component while there is almost no change in the (c) circumferential and (d) longitudinal components.

5.3.2.3. Combined Impact of Image Resolution, SNR and Geometrical Inconsistencies. Figure 5.9 presents the results for the images with anisotropic resolution 3.5x7.0x7.0 mm³, tag distance of 7 mm and SNR 20 when different amounts of shift between tagged image stacks are applied. For all plots, the black curves represent the analysis results on images shifted in-plane, i.e., in the short-axis plane. Red curves stand for the images shifted through-plane along the long axis, where the same stacks are shifted in the transverse direction. Error in

displacement field increases as the stacks are shifted further (Figure 5.9a). When the image stacks are shifted by ± 6 mm in-plane and through plane, the error increases up to $10.1 \pm 5.4\%$ and $9.8 \pm 5.0\%$, respectively. Effect of shifting is more significant on radial strain component (Figure 5.9b). The error is -0.02 ± 0.27 when the shift is ± 6 mm in-plane while it is -0.01 ± 0.32 for through plane shift. However, circumferential and longitudinal strain components are quite robust to any type of shift between image stacks (Figure 5.9b and 5.9c). The localized effects of shifting are further discussed in Supporting Information.

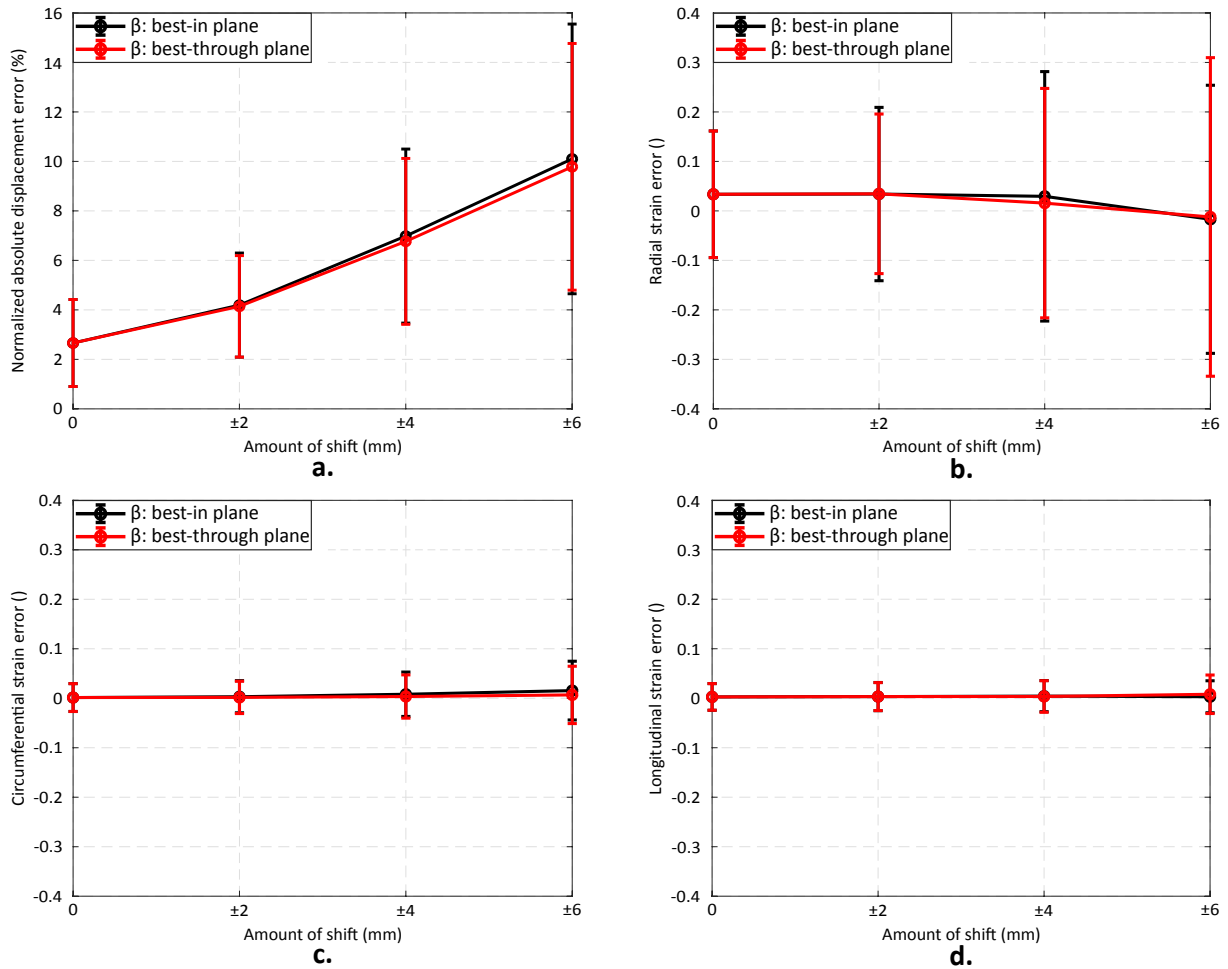


Figure 5.9. Effect of geometrical inconsistencies. Results on images with anisotropic pixel size $3.5 \times 7.0 \times 7.0$ mm³ and SNR 20 for 7 mm tag distance. (a) Normalized mean \pm standard deviations in displacement error norm (%) plotted as a function of in-plane and through plane shift (in mm) between image stacks. (b-d) Mean \pm standard deviations in component-wise Green-Lagrange strain error as a function of in-plane and through plane shift (in mm) between image stacks. Increasing amount of shift leads to an increased error in radial strain component (b) while there is almost no change in the (c) circumferential and (d) longitudinal components.

5.4. Discussion

We have investigated the effect of image resolution, tag distance and SNR on deformation quantification from 3D tagged images and have illustrated the challenges in quantifying radial strain.

For noiseless images, registration can be performed without regularization for all TPR values greater than 2 in case the tag distance is kept constant (see Figure 5.4). Although TPR is a dimensionless parameter essentially controlling the impact of tag distance and image resolution on the motion tracking, the tracking error still differs when varying TPR by changing tag distance (red curve of Figure 5.4) or pixel size (black curve of Figure 5.4). This is due to the fact that the tracking also depends on the different spatial scales of the problem, i.e., the object size, the displacement length, and the mesh size (which defines the tracked displacement characteristic length). Indeed, for an object of given size and an image of given TPR, an image with coarser discretization will lead to more partial voluming and thus larger tracking error. Similarly, for a given object motion, jumps across tag lines will be facilitated on images with smaller tagline distances. Note that such tag jumps are not directly caused by our choice of tracking method or temporal discretization; they are inherent to tracking with periodic tagging patterns and have been reported for other tracking methods such as harmonics phase imaging [Osman et al., 1999]. Therefore, we studied the effect of TPR in the optimal range of tag distance; coarse enough to prevent the tag line jumping during tracking and fine enough to have good image contrast. Practically, for future CMR tagging acquisitions, this suggests using rather large tag distances (≥ 5 mm) to prevent tag jumping when tracking cardiac motion. Focusing on results with 7 mm tag distances (black curve of Figure 5.4), tracking results are not drastically influenced by TPR, i.e., by image resolution. This holds true for the displacement error, as well as for the strain error, in terms of both mean and standard deviation. Radial strain error is generally larger than circumferential and longitudinal strain errors; however, this higher sensitivity of radial strain is not significantly affected by image resolution.

Conversely, for noisy images, SNR has a significant impact on tracking errors (see Figure 5.5), especially when tracking without regularization (red curve of Figure 5.5). Indeed, in this case, the standard deviation of the strain error explodes for low SNR. This is true for all components,

though it is more significant for radial strain compared to circumferential and longitudinal strains. However, the higher error of radial strain can be alleviated by the use of regularization (black curve of Figure 5.5). Indeed, with regularization, even though the radial strain error standard deviation is higher than for circumferential and longitudinal strains, the tracking error is not influenced by SNR.

Looking at the combined effect of image resolution and SNR (see Figure 5.6), we observed a considerable increase in displacement error with increasing pixel size and decreasing SNR. This trend is seen despite the use of optimal regularization and fine temporal discretization, which suggests that the cause may be found in the image properties, i.e., spatial resolution and SNR. More specifically, we found that radial strain was much more sensitive to image characteristics than circumferential and longitudinal components. This is in line with observation made on tagged CMR image processing [Tobon-Gomez et al., 2013; Genet et al., 2018]. The elevated error in the radial component can also be associated to the thickness of the myocardial wall, which is much smaller than the circumference and length of the ventricle [Moore, McVeigh, et al., 2000]. However, in this study, we did not investigate the effect of wall thickness on motion quantification in detail. Instead, we limited the scope of the study to the effect of imaging parameters only, fixing the geometrical and material biomechanical model parameters to normal values. One solution would be to increase the tag line density in the radial direction; however, as discussed previously, this would require to make the tracking more robust with respect to tag jumping. Alternatively, for future CMR acquisitions, tagged image resolution needs to be improved for better radial strain mapping.

The effect of SNR is more pronounced for the estimation of the displacement field and radial strain when combined with the anisotropic voxel sizes (see Figure 5.7 and Figure 5.8). Although the anisotropic images represent a better approximation of the in vivo imaging setting, we do not observe a dramatic increase in error for low SNR values by the choice of optimal β (Figure 5.8a, b). On the contrary, circumferential and longitudinal strains did not show significant increase in error when choosing an anisotropic voxels size within the range evaluated in this study. And again, since this is found with a fine temporal discretization and an optimal motion tracking method, this reinforces the point that reduced radial strain measured on in vivo images is induced by limited image spatial resolution and SNR.

To further study this point and mimic multi breath hold in vivo acquisitions, we investigated geometrical stack misalignment as additional source of error (see Figure 5.9). While the direction of shifting appeared to not influence the error, we observed an increased error more pronounced in the radial strain component while the other two components remain insensitive when stacks are shifted further apart.

Radial strain quantification remains sensitive to low SNR, TPR and slice misalignment, however the quantification of circumferential and longitudinal strains appears to be affected only little across the parameter range investigated in this study. Both global longitudinal strain (GLS) and global circumferential strain (GCS) have been used as prognostic value for disease severity in the clinical setting [Huttin et al., 2016; Reindl et al., 2019], with GLS being the most widely used metric to predict heart failure [Ersboll et al., 2012]. To this end, the tracking method used in this study [Genet et al., 2018], offers a robust way for the assessment of clinically used strain values.

In order to make radial strain measurement more robust and potentially useable in the clinical setting, multiple attempts have already been made. Combining untagged and tagged images has been shown to perform better compared to using only one type of image [Shi et al., 2012; Tobon-Gomez et al., 2013], though the use of untagged images suggests that strain heterogeneities might not be mapped accurately. Proposed as a new imaging modality, SubTag SSFP feature tracking has allowed for acquiring regional deformation and ventricular function in a single MRI scan, hence, achieving shorter scan time and better mechanical assessment [Schrauben et al., 2018]. Lastly, the imaging process itself has also been modeled to understand the effect of partial voluming, which deteriorates the image quality, and as a consequence, deformation assessment [Škardová et al., 2019]. Nevertheless, our study suggests that by improving image resolution, measuring accurate radial strain fields could be achieved based solely on tagged MRI with existing image processing techniques.

5.5. Conclusion

In this study, we systematically investigated the accuracy and precision of deriving LV strain components from CMR tagged images by FE digital image correlation. It shows the robustness

of GLS and GCS to varying image characteristics, supporting their reliability and common usage in the clinical setting. Moreover, the error analyses suggest that it is worthwhile investing into higher spatial resolution when planning tagged CMR acquisitions in order to obtain a robust radial strain estimate.

5.6. Supporting Information

Figure 5.10 represents the dependency of the optimal regularization parameter on image resolution and SNR. The color code shows the value of regularization parameter ranging from 0.0 to 0.3. For isotropic image resolution (Figure 5.10a), change in SNR does not affect the value of optimal regularization strength for small pixel size (1 mm). However, for larger pixel size, regularization strength increases with decreasing SNR. Similarly, for a given SNR, increasing pixel size is compensated with higher regularization strength. For the worst case (pixel size = 3.5 mm and SNR 5), the image registration requires $\beta = 0.2$. For anisotropic image resolution (Figure 5.10b), the dependency of regularization strength on SNR and pixel size follows the same trend as in isotropic images. For the worst case (pixel size = $3.5 \times 7.0 \times 7.0$ mm³ and SNR 5), $\beta = 0.3$ is required.

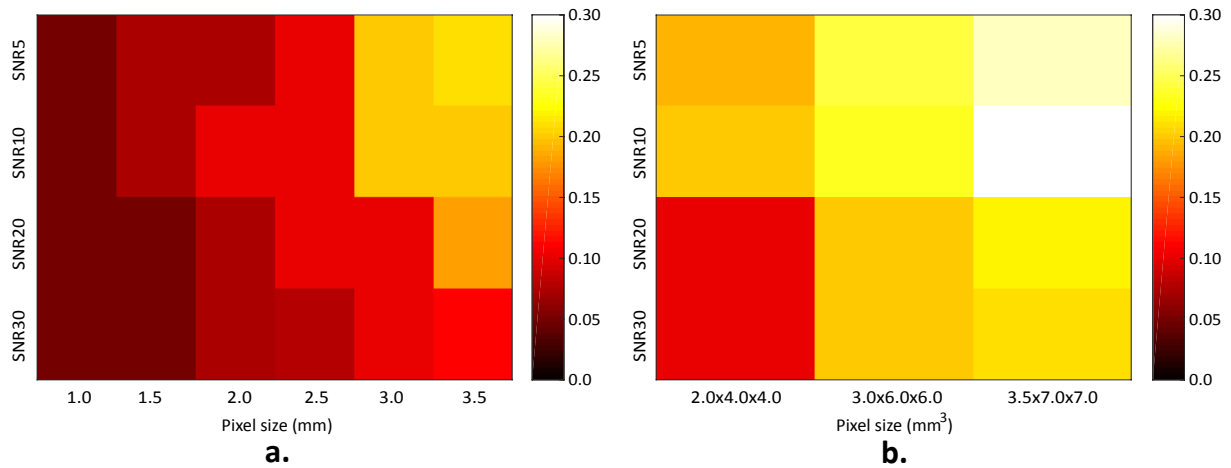


Figure 5.10. Change in optimal regularization strength with respect to image resolution and SNR. Colour code represents the value of regularization strength. (a) The pixel size (in mm) in one direction is shown on x axis for isotropic images. SNR has more impact on the choice of regularization strength as pixel size increases. (b) For anisotropic images, 3D image resolution is represented on x axis (in mm³). For a given SNR, increasing pixel size requires more regularization. Likewise, higher regularization is required for decreasing SNR when pixel size is kept constant.

The regional changes in normalized absolute displacement error (%) and mean \pm standard deviation in strain component errors are plotted for IP and TP shifts in Figure 5.11 and Figure 5.12, respectively.

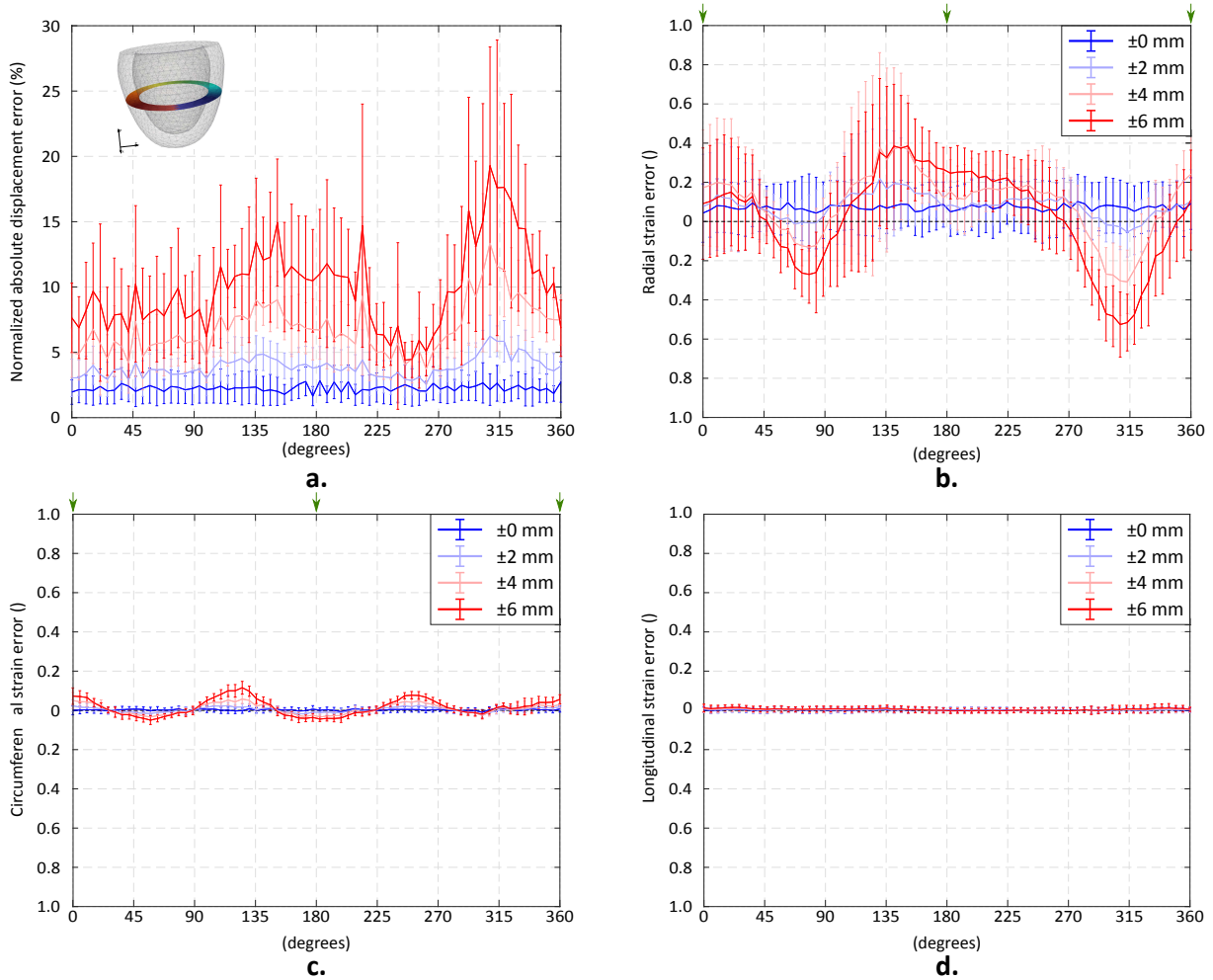


Figure 5.11. Effect of in-plane shift on regional motion quantification. Results on images with anisotropic pixel size $3.5 \times 7.0 \times 7.0 \text{ mm}^3$ and SNR 20 for 7 mm tag distance. For all the plots, colour code shows the amount of in-plane shift ranging from $\pm 0 \text{ mm}$ to $\pm 6 \text{ mm}$. (a) Mean \pm standard deviation in normalized displacement error norm (%) plotted as a function of in-plane angle, α with respect to shift direction. (b-d) Mean \pm standard deviations in component-wise Green-Lagrange strain error as a function of in-plane angle. Increasing amount of shift leads to an increased error in displacement field (a). Radial and circumferential strain errors show the dependency on in-plane angle, especially for the maximum amount of shift, $\pm 6 \text{ mm}$. The shifts are applied at $\alpha = 0^\circ$, $\alpha = 180^\circ$ and $\alpha = 360^\circ$, shown with the green arrows on top (b, c). (d) Longitudinal component is insensitive to any shift.

For any kind of shift, we expect the maximum error to occur in the direction of the shift, where the tag lines are blurred. Hence, for IP shift (Figure 5.11), the errors are plotted with respect to a change in in-plane angle, α , where the shift is applied at $\alpha = 0^\circ$, $\alpha = 180^\circ$ and $\alpha = 360^\circ$,

shown with the green arrows on Figure 5.11b, c. For both the displacement (Figure 5.11a) and strain components (Figures 5.11b, c), maximum errors are observed for the largest amount of shift, ± 6 mm (shown by the red curves). When the image stacks are shifted in-plane, the smallest error is found in opposing sectors orthogonal to the direction of the shift. Hence, we observe some kind of periodicity in the distribution of radial (Figure 5.11b) and circumferential (Figure 5.11c) strain errors as a function of sector position, while the longitudinal component (Figure 5.11d) remains insensitive.

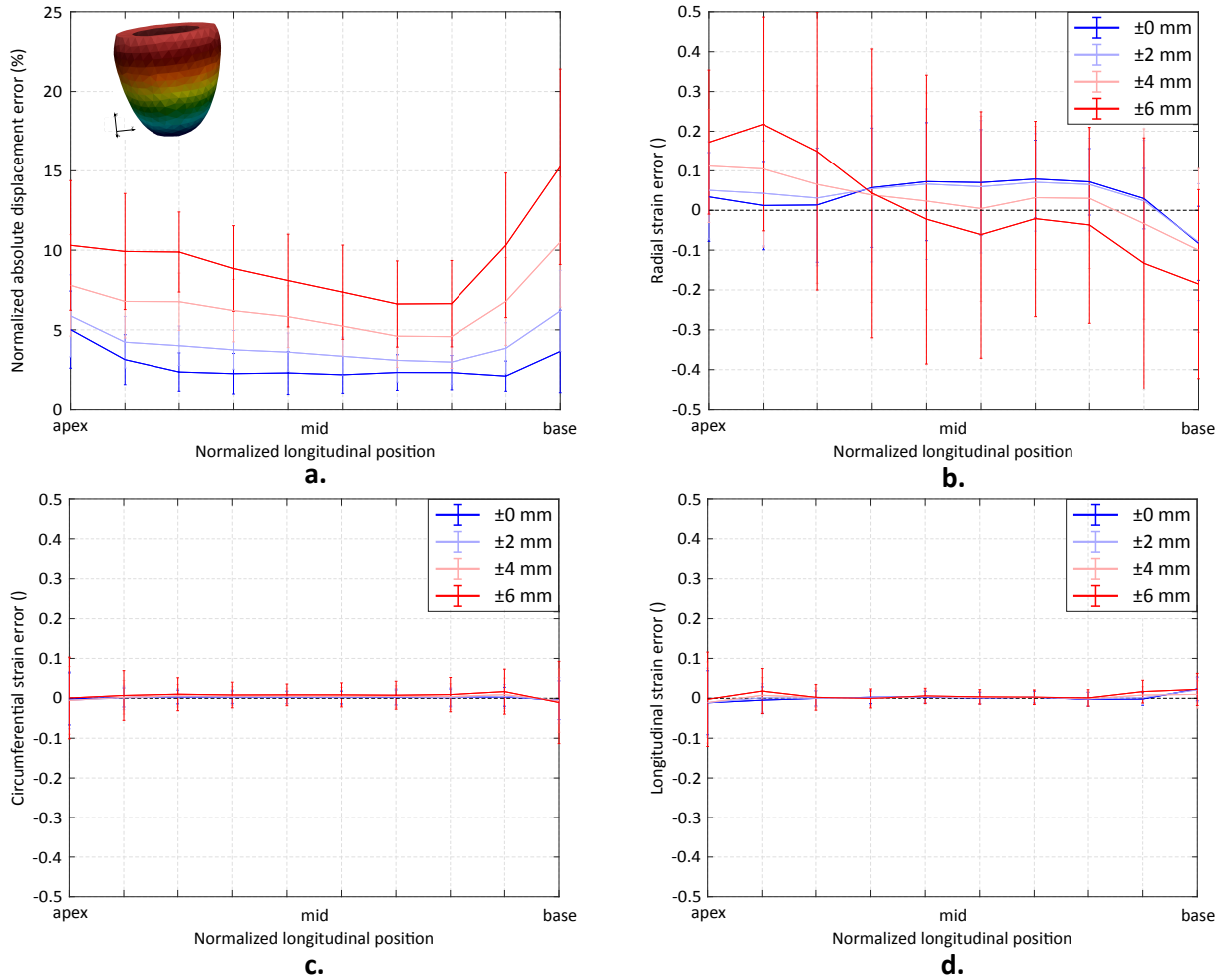


Figure 5.12. Effect of through-plane shift on regional motion quantification. Results on images with anisotropic pixel size $3.5 \times 7.0 \times 7.0$ mm³ and SNR 20 for 7 mm tag distance. For all the plots, colour code shows the amount through-plane shift ranging from ± 0 mm to ± 6 mm. (a) Mean \pm standard deviation in normalized displacement error (%) plotted as a function of normalized longitudinal position. (b-d) Mean \pm standard deviations in component-wise Green-Lagrange strain error as a function of normalized longitudinal position. Increasing amount of shift leads to an increased error in displacement field. Radial strain error increases towards the base and apex, especially for the maximum amount of shift, ± 6 mm, while (c) circumferential and (d) longitudinal components are insensitive to any shift.

The effect of TP shift (Figure 5.12), however, is better observed in the longitudinal direction. For TP shift, we expect to see more error towards base and apex where the tag information is lost due to shifting in the longitudinal direction. For the maximum amount of shift (± 6 mm), the displacement and radial strain error get larger towards the apex and base compared to lower amounts of shift. Circumferential (Figure 5.12c) and longitudinal (Figure 5.12d) strain errors are less sensitive to TP shift.

Chapter 6

Quantification of Left Ventricular Strain and Torsion by Joint Analysis of 3D Tagging and Cine MR Images⁵

6.1. Introduction

CMR is considered the reference standard for the assessment of healthy and diseased myocardium [Alfakih et al., 2004]. Quantification of global cardiac function is widely performed based on LVEF, stroke volume, or myocardial thickness. Despite their common usage for the assessment of cardiac performance, relying on global measures alone may result in misinterpretation of cardiac performance [Abraham & Nishimura, 2001]. Compared to global contractile properties, regional changes have been found to serve better for diagnosis and early intervention in many cardiac diseases [Sutherland et al., 1994; Nagueh et al., 2001; Ibrahim, 2011; Ng et al., 2011]. Among them, IHD is known to cause local dysfunctions of the heart wall while global functional measures remain insensitive to the location and severity of the infarction [Friedberg & Mertens, 2009; Collins, 2015]. Moreover, regional changes in cardiac function are proposed to be a strong indicator of both HCM) (Huang et al., 2017; Serri et al., 2006; Smiseth et al., 2016) and heart failure with preserved LVEF [Hasselberg et al., 2015; Smiseth et al., 2016].

Cine CMR has become one of the clinical work horses to assess the global functional parameters such as ventricular volumes, LVEF and mass [Castillo et al., 2003]. It provides excellent temporal [Barkhausen et al., 2001; Plein et al., 2001] and spatial resolutions, with a higher SNR and tissue contrast than other imaging modalities [Barkhausen et al., 2001; Pereles et al., 2001]. However, material point tracking from cine CMR is challenging due to the lack of contrast within the myocardium [Wu et al., 2014]. Beyond cine imaging, CMR tagging has been

⁵ Manuscript under revision

introduced to quantify local deformation measures, e.g., strain and torsion [Rademakers & Bogaert, 1997; Stuber et al., 1999] by introducing the non-invasive physical markers on the myocardium [Zerhouni et al., 1988], which is followed by a more efficient and fast technique, SPAMM [Axel & Dougherty, 1989a]. The tag fading problem inherent to SPAMM was solved introducing CSPAMM [Fischer et al., 1993], which was later added the capability to track 3D deformation of the heart with the slice-following CSPAMM [Fischer et al., 1994]. More recent improvements in 3D tagging techniques have been focused on the misregistration issues related to multi-slice acquisitions and decreasing the acquisition time [Rutz et al., 2008; Stoeck et al., 2012]. Other than cine and tagged MRI, DENSE allows for a direct visualization of myocardial deformation encoded into the MR signal phase [Kim et al., 2004] and demonstrated to allow the quantification of LV function both on animals [Haggerty et al., 2013, 2014] and in the clinical setting [Bilchick et al., 2014].

Studies on the healthy human heart using CMR tagging have reported regional differences in strain distribution [Young et al., 1994; Moore, Lugo-Olivieri, et al., 2000; Bogaert & Rademakers, 2001]. Although CMR tagging provides regional deformation metrics, the saturation bands generated in the image make it impossible to accurately delineate the endocardial and epicardial borders [Makram et al., 2016]. Given its image quality, a robust assessment of LV functional analysis remains challenging [Schrauben et al., 2018]. Therefore, the patient needs to be scanned separately for the cine and tagged CMR, increasing both the scan time and number of breath-holds [Schrauben et al., 2018]. Alternative methods to CMR tagging such as CMR-FT [Hor et al., 2011] were developed to speed up the existing techniques for clinical feasibility. CMR-FT is similar to speckle tracking echocardiography [Bohs et al., 2000] in terms of its dependence on tracking epicardial and endocardial borders and has been validated against tagged HARP analysis for the assessment of peak average circumferential myocardial strain [Hor et al., 2010] and used in diagnosing cardiac disorders [Hor et al., 2010; Schuster, Paul, et al., 2013]. However, radial strain obtained from this method is not satisfying [Padiyath et al., 2013]. Limited to 2D acquisitions [Schuster et al., 2011], strain measurements obtained from CMR- FT techniques are dependent on the delineation of the endocardial and epicardial contours by the user, leading to limited inter-study reproducibility [Morton et al., 2012] and intra-observer reproducibility [Schuster, Morton, et al., 2013]. Among other strain components, only the GCS agrees with CMR tagging results [Cowan et al., 2015]. However, the

segmental differences cannot be characterized unless tagging is utilized [Augustine et al., 2013; Cowan et al., 2015].

The finite element model (FEM)-based registration technique used in this study has already been tested and validated both on in vivo [Genet et al., 2018] and synthetic MR images [Berberoğlu et al., 2019], and also for the LV torsion quantification in case of impaired LV function [Castellanos et al., 2021]. We further demonstrated that limitations of radial strain quantification from 3DTAG images can be related to limited spatial resolution and SNR [Berberoğlu et al., 2021]. Therefore, we propose an alternative way to improving strain quantification from 3DTAG data here based on joint analysis of cine and tagged CMR to combine the advantages of 3DTAG and cine MR images. The manuscript is organized as follows. We first describe the image dataset and the FEM-based image registration technique in Section 2. Section 3 outlines the analysis results. After a detailed discussion in Section 4, Section 5 concludes with some important remarks.

6.2. Materials and Methods

In this section, we first describe the image datasets used in this study and the FEM-based image registration technique is later summarized. Next, the processing pipeline to couple cine and tagged images is explained. The section concludes with the introduction of metrics used to assess the performance of joint analysis of cine and tagged CMR data, which is referred to as m3DTAG hereafter.

6.2.1. Image Acquisition and Preprocessing

Two datasets are used to demonstrate the performance of the proposed m3DTAG image registration technique. The first one includes 32 image sets retrospectively selected from our previous porcine study [Stoeck et al., 2021]. In brief, imaging was performed on a 1.5T clinical Philips Achieva MR system (32-channel cardiac receiver array). All animal handling procedures and protocols were approved by the Cantonal Veterinary Office (Zurich, Switzerland). The imaging protocol consisted of multi-slice cine CMR in short-axis view with the following parameters: $1.8 \times 1.8 \text{ mm}^2$ spatial resolution, 8 mm slice thickness, 25 heart phases, 1.5ms/3ms

TE/TR as well as 3D tagged imaging [Rutz et al., 2008] acquiring three stacks with orthogonal CSPAMM [Fischer et al., 1993] using the following imaging parameters: 2x2x5 mm³ spatial resolution, 110x110x110 mm³ field-of-view, 26 heart phases, 4mm tagline distance, 4.3ms/9.2ms TE/TR, turbo factor 3, echo planar imaging factor 7.

The second dataset consists of volunteer data from the Cardiac Motion Analysis Challenge [Tobon-Gomez et al., 2013], which is publicly available. The dataset includes cine and 3DTAG images of healthy volunteers. In this study, we excluded five of the volunteers (V4, V5, V7, V8, and V11) due to poor image segmentation quality or slice inter breath-hold misalignment. For both the porcine and human datasets, cine and 3DTAG images were normalized to their maximum pixel intensity and spatially resampled by Lanczos interpolation to obtain an isotropic pixel size using MeVisLab⁶.

6.2.2. FEM-based Image Registration

Though the image coupling strategy described in Section 2.3 is mostly independent from the choice of image registration technique, we now briefly describe the FEM-based image registration technique used in this study, which was detailed in [Genet et al., 2018]. It requires an initial volume mesh that matches the heart phase from which the registration starts. To this end, LV geometries were obtained from the manual segmentation of the porcine dataset, based on the cine images at ES using MeVisLab. Segmentation was performed both on the short-axis and long-axis views. The resulting surface meshes were converted into volume meshes using first-order finite elements using GMSH [Geuzaine & Remacle, 2009]. The local transmural, circumferential and longitudinal directions were assigned to each node and element on the LV mesh with respect to the centroid using the normalized pseudo-prolate spheroidal coordinate system [Genet et al., 2014, 2015]. For the human dataset, the LV geometries at ED frames were readily available along with cine and 3DTAG images. In accordance to the previous studies, we run the registration algorithm for the regularization strength $\beta = 0.1$, which has been found to be a near-optimal value for a wide range of images [Genet et al., 2018; L. C. Lee & Genet, 2019]. For the registration of cine, 3DTAG and m3DTAG images, performed using the FE method, the LV meshes were extruded by an extra layer of

⁶ <http://www.mevislabs.de>

elements with a thickness ranging from 2 to 3 mm around the ventricle, referred to as boundary layer, generated using GMSH. FEM-based image registration utilized in this study is based on the pixel intensities within the mesh, therefore, an accurate tracking of an interface requires inclusion of pixels on both sides, which is solved for the epicardium by adding the boundary layer. Therefore, the purpose of the boundary layer is solely to improve the image registration performance and it is not considered for the strain computation [Genet et al., 2018].

For image registration, a continuum formulation and the discretization technique using the FE method is introduced. I_0 and I_t denote the scalar intensity fields for the images representing the object in the reference, Ω_0 , and current, Ω_t , configurations, respectively. Between these two configurations, we can define a deformation map that translates the reference points $\mathbf{X} \in \Omega_0$ onto their spatial counterparts $\mathbf{x} = \Phi(\mathbf{X}) = \mathbf{X} + \mathbf{U}(\mathbf{X}) \in \Omega_t$, through the displacement field, \mathbf{U} . The registration problem is to find the displacement field between Ω_0 and Ω_t . The task is intrinsically ill-posed due the presence of image noise. Hence, the problem is reformulated as a minimization problem:

$$\text{find } \mathbf{U} = \text{argmin} \{ h = (1 - \beta)\Psi^{\text{im}} + \beta\Psi^{\text{reg}} \}, \quad (6.1)$$

weighted by regularization strength β , the image similarity metric,

$$\Psi^{\text{im}} = \frac{1}{2} \|I_t \circ \Phi - I_0\|_{L^2(\Omega_0)}^2, \quad (6.2)$$

and the regularization energy

$$\Psi^{\text{reg}} = \frac{1}{2} \|\mathbf{div}(\boldsymbol{\sigma})\|_{L^2(\Omega_t)}^2, \quad (6.3)$$

where $\boldsymbol{\sigma}$ is the Cauchy stress tensor. This registration technique has its novelty in utilizing a continuum finite strain formulation of the equilibrium gap principle introduced in [Claire et al., 2004], readily discretizable with standard finite elements. The main advantage of utilizing the equilibrated warping is that it enforces strong mechanical sense to the displacement field without imposing any constraint on the strain magnitude and depends solely on the balance of mechanical equilibrium. The use of finite elements also provides geometrical regularization through the FE mesh.

The classical Ciarlet-Geymonat potential is used to model the strain energy potential

$$\rho_0 \psi = \frac{\kappa}{2} (J^2 - 1 - \ln(J)) + \frac{\mu}{2} (I_C - 3 - 2\ln(J)), \quad (6.4)$$

in terms of bulk and shear modulus, κ and μ , and the volume map, $J = \text{Det}(\mathbf{F})$. The right Cauchy-Green deformation tensor is represented by $\mathbf{C} = \mathbf{F}^T \mathbf{F}$, while $I_C = \text{Tr}(\mathbf{C})$. The variational formulation of Equation 6.1 is obtained by following the general FE procedure, which is then linearized and discretized using standard continuous Lagrange elements. One can refer to [Genet et al., 2018] for more details on the formulation and solution procedure. The method is implemented based on FEniCS⁷ and VTK libraries, and freely available as a Python library⁸.

6.2.3. Coupling SSFP and 3DTAG Images

Figure 6.1 illustrates the pipeline to generate m3DTAG images. First, FEM-based image registration is performed on standard multi-slice balanced SSFP images (Figure 6.1a).

In order to mask the tagged images, the resulting displacement fields are linearly interpolated in time to match the temporal resolution of 3DTAG images according to:

$$\mathbf{d}_{3DTAG}^m = \mathbf{d}_{SSFP}^n + (\mathbf{d}_{SSFP}^{n+1} - \mathbf{d}_{SSFP}^n) \frac{(t_{3DTAG}^m - t_{SSFP}^n)}{(t_{SSFP}^{n+1} - t_{SSFP}^n)}, \quad (6.5)$$

with t_{SSFP}^n and t_{SSFP}^{n+1} corresponding to the acquired heart phases of the bSSFP acquisition and \mathbf{d}_{SSFP}^n and \mathbf{d}_{SSFP}^{n+1} being the corresponding displacement fields. The initial reference mesh is mapped onto the 3DTAG images using the DICOM header information of slice position and angulation and subsequently warped using the interpolated displacement fields (Figure 6.1b). Finally, 3DTAG images are masked using the meshes at each time frame and a background intensity is assigned to the masked region. The background intensity value, denoted γ , is defined as the average of the 95th percentile of the image intensities, considering only the voxels covered by the LV wall. It represents the unique parameter of the coupling strategy, and its impact on the m3DTAG tracking is thoroughly studied in Section 3.1. The corresponding

⁷ <https://www.fenicsproject.org>

⁸ https://gitlab.inria.fr/mgenet/dolfin_warp

short-axis and long-axis views after masking are shown in Figure 6.1c and Figure 6.1d, respectively. m3DTAG image registration is then performed.

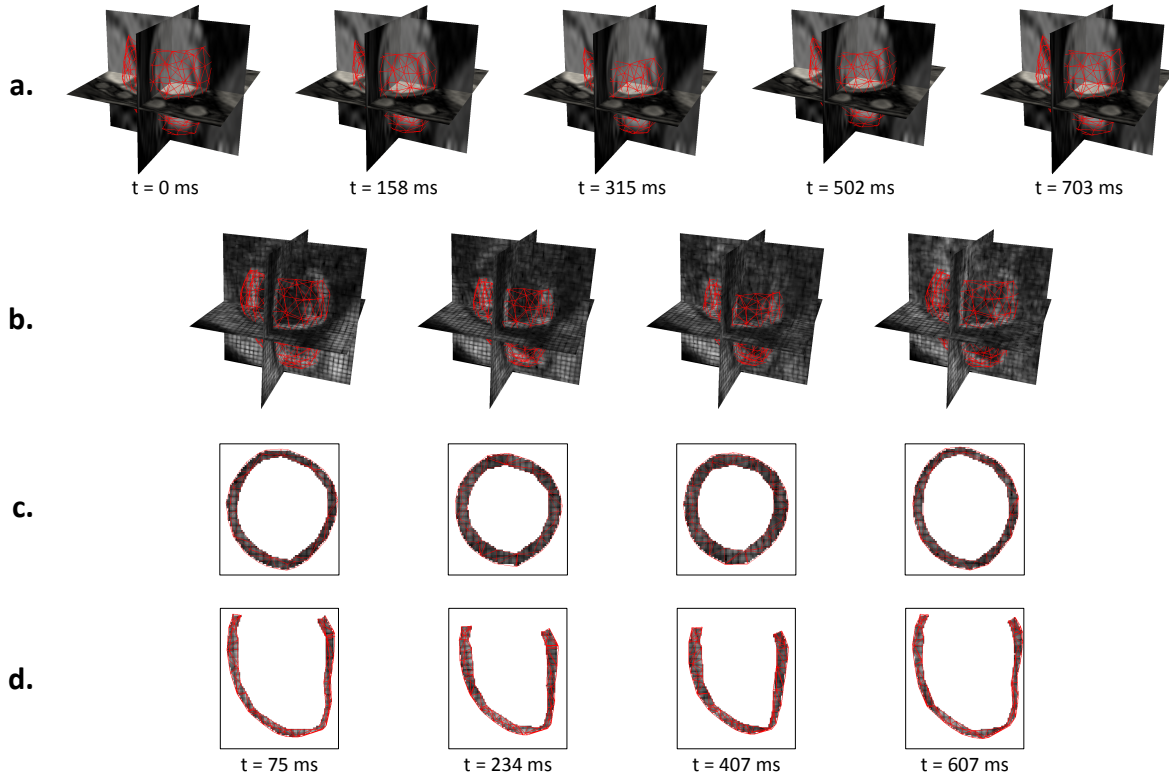


Figure 6.1. m3DTAG image generation pipeline. (a) Mesh configurations obtained from SSFP image registration, which are translated into 3DTAG image coordinates and interpolated in time to match the acquisition time for 3DTAG images, shown in (b) superimposed with 3DTAG images. m3DTAG images on (c) short-axis, and (d) long-axis views, respectively. Masking is performed by keeping the tag line pattern inside the mesh, while the rest of the image intensity (background intensity) is assigned to a constant value.

6.2.4. Metrics Used to Assess m3DTAG Image Registration Performance

FEM-based image registration is performed separately on SSFP, 3DTAG, and m3DTAG images. Performance of m3DTAG image registration is assessed for varying background intensities in terms of two deformation metrics. First the mean \pm standard deviation of the Green-Lagrange strain error is reported. For this purpose, we define the component-wise Green-Lagrange strain error at ES with respect to ED:

$$e^i = s^i - s_{SSFP}^i, \quad (6.6)$$

where e^i is the strain error in s^i , that is the scalar strain value for component s over element i . Reference strains are obtained from SSFP images and represented by s_{SSFP}^i . ES Green-

Lagrange strains are rotated in local pseudo-prolate spheroidal coordinates, and represented by the radial, circumferential, and longitudinal components. In this study, we utilized the P1 elements such that the strain is constant over each element. Therefore, the strain analysis was performed at the element level. The mean (e_{avg}) and standard deviation (e_{std}) in e^i are computed across the elements of a mid LV section for both the 3DTAG and m3DTAG images. For m3DTAG image registration, we compute the averaged e_{avg} and e_{std} over porcine/human datasets for a given background intensity.

The second performance metric is the mean \pm standard deviation in maximum LV twist error. We first define the LV twist, Φ_{img}^t , as the difference in rotations averaged through apical, $\alpha_{img}^{t,apex}$, and basal regions, $\alpha_{img}^{t,base}$, for $img = 3DTAG, SSFP, m3DTAG$ at time frame t . The error in LV twist, e_{img}^Φ , is computed with respect to the 3DTAG image registration,

$$\Phi_{img}^t = \alpha_{img}^{t,apex} + \alpha_{img}^{t,base}, \quad (6.7)$$

$$e_{img}^\Phi = \max|\Phi_{img}^t| + \max|\Phi_{3DTAG}^t|, \quad (6.8)$$

where $\max|\Phi_{img}^t|$ is the maximum LV twist over time. The mean ($e_{avg, img}^\Phi$) and standard deviation ($e_{std, img}^\Phi$) in e_{img}^Φ are computed across LV for SSFP and m3DTAG images. For a given background intensity, $e_{avg, img}^\Phi$ and $e_{std, img}^\Phi$ are averaged over the porcine/human datasets for the m3DTAG image analysis. We further computed the averaged normalized absolute error (%) in LV twist, $\Phi_{err, avg}$, and strain components, $e_{err, avg}$:

$$\Phi_{err, avg} = \frac{1}{N_{case}} \sum_{j=1}^{N_{case}} \frac{|e_{img}^\Phi|}{\max|\Phi_{3DTAG}^t|} 100 (\%), \quad (6.9)$$

$$e_{err, avg} = \frac{1}{N_{case}} \sum_{j=1}^{N_{case}} \frac{\sqrt{\sum_{i=1}^{N_{el}} (s_{m3DTAG}^{j,i} - s_{SSFP}^{j,i})^2}}{\max|s_{SSFP}|} 100 (\%), \quad (6.10)$$

where $s_{m3DTAG}^{j,i}$ and $s_{SSFP}^{j,i}$ are the scalar strain values for m3DTAG and SSFP registrations for the j^{th} porcine/human dataset and i^{th} mesh element, respectively. N_{el} is the total number of elements in the mesh and N_{case} denotes the number of porcine/human datasets over which the normalized absolute error (%) is computed.

In order to compare the m3DTAG registration to the previous tracking challenge [Tobon-Gomez et al., 2013], we compute the normalized markers error, err , using the landmarks tracked by two observers on 3DTAG data and as published in [Tobon-Gomez et al., 2013], using following formula:

$$err = \frac{1}{n_{\text{markers}}} \sum_{m=1}^{n_{\text{markers}}} \frac{\sum_{t=1}^{n_{\text{frames}}} \|\underline{X}^m(t) - \underline{X}^{m,GT}(t)\|}{\sum_{t=1}^{n_{\text{frames}}} \|\underline{X}^{m,GT}(t+1) - \underline{X}^{m,GT}(t)\|}, \quad (6.11)$$

where n_{markers} and n_{frames} denote the number of valid markers within the mesh in the undeformed configuration and the number of time frames, respectively. $\underline{X}^{m,GT}(f)$ stands for the reference/ground truth position of marker m while $\underline{X}^m(t)$ is the tracked position at frame t .

6.3. Results

6.3.1. Analysis of Method Parameters

Figure 6.2 shows the mean \pm standard deviations in maximum LV twist error (Figure 6.2a) and component-wise ES Green-Lagrange strain errors (Figure 6.2b-d) as a function of background intensity normalized by the 95th percentile of the image intensity. The performance assessment of LV twist quantification is performed relative to the results of 3DTAG image registration. The green region in Figure 6.2a represents the error range in SSFP registration, which is -7.08 ± 3.65 and the red curve indicates for the mean \pm standard deviation in LV twist error for m3DTAG registration. m3DTAG images perform better in terms of LV twist quantification in comparison to SSFP images for $\gamma < 1.6$, having the smallest error, -0.03 ± 0.82 , when $\gamma = 0.4$.

For strain, SSFP registration is considered the reference. The mean \pm standard deviation in radial strain error (Figure 6.2b) is 0.46 ± 0.26 for 3DTAG images, represented by the blue region, while the red curve stands for the error in m3DTAG registration. For $\gamma > 1.05$, m3DTAG images yield less error than 3DTAG images and perform close to SSFP registration for $\gamma \in [1.6, 2.0]$. 3DTAG and m3DTAG registrations perform almost equally well for the

circumferential (Figure 6.2c) and longitudinal (Figure 6.2d) strain quantification and the results are not sensitive to a change in background intensity.

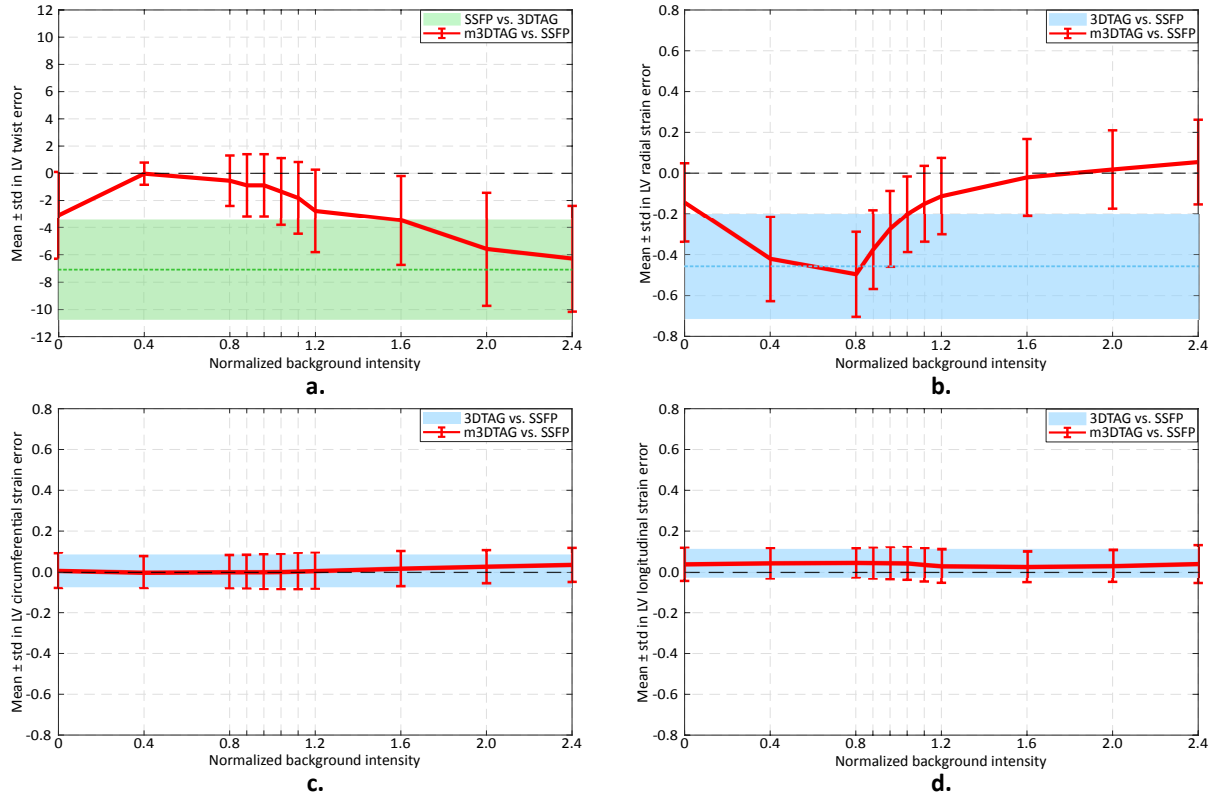


Figure 6.2. Effect of image background intensity on LV twist and strain error after masking of 3DTAG images. (a) Mean \pm standard deviation in LV twist error with respect to 3DTAG image registration, which is assumed to be the reference for the LV twist error computation. Red curve represents the error in m3DTAG registration. Green region represents the error in SSFP images, with the mean value shown by the green dotted line. Higher levels of background intensity results in larger errors in LV twist similar to SSFP. (b) Mean \pm standard deviation in radial strain error with respect to SSFP registration, which yields the reference strains for the strain error computation. Red curve represents the error in m3DTAG registration. Blue region represents the error in 3DTAG registration, with the mean value shown by the blue dotted line. For higher levels of background intensity, there is a decrease in error as m3DTAG tracking performs closer to SSFP tracking. The errors in (c) circumferential and (d) longitudinal strains (shown by the red lines for m3DTAG registration) are insensitive to a change in background intensity.

In order to determine the “optimal” background intensity, γ^* , at which LV twist and radial strain are captured equally well, Figure 6.3 shows the averaged normalized absolute error (%) in LV twist (defined by Equation 6.9), and Green-Lagrange strain components (defined by Equation 6.10). The radial strain and the twist error depend on the background intensity while the circumferential and longitudinal strains remain insensitive. In principle, one can relate the optimal background intensity with the image signal only, independent of the scaling used.

Based on the summation of errors in radial strain and twist, an “optimal” value is found at the minimum of 37.2 %, for $\gamma^* = 1.13$.

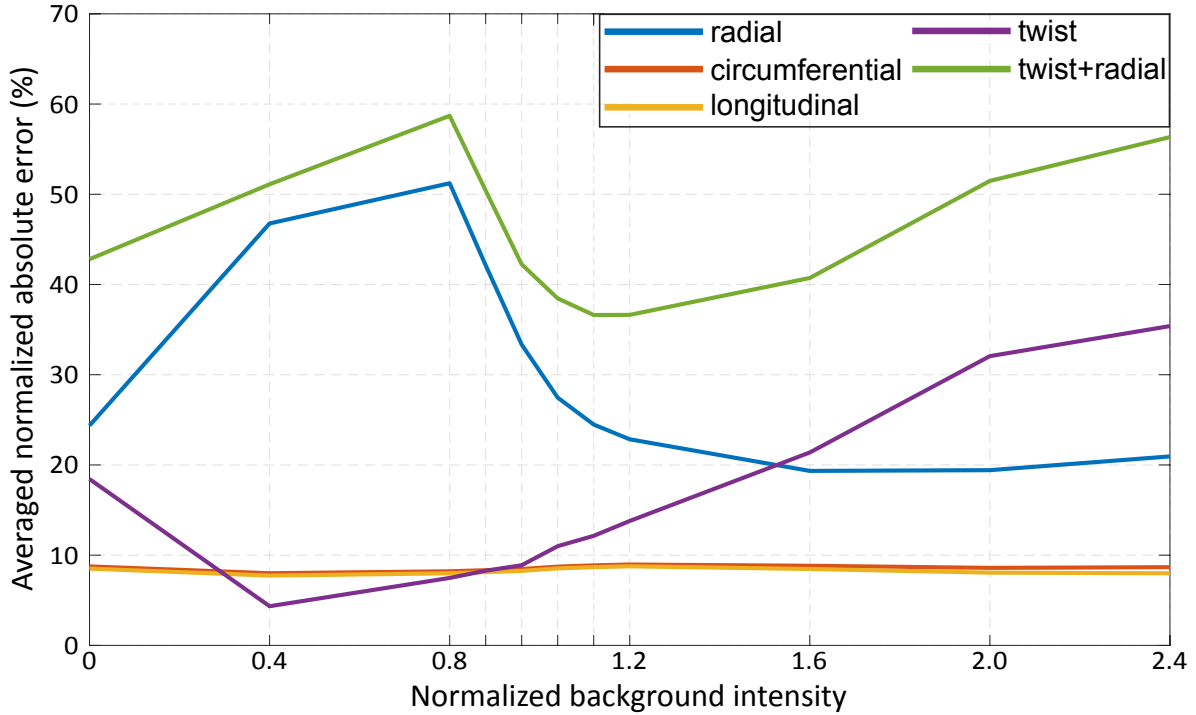


Figure 6.3. Determination of “optimal” image background intensity for m3DTAG analysis of porcine data. Averaged normalized absolute error (%) is plotted for LV twist, and Green-Lagrange strain components. LV twist and the radial strain are the two metrics that significantly vary with respect to image background intensity while the circumferential and longitudinal components remain insensitive. The summation of errors in twist and radial strain yields the optimal background intensity of 1.13, minimizing errors in these two metrics.

6.3.2. Method Validation

After assigning the optimal background intensity, the joint registration technique presented in this paper is validated against the benchmark data of the Cardiac Motion Analysis Challenge [Tobon-Gomez et al., 2013]. The performance of the image tracking algorithms was assessed relative to the manually tracked landmarks over 3DTAG images by two observers. Figure 6.4 shows the normalized marker errors computed using Equation 6.11 for all datasets from the challenge, for SSFP, 3DTAG and m3DTAG images (for $\gamma^* = 1.13$). Figure 6.4 shows the mean and standard deviation in normalized marker errors across all volunteers (separated by the dashed line) for FEM-based registration using SSFP, 3DTAG, and m3DTAG images as well as the challenge competitors: Fraunhofer MEVIS (MEVIS), Bremen, Germany; Imperial College London – University College London (IUCL), UK; Universitat Pompeu Fabra (UPF), Barcelona,

Spain; Inria-Asclepios project (INRIA), France. m3DTAG image registration yields a normalized markers error of 1.39 ± 0.93 . In case of SSFP image registration, it is 2.60 ± 0.64 , 3.04 ± 0.64 and 2.48 ± 0.54 for FEM-based registration, INRIA, and UPF, respectively. The normalized markers errors for 3DTAG image registration are 0.76 ± 0.33 , 0.82 ± 0.31 , 0.68 ± 0.23 , 0.99 ± 0.56 and 0.80 ± 0.25 for FEM-based registration, INRIA, UPF, IUCL, and MEVIS, respectively.

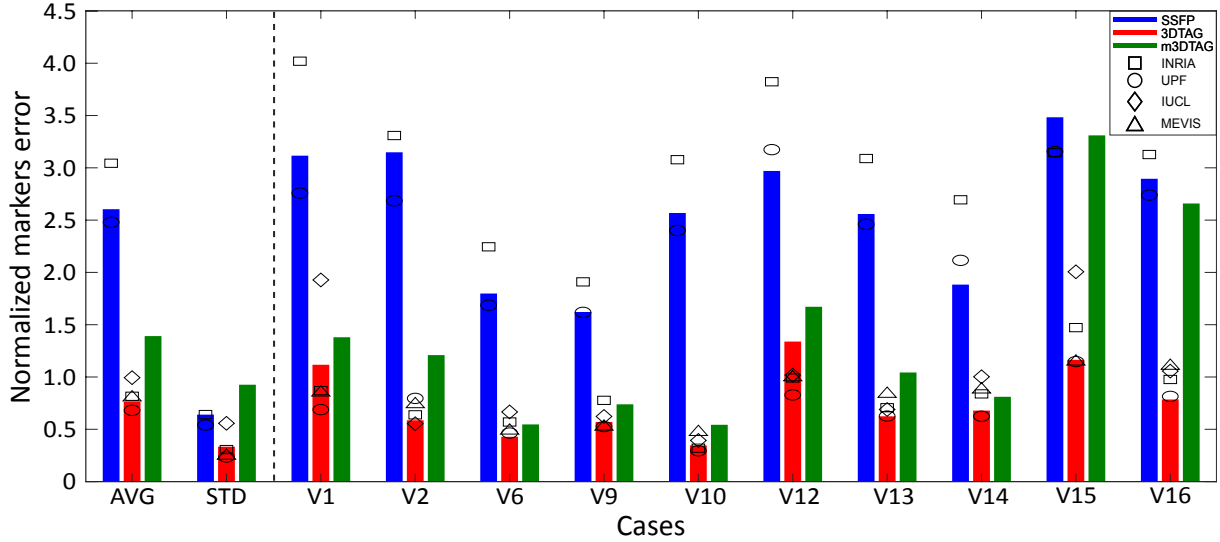


Figure 6.4. Validation of m3DTAG registration using Cardiac Motion Challenge data. Normalized markers errors for FEM-based registration using SSFP, 3DTAG, and m3DTAG images are represented by the blue, red, and green bar plots, respectively. The markers errors for other competitors (INRIA, UPF, IUCL and MEVIS) in the challenge are represented on top of the related bar plots. The average (AVG) and standard deviation (STD) in markers errors over all volunteers are separated by the dashed line. FEM-based registration performs well for all types of images, staying in the same normalized markers error range for the other groups.

6.3.3. Left Ventricular Strain and Twist Quantification

In Figure 6.5, we plotted the maximum LV twist for SSFP, 3DTAG and m3DTAG image registrations, using γ^* for each porcine dataset. The mean \pm standard deviation (AVG) over all porcine datasets is represented by the first group of bar plots and the rest stands for the individual cases included in this study. On average, maximum LV twist for 3DTAG image registration is $11.05^\circ \pm 3.34^\circ$. SSFP registration yields an average maximum LV twist of $3.97^\circ \pm 2.04^\circ$ while m3DTAG registration performs closer to 3DTAG registration with the LV twist value of $9.23^\circ \pm 2.59^\circ$.

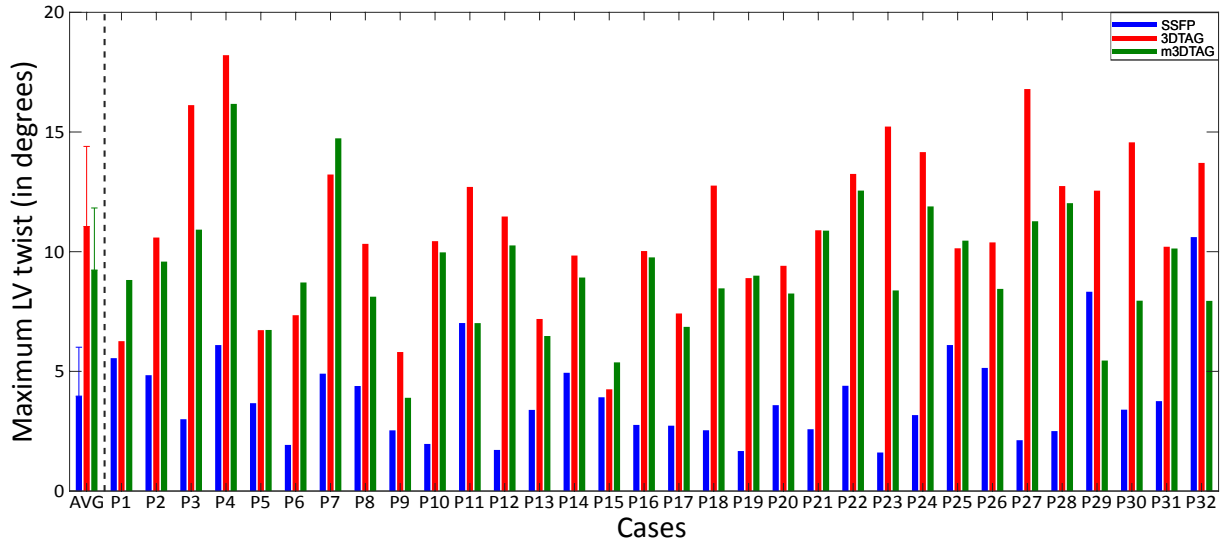


Figure 6.5. Maximum LV twist values for the porcine dataset. Blue, red, and green bars represent the max LV twists for SSFP, 3DTAG, and m3DTAG registrations, respectively. Mean \pm standard deviation (AVG) in LV twist computed over all animals are separated by a dashed line. m3DTAG registration performs closer to 3DTAG registration in terms of LV twist quantification while SSFP yields comparably lower LV twist.

Figure 6.6 represents the ES Green-Lagrange strain components for SSFP, 3DTAG, and m3DTAG image registrations. For each component, mean \pm standard deviation (AVG) in ES Green-Lagrange strains over all porcine datasets is represented as the first group of bar plots separated by a dashed line. The average ES radial strain for m3DTAG registration is 0.50 ± 0.20 while it is 0.20 ± 0.16 for 3DTAG and 0.65 ± 0.22 for SSFP image registrations (Figure 6.6a). For the circumferential component, all types of images perform equally: the average ES strains are 0.14 ± 0.07 , 0.14 ± 0.05 and 0.14 ± 0.07 for m3DTAG, 3DTAG and SSFP registrations, respectively (Figure 6.6b).

The average longitudinal strains are 0.14 ± 0.07 , 0.13 ± 0.05 and 0.17 ± 0.04 for m3DTAG, 3DTAG and SSFP registrations, respectively (Figure 6.6c). The pairwise t-test between the m3DTAG and SSFP registration yields the following p-values: $p_{rr} < 0.05$, $p_{cc} = 0.05$, $p_{ll} < 0.05$ and $p_{\phi} < 0.05$, for radial, circumferential, longitudinal strain components, and the twist, respectively. The p-values computed for m3DTAG and 3DTAG registrations are $p_{rr} < 0.05$, $p_{cc} = 0.73$, $p_{ll} = 0.19$ and $p_{\phi} < 0.05$.

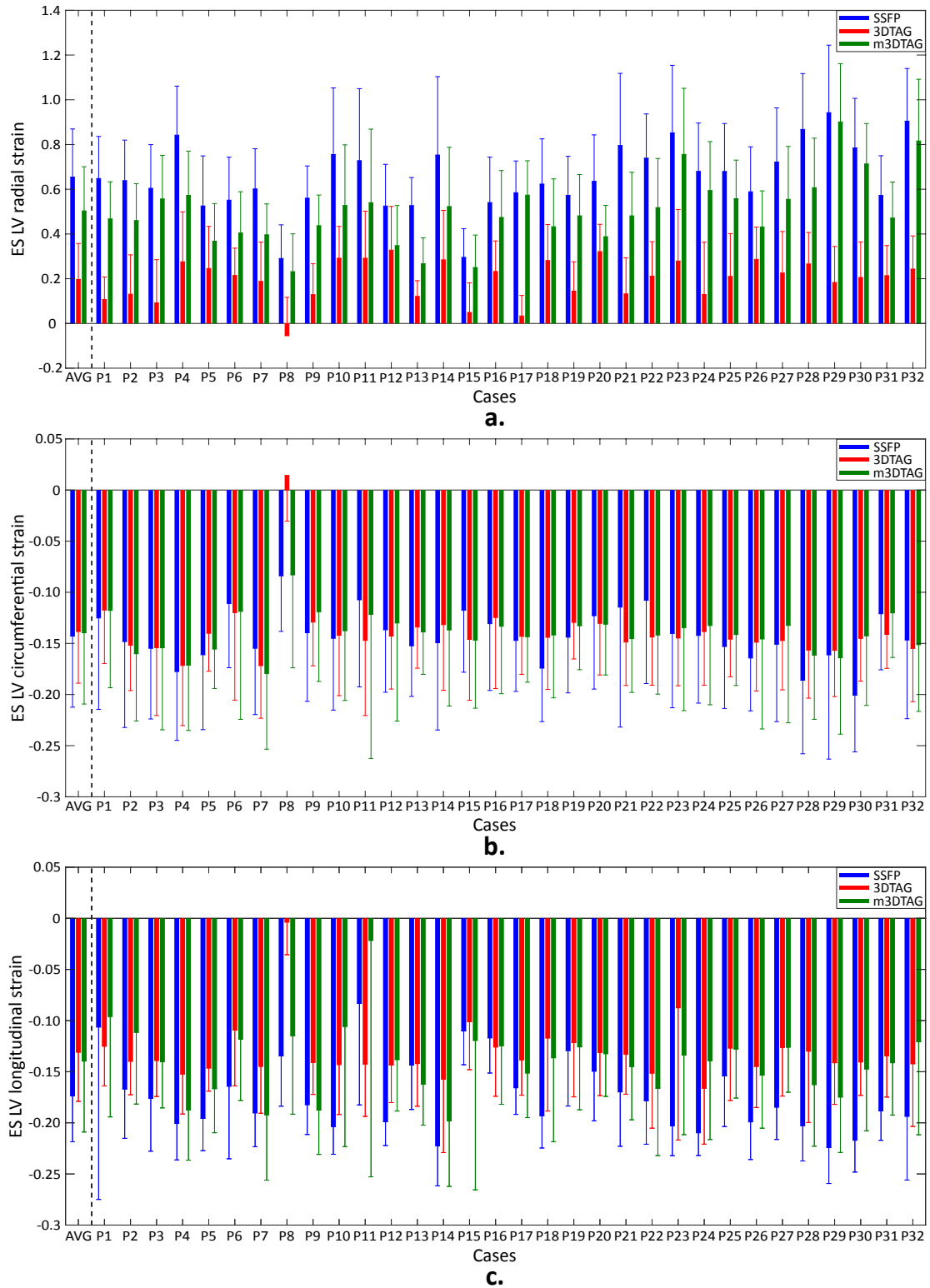


Figure 6.6. End-systolic Green-Lagrange strain components for the porcine dataset. Blue, red, and green bars represent the results for SSFP, 3DTAG, and m3DTAG registrations, respectively. (a) Radial, (b) circumferential and (c) longitudinal strains are represented both for the averaged (AVG) values over all image sets (separated by a dashed line) and individual cases. On average, m3DTAG registration performs closer to SSFP registration in terms of radial strain quantification while circumferential and longitudinal strains are captured almost equally for any type of image.

For the optimal background intensity, we performed Bland-Altman analysis to assess the agreement between SSFP, 3DTAG and m3DTAG registrations in terms of maximum LV twist and ES LV Green-Lagrange strain components, see Figure 6.7. For each plot, the 95% agreement interval is shown by the solid lines and the corresponding mean value by the dotted lines. Mean differences in max LV twist in SSFP and m3DTAG registrations with respect to reference 3DTAG registration are 7.09° and -1.82° , respectively (Figure 6.7a). Mean differences in ES LV radial strain in 3DTAG and m3DTAG registrations with respect to reference SSFP registration are -0.457 and -0.151 , respectively (Figure 6.7b).

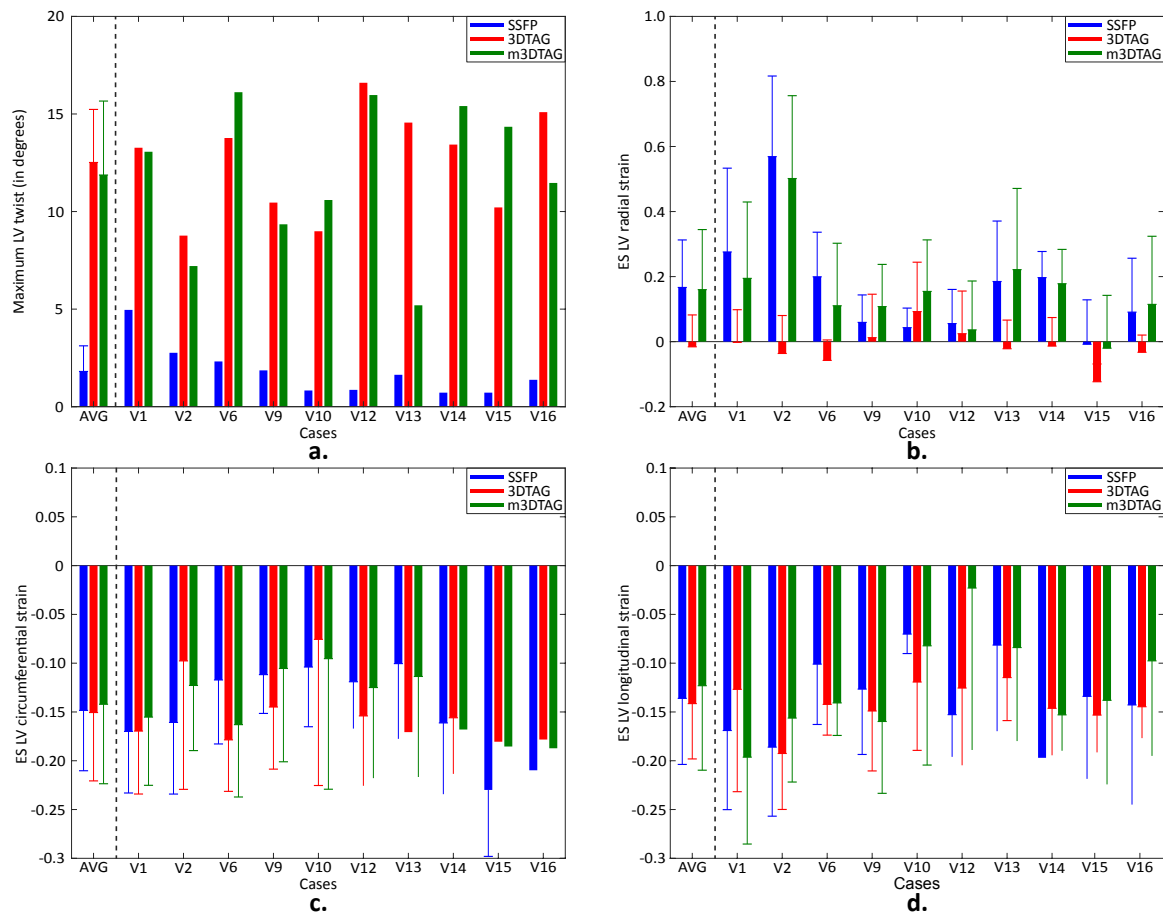


Figure 6.7. Bland-Altman analysis to assess the agreement between SSFP, 3DTAG and m3DTAG registrations for the optimal background intensity. The solid and dotted lines represent the 95% agreement interval and the mean difference, respectively, with the color code represented by the legend. (a) Comparison of SSFP and m3DTAG registrations for max LV twist assessment with respect to 3DTAG registration. The absolute mean of the difference between m3DTAG and 3DTAG is smaller than the one between SSFP and 3DTAG with a smaller agreement interval. (b) Comparison of 3DTAG and m3DTAG registrations for radial strain with respect to SSFP registration. m3DTAG registration underestimates the SSFP registration less than 3DTAG does with a relatively smaller agreement interval. For the (c) circumferential and (d) longitudinal components, both images yield similar errors with respect to SSFP registration.

For the circumferential component, 3DTAG and m3DTAG perform almost the same, with the respective mean errors 0.00447 and 0.00328 (Figure 6.7c). The mean difference for longitudinal component is slightly larger for 3DTAG and m3DTAG registrations; 0.0428 and 0.0341, respectively (Figure 6.7d).

Following the same approach as in the porcine data analysis, we run the registration algorithm on each image type; SSFP, 3DTAG, and m3DTAG for the Cardiac Motion Analysis Challenge data [Tobon-Gomez et al., 2013]. Figure 6.8 shows the analysis results in terms of the maximum LV twist (Figure 6.8a) and the component-wise ES Green-Lagrange strains (Figure 6.8b-d). The mean and standard deviation (AVG) in LV twist over all the volunteers included in this study are $1.80^\circ \pm 1.31^\circ$, $12.5^\circ \pm 2.72^\circ$ and $11.87^\circ \pm 3.79^\circ$ for SSFP, 3DTAG and m3DTAG registrations, respectively, and separated by a dashed line (Figure 6.8a). The averaged values (AVG) for all strain components are represented by the first group of bar plots (Figure 6.8b-d). The averaged ES radial strains are 0.17 ± 0.15 , -0.02 ± 0.10 and 0.16 ± 0.18 for SSFP, 3DTAG and m3DTAG images, respectively. SSFP and m3DTAG images performed equally well although 3DTAG registration yields negative radial strain. The averaged ES circumferential strains are 0.15 ± 0.06 , 0.15 ± 0.07 and 0.14 ± 0.08 while the longitudinal ones are 0.14 ± 0.07 , 0.14 ± 0.06 and 0.12 ± 0.09 for SSFP, 3DTAG and m3DTAG registrations, respectively. The pairwise t-test between the m3DTAG and SSFP registration yields the following p-values for the strain components and the twist: $p_{rr} = 0.74$, $p_{cc} = 0.47$, $p_{ll} = 0.44$ and $p_\phi < 0.05$ while they are $p_{rr} < 0.05$, $p_{cc} = 0.35$, $p_{ll} = 0.23$ and $p_\phi = 0.48$ when m3DTAG and 3DTAG registrations are compared.

6.4. Discussion

In this study, we have proposed to combine the advantageous features of two imaging modalities: cine and 3DTAG CMR. This technique allowed us to obtain the global shape information from the cine MR images while the regional deformation is acquired from the tagged data.

The performance of the m3DTAG registration and the acquired myocardial deformation measures are strongly dependent on the mask, and by that the way we temporally interpolate

the displacement fields from SSFP registration. The linear interpolation scheme utilized here could be improved by using higher order temporal functions to get a more accurate deformation estimate.

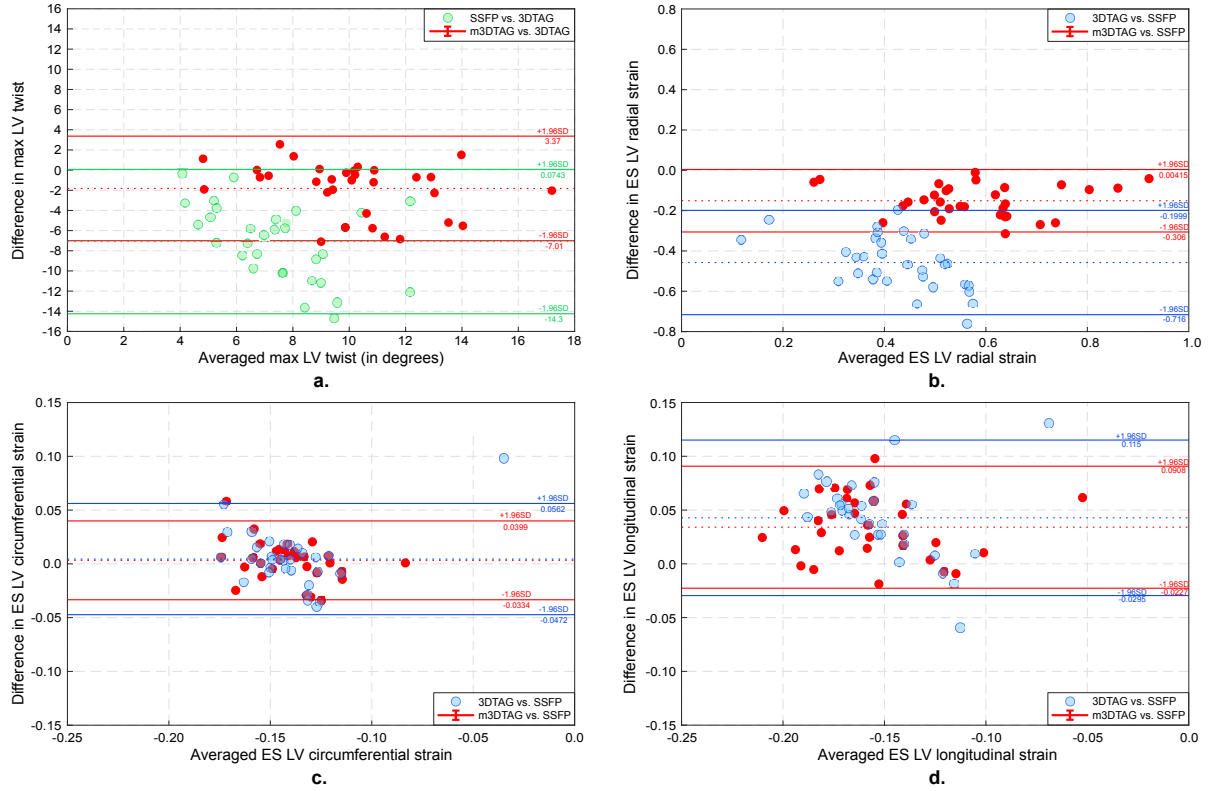


Figure 6.8. Results on Cardiac Motion Analysis Challenge data. Blue, red, and green bars represent SSFP, 3DTAG, and m3DTAG registrations, respectively. (a) Maximum LV twist plotted for each volunteer with the average (AVG) over all volunteers (separated by a dashed line) included in the study. m3DTAG registration performs closer to 3DTAG registration in terms of LV twist quantification while SSFP yields comparably lower LV twist. End-systolic (b) radial, (c) circumferential and (d) longitudinal strains are also represented for each volunteer with the averaged values (AVG) over all volunteers separated by a dashed line. In terms of radial strain quantification, compared to 3DTAG registration, there is a significant improvement on average when m3DTAG images are used. For the circumferential and longitudinal strains, SSFP and 3DTAG perform equally while m3DTAG images slightly underestimate the average values.

The error as function of background intensities for these LV twist and Green-Lagrange ES strain reveals that m3DTAG registration performs similar to SSFP registration as image background intensity gets closer to the limits of the intensity range utilized, which can be explained with the higher image contrast between LV wall and the image background. Likewise, assigning image background intensity values close to average image intensity results in a decrease in

image contrast around LV wall, hence, the m3DTAG registration performs closer to 3DTAG registration. Although we have observed a clear change in LV twist and radial strain errors for varying image background intensity, the errors in circumferential and longitudinal strain components stayed in the same range as SSFP image tracking error. Therefore, we defined the “optimal” image background intensity using the summation of normalized absolute error (%) in LV twist and radial strain component. The FEM-based image registration technique utilized here can be further improved by applying different weighting terms for the errors related to cine and 3DTAG registrations owing to the reverse trend in the change in LV twist and radial strain errors for varying image background intensity.

After determining the optimal background intensity, we first validated our joint analysis technique on the Cardiac Motion Tracking Challenge data [Tobon-Gomez et al., 2013] before presenting the strain and twist analysis results. The markers error computation is based on the manually tracked landmarks over 3DTAG. It was previously shown that FEM-based registration performs quite satisfactory in terms of markers errors for SSFP and 3DTAG image analysis [Genet et al., 2018]. For all the cases, except V15, m3DTAG registration performs better than SSFP images in terms of markers error while it is slightly worse than 3DTAG images for most of the cases. The averaged errors presented by the first two groups of bar plots in Figure 6.4 reveal that markers error for m3DTAG registration stays in the error range that the challenge contributors have, proving the performance of our joint analysis technique. Nevertheless, it is interesting to see that the markers error is generally larger with m3DTAG compared to 3DTAG, despite radial strains appearing in a more physiological range. For instance, for volunteers V15 and V16, 3DTAG yields lower markers error than m3DTAG while producing negative radial strain whereas strains obtained from m3DTAG are more physiological. One reason may be that the markers were manually positioned on the images for the challenge, which contain a bias due to low resolution and SNR as established in [Berberoğlu et al., 2021]. Consequently, these markers might not provide accurate ground truth for the actual tissue motion.

The combined approach of m3DTAG registration leverages the lack of capability to track LV twist of SSFP registration and outperforms 3DTAG image registration in the assessment of radial strain. In terms of circumferential and longitudinal strain components, we do not

observe a significant difference for any image type. We performed the same study on human dataset, and analyzed maximum LV twist and ES strain components for SSFP, 3DTAG and m3DTAG registrations, and observed the same trend in both performance metrics. We further performed pairwise t-test on m3DTAG images in comparison to SSFP and 3DTAG, for both the porcine and human datasets to find out if the difference between registration results is systematic or random. For both porcine and human datasets, we did not observe a statistically significant difference for circumferential and longitudinal strain components, as expected. For the porcine data, we found statistically significant differences in radial strain component both for the SSFP and 3DTAG registrations in comparison to m3DTAG, which can be related to the shift between the means of two datasets. The bias in radial strain estimation is systematic and can be attributed to the tracking method itself. Although for the volunteer dataset, we have higher p-values for the radial strain, it does not mean that there is no bias in the analysis results; this might be due to the random error component caused by the variational slice misalignment.

In order to investigate the agreement between SSFP, 3DTAG and m3DTAG registrations, we performed a Bland-Altman analysis for the porcine dataset, using the optimal background intensity. Similar to Figure 6.2, m3DTAG performance was assessed for LV twist and strain quantification with respect to 3DTAG and SSFP registration, respectively. In terms of the circumferential and longitudinal strain components, the mean differences obtained from comparing m3DTAG and 3DTAG with SSFP are close to each other, that supports our findings stated above. For LV twist, however, m3DTAG registration yields a mean difference closer to zero and smaller than 3DTAG registration. The superiority of m3DTAG registration over 3DTAG for the radial strain quantification is shown by a smaller absolute mean error.

Regarding the human datasets, it appears that quite low ES radial strain is measured even for SSFP images, that might have several underlying reasons: The FEM-based image registration technique is dependent on the segmentation and the image quality. The tracking performance drastically decreases in case the segmentation covers structures other than the ventricular wall. As mentioned in Section 2.1, we had to exclude five volunteer datasets due to slice misalignment. Moreover, the performance of m3DTAG registration in capturing the global shape information is correlated with SSFP registration. Any improper SSFP registration results

in masking inaccurately of 3DTAG images, potentially including the structures outside the ventricle. Hence, m3DTAG registration performance decreases drastically if SSFP registration is not good enough. Despite the low radial strains from SSFP and m3DTAG registrations found in the human datasets, we still make the point; the m3DTAG images yield better radial strain estimation compared to 3DTAG only while being superior to SSFP registration in terms of twist quantification.

In order to improve the cardiac motion quantification, several techniques have been proposed to combine the tagged and untagged images [Shi et al., 2012; Tobon-Gomez et al., 2013]. Recent studies on this area focus on the improvement of current techniques that allow for the quantification of the regional and global ventricular properties on a single scan, e.g., SubTag SSFP [Schrauben et al., 2018]. This method allows for combining the assessment of both the ventricular function and more accurate regional strain in a single scan, although it still suffers from assessing the segmental heterogeneity in strain distribution.

6.5. Conclusion

This study shows that combined processing of cine and 3DTAG images provides better quantification of LV deformation as either data source alone. m3DTAG images yield better radial strain estimation compared to 3DTAG only while being superior to SSFP registration in terms of twist quantification. Moreover, performance of the FEM-based image registration on m3DTAG images is comparable to the benchmark techniques in terms of manually tracked markers error while yielding more physiological myocardial deformation measures.

Chapter 7

Discussion and Outlook

In this thesis, we have performed a detailed analysis of LV deformation quantification from 3D tagging and cine CMR. We investigated the impact of tag distance, image resolution, and SNR on strain quantification from tagged CMR and proposed a combined image registration method of cine and tagged CMR for a more accurate quantification of myocardial deformation. The research results presented here are important to obtain robust LV radial strain and rotation estimation both from the image acquisition and post-processing perspectives.

7.1. Discussion

Non-invasive assessment of myocardial function is commonly performed by echocardiography and cardiac magnetic resonance in clinical cardiology. Although echocardiogram performs superior to MRI in terms of its cost-effectiveness, near real-time scanning capabilities, and the fast image post-processing tools, MRI has been gaining popularity with the recent advances in reducing the scan time [Piccini et al., 2012; Vincenti et al., 2014] and respiratory motion artifacts [Stehning et al., 2005]. Moreover, MRI provides a more accurate functional assessment due to its excellent spatial resolution while characterizing several aspects of the heart, e.g., cardiac structure and function, perfusion, viability. Today, MRI has a wide range of applications in the clinical setting, allowing for a non-invasive assessment of cardiac function. It has been the method of choice to evaluate cardiac dysfunctions, including congenital heart diseases [Gutiérrez et al., 2008], cardiomyopathies [Nelson et al., 2000; Edvardsen et al., 2006] and ischemic heart disease [Kelle & Nagel, 2008].

Accurate quantification of myocardial deformation metrics, strain, and torsion, holds the potential for a more comprehensive characterization of regional myocardial function. Besides its diagnostic and prognostic utility, strain can be used as a clinical biomarker for the follow-up

of patients due to its sensitivity to subtle alterations in cardiac function [Voigt & Cvijic, 2019]. Moreover, it might be actively used in the clinical setting for therapy planning of patients who receive CRT or heart transplantation. Cine and tagged CMR sequences are commonly used to assess myocardial deformation, having their own advantageous features. Cine CMR is the routine imaging technique for the assessment of global functional parameters while tagged CMR allows for a more regional characterization. The tracking performance on tagged CMR, especially the radial strain assessment, is highly affected by the image quality. In addition to the limited number of tags in radial direction, low temporal resolution and the decreased quality of tagged CMR due to the tag fading problem [Shi et al., 2012] remain the main limitations for accurate motion quantification. Moreover, the tag lines generated in the myocardium hamper the detection of the myocardial borders for an accurate functional analysis. Although cine CMR allows for reliable segmentation of epicardial and endocardial borders, thereby, more accurate assessment of radial deformation, the lack of features within the myocardial wall limits the assessment of regional distributions of deformation metrics [Augustine et al., 2013].

In the first part of the thesis, we validated [Berberoğlu et al., 2019] a recently proposed FEM-based image tracking technique that includes mechanical regularization [Genet et al., 2018]. We further investigated the effects of image properties on motion tracking performance using synthetic LV tagged CMR [Berberoğlu et al., 2021]. The analysis results reveal several findings, especially on the challenges of radial strain quantification. For individual and combined changes in tag distance, image resolution, or SNR, we could acquire robust estimates of global circumferential and GLS, which might explain their common usage for functional assessment in clinical practice. The radial strain quantification, however, is compromised by the increased image pixel size and decreased SNR on tagged CMR, which helped us to address a long-standing debate. In order to achieve robust radial strain estimates, image resolution needs to be improved significantly, although there is no doubt that investing in post-processing techniques is also required for accurate and fast myocardial deformation analysis. Higher spatial resolution imaging is, however, limited by the hardware-related factors and can only be achieved at the cost of increased scan times [Yuhua Chen et al., 2018]. In the future, advancements in CMR hardware, encoding, and reconstruction strategies will help optimize the acquired image quality in terms of image resolution and SNR.

At this point, image fusion strategies play an important role in compensating for the limitations of cine and tagged CMR [Shi et al., 2012; Schrauben et al., 2018]. In this respect, the second part of the thesis focuses on improving cardiac motion estimation by combining the advantageous features of cine and tagged CMR. The performance of a combined registration technique was assessed in terms of maximum LV twist error and Green-Lagrange ES strain error with respect to separate cine and tagged CMR image registrations. To validate our combined registration technique, we have used the images and the tracking results from the Cardiac Motion Tracking Challenge [Tobon-Gomez et al., 2013]. We have compared ES Green-Lagrange strains and LV twist obtained from tagged, cine, and masked tagged CMR registrations both on the porcine and volunteer datasets. Masked tagged CMR was superior to tagged CMR in the radial strain quantification while the twist quantification was significantly improved compared to cine CMR registration. All image types performed equally well for circumferential and longitudinal strain quantification. This study stands as a systematic work, including the validation and analysis of the tagged CMR registration technique, showing the improved capability of LV strain and twist quantification when two imaging modalities are combined.

Although myocardial strain is gaining popularity with the advances in image acquisition and post-processing techniques, rigorous validation is required for its clinical acceptance as there is significant variability among image processing techniques. At that point, ML-based methods can be promising by offering an automated and user-independent way for motion quantification, thereby, limiting the inter- and intra-observer variability.

7.2. Outlook

Referring to our research presented here, other than investing into image processing techniques, the improvement should be made at the image acquisition stage for better image resolution to achieve more robust myocardial deformation estimates. In addition to the circumferential and longitudinal strain components, radial strain quantification should also be adopted into routine clinical examinations as it will certainly open a new perspective in assessing the contractile properties of the myocardium before irreversible dysfunction develops. Advances in image acquisition and tagged motion analysis techniques will accelerate the incorporation of local deformation metrics in clinical use, which will certainly reveal the clinical

significance of radial strain and twist. Meanwhile, combined image analysis techniques are a promising alternative to assess regional and global myocardial deformation.

ML-based approaches have been used for cardiac motion analysis [Leiner et al., 2019]. They offer an automated way for accurate and efficient quantification of myocardial function and integration of imaging and clinical data. Moreover, they provide an efficient way to reduce the variability of CMR image post-processing approaches and robust techniques for feature extraction, tracking, and deformation quantification [Shen et al., 2005]. Although the usage of ML-based techniques is limited in the clinical setting for now, the research findings reveal their power in mapping myocardial strain from tagged and cine CMR images. The main limitation in the application of ML-based techniques is the need for a large set of training data and the labeled datasets to learn the parameters. Especially for disease classification, the lack of image datasets for rare diseases, or rare images of common diseases, e.g., congenital heart diseases [Leiner et al., 2019], might result in misinterpretation of such clinical cases [Ker et al., 2017].

Abbreviations

0D:	Zero Dimensional
3D:	Three Dimensional
CMR:	Cardiac Magnetic Resonance
CRT:	Cardiac Resynchronization Therapy
CSPAMM:	Complementary SPAMM
CVD:	Cardiovascular Disease
DENSE:	Displacement encoding with stimulated echoes
ED:	End-Diastolic
ES:	End-Systolic
FE:	Finite Element
FEM:	Finite Element Model
FT:	Feature Tracking
GCS:	Global Circumferential Strain
GLS:	Global Longitudinal Strain
HARP:	HARmonic-Phase
HCM:	Hypertrophic Cardiomyopathy
IHD:	Ischemic Heart Disease
INRIA:	Inria-Asclepios Project, France
IP:	In-Plane
IUCL:	Imperial College London – University College London, UK
LV:	Left-Ventricular
LVEF:	LV Ejection Fraction
MEVIS:	Fraunhofer MEVIS, Bremen, Germany
MI:	Myocardial Infarction
ML:	Machine Learning
MR:	Magnetic Resonance
MRI:	Magnetic Resonance Imaging
SinMod:	Sine-Wave Modeling

Abbreviations

SNR:	Signal-to-Noise Ratio
SPAMM:	Spatial Modulation of Magnetization
SSFP:	Steady State Free Precession
SubTag:	Subtly-tagged
TP:	Through-Plane
TPR:	Tag distance to Pixel size Ratio
UPF:	Universitat Pompeu Fabra, Barcelona, Spain

Bibliography

- Abd-Elmoniem, K. Z., Osman, N. F., Prince, J. L., & Stuber, M. (2007). Three-dimensional magnetic resonance myocardial motion tracking from a single image plane. *Magnetic Resonance in Medicine*. doi:10.1002/mrm.21267
- Abraham, T. P., Dimaano, V. L., & Liang, H.-Y. (2007). Role of tissue Doppler and strain echocardiography in current clinical practice. *Circulation*, 116(22), 2597–2609. doi:10.1161/CIRCULATIONAHA.106.647172
- Abraham, T. P., & Nishimura, R. A. (2001). Myocardial strain: Can we finally measure contractility? *Journal of the American College of Cardiology*, 37(3), 731–734. doi:10.1016/S0735-1097(00)01173-6
- Abraham, T. P., Nishimura, R. A., Holmes, D. R., Belohlavek, M., & Seward, J. B. (2002). Strain rate imaging for assessment of regional myocardial function: Results from a clinical model of septal ablation. *Circulation*. doi:10.1161/01.CIR.0000013423.33806.77
- Aguado-Sierra, J., Krishnamurthy, A., Villongco, C., Chuang, J., Howard, E., Gonzales, M. J., Omens, J., Krummen, D. E., Narayan, S., Kerckhoffs, R. C. P., & McCulloch, A. D. (2011). Patient-specific modeling of dyssynchronous heart failure: A case study. *Progress in Biophysics and Molecular Biology*. doi:10.1016/j.pbiomolbio.2011.06.014
- Aletras, A. H., Balaban, R. S., & Wen, H. (1999). High-Resolution Strain Analysis of the Human Heart with Fast-DENSE. *Journal of Magnetic Resonance*. doi:10.1006/jmre.1999.1821
- Aletras, A. H., Ding, S., Balaban, R. S., & Wen, H. (1999). DENSE: Displacement Encoding with Stimulated Echoes in Cardiac Functional MRI. In *Journal of Magnetic Resonance*. doi:10.1006/jmre.1998.1676
- Alfakih, K., Reid, S., Jones, T., & Sivananthan, M. (2004). Assessment of ventricular function and mass by cardiac magnetic resonance imaging. *European Radiology*, 14(10), 1813–1822. doi:10.1007/s00330-004-2387-0
- Aliev, R. R., & Panfilov, A. V. (1996). A Simple Two-variable Model of Cardiac Excitation. *Chaos, Solitons and Fractals*. doi:10.1016/0960-0779(95)00089-5
- Allen, H. D., Driscoll, D. J., Shaddy, R. E., & Feltes, T. F. (2013). *Moss & Adams' heart disease in infants, children, and adolescents: including the fetus and young adult*. Lippincott Williams & Wilkins.
- Alnæs, M., Blechta, J., Hake, J., Johansson, A., Kehlet, B., Logg, A., Richardson, C., Ring, J., Rognes, M. E., & Wells, G. N. (2015). The FEniCS project version 1.5. *Archive of Numerical Software*, 3(100).
- Alonso, S., Bar, M., & Echebarria, B. (2016). Nonlinear physics of electrical wave propagation in the heart: A review. In *Reports on Progress in Physics*. doi:10.1088/0034-4885/79/9/096601
- Ambrosi, D., Arioli, G., Nobile, F., & Quarteroni, A. (2011). Electromechanical coupling in cardiac dynamics: The active strain approach. *SIAM Journal on Applied Mathematics*. doi:10.1137/100788379
- Amini, A. A., Chen, Y., Elayyadi, M., & Radeva, P. (2001). Tag surface reconstruction and tracking of myocardial beads from SPAMM-MRI with parametric B-spline surfaces. *IEEE Transactions on Medical Imaging*. doi:10.1109/42.913176
- Amundsen, B. H., Helle-Valle, T., Edvardsen, T., Torp, H., Crosby, J., Lyseggen, E., Støylen, A.,

- Ihlen, H., Lima, J. A. C., Smiseth, O. A., & Slørdahl, S. A. (2006). Noninvasive myocardial strain measurement by speckle tracking echocardiography: Validation against sonomicrometry and tagged magnetic resonance imaging. *Journal of the American College of Cardiology*. doi:10.1016/j.jacc.2005.10.040
- Arai, A. E. (2011). The cardiac magnetic resonance (CMR) approach to assessing myocardial viability. *Journal of Nuclear Cardiology : Official Publication of the American Society of Nuclear Cardiology*, 18(6), 1095–1102. doi:10.1007/s12350-011-9441-5
- Arts, T., Prinzen, F. W., Delhaas, T., Milles, J. R., Rossi, A. C., & Clarysse, P. (2010). Mapping displacement and deformation of the heart with local sine-wave modeling. *IEEE Transactions on Medical Imaging*, 29(5), 1114–1123. doi:10.1109/TMI.2009.2037955
- Arts, T., Reneman, R. S., & Veenstra, P. C. (1979). A model of the mechanics of the left ventricle. *Annals of Biomedical Engineering*, 7(3), 299–318. doi:10.1007/BF02364118
- Assomull, R. G., Pennell, D. J., & Prasad, S. K. (2007). Cardiovascular magnetic resonance in the evaluation of heart failure. In *Heart*. doi:10.1136/hrt.2003.025304
- Assomull, R. G., Prasad, S. K., Lyne, J., Smith, G., Burman, E. D., Khan, M., Sheppard, M. N., Poole-Wilson, P. A., & Pennell, D. J. (2006). Cardiovascular Magnetic Resonance, Fibrosis, and Prognosis in Dilated Cardiomyopathy. *Journal of the American College of Cardiology*. doi:10.1016/j.jacc.2006.07.049
- Augustin, C. M., Neic, A., Liebmann, M., Prassl, A. J., Niederer, S. A., Haase, G., & Plank, G. (2016). Anatomically accurate high resolution modeling of human whole heart electromechanics: A strongly scalable algebraic multigrid solver method for nonlinear deformation. *Journal of Computational Physics*. doi:10.1016/j.jcp.2015.10.045
- Augustine, D., Lewandowski, A. J., Lazdam, M., Rai, A., Francis, J., Myerson, S., Noble, A., Becher, H., Neubauer, S., Petersen, S. E., & Leeson, P. (2013). Global and regional left ventricular myocardial deformation measures by magnetic resonance feature tracking in healthy volunteers: Comparison with tagging and relevance of gender. *Journal of Cardiovascular Magnetic Resonance*. doi:10.1186/1532-429X-15-8
- Axel, L., & Dougherty, L. (1989a). Heart wall motion: Improved method for spatial modulation of magnetization for MR imaging. *Radiology*. doi:10.1148/radiology.172.2.2748813
- Axel, L., & Dougherty, L. (1989b). MR imaging of motion with spatial modulation of magnetization. *Radiology*. doi:10.1148/radiology.171.3.2717762
- Azhari, H., Weiss, J. L., Rogers, W. J., Siu, C. O., & Shapiro, E. P. (1995). A noninvasive comparative study of myocardial strains in ischemic canine hearts using tagged MRI in 3-D. *American Journal of Physiology - Heart and Circulatory Physiology*. doi:10.1152/ajpheart.1995.268.5.h1918
- Bach, D. S., Beanlands, R. S., Schwaiger, M., & Armstrong, W. F. (1995). Heterogeneity of ventricular function and myocardial oxidative metabolism in nonischemic dilated cardiomyopathy. *Journal of the American College of Cardiology*, 25(6), 1258–1262. doi:10.1016/0735-1097(95)00019-Z
- Badimon, J. J., & Fuster, V. (2002). Can we image the “active” thrombus? In *Arteriosclerosis, thrombosis, and vascular biology* (Vol. 22, Issue 11, pp. 1753–1754). doi:10.1161/01.atv.0000041841.81842.14
- Bai, W., Sinclair, M., Tarroni, G., Oktay, O., Rajchl, M., Vaillant, G., Lee, A. M., Aung, N., Lukaschuk, E., Sanghvi, M. M., Zemrak, F., Fung, K., Paiva, J. M., Carapella, V., Kim, Y. J., Suzuki, H., Kainz, B., Matthews, P. M., Petersen, S. E., ... Rueckert, D. (2018). Automated cardiovascular magnetic resonance image analysis with fully convolutional networks. *Journal of Cardiovascular Magnetic Resonance*, 20(1), 1–12. doi:10.1186/s12968-018-

0471-x

- Barkhausen, J., Ruehm, S. G., Goyen, M., Buck, T., Laub, G., & Debatin, J. F. (2001). MR evaluation of ventricular function: True fast imaging with steady-state precession versus fast low-angle shot cine MR imaging: Feasibility study. *Radiology*. doi:10.1148/radiology.219.1.r01ap12264
- Bartunek, J., Vanderheyden, M., Vandekerckhove, B., Mansour, S., De Bruyne, B., De Bondt, P., Van Haute, I., Lootens, N., Heyndrickx, G., & Wijns, W. (2005). Intracoronary injection of CD133-positive enriched bone marrow progenitor cells promotes cardiac recovery after recent myocardial infarction: feasibility and safety. *Circulation*, 112(9 Suppl), I178-83. doi:10.1161/CIRCULATIONAHA.104.522292
- Becker, M., Kramann, R., Franke, A., Breithardt, O.-A., Heussen, N., Knackstedt, C., Stellbrink, C., Schauerte, P., Kelm, M., & Hoffmann, R. (2007). Impact of left ventricular lead position in cardiac resynchronization therapy on left ventricular remodelling. A circumferential strain analysis based on 2D echocardiography. *European Heart Journal*, 28(10), 1211–1220. doi:10.1093/eurheartj/ehm034
- Berberoglu, E., Onur Solmaz, H., & Göktepe, S. (2014). Computational modeling of coupled cardiac electromechanics incorporating cardiac dysfunctions. *European Journal of Mechanics, A/Solids*. doi:10.1016/j.euomechsol.2014.02.021
- Berberoglu, E., Stoeck, C., Moireau, P., Kozerke, S., & Genet, M. (2019). Validation of Finite Element Image Registration-based Cardiac Strain Estimation from Magnetic Resonance Images. *PAMM*. doi:10.1002/pamm.201900418
- Berberoglu, E., Stoeck, C. T., Moireau, P., Kozerke, S., & Genet, M. (2021). In-silico study of accuracy and precision of left-ventricular strain quantification from 3D tagged MRI. *PLoS One*, 16(11), e0258965. doi:10.1371/journal.pone.0258965
- Bestel, J., Clément, F., & Sorine, M. (2001). *A Biomechanical Model of Muscle Contraction BT - Medical Image Computing and Computer-Assisted Intervention – MICCAI 2001* (W. J. Niessen & M. A. Viergever (eds.); pp. 1159–1161). Springer Berlin Heidelberg.
- Bilchick, K. C., Dimaano, V., Wu, K. C., Helm, R. H., Weiss, R. G., Lima, J. A., Berger, R. D., Tomaselli, G. F., Bluemke, D. A., Halperin, H. R., Abraham, T., Kass, D. A., & Lardo, A. C. (2008). Cardiac magnetic resonance assessment of dyssynchrony and myocardial scar predicts function class improvement following cardiac resynchronization therapy. *JACC. Cardiovascular Imaging*, 1(5), 561–568. doi:10.1016/j.jcmg.2008.04.013
- Bilchick, K. C., Kuruvilla, S., Hamirani, Y. S., Ramachandran, R., Clarke, S. A., Parker, K. M., Stukenborg, G. J., Mason, P., Ferguson, J. D., Moorman, J. R., Malhotra, R., Mangrum, J. M., Darby, A. E., Dimarco, J., Holmes, J. W., Salerno, M., Kramer, C. M., & Epstein, F. H. (2014). Impact of mechanical activation, scar, and electrical timing on cardiac resynchronization therapy response and clinical outcomes. *Journal of the American College of Cardiology*, 63(16), 1657–1666. doi:10.1016/j.jacc.2014.02.533
- Bistoquet, A., Oshinski, J., & Škrinjar, O. (2007). Left ventricular deformation recovery from cine MRI using an incompressible model. *IEEE Transactions on Medical Imaging*. doi:10.1109/TMI.2007.903693
- Bistoquet, A., Oshinski, J., & Škrinjar, O. (2008). Myocardial deformation recovery from cine MRI using a nearly incompressible biventricular model. *Medical Image Analysis*. doi:10.1016/j.media.2007.10.009
- Bogaert, J., Bosmans, H., Maes, A., Suetens, P., Marchal, G., & Rademakers, F. E. (2000). Remote myocardial dysfunction after acute anterior myocardial infarction: impact of left ventricular shape on regional function: a magnetic resonance myocardial tagging study.

- J Am Coll Cardiol*. doi:10.1016/s0735-1097(00)00601-x
- Bogaert, J., & Rademakers, F. E. (2001). Regional nonuniformity of normal adult human left ventricle. *American Journal of Physiology. Heart and Circulatory Physiology*, 280(2), H610-20. doi:10.1152/ajpheart.2001.280.2.H610
- Bohs, L. N., Geiman, B. J., Anderson, M. E., Gebhart, S. C., & Trahey, G. E. (2000). Speckle tracking for multi-dimensional flow estimation. *Ultrasonics*. doi:10.1016/S0041-624X(99)00182-1
- Bosmans, H., Bogaert, J., Rademakers, F., Marchal, G., Laub, G., Versehakelen, J., & Baert, A. L. (1996). Left ventricular radial tagging acquisition using gradient-recalled-echo techniques: Sequence optimization. *Magnetic Resonance Materials in Physics, Biology and Medicine*. doi:10.1007/BF01772519
- Bovendeerd, P. H. (2012). Modeling of cardiac growth and remodeling of myofiber orientation. In *Journal of Biomechanics*. doi:10.1016/j.jbiomech.2011.11.029
- Bovendeerd, P. H., Arts, T., Huyghe, J. M., van Campen, D. H., & Reneman, R. S. (1992). Dependence of local left ventricular wall mechanics on myocardial fiber orientation: a model study. *Journal of Biomechanics*, 25(10), 1129–1140. doi:10.1016/0021-9290(92)90069-d
- Brickner, M. E., Hillis, L. D., & Lange, R. A. (2000). Congenital Heart Disease in Adults. *New England Journal of Medicine*, 342(5), 334–342. doi:10.1056/NEJM200002033420507
- Bristow, M. R., Saxon, L. A., Boehmer, J., Krueger, S., Kass, D. A., De Marco, T., Carson, P., DiCarlo, L., DeMets, D., White, B. G., DeVries, D. W., & Feldman, A. M. (2004). Cardiac-Resynchronization Therapy with or without an Implantable Defibrillator in Advanced Chronic Heart Failure. *New England Journal of Medicine*, 350(21), 2140–2150. doi:10.1056/NEJMoa032423
- Brower, R. W., ten Katen, H. J., & Meester, G. T. (1978). Direct method for determining regional myocardial shortening after bypass surgery from radiopaque markers in man. *The American Journal of Cardiology*. doi:10.1016/0002-9149(78)90879-2
- Bryant, D. J., Payne, J. A., Firmin, D. N., & Longmore, D. B. (1984). Measurement of flow with NMR imaging using a gradient pulse and phase difference technique. *Journal of Computer Assisted Tomography*, 8(4), 588–593. doi:10.1097/00004728-198408000-00002
- Castellanos, D. A., Škardová, K., Bhattaru, A., Berberoglu, E., Greil, G., Tandon, A., Dillenbeck, J., Burkhardt, B., Hussain, T., Genet, M., & Chabiniok, R. (2021). Left Ventricular Torsion Obtained Using Equilibrated Warping in Patients with Repaired Tetralogy of Fallot. *Pediatric Cardiology*, 42(6), 1275–1283. doi:10.1007/s00246-021-02608-y
- Castillo, E., Lima, J. A. C., & Bluemke, D. A. (2003). Regional Myocardial Function: Advances in MR Imaging and Analysis. In *Radiographics*. doi:10.1148/rg.23si035512
- Cerqueira, M. D., Weissman, N. J., Dilsizian, V., Jacobs, A. K., Kaul, S., Laskey, W. K., Pennell, D. J., Rumberger, J. A., Ryan, T., & Verani, M. S. (2002). Standardized myocardial segmentation and nomenclature for tomographic imaging of the heart: A statement for healthcare professionals from the Cardiac Imaging Committee of the Council on Clinical Cardiology of the American Heart Association. *Journal of Nuclear Cardiology*. doi:10.1067/mnc.2002.123122
- Chabiniok, R., Moireau, P., Lesault, P. F., Rahmouni, A., Deux, J. F., & Chapelle, D. (2012). Estimation of tissue contractility from cardiac cine-MRI using a biomechanical heart model. *Biomechanics and Modeling in Mechanobiology*. doi:10.1007/s10237-011-0337-8

- Chabiniok, R., Wang, V. Y., Hadjicharalambous, M., Asner, L., Lee, J., Sermesant, M., Kuhl, E., Young, A. A., Moireau, P., Nash, M. P., Chapelle, D., & Nordsletten, D. A. (2016). Multiphysics and multiscale modelling, data-model fusion and integration of organ physiology in the clinic: ventricular cardiac mechanics. *Interface Focus*, 6(2), 20150083. doi:10.1098/rsfs.2015.0083
- Chalil, S., Foley, P. W. X., Muyhaldeen, S. A., Patel, K. C. R., Yousef, Z. R., Smith, R. E. A., Frenneaux, M. P., & Leyva, F. (2007). Late gadolinium enhancement-cardiovascular magnetic resonance as a predictor of response to cardiac resynchronization therapy in patients with ischaemic cardiomyopathy. *Europace : European Pacing, Arrhythmias, and Cardiac Electrophysiology: Journal of the Working Groups on Cardiac Pacing, Arrhythmias, and Cardiac Cellular Electrophysiology of the European Society of Cardiology*, 9(11), 1031–1037. doi:10.1093/europace/eum133
- Chapelle, D., Le Tallec, P., Moireau, P., & Sorine, M. (2012). An energy-preserving muscle tissue model: formulation and compatible discretizations. *International Journal for Multiscale Computational Engineering*, 10(2), 189–211. doi:10.1615/IntJMultCompEng.2011002360
- Charoenpanichkit, C., & Hundley, W. G. (2010). The 20 year evolution of dobutamine stress cardiovascular magnetic resonance. *Journal of Cardiovascular Magnetic Resonance*, 12(1), 59. doi:10.1186/1532-429X-12-59
- Chen, T., Wang, X., Chung, S., Metaxas, D., & Axel, L. (2010). Automated 3D motion tracking using gabor filter bank, robust point matching, and deformable models. *IEEE Transactions on Medical Imaging*. doi:10.1109/TMI.2009.2021041
- Chen, Y., Shi, F., Christodoulou, A. G., Xie, Y., Zhou, Z., & Li, D. (2018). *Efficient and Accurate MRI Super-Resolution Using a Generative Adversarial Network and 3D Multi-level Densely Connected Network BT - Medical Image Computing and Computer Assisted Intervention – MICCAI 2018* (A. F. Frangi, J. A. Schnabel, C. Davatzikos, C. Alberola-López, & G. Fichtinger (eds.); pp. 91–99). Springer International Publishing.
- Chitiboi, T., Kanski, M., Tautz, L., Hennemuth, A., Halpern, D., Sherrid, M., & Axel, L. (2020). Analysis of three-chamber view conventional and tagged cine MRI in patients with suspected hypertrophic cardiomyopathy. *Magma (New York, N.Y.)*, 33(5), 613–626. doi:10.1007/s10334-020-00836-6
- Choudhury, R. P., Fuster, V., & Fayad, Z. A. (2004). Molecular, cellular and functional imaging of atherothrombosis. *Nature Reviews. Drug Discovery*, 3(11), 913–925. doi:10.1038/nrd1548
- Ciarlet, P. G. (1982). *Quelques remarques sur les problèmes d'existence en élasticité non linéaire*. INRIA.
- Claire, D., Hild, F., & Roux, S. (2004). A finite element formulation to identify damage fields: The equilibrium gap method. *International Journal for Numerical Methods in Engineering*. doi:10.1002/nme.1057
- Cleland, J., Freemantle, N., Ghio, S., Fruhwald, F., Shankar, A., Marijanowski, M., Verboven, Y., & Tavazzi, L. (2008). Predicting the long-term effects of cardiac resynchronization therapy on mortality from baseline variables and the early response a report from the CARE-HF (Cardiac Resynchronization in Heart Failure) Trial. *Journal of the American College of Cardiology*, 52(6), 438–445. doi:10.1016/j.jacc.2008.04.036
- Collins, J. D. (2015). Global and regional functional assessment of ischemic heart disease with cardiac MR imaging. In *Radiologic Clinics of North America*. doi:10.1016/j.rcl.2014.11.001
- Corrado, C., & Niederer, S. A. (2016). A two-variable model robust to pacemaker behaviour for the dynamics of the cardiac action potential. *Mathematical Biosciences*.

- doi:10.1016/j.mbs.2016.08.010
- Costa, K. D., Hunter, P. J., Rogers, J. M., Guccione, J. M., Waldman, L. K., & McCulloch, A. D. (1996). A Three-Dimensional Finite Element Method for Large Elastic Deformations of Ventricular Myocardium: I—Cylindrical and Spherical Polar Coordinates. *Journal of Biomechanical Engineering*, 118(4), 452–463. doi:10.1115/1.2796031
- Costa, K. D., Takayama, Y., McCulloch, A. D., & Covell, J. W. (1999). Laminar fiber architecture and three-dimensional systolic mechanics in canine ventricular myocardium. *American Journal of Physiology - Heart and Circulatory Physiology*. doi:10.1152/ajpheart.1999.276.2.h595
- Cowan, B. R., Peereboom, S. M., Greiser, A., Guehring, J., & Young, A. A. (2015). Image Feature Determinants of Global and Segmental Circumferential Ventricular Strain from Cine CMR. In *JACC: Cardiovascular Imaging*. doi:10.1016/j.jcmg.2014.10.005
- Croisille, P., Moore, C. C., Judd, R. M., Lima, J. A. C., Arai, M., McVeigh, E. R., Becker, L. C., & Zerhouni, E. A. (1999). Differentiation of viable and nonviable myocardium by the use of three-dimensional tagged MRI in 2-day-old reperfused canine infarcts. *Circulation*. doi:10.1161/01.CIR.99.2.284
- Dandel, M., Lehmkuhl, H., Knosalla, C., Suramelashvili, N., & Hetzer, R. (2009). Strain and Strain Rate Imaging by Echocardiography - Basic Concepts and Clinical Applicability. *Current Cardiology Reviews*. doi:10.2174/157340309788166642
- Delfino, J. G., Fornwalt, B. K., Eisner, R. L., Leon, A. R., & Oshinski, J. N. (2008). Determination of transmural, endocardial, and epicardial radial strain and strain rate from phase contrast MR velocity data. *Journal of Magnetic Resonance Imaging*. doi:10.1002/jmri.21211
- Deng, X., & Denney, T. S. (2004). Three-dimensional myocardial strain reconstruction from tagged MRI using a cylindrical B-spline model. *IEEE Transactions on Medical Imaging*. doi:10.1109/TMI.2004.827961
- Deng, X., & Denney, T. S. (2005). Combined tag tracking and strain reconstruction from tagged cardiac MR images without user-defined myocardial contours. *Journal of Magnetic Resonance Imaging*. doi:10.1002/jmri.20234
- Dokos, S., Smaill, B. H., Young, A. A., & LeGrice, I. J. (2002). Shear properties of passive ventricular myocardium. *American Journal of Physiology - Heart and Circulatory Physiology*. doi:10.1152/ajpheart.00111.2002
- Dolk, H., Loane, M., & Garne, E. (2011). Congenital heart defects in Europe: Prevalence and perinatal mortality, 2000 to 2005. *Circulation*. doi:10.1161/CIRCULATIONAHA.110.958405
- Doost, S. N., Ghista, D., Su, B., Zhong, L., & Morsi, Y. S. (2016). Heart blood flow simulation: A perspective review. *BioMedical Engineering Online*. doi:10.1186/s12938-016-0224-8
- Dorn, G. W., Robbins, J., & Sugden, P. H. (2003). Phenotyping hypertrophy: Eschew obfuscation. In *Circulation Research*. doi:10.1161/01.RES.0000077012.11088.BC
- Earls, J. P., Ho, V. B., Foo, T. K., Castillo, E., & Flamm, S. D. (2002). Cardiac MRI: Recent progress and continued challenges. In *Journal of Magnetic Resonance Imaging*. doi:10.1002/jmri.10154
- Edvardsen, T., Rosen, B. D., Pan, L., Jerosch-Herold, M., Lai, S., Hundley, W. G., Sinha, S., Kronmal, R. A., Bluemke, D. A., & Lima, J. A. C. (2006). Regional diastolic dysfunction in individuals with left ventricular hypertrophy measured by tagged magnetic resonance imaging - The Multi-Ethnic Study of Atherosclerosis (MESA). *American Heart Journal*. doi:10.1016/j.ahj.2005.02.018

- Engblom, H., Hedström, E., Heiberg, E., Wagner, G. S., Pahlm, O., & Arheden, H. (2009). Rapid initial reduction of hyperenhanced myocardium after reperfused first myocardial infarction suggests recovery of the peri-infarction zone: one-year follow-up by MRI. *Circulation. Cardiovascular Imaging*, 2(1), 47–55. doi:10.1161/CIRCIMAGING.108.802199
- Ennis, D. B., Epstein, F. H., Kellman, P., Fananapazir, L., McVeigh, E. R., & Arai, A. E. (2003). Assessment of regional systolic and diastolic dysfunction in familial hypertrophic cardiomyopathy using MR tagging. *Magnetic Resonance in Medicine*. doi:10.1002/mrm.10543
- Ersboll, M., Valeur, N., Mogensen, U. M., Andersen, M. J., Moller, J. E., Hassager, C., Sogaard, P., & Kober, L. (2012). Relationship between left ventricular longitudinal deformation and clinical heart failure during admission for acute myocardial infarction: A two-dimensional speckle-tracking study. *Journal of the American Society of Echocardiography*. doi:10.1016/j.echo.2012.09.006
- Espe, E. K., Aronsen, J. M., Skårdal, K., Schneider, J. E., Zhang, L., & Sjaastad, I. (2013). Novel insight into the detailed myocardial motion and deformation of the rodent heart using high-resolution phase contrast cardiovascular magnetic resonance. *Journal of Cardiovascular Magnetic Resonance*. doi:10.1186/1532-429X-15-82
- Fahmy, A. S., Pan, L., Stuber, M., & Osman, N. F. (2006). Correction of through-plane deformation artifacts in stimulated echo acquisition mode cardiac imaging. *Magnetic Resonance in Medicine*. doi:10.1002/mrm.20781
- Fallah-Rad, N., Walker, J. R., Wassef, A., Lytwyn, M., Bohonis, S., Fang, T., Tian, G., Kirkpatrick, I. D. C., Singal, P. K., Krahn, M., Grenier, D., & Jassal, D. S. (2011). The utility of cardiac biomarkers, tissue velocity and strain imaging, and cardiac magnetic resonance imaging in predicting early left ventricular dysfunction in patients with human epidermal growth factor receptor ii-positive breast cancer treated with ad. *Journal of the American College of Cardiology*. doi:10.1016/j.jacc.2010.11.063
- Feng, L., Donnino, R., Babb, J., Axel, L., & Kim, D. (2009). Numerical and in vivo validation of fast cine displacement-encoded with stimulated echoes (DENSE) MRI for quantification of regional cardiac function. *Magnetic Resonance in Medicine*. doi:10.1002/mrm.22045
- Ferdian, E., Suinesiaputra, A., Fung, K., Aung, N., Lukaschuk, E., Barutcu, A., Maclean, E., Paiva, J., Piechnik, S. K., Neubauer, S., Petersen, S. E., & Young, A. A. (2020). Fully automated myocardial strain estimation from cardiovascular MRI-Tagged images using a deep learning framework in the UK biobank. *Radiology: Cardiothoracic Imaging*, 2(1). doi:10.1148/ryct.2020190032
- Fischer, S. E., McKinnon, G. C., Maier, S. E., & Boesiger, P. (1993). Improved myocardial tagging contrast. *Magnetic Resonance in Medicine*. doi:10.1002/mrm.1910300207
- Fischer, S. E., McKinnon, G. C., Scheidegger, M. B., Prins, W., Meier, D., & Boesiger, P. (1994). True myocardial motion tracking. *Magnetic Resonance in Medicine*. doi:10.1002/mrm.1910310409
- Fitchett, D. H., Gupta, M., Farkouh, M. E., & Verma, S. (2014). Coronary artery revascularization in patients with diabetes mellitus. *Circulation*, 130(12), e104–e106. doi:10.1161/CIRCULATIONAHA.113.007968
- FitzHugh, R. (1961). Impulses and Physiological States in Theoretical Models of Nerve Membrane. *Biophysical Journal*. doi:10.1016/S0006-3495(61)86902-6
- Fleming, C. P., Ripplinger, C. M., Webb, B., Efimov, I. R., & Rollins, A. M. (2008). Quantification of cardiac fiber orientation using optical coherence tomography. *Journal of Biomedical Optics*. doi:10.1117/1.2937470

- Florack, L., & Van Assen, H. (2010). A new methodology for multiscale myocardial deformation and strain analysis based on tagging MRI. *International Journal of Biomedical Imaging*. doi:10.1155/2010/341242
- Frahm, J., Merboldt, K. D., Hänicke, W., & Haase, A. (1985). Stimulated echo imaging. *Journal of Magnetic Resonance (1969)*, 64(1), 81–93. doi:10.1016/0022-2364(85)90033-2
- Frangi, A. F., Niessen, W. J., & Viergever, M. A. (2001). Three-dimensional modeling for functional analysis of cardiac images: A review. *IEEE Transactions on Medical Imaging*. doi:10.1109/42.906421
- Fraser, K. H., Taskin, M. E., Griffith, B. P., & Wu, Z. J. (2011). The use of computational fluid dynamics in the development of ventricular assist devices. *Medical Engineering & Physics*, 33(3), 263–280. doi:10.1016/j.medengphy.2010.10.014
- Friedberg, M. K., & Mertens, L. (2009). Tissue velocities, strain, and strain rate for echocardiographic assessment of ventricular function in congenital heart disease. In *European Journal of Echocardiography*. doi:10.1093/ejechocard/jep045
- Fritz, T., Wieners, C., Seemann, G., Steen, H., & Dössel, O. (2014). Simulation of the contraction of the ventricles in a human heart model including atria and pericardium. *Biomechanics and Modeling in Mechanobiology*. doi:10.1007/s10237-013-0523-y
- Fujita, N., Duerinckx, A. J., & Higgins, C. B. (1993). Variation in left ventricular regional wall stress with cine magnetic resonance imaging: normal subjects versus dilated cardiomyopathy. *American Heart Journal*, 125(5 Pt 1), 1337–1345. doi:10.1016/0002-8703(93)91004-x
- Garot, J., Bluemke, D. A., Osman, N. F., Rochitte, C. E., McVeigh, E. R., Zerhouni, E. A., Prince, J. L., & Lima, J. A. C. (2000). Fast determination of regional myocardial strain fields from tagged cardiac images using harmonic phase MRI. *Circulation*. doi:10.1161/01.CIR.101.9.981
- Genet, M., Lee, L. C., Ge, L., Acevedo-Bolton, G., Jeung, N., Martin, A., Cambronero, N., Boyle, A., Yeghiazarians, Y., Kozerke, S., & Guccione, J. M. (2015). A Novel Method for Quantifying Smooth Regional Variations in Myocardial Contractility Within an Infarcted Human Left Ventricle Based on Delay-Enhanced Magnetic Resonance Imaging. *Journal of Biomechanical Engineering*. doi:10.1115/1.4030667
- Genet, M., Lee, L. C., Nguyen, R., Haraldsson, H., Acevedo-Bolton, G., Zhang, Z., Ge, L., Ordoas, K., Kozerke, S., & Guccione, J. M. (2014). Distribution of normal human left ventricular myofiber stress at end diastole and end systole: a target for in silico design of heart failure treatments. *Journal of Applied Physiology*, 117(2), 142–152. doi:10.1152/jappphysiol.00255.2014
- Genet, M., Stoeck, C. T., Deuster, C. Von, Lee, L. C., & Kozerke, S. (2018). Equilibrated Warping: Finite Element Image Registration with Finite Strain Equilibrium Gap Regularization. *Medical Image Analysis*, 50, 1–22. doi:10.1016/j.media.2018.07.007
- Genet, M., Stoeck, C. T., von Deuster, C., Lee, L. C., Guccione, J. M., & Kozerke, S. (2016). Finite Element Digital Image Correlation for Cardiac Strain Analysis from Accelerated 3D Whole-Heart Tagging. *Proceedings of the 24th ISMRM*, 3136.
- Geuzaine, C., & Remacle, J.-F. (2009). Gmsh: a Three-Dimensional Finite Element Mesh Generator with Built-in Pre- and Post-Processing. *Facilities. Int. J. Numer. Meth. Eng.*
- Geva, T., Sahn, D. J., & Powell, A. J. (2003). Magnetic resonance imaging of congenital heart disease in adults. *Progress in Pediatric Cardiology*, 17(1), 21–39. doi:10.1016/S1058-9813(03)00010-9
- Geyer, H., Caracciolo, G., Abe, H., Wilansky, S., Carerj, S., Gentile, F., Nesser, H. J., Khandheria,

- B., Narula, J., & Sengupta, P. P. (2010). Assessment of Myocardial Mechanics Using Speckle Tracking Echocardiography: Fundamentals and Clinical Applications. In *Journal of the American Society of Echocardiography*. doi:10.1016/j.echo.2010.02.015
- Ghadimi, S., Auger, D. A., Feng, X., Sun, C., Meyer, C. H., Bilchick, K. C., Cao, J. J., Scott, A. D., Oshinski, J. N., Ennis, D. B., & Epstein, F. H. (2021). Fully-automated global and segmental strain analysis of DENSE cardiovascular magnetic resonance using deep learning for segmentation and phase unwrapping. *Journal of Cardiovascular Magnetic Resonance : Official Journal of the Society for Cardiovascular Magnetic Resonance*, 23(1), 20. doi:10.1186/s12968-021-00712-9
- Gilbert, S. H., Benson, A. P., Li, P., & Holden, A. V. (2007). Regional localisation of left ventricular sheet structure: integration with current models of cardiac fibre, sheet and band structure. In *European Journal of Cardio-thoracic Surgery*. doi:10.1016/j.ejcts.2007.03.032
- Göktepe, S., Menzel, A., & Kuhl, E. (2014). The generalized Hill model: A kinematic approach towards active muscle contraction. *Journal of the Mechanics and Physics of Solids*. doi:10.1016/j.jmps.2014.07.015
- Gonzales, M. J., Sturgeon, G., Krishnamurthy, A., Hake, J., Jonas, R., Stark, P., Rappel, W. J., Narayan, S. M., Zhang, Y., Segars, W. P., & McCulloch, A. D. (2013). A three-dimensional finite element model of human atrial anatomy: New methods for cubic Hermite meshes with extraordinary vertices. *Medical Image Analysis*. doi:10.1016/j.media.2013.03.005
- Götte, M. J. W., Germans, T., Rüssel, I. K., Zwanenburg, J. J. M., Marcus, J. T., van Rossum, A. C., & van Veldhuisen, D. J. (2006). Myocardial Strain and Torsion Quantified by Cardiovascular Magnetic Resonance Tissue Tagging. Studies in Normal and Impaired Left Ventricular Function. In *Journal of the American College of Cardiology*. doi:10.1016/j.jacc.2006.07.048
- Gotte, M. J. W., Van Rossum, A. C., Marcus, J. T., Kuijter, J. P. A., Axel, L., & Visser, C. A. (1999). Recognition of infarct localization by specific changes in intramural myocardial mechanics. *American Heart Journal*. doi:10.1016/S0002-8703(99)70068-2
- Götte, M. J. W., Van Rossum, A. C., Twisk, J. W. R., Kuijter, J. P. A., Marcus, J. T., & Visser, C. A. (2001). Quantification of regional contractile function after infarction: Strain analysis superior to wall thickening analysis in discriminating infarct from remote myocardium. *Journal of the American College of Cardiology*. doi:10.1016/S0735-1097(00)01186-4
- Grothues, F., Smith, G. C., Moon, J. C. C., Bellenger, N. G., Collins, P., Klein, H. U., & Pennell, D. J. (2002). Comparison of interstudy reproducibility of cardiovascular magnetic resonance with two-dimensional echocardiography in normal subjects and in patients with heart failure or left ventricular hypertrophy. *American Journal of Cardiology*. doi:10.1016/S0002-9149(02)02381-0
- Guccione, J. M., Costa, K. D., & McCulloch, A. D. (1995). Finite element stress analysis of left ventricular mechanics in the beating dog heart. *Journal of Biomechanics*, 28(10), 1167–1177. doi:10.1016/0021-9290(94)00174-3
- Guccione, J. M., McCulloch, A. D., & Waldman, L. K. (1991). Passive Material Properties of Intact Ventricular Myocardium Determined From a Cylindrical Model. *Journal of Biomechanical Engineering*. doi:10.1115/1.2894084
- Guccione, J. M., Waldman, L. K., & McCulloch, A. D. (1993). Mechanics of Active Contraction in Cardiac Muscle: Part II—Cylindrical Models of the Systolic Left Ventricle. *Journal of Biomechanical Engineering*, 115(1), 82–90. doi:10.1115/1.2895474
- Gulrajani, R. M. (1988). Models of the electrical activity of the heart and computer simulation

- of the electrocardiogram. *Critical Reviews in Biomedical Engineering*.
- Gurev, V., Lee, T., Constantino, J., Arevalo, H., & Trayanova, N. A. (2011). Models of cardiac electromechanics based on individual hearts imaging data: image-based electromechanical models of the heart. *Biomechanics and Modeling in Mechanobiology*, 10(3), 295–306. doi:10.1007/s10237-010-0235-5
- Gutiérrez, F. R., Ho, M.-L., & Siegel, M. J. (2008). Practical applications of magnetic resonance in congenital heart disease. *Magnetic Resonance Imaging Clinics of North America*, 16(3), 403–435, v. doi:10.1016/j.mric.2008.04.003
- Haggerty, C. M., Kramer, S. P., Binkley, C. M., Powell, D. K., Mattingly, A. C., Charnigo, R., Epstein, F. H., & Fornwalt, B. K. (2013). Reproducibility of cine displacement encoding with stimulated echoes (DENSE) cardiovascular magnetic resonance for measuring left ventricular strains, torsion, and synchrony in mice. *Journal of Cardiovascular Magnetic Resonance : Official Journal of the Society for Cardiovascular Magnetic Resonance*, 15(1), 71. doi:10.1186/1532-429X-15-71
- Haggerty, C. M., Kramer, S. P., Skrinjar, O., Binkley, C. M., Powell, D. K., Mattingly, A. C., Epstein, F. H., & Fornwalt, B. K. (2014). Quantification of left ventricular volumes, mass, and ejection fraction using cine displacement encoding with stimulated echoes (DENSE) MRI. *Journal of Magnetic Resonance Imaging: JMRI*, 40(2), 398–406. doi:10.1002/jmri.24350
- Hales, P. W., Schneider, J. E., Burton, R. A. B., Wright, B. J., Bollensdorff, C., & Kohl, P. (2012). Histo-anatomical structure of the living isolated rat heart in two contraction states assessed by diffusion tensor MRI. *Progress in Biophysics and Molecular Biology*. doi:10.1016/j.pbiomolbio.2012.07.014
- Hamano, K., Nishida, M., Hirata, K., Mikamo, A., Li, T. S., Harada, M., Miura, T., Matsuzaki, M., & Esato, K. (2001). Local implantation of autologous bone marrow cells for therapeutic angiogenesis in patients with ischemic heart disease: clinical trial and preliminary results. *Japanese Circulation Journal*, 65(9), 845–847. doi:10.1253/jcj.65.845
- Hammouda, K., Khalifa, F., Abdeltawab, H., Elnakib, A., Giridharan, G. A., Zhu, M., Ng, C. K., Dassanayaka, S., Kong, M., Darwish, H. E., Mohamed, T. M. A., Jones, S. P., & El-Baz, A. (2020). A New Framework for Performing Cardiac Strain Analysis from Cine MRI Imaging in Mice. *Scientific Reports*, 10(1), 1–15. doi:10.1038/s41598-020-64206-x
- Hasselberg, N. E., Haugaa, K. H., Sarvari, S. I., Gullestad, L., Andreassen, A. K., Smiseth, O. A., & Edvardsen, T. (2015). Left ventricular global longitudinal strain is associated with exercise capacity in failing hearts with preserved and reduced ejection fraction. *European Heart Journal Cardiovascular Imaging*. doi:10.1093/ehjci/jeu277
- Heimdal, A., Stoylen, A., Torp, H., & Skjaerpe, T. (1998). Real-time strain rate imaging of the left ventricle by ultrasound. *Journal of the American Society of Echocardiography*. doi:10.1016/S0894-7317(98)70151-8
- Helm, P., Beg, M. F., Miller, M. I., & Winslow, R. L. (2005). Measuring and mapping cardiac fiber and laminar architecture using diffusion tensor MR imaging. *Annals of the New York Academy of Sciences*. doi:10.1196/annals.1341.026
- Herschman, H. R. (2003). Molecular imaging: looking at problems, seeing solutions. *Science (New York, N.Y.)*, 302(5645), 605–608. doi:10.1126/science.1090585
- Hess, A. T., Zhong, X., Spottiswoode, B. S., Epstein, F. H., & Meintjes, E. M. (2009). Myocardial 3D strain calculation by combining cine Displacement Encoding with Stimulated Echoes (DENSE) and cine strain encoding (SENC) imaging. *Magnetic Resonance in Medicine*. doi:10.1002/mrm.21984

- Heydari, B., Jerosch-Herold, M., & Kwong, R. Y. (2012). Imaging for planning of cardiac resynchronization therapy. *JACC. Cardiovascular Imaging*, 5(1), 93–110. doi:10.1016/j.jcmg.2011.11.006
- Higgins, S. L., Hummel, J. D., Niazi, I. K., Giudici, M. C., Worley, S. J., Saxon, L. A., Boehmer, J. P., Higginbotham, M. B., De Marco, T., Foster, E., & Yong, P. G. (2003). Cardiac resynchronization therapy for the treatment of heart failure in patients with intraventricular conduction delay and malignant ventricular tachyarrhythmias. *Journal of the American College of Cardiology*, 42(8), 1454–1459. doi:10.1016/s0735-1097(03)01042-8
- Hill, A. V. (1938). The heat of shortening and the dynamic constants of muscle. *Proceedings of the Royal Society of London. Series B - Biological Sciences*, 126(843), 136–195. doi:10.1098/rspb.1938.0050
- Hill, A. V. (1949). The abrupt transition from rest to activity in muscle. *Proceedings of the Royal Society of London. Series B, Biological Sciences*, 136(884), 399–420. doi:10.1098/rspb.1949.0033
- Hills, B. A., & Butler, B. D. (1985). Phospholipids identified on the pericardium and their ability to impart boundary lubrication. *Annals of Biomedical Engineering*. doi:10.1007/BF02584258
- Hodgkin, A. L., & Huxley, A. F. (1952). A quantitative description of membrane current and its application to conduction and excitation in nerve. *The Journal of Physiology*. doi:10.1113/jphysiol.1952.sp004764
- Holt, J. P. (1970). The normal pericardium. *The American Journal of Cardiology*. doi:10.1016/0002-9149(70)90702-2
- Holzapfel, G. A., & Ogden, R. W. (2009). Constitutive modelling of passive myocardium: A structurally based framework for material characterization. *Philosophical Transactions of the Royal Society A: Mathematical, Physical and Engineering Sciences*. doi:10.1098/rsta.2009.0091
- Hor, K. N., Baumann, R., Pedrizzetti, G., Tonti, G., Gottliebson, W. M., Taylor, M., Benson, W., & Mazur, W. (2011). Magnetic Resonance Derived Myocardial Strain Assessment Using Feature Tracking. *Journal of Visualized Experiments*. doi:10.3791/2356
- Hor, K. N., Gottliebson, W. M., Carson, C., Wash, E., Cnota, J., Fleck, R., Wansapura, J., Klimeczek, P., Al-Khalidi, H. R., Chung, E. S., Benson, D. W., & Mazur, W. (2010). Comparison of Magnetic Resonance Feature Tracking for Strain Calculation With Harmonic Phase Imaging Analysis. *JACC: Cardiovascular Imaging*. doi:10.1016/j.jcmg.2009.11.006
- Hu, Z., Metaxas, D., & Axel, L. (2003). In vivo strain and stress estimation of the heart left and right ventricles from MRI images. *Medical Image Analysis*, 7(4), 435–444. doi:10.1016/S1361-8415(03)00032-X
- Huang, J., Abendschein, D., Dâvila-Român, V. G., & Amini, A. A. (1999). Spatio-temporal tracking of myocardial deformations with a 4-D B-spline model from tagged MRI. *IEEE Transactions on Medical Imaging*. doi:10.1109/42.811299
- Huang, J., Yan, Z. N., Fan, L., Rui, Y. F., & Song, X. T. (2017). Left ventricular systolic function changes in hypertrophic cardiomyopathy patients detected by the strain of different myocardium layers and longitudinal rotation. *BMC Cardiovascular Disorders*. doi:10.1186/s12872-017-0651-x
- Hughes, D., & Siegel, M. J. (2010). MRI of complex cyanotic congenital heart disease: pre- and post surgical considerations. *The International Journal of Cardiovascular Imaging*,

- 26(Suppl 2), 333–343. doi:10.1007/s10554-010-9732-y
- Humphrey, J. D., Strumpf, R. K., & Yin, F. C. P. (1990). Determination of a constitutive relation for passive myocardium: II. -Parameter estimation. *Journal of Biomechanical Engineering*. doi:10.1115/1.2891194
- Humphrey, J. D., & Yin, F. C. P. (1987). On constitutive relations and finite deformations of passive cardiac tissue: I. A pseudostrain-energy function. *Journal of Biomechanical Engineering*. doi:10.1115/1.3138684
- Hunter, J. J., & Chien, K. R. (1999). Signaling Pathways for Cardiac Hypertrophy and Failure. *New England Journal of Medicine*. doi:10.1056/nejm199910213411706
- Hunter, P. J., McCulloch, A. D., & Ter Keurs, H. E. D. J. (1998). Modelling the mechanical properties of cardiac muscle. *Progress in Biophysics and Molecular Biology*. doi:10.1016/S0079-6107(98)00013-3
- Hunter, P. J., Nielsen, P. M., Smaill, B. H., LeGrice, I. J., & Hunter, I. W. (1992). An anatomical heart model with applications to myocardial activation and ventricular mechanics. *Critical Reviews in Biomedical Engineering*, 20(5–6), 403–426.
- Hunter, P. J., Pullan, A. J., & Smaill, B. H. (2003). Modeling Total Heart Function. *Annual Review of Biomedical Engineering*, 5(1), 147–177. doi:10.1146/annurev.bioeng.5.040202.121537
- Huttin, O., Coiro, S., Selton-Suty, C., Juillière, Y., Donal, E., Magne, J., Sadoul, N., Zannad, F., Rossignol, P., & Girerd, N. (2016). Prediction of left ventricular remodeling after a myocardial infarction: Role of myocardial deformation: A systematic review and meta-analysis. In *PLoS ONE*. doi:10.1371/journal.pone.0168349
- Huxley, A. F. (1957). Muscle structure and theories of contraction. *Progress in Biophysics and Biophysical Chemistry*, 7, 255–318.
- Huxley, H. E. (1963). Electron microscope studies on the structure of natural and synthetic protein filaments from striated muscle. *Journal of Molecular Biology*, 7(3), 281–IN30. doi:10.1016/S0022-2836(63)80008-X
- Ibrahim, E. S. H. (2011). Myocardial tagging by Cardiovascular Magnetic Resonance: evolution of techniques--pulse sequences, analysis algorithms, and applications. *Journal of Cardiovascular Magnetic Resonance*, 13(1), 36. doi:10.1186/1532-429X-13-36
- Ibrahim, E. S. H. (2017). Heart mechanics: Magnetic resonance imaging mathematical modeling, pulse sequences, and image analysis. In *Heart Mechanics: Magnetic Resonance Imaging-Mathematical Modeling, Pulse Sequences, and Image Analysis*. doi:10.1201/9781315119083
- Ibrahim, E. S. H., Stuber, M., Fahmy, A. S., Abd-Elmoniem, K. Z., Sasano, T., Abraham, M. R., & Osman, N. F. (2007). Real-time MR imaging of myocardial regional function using strain-encoding (SENC) with tissue through-plane motion tracking. *Journal of Magnetic Resonance Imaging*. doi:10.1002/jmri.21125
- Imbalzano, E., Zito, C., Carerj, S., Oretto, G., Mandraffino, G., Cusmà-Piccione, M., Di Bella, G., Saitta, C., & Saitta, A. (2011). Left ventricular function in hypertension: New insight by speckle tracking echocardiography. *Echocardiography*, 28(6), 649–657. doi:10.1111/j.1540-8175.2011.01410.x
- Imperiale, A., Chabiniok, R., Moireau, P., & Chapelle, D. (2011). Constitutive parameter estimation methodology using tagged-MRI data. *Lecture Notes in Computer Science (Including Subseries Lecture Notes in Artificial Intelligence and Lecture Notes in Bioinformatics)*. doi:10.1007/978-3-642-21028-0_52
- Ingels, N. B., Daughters, G. T., Stinson, E. B., & Alderman, E. L. (1980). Evaluation of methods

- for quantitating left ventricular segmental wall motion using myocardial markers as a standard. *Circulation*, 61(5), 966–972. doi:10.1161/01.CIR.61.5.966
- Inoue, Y., Yang, X., Nagao, M., Higashino, H., Hosokawa, K., Kido, T., Kurata, A., Okayama, H., Higaki, J., Mochizuki, T., & Murase, K. (2010). Peri-infarct dysfunction in post-myocardial infarction: Assessment of 3-T tagged and late enhancement MRI. *European Radiology*. doi:10.1007/s00330-009-1657-2
- Jaffer, F. A., Libby, P., & Weissleder, R. (2006). Molecular and Cellular Imaging of Atherosclerosis: Emerging Applications. *Journal of the American College of Cardiology*, 47(7), 1328–1338. doi:10.1016/j.jacc.2006.01.029
- Jaffer, F. A., Libby, P., & Weissleder, R. (2007). Molecular imaging of cardiovascular disease. *Circulation*, 116(9), 1052–1061. doi:10.1161/CIRCULATIONAHA.106.647164
- Jaffer, F. A., & Weissleder, R. (2004). Seeing within: molecular imaging of the cardiovascular system. *Circulation Research*, 94(4), 433–445. doi:10.1161/01.RES.0000119321.18573.5A
- Jaffer, F. A., & Weissleder, R. (2005). Molecular imaging in the clinical arena. *JAMA*, 293(7), 855–862. doi:10.1001/jama.293.7.855
- Janssens, S., Dubois, C., Bogaert, J., Theunissen, K., Deroose, C., Desmet, W., Kalantzi, M., Herbots, L., Sinnaeve, P., Dens, J., Maertens, J., Rademakers, F., Dymarkowski, S., Gheysens, O., Van Cleemput, J., Bormans, G., Nuyts, J., Belmans, A., Mortelmans, L., ... Van de Werf, F. (2006). Autologous bone marrow-derived stem-cell transfer in patients with ST-segment elevation myocardial infarction: double-blind, randomised controlled trial. *Lancet (London, England)*, 367(9505), 113–121. doi:10.1016/S0140-6736(05)67861-0
- Jeung, M. Y., Germain, P., Croisille, P., Ghannudi, S. El, Roy, C., & Gangi, A. (2012). Myocardial tagging with MR imaging: Overview of normal and pathologic findings. *Radiographics*. doi:10.1148/rg.325115098
- Jöbsis, P. D., Ashikaga, H., Wen, H., Rothstein, E. C., Horvath, K. A., McVeigh, E. R., & Balaban, R. S. (2007). The visceral pericardium: Macromolecular structure and contribution to passive mechanical properties of the left ventricle. *American Journal of Physiology - Heart and Circulatory Physiology*. doi:10.1152/ajpheart.00967.2007
- Jung, B., Föll, D., Böttler, P., Petersen, S., Hennig, J., & Markl, M. (2006). Detailed analysis of myocardial motion in volunteers and patients using high-temporal-resolution MR tissue phase mapping. *Journal of Magnetic Resonance Imaging*. doi:10.1002/jmri.20703
- Kanzaki, Y., Terasaki, F., Okabe, M., Fujita, S., Katashima, T., Otsuka, K., & Ishizaka, N. (2010). Three-dimensional architecture of cardiomyocytes and connective tissue in human heart revealed by scanning electron microscopy. *Circulation*. doi:10.1161/CIRCULATIONAHA.110.979815
- Kayvanpour, E., Mansi, T., Sedaghat-Hamedani, F., Amr, A., Neumann, D., Georgescu, B., Seegerer, P., Kamen, A., Haas, J., Frese, K. S., Irawati, M., Wirsz, E., King, V., Buss, S., Mereles, D., Zitron, E., Keller, A., Katus, H. A., Comaniciu, D., & Meder, B. (2015). Towards Personalized Cardiology: Multi-Scale Modeling of the Failing Heart. *PloS One*, 10(7), e0134869. doi:10.1371/journal.pone.0134869
- Kelle, S., & Nagel, E. (2008). The Role of Magnetic Resonance Imaging in the Detection of Coronary Artery Disease. *US Cardiology Review*. doi:10.15420/usc.2008.5.1.31
- Ker, J., Wang, L., Rao, J., & Lim, T. (2017). Deep Learning Applications in Medical Image Analysis. *IEEE Access*, 6, 9375–9379. doi:10.1109/ACCESS.2017.2788044
- Kerckhoffs, R. C. P., Bovendeerd, P. H., Kotte, J. C. S., Prinzen, F. W., Smits, K., & Arts, T. (2003).

- Homogeneity of cardiac contraction despite physiological asynchrony of depolarization: A model study. *Annals of Biomedical Engineering*. doi:10.1114/1.1566447
- Kerckhoffs, R. C. P., Lumens, J., Vernooy, K., Omens, J. H., Mulligan, L. J., Delhaas, T., Arts, T., McCulloch, A. D., & Prinzen, F. W. (2008). Cardiac resynchronization: Insight from experimental and computational models. *Progress in Biophysics and Molecular Biology*, 97(2), 543–561. doi:10.1016/j.pbiomolbio.2008.02.024
- Kerckhoffs, R. C. P., Neal, M. L., Gu, Q., Bassingthwaite, J. B., Omens, J. H., & McCulloch, A. D. (2007). Coupling of a 3D finite element model of cardiac ventricular mechanics to lumped systems models of the systemic and pulmonic circulation. *Annals of Biomedical Engineering*. doi:10.1007/s10439-006-9212-7
- Kerwin, W. S., & Prince, J. L. (1998). Cardiac material markers from tagged MR images. *Medical Image Analysis*. doi:10.1016/S1361-8415(98)80015-7
- Kheyfets, V. O., O'Dell, W., Smith, T., Reilly, J. J., & Finol, E. A. (2013). Considerations for numerical modeling of the pulmonary circulation - A review with a focus on pulmonary hypertension. In *Journal of Biomechanical Engineering*. doi:10.1115/1.4024141
- Kim, D., Gilson, W. D., Kramer, C. M., & Epstein, F. H. (2004). Myocardial Tissue Tracking with Two-dimensional Cine Displacement-encoded MR Imaging: Development and Initial Evaluation. *Radiology*. doi:10.1148/radiol.2303021213
- Klabunde, R. E. (2005). Cardiovascular physiology concepts / Richard E. Klabunde. In *Cardiovascular physiology concepts*.
- Knutsson, H., & Andersson, M. (2005). Morphons: segmentation using elastic canvas and paint on priors. *IEEE International Conference on Image Processing 2005*, 2, II–1226. doi:10.1109/ICIP.2005.1530283
- Korosoglou, G., Lehrke, S., Wochele, A., Hoerig, B., Lossnitzer, D., Steen, H., Giannitsis, E., Osman, N. F., & Katus, H. A. (2010). Strain-encoded CMR for the detection of inducible ischemia during intermediate stress. *JACC: Cardiovascular Imaging*. doi:10.1016/j.jcmg.2009.11.015
- Korosoglou, G., Lossnitzer, D., Schellberg, D., Lewien, A., Wochele, A., Schaeufele, T., Neizel, M., Steen, H., Giannitsis, E., Katus, H. A., & Osman, N. F. (2009). Strain-encoded cardiac MRI as an adjunct for dobutamine stress testing incremental value to conventional wall motion analysis. *Circulation: Cardiovascular Imaging*. doi:10.1161/CIRCIMAGING.108.790105
- Kowallick, J. T., Morton, G., Lamata, P., Jogiya, R., Kutty, S., Hasenfuß, G., Lotz, J., Chiribiri, A., Nagel, E., & Schuster, A. (2017). Quantitative assessment of left ventricular mechanical dyssynchrony using cine cardiovascular magnetic resonance imaging: Inter-study reproducibility. *JRSM Cardiovascular Disease*, 6, 2048004017710142. doi:10.1177/2048004017710142
- Kozerke, S., Scheidegger, M. B., Pedersen, E. M., & Boesiger, P. (1999). Heart motion adapted cine phase-contrast flow measurements through the aortic valve. *Magnetic Resonance in Medicine*, 42(5), 970–978. doi:10.1002/(sici)1522-2594(199911)42:5<970::aid-mrm18>3.0.co;2-i
- Kraitchman, D. L., & Bulte, J. W. M. (2008). Imaging of stem cells using MRI. *Basic Research in Cardiology*, 103(2), 105–113. doi:10.1007/s00395-008-0704-5
- Kraitchman, D. L., Sampath, S., Castillo, E., Derbyshire, J. A., Boston, R. C., Bluemke, D. A., Gerber, B. L., Prince, J. L., & Osman, N. F. (2003). Quantitative ischemia detection during cardiac magnetic resonance stress testing by use of FastHARP. *Circulation*. doi:10.1161/01.CIR.0000062684.47526.47

- Kraitchman, D. L., Young, A. A., Chang, C. N., & Axel, L. (1995). Semi-automatic tracking of myocardial motion in MR tagged images. *IEEE Transactions on Medical Imaging*, 14(3), 422–433. doi:10.1109/42.414606
- Kramer, C. M., Lima, J. A. C., Reichek, N., Ferrari, V. A., Llaneras, M. R., Palmon, L. C., Yeh, I. T., Tallant, B., & Axel, L. (1993). Regional differences in function within noninfarcted myocardium during left ventricular remodeling. *Circulation*. doi:10.1161/01.CIR.88.3.1279
- Kuijjer, J. P., Marcus, J. T., Götte, M. J., van Rossum, A. C., & Heethaar, R. M. (1999). Simultaneous MRI tagging and through-plane velocity quantification: a three-dimensional myocardial motion tracking algorithm. *Journal of Magnetic Resonance Imaging: JMRI*, 9(3), 409–419. doi:10.1002/(sici)1522-2586(199903)9:3<409::aid-jmri8>3.0.co;2-d
- Kuijjer, J. P., Marcus, J. T., Götte, M. J. W., van Rossum, A. C., & Heethaar, R. M. (2000). Three-dimensional myocardial strain analysis based on short- and long-axis magnetic resonance tagged images using a 1D displacement field. *Magnetic Resonance Imaging*, 18(5), 553–564. doi:10.1016/S0730-725X(00)00146-6
- Kuijjer, J. P., Marcus, J. T., Götte, M. J. W., Van Rossum, A. C., & Heethaar, R. M. (2002). Three-dimensional myocardial strains at end-systole and during diastole in the left ventricle of normal humans. *Journal of Cardiovascular Magnetic Resonance*. doi:10.1081/JCMR-120013299
- Kumar, V., Abbas, A. K., & Fausto, N. (2005). Robbins and Cotran Pathologic Basis of Disease. In *Robbins and Cotran Pathologic Basis of Disease*.
- Kutty, S., Rangamani, S., Venkataraman, J., Li, L., Schuster, A., Fletcher, S. E., Danford, D. A., & Beerbaum, P. (2013). Reduced global longitudinal and radial strain with normal left ventricular ejection fraction late after effective repair of aortic coarctation: A CMR feature tracking study. *International Journal of Cardiovascular Imaging*. doi:10.1007/s10554-012-0061-1
- La Gerche, A., Claessen, G., Van de Bruaene, A., Pattyn, N., Van Cleemput, J., Gewillig, M., Bogaert, J., Dymarkowski, S., Claus, P., & Heidbuchel, H. (2013). Cardiac MRI: a new gold standard for ventricular volume quantification during high-intensity exercise. *Circulation. Cardiovascular Imaging*, 6(2), 329–338. doi:10.1161/circimaging.112.980037
- Land, S., & Niederer, S. A. (2018). Influence of atrial contraction dynamics on cardiac function. *International Journal for Numerical Methods in Biomedical Engineering*. doi:10.1002/cnm.2931
- Land, S., Niederer, S. A., Aronsen, J. M., Espe, E. K. S., Zhang, L., Louch, W. E., Sjaastad, I., Sejersted, O. M., & Smith, N. P. (2012). An analysis of deformation-dependent electromechanical coupling in the mouse heart. *Journal of Physiology*. doi:10.1113/jphysiol.2012.231928
- Le Grice, I. J., Hunter, P. J., & Smaill, B. H. (1997). Laminar structure of the heart: A mathematical model. *American Journal of Physiology - Heart and Circulatory Physiology*. doi:10.1152/ajpheart.1997.272.5.h2466
- Le Grice, I. J., Smaill, B. H., Chai, L. Z., Edgar, S. G., Gavin, J. B., & Hunter, P. J. (1995). Laminar structure of the heart: Ventricular myocyte arrangement and connective tissue architecture in the dog. *American Journal of Physiology - Heart and Circulatory Physiology*. doi:10.1152/ajpheart.1995.269.2.h571
- Le Grice, I. J., Takayama, Y., & Covell, J. W. (1995). Transverse shear along myocardial cleavage planes provides a mechanism for normal systolic wall thickening. *Circulation Research*.

- doi:10.1161/01.RES.77.1.182
- Lee, K. S., Marwick, T. H., Cook, S. A., Go, R. T., Fix, J. S., James, K. B., Sapp, S. K., MacIntyre, W. J., & Thomas, J. D. (1994). Prognosis of patients with left ventricular dysfunction, with and without viable myocardium after myocardial infarction. Relative efficacy of medical therapy and revascularization. *Circulation*, 90(6), 2687–2694. doi:10.1161/01.cir.90.6.2687
- Lee, L. C., & Genet, M. (2019). Validation of Equilibrated Warping—Image Registration with Mechanical Regularization—On 3D Ultrasound Images. *Lecture Notes in Computer Science (Including Subseries Lecture Notes in Artificial Intelligence and Lecture Notes in Bioinformatics)*. doi:10.1007/978-3-030-21949-9_36
- Lee, L. C., Genet, M., Dang, A. B., Ge, L., Guccione, J. M., & Ratcliffe, M. B. (2014). Applications of computational modeling in cardiac surgery. *Journal of Cardiac Surgery*, 29(3), 293–302. doi:10.1111/jocs.12332
- Leiner, T., Rueckert, D., Suinesiaputra, A., Baeßler, B., Nezafat, R., Išgum, I., & Young, A. A. (2019). Machine learning in cardiovascular magnetic resonance: Basic concepts and applications. *Journal of Cardiovascular Magnetic Resonance*, 21(1), 1–14. doi:10.1186/s12968-019-0575-y
- Leiner, T., & Strijkers, G. (2018). Advances in cardiovascular MR imaging. *Magnetic Resonance Materials in Physics, Biology and Medicine*, 31(1), 3–6. doi:10.1007/s10334-018-0676-x
- Lekadir, K., Pashaei, A., Hoogendoorn, C., Pereanez, M., Alba, X., & Frangi, A. F. (2014). Effect of statistically derived fiber models on the estimation of cardiac electrical activation. *IEEE Transactions on Biomedical Engineering*. doi:10.1109/TBME.2014.2327025
- Libby, P. (2012). Inflammation in atherosclerosis. *Arteriosclerosis, Thrombosis, and Vascular Biology*, 32(9), 2045–2051. doi:10.1161/ATVBAHA.108.179705
- Light, N., & Champion, A. E. (1984). Characterization of muscle epimysium, perimysium and endomysium collagens. *Biochemical Journal*. doi:10.1042/bj2191017
- Lim, K. M., Constantino, J., Gurev, V., Zhu, R., Shim, E. B., & Trayanova, N. A. (2012). Comparison of the effects of continuous and pulsatile left ventricular-assist devices on ventricular unloading using a cardiac electromechanics model. *The Journal of Physiological Sciences*, 62(1), 11–19. doi:10.1007/s12576-011-0180-9
- Liu, W., Chen, J., Ji, S., Allen, J. S., Bayly, P. V., Wickline, S. A., & Yu, X. (2004). Harmonic phase MR tagging for direct quantification of Lagrangian strain in rat hearts after myocardial infarction. *Magnetic Resonance in Medicine*, 52(6), 1282–1290. doi:10.1002/mrm.20276
- Loecher, M., Hannum, A. J., Perotti, L. E., & Ennis, D. B. (2021). Arbitrary Point Tracking with Machine Learning to Measure Cardiac Strains in Tagged MRI. *Functional Imaging and Modeling of the Heart : ... International Workshop, FIMH ..., Proceedings. FIMH*, 12738, 213–222. doi:10.1007/978-3-030-78710-3_21
- Lorenz, C. H., Flacke, S., & Fischer, S. E. (2000). Noninvasive modalities. Cardiac MR imaging. *Cardiology Clinics*, 18(3), 557–570. doi:10.1016/s0733-8651(05)70161-2
- Maier, S. E., Fischer, S. E., McKinnon, G. C., Hess, O. M., Kraysenbuehl, H. P., & Boesiger, P. (1992). Evaluation of left ventricular segmental wall motion in hypertrophic cardiomyopathy with myocardial tagging. *Circulation*. doi:10.1161/01.CIR.86.6.1919
- Makram, A. W., Khalifa, A. M., El-Rewaidy, H., Fahmy, A. S., & Ibrahim, E. S. H. (2016). Assessment of cardiac mass from tagged magnetic resonance images. *Japanese Journal of Radiology*, 34(2), 158–165. doi:10.1007/s11604-015-0504-4
- Mansi, T., Pennec, X., Sermesant, M., Delingette, H., & Ayache, N. (2011). ILogDemons: A demons-based registration algorithm for tracking incompressible elastic biological

- tissues. *International Journal of Computer Vision*. doi:10.1007/s11263-010-0405-z
- Marchesseau, S., Delingette, H., Sermesant, M., & Ayache, N. (2013). Fast parameter calibration of a cardiac electromechanical model from medical images based on the unscented transform. *Biomechanics and Modeling in Mechanobiology*. doi:10.1007/s10237-012-0446-z
- Marcu, C. B., Beek, A. M., & Van Rossum, A. C. (2006). Clinical applications of cardiovascular magnetic resonance imaging. In *CMAJ*. doi:10.1503/cmaj.060566
- Marcus, J. T., Götte, M. J. W., Van Rossum, A. C., Kuijter, J. P. A., Heethaar, R. M., Axel, L., & Visser, C. A. (1997). Myocardial function in infarcted and remote regions early after infarction in man: Assessment by magnetic resonance tagging and strain analysis. *Magnetic Resonance in Medicine*. doi:10.1002/mrm.1910380517
- Maret, E., Todt, T., Brudin, L., Nylander, E., Swahn, E., Ohlsson, J. L., & Engvall, J. E. (2009). Functional measurements based on feature tracking of cine magnetic resonance images identify left ventricular segments with myocardial scar. *Cardiovascular Ultrasound*. doi:10.1186/1476-7120-7-53
- Matthaei, D., Frahm, J., Haase, A., & Hanicke, W. (1985). REGIONAL PHYSIOLOGICAL FUNCTIONS DEPICTED BY SEQUENCES OF RAPID MAGNETIC RESONANCE IMAGES. In *The Lancet*. doi:10.1016/S0140-6736(85)90158-8
- McCormick, M., Nordsletten, D., Lamata, P., & Smith, N. P. (2014). Computational analysis of the importance of flow synchrony for cardiac ventricular assist devices. *Computers in Biology and Medicine*, 49, 83–94. doi:10.1016/j.combiomed.2014.03.013
- McLeod, K., Prakosa, A., Mansi, T., Sermesant, M., & Pennec, X. (2012). An incompressible log-domain demons algorithm for tracking heart tissue. *Lecture Notes in Computer Science (Including Subseries Lecture Notes in Artificial Intelligence and Lecture Notes in Bioinformatics)*. doi:10.1007/978-3-642-28326-0_6
- McVeigh, E. R., & Bolster, B. D. (1998). Improved sampling of myocardial motion with variable separation tagging. *Magnetic Resonance in Medicine*. doi:10.1002/mrm.1910390421
- Meier, G. D., Bove, A. A., Santamore, W. P., & Lynch, P. R. (2017). Contractile function in canine right ventricle. *American Journal of Physiology-Heart and Circulatory Physiology*. doi:10.1152/ajpheart.1980.239.6.h794
- Mishiro, Y., Oki, T., Iuchi, A., Tabata, T., Yamada, H., Abe, M., Onose, Y., Ito, S., Nishitani, H., Harada, M., & Taoka, Y. (1999). Regional left ventricular myocardial contraction abnormalities and asynchrony in patients with hypertrophic cardiomyopathy evaluated by magnetic resonance spatial modulation of magnetization myocardial tagging. *Japanese Circulation Journal*. doi:10.1253/jcj.63.442
- Miyatake, K., Yamagishi, M., Tanaka, N., Uematsu, M., Yamazaki, N., Mine, Y., Sano, A., & Hiramata, M. (1995). New method for evaluating left ventricular wall motion by color-coded tissue doppler imaging: In vitro and in vivo studies. *Journal of the American College of Cardiology*. doi:10.1016/0735-1097(94)00421-L
- Montillo, A., Metaxas, D., & Axel, L. (2004). Extracting tissue deformation using Gabor filter banks. *Medical Imaging 2004: Physiology, Function, and Structure from Medical Images*. doi:10.1117/12.536860
- Moon, J. C. C., Fisher, N. G., McKenna, W. J., & Pennell, D. J. (2004). Detection of apical hypertrophic cardiomyopathy by cardiovascular magnetic resonance in patients with non-diagnostic echocardiography. *Heart*. doi:10.1136/hrt.2003.014969
- Moore, C. C., Lugo-Olivieri, C. H., McVeigh, E. R., & Zerhouni, E. A. (2000). Three-dimensional systolic strain patterns in the normal human left ventricle: Characterization with tagged

- MR imaging. *Radiology*. doi:10.1148/radiology.214.2.r00fe17453
- Moore, C. C., McVeigh, E. R., & Zerhouni, E. A. (2000). Quantitative tagged magnetic resonance imaging of the normal human left ventricle. In *Topics in Magnetic Resonance Imaging*. doi:10.1097/00002142-200012000-00005
- Moore, C. C., Reeder, S. B., & McVeigh, E. R. (1994). Tagged MR imaging in a deforming phantom: Photographic validation. *Radiology*. doi:10.1148/radiology.190.3.8115625
- Morton, G., Schuster, A., Jogiya, R., Kutty, S., Beerbaum, P., & Nagel, E. (2012). Inter-study reproducibility of cardiovascular magnetic resonance myocardial feature tracking. *Journal of Cardiovascular Magnetic Resonance*. doi:10.1186/1532-429X-14-43
- Morton, G., Schuster, A., Perera, D., & Nagel, E. (2010). Cardiac magnetic resonance imaging to guide complex revascularization in stable coronary artery disease. *European Heart Journal*, 31(18), 2209–2215. doi:10.1093/eurheartj/ehq256
- Mosher, T. J., & Smith, M. B. (1990). A DANTE tagging sequence for the evaluation of translational sample motion. *Magnetic Resonance in Medicine*. doi:10.1002/mrm.1910150215
- Myers, J. H., Stirling, M. C., Choy, M., Buda, A. J., & Gallagher, K. P. (1986). Direct measurement of inner and outer wall thickening dynamics with epicardial echocardiography. *Circulation*. doi:10.1161/01.CIR.74.1.164
- Nagel, E., Lehmkuhl, H. B., Bocksch, W., Klein, C., Vogel, U., Frantz, E., Ellmer, A., Dreyse, S., & Fleck, E. (1999). Noninvasive diagnosis of ischemia-induced wall motion abnormalities with the use of high-dose dobutamine stress MRI: Comparison with dobutamine stress echocardiography. *Circulation*. doi:10.1161/01.CIR.99.6.763
- Naghavi, M., Libby, P., Falk, E., Casscells, S. W., Litovsky, S., Rumberger, J., Badimon, J. J., Stefanadis, C., Moreno, P., Pasterkamp, G., Fayad, Z., Stone, P. H., Waxman, S., Raggi, P., Madjid, M., Zarrabi, A., Burke, A., Yuan, C., Fitzgerald, P. J., ... Ridker, P. M. (2003). *Review : Current Perspective From Vulnerable Plaque to Vulnerable Patient A Call for New Definitions and Risk Assessment Strategies: Part II*. 1772–1778. doi:10.1161/01.CIR.0000087481.55887.C9
- Naghavi, M., Libby, P., Falk, E., Casscells, S. W., Litovsky, S., Rumberger, J., Badimon, J. J., Stefanadis, C., Moreno, P., Pasterkamp, G., Fayad, Z., Stone, P. H., Waxman, S., Raggi, P., Madjid, M., Zarrabi, A., Burke, A., Yuan, C., Fitzgerald, P. J., ... Willerson, J. T. (2003). From vulnerable plaque to vulnerable patient: a call for new definitions and risk assessment strategies: Part I. *Circulation*, 108(14), 1664–1672. doi:10.1161/01.CIR.0000087480.94275.97
- Nagueh, S. F., Bachinski, L. L., Meyer, D., Hill, R., Zoghbi, W. A., Tam, J. W., Quiñones, M. A., Roberts, R., & Marian, A. J. (2001). Tissue Doppler imaging consistently detects myocardial abnormalities in patients with hypertrophic cardiomyopathy and provides a novel means for an early diagnosis before and independently of hypertrophy. *Circulation*, 104(2), 128–130. doi:10.1161/01.CIR.104.2.128
- Nagumo, J., Arimoto, S., & Yoshizawa, S. (1962). An Active Pulse Transmission Line Simulating Nerve Axon. *Proceedings of the IRE*. doi:10.1109/JRPROC.1962.288235
- Nasiraei-Moghaddam, A., & Paul Finn, J. (2014). Tagging of cardiac magnetic resonance images in the polar coordinate system: Physical principles and practical implementation. *Magnetic Resonance in Medicine*. doi:10.1002/mrm.24839
- Neizel, M., Lossnitzer, D., Korosoglou, G., Schäufele, T., Lewien, A., Steen, H., Katus, H. A., Osman, N. F., & Giannitsis, E. (2009). Strain-encoded (SENC) magnetic resonance imaging to evaluate regional heterogeneity of myocardial strain in healthy volunteers:

- Comparison with conventional tagging. *Journal of Magnetic Resonance Imaging*. doi:10.1002/jmri.21612
- Nelson, G. S., Curry, C. W., Wyman, B. T., Kramer, A., Declerck, J., Talbot, M., Douglas, M. R., Berger, R. D., McVeigh, E. R., & Kass, D. A. (2000). Predictors of systolic augmentation from left ventricular preexcitation in patients with dilated cardiomyopathy and intraventricular conduction delay. *Circulation*. doi:10.1161/01.CIR.101.23.2703
- Nesbitt, G. C., Mankad, S., & Oh, J. K. (2009). Strain imaging in echocardiography: Methods and clinical applications. In *International Journal of Cardiovascular Imaging*. doi:10.1007/s10554-008-9414-1
- Ng, A. C. T., Delgado, V., Bertini, M., Antoni, M. L., Van Bommel, R. J., Van Rijnsoever, E. P. M., Van Der Kley, F., Ewe, S. H., Witkowski, T., Auger, D., Nucifora, G., Schuijf, J. D., Poldermans, D., Leung, D. Y., Schalij, M. J., & Bax, J. J. (2011). Alterations in multidirectional myocardial functions in patients with aortic stenosis and preserved ejection fraction: A two-dimensional speckle tracking analysis. *European Heart Journal*, 32(12), 1542–1550. doi:10.1093/eurheartj/ehr084
- Nguyen, T. D., Reeves, S. J., & Denney, T. S. (2003). On the optimality of magnetic resonance tag patterns for heart wall motion estimation. *IEEE Transactions on Image Processing*. doi:10.1109/TIP.2003.812387
- Nichols, W. W., O'Rourke, M. F., Vlachopoulos, C., Hoeks, A. P., & Reneman, R. S. (2011). McDonald's blood flow in arteries theoretical, experimental and clinical principles. In *McDonald's Blood Flow in Arteries, Sixth Edition: Theoretical, Experimental and Clinical Principles*. doi:10.1111/j.1540-8175.1991.tb01207.x
- Niederer, S. A., Hunter, P. J., & Smith, N. P. (2006). A quantitative analysis of cardiac myocyte relaxation: a simulation study. *Biophysical Journal*, 90(5), 1697–1722. doi:10.1529/biophysj.105.069534
- Noble, D. (2002). Modeling the heart - From genes to cells to the whole organ. In *Science*. doi:10.1126/science.1069881
- Nucifora, G., Muser, D., Morocutti, G., Piccoli, G., Zanuttini, D., Gianfagna, P., & Proclemer, A. (2014). Disease-specific differences of left ventricular rotational mechanics between cardiac amyloidosis and hypertrophic cardiomyopathy. *American Journal of Physiology - Heart and Circulatory Physiology*. doi:10.1152/ajpheart.00251.2014
- O'Hanlon, R., Assomull, R. G., & Prasad, S. K. (2007). Use of cardiovascular magnetic resonance for diagnosis and management in hypertrophic cardiomyopathy. In *Current Cardiology Reports*. doi:10.1007/s11886-007-0010-0
- Ortega, M., Triedman, J. K., Geva, T., & Harrild, D. M. (2011). Relation of left ventricular dyssynchrony measured by cardiac magnetic resonance tissue tracking in repaired tetralogy of fallot to ventricular tachycardia and death. *The American Journal of Cardiology*, 107(10), 1535–1540. doi:10.1016/j.amjcard.2011.01.032
- Osman, N. F., Kerwin, W. S., McVeigh, E. R., & Prince, J. L. (1999). Cardiac motion tracking using CINE harmonic phase (HARP) magnetic resonance imaging. *Magnetic Resonance in Medicine*, 42(6), 1048–1060. doi:10.1002/(SICI)1522-2594(199912)42:6<1048::AID-MRM9>3.0.CO;2-M
- Osman, N. F., McVeigh, E. R., & Prince, J. L. (2000). Imaging heart motion using harmonic phase MRI. *IEEE Transactions on Medical Imaging*. doi:10.1109/42.845177
- Osman, N. F., Sampath, S., Atalar, E., & Prince, J. L. (2001). Imaging longitudinal cardiac strain on short-axis images using strain-encoded MRI. *Magnetic Resonance in Medicine*. doi:10.1002/mrm.1195

- Padiyath, A., Gribben, P., Abraham, J. R., Li, L., Rangamani, S., Schuster, A., Danford, D. A., Pedrizzetti, G., & Kutty, S. (2013). Echocardiography and cardiac magnetic resonance-based feature tracking in the assessment of myocardial mechanics in tetralogy of fallot: An intermodality comparison. *Echocardiography*. doi:10.1111/echo.12016
- Paetsch, I., Jahnke, C., Ferrari, V. A., Rademakers, F. E., Pellikka, P. A., Hundley, W. G., Poldermans, D., Bax, J. J., Wegscheider, K., Fleck, E., & Nagel, E. (2006). Determination of interobserver variability for identifying inducible left ventricular wall motion abnormalities during dobutamine stress magnetic resonance imaging. *European Heart Journal*. doi:10.1093/eurheartj/ehi883
- Pai, V. M., & Axel, L. (2006). Advances in MRI tagging techniques for determining regional myocardial strain. In *Current Cardiology Reports*. doi:10.1007/s11886-006-0011-4
- Palit, A., Bhudia, S. K., Arvanitis, T. N., Sherwood, V., Wayte, S., Turley, G. A., & Williams, M. A. (2015). Effect of fibre orientation on diastolic mechanics of human ventricle. *Proceedings of the Annual International Conference of the IEEE Engineering in Medicine and Biology Society, EMBS*. doi:10.1109/EMBC.2015.7319887
- Pan, L., Lima, J. A. C., & Osman, N. F. (2003). Fast tracking of cardiac motion using 3D-HARP. *Lecture Notes in Computer Science (Including Subseries Lecture Notes in Artificial Intelligence and Lecture Notes in Bioinformatics)*. doi:10.1007/978-3-540-45087-0_51
- Pan, L., Prince, J. L., Lima, J. A. C., & Osman, N. F. (2005). Fast tracking of cardiac motion using 3D-HARP. *IEEE Transactions on Biomedical Engineering*. doi:10.1109/TBME.2005.851490
- Pan, L., Stuber, M., Kraitichman, D. L., Fritzges, D. L., Gilson, W. D., & Osman, N. F. (2006). Real-time imaging of regional myocardial function using fast-SENC. *Magnetic Resonance in Medicine*. doi:10.1002/mrm.20770
- Partington, S. L., & Valente, A. M. (2013). Cardiac magnetic resonance in adults with congenital heart disease. *Methodist DeBakey Cardiovascular Journal*, 9(3), 156–162. doi:10.14797/mdcj-9-3-156
- Peirlinck, M., Sack, K. L., De Backer, P., Morais, P., Segers, P., Franz, T., & De Beule, M. (2019). Kinematic boundary conditions substantially impact in silico ventricular function. *International Journal for Numerical Methods in Biomedical Engineering*. doi:10.1002/cnm.3151
- Pelliccia, A., Maron, B. J., De Luca, R., Di Paolo, F. M., Spataro, A., & Culasso, F. (2002). Remodeling of left ventricular hypertrophy in elite athletes after long-term deconditioning. *Circulation*. doi:10.1161/hc0802.104534
- Peng, P., Lekadir, K., Gooya, A., Shao, L., Petersen, S. E., & Frangi, A. F. (2016). A review of heart chamber segmentation for structural and functional analysis using cardiac magnetic resonance imaging. In *Magnetic Resonance Materials in Physics, Biology and Medicine*. doi:10.1007/s10334-015-0521-4
- Pennell, D. J., Sechtem, U. P., Higgins, C. B., Manning, W. J., Pohost, G. M., Rademakers, F. E., Van Rossum, A. C., Shaw, L. J., & Yucel, E. K. (2004). Clinical indications for cardiovascular magnetic resonance (CMR): Consensus Panel report. *European Heart Journal*. doi:10.1016/j.ehj.2004.06.040
- Pennell, D. J., Underwood, S. R., Manzara, C. C., Swanton, R. H., Walker, J. M., Ell, P. J., & Longmore, D. B. (1992). Magnetic resonance imaging during dobutamine stress in coronary artery disease. *The American Journal of Cardiology*. doi:10.1016/0002-9149(92)91386-I
- Pereles, F. S., Kapoor, V., Carr, J. C., Simonetti, O. P., Krupinski, E. A., Baskaran, V., & Finn, J. P. (2001). Usefulness of segmented trueFISP cardiac pulse sequence in evaluation of

- congenital and acquired adult cardiac abnormalities. *American Journal of Roentgenology*. doi:10.2214/ajr.177.5.1771155
- Pfaller, M. R., Hörmann, J. M., Weigl, M., Nagler, A., Chabiniok, R., Bertoglio, C., & Wall, W. A. (2019). The importance of the pericardium for cardiac biomechanics: from physiology to computational modeling. *Biomechanics and Modeling in Mechanobiology*. doi:10.1007/s10237-018-1098-4
- Phatak, N. S., Maas, S. A., Veress, A. I., Pack, N. A., Di Bella, E. V. R., & Weiss, J. A. (2009). Strain measurement in the left ventricle during systole with deformable image registration. *Medical Image Analysis*. doi:10.1016/j.media.2008.07.004
- Piccini, D., Littmann, A., Nielles-Vallespin, S., & Zenge, M. O. (2012). Respiratory self-navigation for whole-heart bright-blood coronary MRI: methods for robust isolation and automatic segmentation of the blood pool. *Magnetic Resonance in Medicine*, 68(2), 571–579. doi:10.1002/mrm.23247
- Plein, S., Bloomer, T. N., Ridgway, J. P., Jones, T. R., Bainbridge, G. J., & Sivananthan, M. U. (2001). Steady-state free precession magnetic resonance imaging of the heart: Comparison with segmented K-space gradient-echo imaging. *Journal of Magnetic Resonance Imaging*. doi:10.1002/jmri.1178
- Plonsey, R., & Barr, R. C. (1987). Mathematical modeling of electrical activity of the heart. *Journal of Electrocardiology*. doi:10.1016/S0022-0736(87)80019-5
- Pouleur, A.-C., Knappe, D., Shah, A. M., Uno, H., Bourgoun, M., Foster, E., McNitt, S., Hall, W. J., Zareba, W., Goldenberg, I., Moss, A. J., Pfeffer, M. A., & Solomon Scott D., for the M.-C. I. (2011). Relationship between improvement in left ventricular dyssynchrony and contractile function and clinical outcome with cardiac resynchronization therapy: the MADIT-CRT trial. *European Heart Journal*, 32(14), 1720–1729. doi:10.1093/eurheartj/ehr185
- Puyol-Anton, E., Ruijsink, B., Bai, W., Langet, H., De Craene, M., Schnabel, J. A., Piro, P., King, A. P., & Sinclair, M. (2018). Fully automated myocardial strain estimation from cine MRI using convolutional neural networks. *Proceedings - International Symposium on Biomedical Imaging*. doi:10.1109/ISBI.2018.8363772
- Qian, Z., Metaxas, D. N., & Axel, L. (2006). Extraction and tracking of MRI tagging sheets using a 3D gabor filter bank. *Annual International Conference of the IEEE Engineering in Medicine and Biology - Proceedings*. doi:10.1109/IEMBS.2006.259542
- Qin, X., & Fei, B. (2015). DTI template-based estimation of cardiac fiber orientations from 3D ultrasound. *Medical Physics*. doi:10.1118/1.4921121
- Quarteroni, A., Formaggia, L., & Veneziani, A. (2009). Cardiovascular Mathematics: Modeling and simulation of the circulatory system. *Modeling, Simulation and Applications*.
- Quarteroni, A., Lassila, T., Rossi, S., & Ruiz-Baier, R. (2017). Integrated Heart—Coupling multiscale and multiphysics models for the simulation of the cardiac function. *Computer Methods in Applied Mechanics and Engineering*. doi:10.1016/j.cma.2016.05.031
- Quarteroni, A., Manzoni, A., & Vergara, C. (2017). The cardiovascular system: Mathematical modelling, numerical algorithms and clinical applications. *Acta Numerica*. doi:10.1017/S0962492917000046
- Quarteroni, A., Tuveri, M., & Veneziani, A. (2000). Computational vascular fluid dynamics: Problems, models and methods. *Computing and Visualization in Science*. doi:10.1007/s007910050039
- Rademakers, F. E., & Bogaert, J. (1997). Left ventricular myocardial tagging. *The International Journal of Cardiac Imaging*, 13(3), 233–245. doi:10.1023/A:1005731100601

- Radeva, P., Amini, A. A., & Huang, J. (1997). Deformable B-Solids and Implicit Snakes for 3D Localization and Tracking of SPAMM MRI Data. *Computer Vision and Image Understanding*. doi:10.1006/cviu.1997.0611
- Rankin, J. S., McHale, P. A., Arentzen, C. E., Ling, D., Greenfield, J. C., & Anderson, R. W. (1976). The three dimensional dynamic geometry of the left ventricle in the conscious dog. In *Circulation Research*. doi:10.1161/01.RES.39.3.304
- Rebergen, S. A., & De Roos, A. (2000). Congenital heart disease. Evaluation of anatomy and function by MRI. *Herz*. doi:10.1007/s000590050029
- Reichek, N. (1999). MRI myocardial tagging. *Journal of Magnetic Resonance Imaging : JMRI*, 10(5), 609–616. doi:10.1002/(sici)1522-2586(199911)10:5<609::aid-jmri4>3.0.co;2-2
- Reindl, M., Tiller, C., Holzknecht, M., Lechner, I., Beck, A., Plappert, D., Gorzala, M., Pamminger, M., Mayr, A., Klug, G., Bauer, A., Metzler, B., & Reinstadler, S. J. (2019). Prognostic Implications of Global Longitudinal Strain by Feature-Tracking Cardiac Magnetic Resonance in ST-Elevation Myocardial Infarction. *Circulation. Cardiovascular Imaging*. doi:10.1161/CIRCIMAGING.119.009404
- Reller, M. D., Strickland, M. J., Riehle-Colarusso, T., Mahle, W. T., & Correa, A. (2008). Prevalence of congenital heart defects in metropolitan Atlanta, 1998-2005. *The Journal of Pediatrics*, 153(6), 807–813. doi:10.1016/j.jpeds.2008.05.059
- Reneman, R. S., Hunter, W. C., Corsel, J. W., Arts, T., Muijtjens, A. M. M., & Douglas, A. S. (2011). *Macroscopic Three-Dimensional Motion Patterns of the Left Ventricle*. doi:10.1007/978-1-4615-2946-0_37
- Rickers, C., Wilke, N. M., Jerosch-Herold, M., Casey, S. A., Panse, P., Panse, N., Weil, J., Zenovich, A. G., & Maron, B. J. (2005). Utility of cardiac magnetic resonance imaging in the diagnosis of hypertrophic cardiomyopathy. *Circulation*. doi:10.1161/CIRCULATIONAHA.104.507723
- Rogers, W. J., Kramer, C. M., Geskin, G., Hu, Y. L., Theobald, T. M., Vido, D. A., Petruolo, S., & Reichek, N. (1999). Early contrast-enhanced MRI predicts late functional recovery after reperfused myocardial infarction. *Circulation*. doi:10.1161/01.CIR.99.6.744
- Rohmer, D., Sitek, A., & Gullberg, G. T. (2007). Reconstruction and visualization of fiber and laminar structure in the normal human heart from ex vivo diffusion tensor magnetic resonance imaging (DTMRI) data. *Investigative Radiology*. doi:10.1097/RLI.0b013e3181238330
- Romano, S., Judd, R. M., Kim, R. J., Kim, H. W., Klem, I., Heitner, J. F., Shah, D. J., Jue, J., White, B. E., Indorkar, R., Shenoy, C., & Farzaneh-Far, A. (2018). Feature-Tracking Global Longitudinal Strain Predicts Death in a Multicenter Population of Patients With Ischemic and Nonischemic Dilated Cardiomyopathy Incremental to Ejection Fraction and Late Gadolinium Enhancement. *JACC. Cardiovascular Imaging*, 11(10), 1419–1429. doi:10.1016/j.jcmg.2017.10.024
- Rosen, B. D., Lima, J. A. C., Nasir, K., Edvardsen, T., Folsom, A. R., Lai, S., Bluemke, D. A., & Jerosch-Herold, M. (2006). Lower myocardial perfusion reserve is associated with decreased regional left ventricular function in asymptomatic participants of the Multi-Ethnic Study of Atherosclerosis. *Circulation*. doi:10.1161/CIRCULATIONAHA.105.588525
- Ross, J. J. (1999). Regional myocardial function and microvascular dysfunction. Does the alternate cascade represent ischemia? In *Cardiologia (Rome, Italy)* (Vol. 44, Issue 9, pp. 797–799).
- Rossi, S., Lassila, T., Ruiz-Baier, R., Sequeira, A., & Quarteroni, A. (2014). Thermodynamically consistent orthotropic activation model capturing ventricular systolic wall thickening in

- cardiac electromechanics. *European Journal of Mechanics, A/Solids*. doi:10.1016/j.euromechsol.2013.10.009
- Rubler, S., Damani, P. M., & Pinto, E. R. (1977). Cardiac size and performance during pregnancy estimated with echocardiography. *The American Journal of Cardiology*. doi:10.1016/0002-9149(77)90068-6
- Runqing, X., Xie, M., Wang, X., & Lü, Q. (2006). Assessment of regional myocardial function in patients with hypertrophic cardiomyopathy by tissue strain imaging. *Journal of Huazhong University of Science and Technology. Medical Sciences = Hua Zhong Ke Ji Da Xue Xue Bao. Yi Xue Ying De Wen Ban = Huazhong Keji Daxue Xuebao. Yixue Yingdewen Ban*. doi:10.1007/BF02829568
- Rutz, A. K., Manka, R., Kozerke, S., Roas, S., Boesiger, P., & Schwitter, J. (2009). Left ventricular dyssynchrony in patients with left bundle branch block and patients after myocardial infarction: integration of mechanics and viability by cardiac magnetic resonance. *European Heart Journal*, 30(17), 2117–2127. doi:10.1093/eurheartj/ehp212
- Rutz, A. K., Ryf, S., Plein, S., Boesiger, P., & Kozerke, S. (2008). Accelerated whole-heart 3D CSPAMM for myocardial motion quantification. *Magnetic Resonance in Medicine*. doi:10.1002/mrm.21363
- Ryf, S., Spiegel, M. A., Gerber, M., & Boesiger, P. (2002). Myocardial tagging with 3D-CSPAMM. *Journal of Magnetic Resonance Imaging*. doi:10.1002/jmri.10145
- Sagawa, K., Lie, R. K., & Schaefer, J. (1990). Translation of Otto frank's paper "Die Grundform des arteriellen Pulses" zeitschrift für biologie 37: 483-526 (1899). *Journal of Molecular and Cellular Cardiology*. doi:10.1016/0022-2828(90)91459-K
- Sainte-Marie, J., Chapelle, D., Cimrman, R., & Sorine, M. (2006). Modeling and estimation of the cardiac electromechanical activity. *Computers and Structures*. doi:10.1016/j.compstruc.2006.05.003
- Salvo, G. Di, Pergola, V., Fadel, B., Bulbul, Z. Al, & Caso, P. (2015). Strain echocardiography and myocardial mechanics: From basics to clinical applications. In *Journal of Cardiovascular Echography*. doi:10.4103/2211-4122.158415
- Sampath, S., Derbyshire, J. A., Atalar, E., Osman, N. F., & Prince, J. L. (2003). Real-time imaging of two-dimensional cardiac strain using a harmonic phase magnetic resonance imaging (HARP-MRI) pulse sequence. *Magnetic Resonance in Medicine*. doi:10.1002/mrm.10509
- Sampath, S., Osman, N. F., & Prince, J. L. (2009). A combined harmonic phase and strain-encoded pulse sequence for measuring three-dimensional strain. *Magnetic Resonance Imaging*. doi:10.1016/j.mri.2008.05.020
- Sands, G. B., Gerneke, D. A., Hooks, D. A., Green, C. R., Smaill, B. H., & Legrice, I. J. (2005). Automated imaging of extended tissue volumes using confocal microscopy. *Microscopy Research and Technique*. doi:10.1002/jemt.20200
- Sandstede, J. J. W. (2003). Assessment of myocardial viability by MR imaging. *European Radiology*, 13(1), 52–61. doi:10.1007/s00330-002-1701-y
- Sarvari, S. I., Haugaa, K. H., Zahid, W., Bendz, B., Aakhus, S., Aaberge, L., & Edvardsen, T. (2013). Layer-specific quantification of myocardial deformation by strain echocardiography may reveal significant CAD in patients with non-ST-segment elevation acute coronary syndrome. *JACC: Cardiovascular Imaging*. doi:10.1016/j.jcmg.2013.01.009
- Schmid, H., Nash, M. P., Young, A. A., & Hunter, P. J. (2006). Myocardial material parameter estimation - A comparative study for simple shear. *Journal of Biomechanical Engineering*. doi:10.1115/1.2244576
- Scholtz, L., Sarkin, A., & Lockhat, Z. (2014). Current clinical applications of cardiovascular

- magnetic resonance imaging. *Cardiovascular Journal of Africa*. doi:10.5830/CVJA-2014-021
- Schrauben, E. M., Cowan, B. R., Greiser, A., & Young, A. A. (2018). Left ventricular function and regional strain with subtly-tagged steady-state free precession feature tracking. *Journal of Magnetic Resonance Imaging*, 47(3), 787–797. doi:10.1002/jmri.25819
- Schuster, A., Hor, K. N., Kowallick, J. T., Beerbaum, P., & Kutty, S. (2016). Cardiovascular Magnetic Resonance Myocardial Feature Tracking: Concepts and Clinical Applications. *Circulation: Cardiovascular Imaging*. doi:10.1161/CIRCIMAGING.115.004077
- Schuster, A., Kutty, S., Padiyath, A., Parish, V., Gribben, P., Danford, D. A., Makowski, M. R., Bigalke, B., Beerbaum, P., & Nagel, E. (2011). Cardiovascular magnetic resonance myocardial feature tracking detects quantitative wall motion during dobutamine stress. *Journal of Cardiovascular Magnetic Resonance*. doi:10.1186/1532-429X-13-58
- Schuster, A., Morton, G., Hussain, S. T., Jogiya, R., Kutty, S., Asrress, K. N., Makowski, M. R., Bigalke, B., Perera, D., Beerbaum, P., & Nagel, E. (2013). The intra-observer reproducibility of cardiovascular magnetic resonance myocardial feature tracking strain assessment is independent of field strength. *European Journal of Radiology*. doi:10.1016/j.ejrad.2012.11.012
- Schuster, A., Paul, M., Bettencourt, N., Morton, G., Chiribiri, A., Ishida, M., Hussain, S., Jogiya, R., Kutty, S., Bigalke, B., Perera, D., & Nagel, E. (2013). Cardiovascular magnetic resonance myocardial feature tracking for quantitative viability assessment in ischemic cardiomyopathy. *International Journal of Cardiology*. doi:10.1016/j.ijcard.2011.10.137
- Sengupta, P. P., Tajik, A. J., Chandrasekaran, K., & Khandheria, B. K. (2008). Twist Mechanics of the Left Ventricle. Principles and Application. *JACC: Cardiovascular Imaging*, 1(3), 366–376. doi:10.1016/j.jcmg.2008.02.006
- Sermesant, M., Chabiniok, R., Chinchapatnam, P., Mansi, T., Billet, F., Moireau, P., Peyrat, J. M., Wong, K., Relan, J., Rhode, K., Ginks, M., Lambiase, P., Delingette, H., Sorine, M., Rinaldi, C. A., Chapelle, D., Razavi, R., & Ayache, N. (2012). Patient-specific electromechanical models of the heart for the prediction of pacing acute effects in CRT: A preliminary clinical validation. *Medical Image Analysis*. doi:10.1016/j.media.2011.07.003
- Sermesant, M., Forest, C., Pennec, X., Delingette, H., & Ayache, N. (2003). Deformable biomechanical models: application to 4D cardiac image analysis. *Medical Image Analysis*, 7(4), 475–488. doi:10.1016/s1361-8415(03)00068-9
- Serri, K., Reant, P., Lafitte, M., Berhouet, M., Le Bouffos, V., Roudaut, R., & Lafitte, S. (2006). Global and regional myocardial function quantification by two-dimensional strain: Application in hypertrophic cardiomyopathy. *Journal of the American College of Cardiology*. doi:10.1016/j.jacc.2005.10.061
- Setser, R. M., Kasper, J. M., Lieber, M. L., Starling, R. C., McCarthy, P. M., & White, R. D. (2003). Persistent abnormal left ventricular systolic torsion in dilated cardiomyopathy after partial left ventriculectomy. *Journal of Thoracic and Cardiovascular Surgery*. doi:10.1016/S0022-5223(03)00050-3
- Sharp, M. K., & Dharmalingam, R. K. (1999). Development of a hydraulic model of the human systemic circulation. *ASAIO Journal*. doi:10.1097/00002480-199911000-00006
- Shehata, M., Cheng, S., Osman, N., Bluemke, D., & Lima, J. (2009). Myocardial tissue tagging with cardiovascular magnetic resonance. In *Journal of Cardiovascular Magnetic Resonance*. doi:10.1186/1532-429X-11-55
- Shen, D., Sundar, H., Xue, Z., Fan, Y., & Litt, H. (2005). Consistent estimation of cardiac motions

- by 4D image registration. *Medical Image Computing and Computer-Assisted Intervention: MICCAI ... International Conference on Medical Image Computing and Computer-Assisted Intervention*. doi:10.1007/11566489_111
- Shi, W., Zhuang, X., Wang, H., Duckett, S., Luong, D. V. N., Tobon-Gomez, C., Tung, K., Edwards, P. J., Rhode, K. S., Razavi, R. S., Ourselin, S., & Rueckert, D. (2012). A comprehensive cardiac motion estimation framework using both untagged and 3-D tagged MR images based on nonrigid registration. *IEEE Transactions on Medical Imaging*. doi:10.1109/TMI.2012.2188104
- Shimoni, S., Gendelman, G., Ayzenberg, O., Smirin, N., Lysyansky, P., Edri, O., Deutsch, L., Caspi, A., & Friedman, Z. (2011). Differential effects of coronary artery stenosis on myocardial function: The value of myocardial strain analysis for the detection of coronary artery disease. *Journal of the American Society of Echocardiography*. doi:10.1016/j.echo.2011.03.007
- Silber, S., Albertsson, P., Avilés, F. F., Camici, P. G., Colombo, A., Hamm, C., Jørgensen, E., Marco, J., Nordrehaug, J.-E., Ruzyllo, W., Urban, P., Stone, G. W., & Wijns, W. (2005). Guidelines for percutaneous coronary interventions. The Task Force for Percutaneous Coronary Interventions of the European Society of Cardiology. *European Heart Journal*, 26(8), 804–847. doi:10.1093/eurheartj/ehi138
- Simonetti, O. P., Kim, R. J., Fieno, D. S., Hillenbrand, H. B., Wu, E., Bundy, J. M., Finn, J. P., & Judd, R. M. (2001). An improved MR imaging technique for the visualization of myocardial infarction. *Radiology*. doi:10.1148/radiology.218.1.r01ja50215
- Simpson, R. M., Keegan, J., & Firmin, D. N. (2013). MR assessment of regional myocardial mechanics. *Journal of Magnetic Resonance Imaging: JMRI*, 37(3), 576–599. doi:10.1002/jmri.23756
- Škardová, K., Rambašek, M., Chabiniok, R., & Genet, M. (2019). Mechanical and Imaging Models-Based Image Registration. In *Lecture Notes in Computational Vision and Biomechanics* (Vol. 34, pp. 77–85). doi:10.1007/978-3-030-32040-9_9
- Smaill, B., & Hunter, P. (1991). *Structure and Function of the Diastolic Heart: Material Properties of Passive Myocardium*. doi:10.1007/978-1-4612-3118-9_1
- Smiseth, O. A., Torp, H., Opdahl, A., Haugaa, K. H., & Urheim, S. (2016). Myocardial strain imaging: How useful is it in clinical decision making? In *European Heart Journal*. doi:10.1093/eurheartj/ehv529
- Soler, R., Rodríguez, E., Monserrat, L., Méndez, C., & Martínez, C. (2006). Magnetic resonance imaging of delayed enhancement in hypertrophic cardiomyopathy: Relationship with left ventricular perfusion and contractile function. *Journal of Computer Assisted Tomography*. doi:10.1097/00004728-200605000-00011
- Stehning, C., Börnert, P., Nehrke, K., Eggers, H., & Stuber, M. (2005). Free-breathing whole-heart coronary MRA with 3D radial SSFP and self-navigated image reconstruction. *Magnetic Resonance in Medicine*, 54(2), 476–480. doi:10.1002/mrm.20557
- Steinmetz, M., Broder, M., Hösch, O., Lamata, P., Kutty, S., Kowallick, J. T., Staab, W., Ritter, C. O., Hasenfuß, G., Paul, T., Lotz, J., & Schuster, A. (2018). Atrio-ventricular deformation and heart failure in Ebstein's Anomaly - A cardiovascular magnetic resonance study. *International Journal of Cardiology*, 257, 54–61. doi:10.1016/j.ijcard.2017.11.097
- Stergiopoulos, N., Westerhof, B. E., & Westerhof, N. (1999). Total arterial inertance as the fourth element of the windkessel model. *American Journal of Physiology - Heart and Circulatory Physiology*. doi:10.1152/ajpheart.1999.276.1.h81
- Stoeck, C. T., Manka, R., Boesiger, P., & Kozerke, S. (2012). Undersampled Cine 3D tagging for

- rapid assessment of cardiac motion. *Journal of Cardiovascular Magnetic Resonance*. doi:10.1186/1532-429X-14-60
- Stoeck, C. T., von Deuster, C., Fuetterer, M., Polacin, M., Waschkies, C. F., van Gorkum, R. J. H., Kron, M., Fleischmann, T., Cesarovic, N., Weisskopf, M., & Kozerke, S. (2021). Cardiovascular magnetic resonance imaging of functional and microstructural changes of the heart in a longitudinal pig model of acute to chronic myocardial infarction. *Journal of Cardiovascular Magnetic Resonance*, 23(1), 1–14. doi:10.1186/s12968-021-00794-5
- Stuber, M., Scheidegger, M. B., Fischer, S. E., Nagel, E., Steinemann, F., Hess, O. M., & Boesiger, P. (1999). Alterations in the local myocardial motion pattern in patients suffering from pressure overload due to aortic stenosis. *Circulation*. doi:10.1161/01.CIR.100.4.361
- Sudak, F. N. (1965). Intrapericardial and intracardiac pressures and the events of the cardiac cycle in *Mustelus canis* (Mitchill). *Comparative Biochemistry And Physiology*. doi:10.1016/0010-406X(65)90255-0
- Sudarshan, V., Acharya, U. R., Ng, E. Y. K., Meng, C. S., Tan, R. S., & Ghista, D. N. (2015). Automated Identification of Infarcted Myocardium Tissue Characterization Using Ultrasound Images: A Review. In *IEEE Reviews in Biomedical Engineering*. doi:10.1109/RBME.2014.2319854
- Suffoletto, M. S., Dohi, K., Cannesson, M., Saba, S., & Gorcsan, J. 3rd. (2006). Novel speckle-tracking radial strain from routine black-and-white echocardiographic images to quantify dyssynchrony and predict response to cardiac resynchronization therapy. *Circulation*, 113(7), 960–968. doi:10.1161/CIRCULATIONAHA.105.571455
- Sürder, D., Manka, R., Lo Cicero, V., Moccetti, T., Rufibach, K., Soncin, S., Turchetto, L., Radrizzani, M., Astori, G., Schwitter, J., Erne, P., Zuber, M., Auf der Maur, C., Jamshidi, P., Gaemperli, O., Windecker, S., Moschovitis, A., Wahl, A., Bühler, I., ... Corti, R. (2013). Intracoronary injection of bone marrow-derived mononuclear cells early or late after acute myocardial infarction: effects on global left ventricular function. *Circulation*, 127(19), 1968–1979. doi:10.1161/CIRCULATIONAHA.112.001035
- Sürder, D., Manka, R., Moccetti, T., Lo Cicero, V., Emmert, M. Y., Klersy, C., Soncin, S., Turchetto, L., Radrizzani, M., Zuber, M., Windecker, S., Moschovitis, A., Bühler, I., Kozerke, S., Erne, P., Lüscher, T. F., & Corti, R. (2016). Effect of Bone Marrow-Derived Mononuclear Cell Treatment, Early or Late After Acute Myocardial Infarction: Twelve Months CMR and Long-Term Clinical Results. *Circulation Research*, 119(3), 481–490. doi:10.1161/CIRCRESAHA.116.308639
- Sutherland, G. R., Stewart, M. J., Groundstroem, K. W. E., Moran, C. M., Fleming, A., Guell-Peris, F. J., Riemersma, R. A., Fenn, L. N., Fox, K. A. A., & McDicken, W. N. (1994). Color Doppler Myocardial Imaging: A New Technique for the Assessment of Myocardial function. *Journal of the American Society of Echocardiography*. doi:10.1016/S0894-7317(14)80001-1
- Taylor, R. J., Umar, F., Moody, W. E., Meyyappan, C., Stegemann, B., Townend, J. N., Hor, K. N., Misalski-Jamka, T., Mazur, W., Steeds, R. P., & Leyva, F. (2014). Feature-tracking cardiovascular magnetic resonance as a novel technique for the assessment of mechanical dyssynchrony. *International Journal of Cardiology*, 175(1), 120–125. doi:10.1016/j.ijcard.2014.04.268
- Ten Tusscher, K. H. W. J., Noble, D., Noble, P. J., & Panfilov, A. V. (2004). A model for human ventricular tissue. *American Journal of Physiology - Heart and Circulatory Physiology*. doi:10.1152/ajpheart.00794.2003
- Ter Keurs, H. E. D. J., Bucx, J. J., de Tombe, P. P., Backx, P., & Iwazumi, T. (1988). The effects of

- sarcomere length and Ca^{++} on force and velocity of shortening in cardiac muscle. *Advances in Experimental Medicine and Biology*. doi:10.1007/978-94-009-1313-4_6
- Ter Keurs, H. E. D. J., Rijnsburger, W. H., Van Heuningen, R., & Nagelsmit, M. J. (1980). Tension development and sarcomere length in rat cardiac trabeculae. Evidence of length-dependent activation. *Circulation Research*. doi:10.1161/01.RES.46.5.703
- Thygesen, K., Alpert, J. S., Jaffe, A. S., Simoons, M. L., Chaitman, B. R., White, H. D., Katus, H. A., Apple, F. S., Lindahl, B., Morrow, D. A., Clemmensen, P. M., Johanson, P., Hod, H., Underwood, R., Bax, J. J., Bonow, R. O., Pinto, F., Gibbons, R. J., Fox, K. A., ... Wagner, D. R. (2012). Third universal definition of myocardial infarction. *European Heart Journal*. doi:10.1093/eurheartj/ehs184
- Timmis, A., Townsend, N., Gale, C. P., Torbica, A., Lettino, M., Petersen, S. E., Mossialos, E. A., Maggioni, A. P., Kazakiewicz, D., May, H. T., De Smedt, D., Flather, M., Zuhlke, L., Beltrame, J. F., Huculeci, R., Tavazzi, L., Hindricks, G., Bax, J., Casadei, B., ... Vardas, P. (2020). European Society of Cardiology: Cardiovascular Disease Statistics 2019. *European Heart Journal*, 41(1), 12–85. doi:10.1093/eurheartj/ehz859
- Tobon-Gomez, C., De Craene, M., McLeod, K., Tautz, L., Shi, W., Hennemuth, A., Prakosa, A., Wang, H., Carr-White, G., Kapetanakis, S., Lutz, A., Rasche, V., Schaeffter, T., Butakoff, C., Friman, O., Mansi, T., Sermesant, M., Zhuang, X., Ourselin, S., ... Rhode, K. S. (2013). Benchmarking framework for myocardial tracking and deformation algorithms: An open access database. *Medical Image Analysis*, 17(6), 632–648. doi:10.1016/j.media.2013.03.008
- Tözeren, A. (1985). Continuum rheology of muscle contraction and its application to cardiac contractility. *Biophysical Journal*, 47(3), 303–309. doi:10.1016/S0006-3495(85)83920-5
- Trayanova, N. A. (2011). Whole-heart modeling : Applications to cardiac electrophysiology and electromechanics. In *Circulation Research*. doi:10.1161/CIRCRESAHA.110.223610
- Tueni, N. (2021). *Multiscale experimental and theoretical investigation of the structure-property relationships in the myocardium* [École Polytechnique]. <https://tel.archives-ouvertes.fr/tel-03330458>
- Tueni, N., Vizet, J., Genet, M., Pierangelo, A., & Allain, J.-M. (2020). Microstructural deformation observed by Mueller polarimetry during traction assay on myocardium samples. *Scientific Reports*, 10(1), 20531. doi:10.1038/s41598-020-76820-w
- Tustison, N. J., Dávila-Román, V. G., & Amini, A. A. (2003). Myocardial kinematics from tagged MRI based on a 4-D B-spline model. *IEEE Transactions on Biomedical Engineering*. doi:10.1109/TBME.2003.814530
- Ubbink, S. W. J., Bovendeerd, P. H., Delhaas, T., Arts, T., & van de Vosse, F. N. (2006). Towards model-based analysis of cardiac MR tagging data: Relation between left ventricular shear strain and myofiber orientation. *Medical Image Analysis*. doi:10.1016/j.media.2006.04.001
- Uematsu, M., Miyatake, K., Tanaka, N., Matsuda, H., Sano, A., Yamazaki, N., Hirama, M., & Yamagishi, M. (1995). Myocardial velocity gradient as a new indicator of regional left ventricular contraction: detection by a two-dimensional tissue Doppler imaging technique. *Journal of the American College of Cardiology*, 26(1), 217–223. doi:10.1016/0735-1097(95)00158-v
- Uusitalo, V., Luotolahti, M., Pietilä, M., Wendelin-Saarenhovi, M., Hartiala, J., Saraste, M., Knuuti, J., & Saraste, A. (2016). Two-Dimensional Speckle-Tracking during Dobutamine Stress Echocardiography in the Detection of Myocardial Ischemia in Patients with Suspected Coronary Artery Disease. *Journal of the American Society of Echocardiography*.

- doi:10.1016/j.echo.2015.12.013
- Vadakkumpadan, F., Arevalo, H., Prassl, A. J., Chen, J., Kicking, F., Kohl, P., Plank, G., & Trayanova, N. (2010). Image-based models of cardiac structure in health and disease. *Wiley Interdisciplinary Reviews. Systems Biology and Medicine*, 2(4), 489–506. doi:10.1002/wsbm.76
- Van De Vosse, F. N., & Stergiopoulos, N. (2011). Pulse wave propagation in the arterial tree. *Annual Review of Fluid Mechanics*. doi:10.1146/annurev-fluid-122109-160730
- Van Der Linde, D., Konings, E. E. M., Slager, M. A., Witsenburg, M., Helbing, W. A., Takkenberg, J. J. M., & Roos-Hesselink, J. W. (2011). Birth prevalence of congenital heart disease worldwide: A systematic review and meta-analysis. In *Journal of the American College of Cardiology*. doi:10.1016/j.jacc.2011.08.025
- Veress, A. I., Weiss, J. A., Rabbitt, R. D., Lee, J. N., & Gullberg, G. T. (2001). Measurement of 3D left ventricular strains during diastole using image warping and untagged MRI images. *Computers in Cardiology*. doi:10.1109/CIC.2001.977617
- Vetter, F. J., & McCulloch, A. D. (1998). Three-dimensional analysis of regional cardiac function: a model of rabbit ventricular anatomy. *Progress in Biophysics and Molecular Biology*, 69(2–3), 157–183. doi:10.1016/s0079-6107(98)00006-6
- Vigneault, D. M., Xie, W., Bluemke, D. A., & Noble, J. A. (2017). Feature tracking cardiac magnetic resonance via deep learning and spline optimization. *Lecture Notes in Computer Science (Including Subseries Lecture Notes in Artificial Intelligence and Lecture Notes in Bioinformatics)*. doi:10.1007/978-3-319-59448-4_18
- Villarreal, F. J., Waldman, L. K., & Lew, Y. W. (1988). Technique for measuring regional two-dimensional finite strains in canine left ventricle. *Circulation Research*. doi:10.1161/01.RES.62.4.711
- Vincenti, G., Monney, P., Chaptinel, J., Rutz, T., Coppo, S., Zenge, M. O., Schmidt, M., Nadar, M. S., Piccini, D., Chèvre, P., Stuber, M., & Schwitler, J. (2014). Compressed sensing single-breath-hold CMR for fast quantification of LV function, volumes, and mass. *JACC: Cardiovascular Imaging*, 7(9), 882–892. doi:10.1016/j.jcmg.2014.04.016
- Virani, S. S., Alonso, A., Aparicio, H. J., Benjamin, E. J., Bittencourt, M. S., Callaway, C. W., Carson, A. P., Chamberlain, A. M., Cheng, S., Delling, F. N., Elkind, M. S. V., Evenson, K. R., Ferguson, J. F., Gupta, D. K., Khan, S. S., Kissela, B. M., Knutson, K. L., Lee, C. D., Lewis, T. T., ... Tsao, C. W. (2021). Heart Disease and Stroke Statistics-2021 Update: A Report From the American Heart Association. *Circulation*, 143(8), e254–e743. doi:10.1161/CIR.0000000000000950
- Voigt, J. U., Arnold, M. F., Karlsson, M., Hübner, L., Kukulski, T., Hatle, L., & Sutherland, G. R. (2000). Assessment of regional longitudinal myocardial strain rate derived from Doppler myocardial imaging indexes in normal and infarcted myocardium. *Journal of the American Society of Echocardiography*. doi:10.1067/mje.2000.105631
- Voigt, J. U., & Cijic, M. (2019). 2- and 3-Dimensional Myocardial Strain in Cardiac Health and Disease. *JACC. Cardiovascular Imaging*, 12(9), 1849–1863. doi:10.1016/j.jcmg.2019.01.044
- Wang, H., & Amini, A. A. (2012). Cardiac motion and deformation recovery from MRI: A review. In *IEEE Transactions on Medical Imaging*. doi:10.1109/TMI.2011.2171706
- Wang, H., Shi, W., Zhuang, X., Duckett, S., Tung, K., Edwards, P., Razavi, R., Ourselin, S., & Rueckert, D. (2012). Automatic Cardiac Motion Tracking Using Both Untagged and 3D Tagged MR Images. In O. Camara, E. Konukoglu, M. Pop, K. Rhode, M. Sermesant, & A. Young (Eds.), *Statistical Atlases and Computational Models of the Heart. Imaging and*

- Modelling Challenges* (pp. 45–54). Springer Berlin Heidelberg.
- Wang, H., Stoeck, C. T., Kozerke, S., & Amini, A. A. (2013). Analysis of 3D cardiac deformations with 3D SinMod. *Proceedings of the Annual International Conference of the IEEE Engineering in Medicine and Biology Society, EMBS*, 4386–4389. doi:10.1109/EMBC.2013.6610518
- Wang, V. Y., Lam, H. I., Ennis, D. B., Cowan, B. R., Young, A. A., & Nash, M. P. (2009). Modelling passive diastolic mechanics with quantitative MRI of cardiac structure and function. *Medical Image Analysis*. doi:10.1016/j.media.2009.07.006
- Warnes, C. A. (2006). Transposition of the great arteries. *Circulation*, 114(24), 2699–2709. doi:10.1161/CIRCULATIONAHA.105.592352
- Westerhof, N., Elzinga, G., & Sipkema, P. (1971). An artificial arterial system for pumping hearts. *Journal of Applied Physiology*. doi:10.1152/jappl.1971.31.5.776
- White, J. A., Yee, R., Yuan, X., Krahn, A., Skanes, A., Parker, M., Klein, G., & Drangova, M. (2006). Delayed enhancement magnetic resonance imaging predicts response to cardiac resynchronization therapy in patients with intraventricular dyssynchrony. *Journal of the American College of Cardiology*, 48(10), 1953–1960. doi:10.1016/j.jacc.2006.07.046
- Wollert, K. C., Meyer, G. P., Lotz, J., Ringes-Lichtenberg, S., Lippolt, P., Breidenbach, C., Fichtner, S., Korte, T., Hornig, B., Messinger, D., Arseniev, L., Hertenstein, B., Ganser, A., & Drexler, H. (2004). Intracoronary autologous bone-marrow cell transfer after myocardial infarction: the BOOST randomised controlled clinical trial. *Lancet (London, England)*, 364(9429), 141–148. doi:10.1016/S0140-6736(04)16626-9
- Wong, A. Y. K. (1971). Mechanics of cardiac muscle, based on Huxley's model: Mathematical simulation of isometric contraction. *Journal of Biomechanics*, 4(6), 529–540. doi:10.1016/0021-9290(71)90042-X
- Wong, A. Y. K. (1972). Mechanics of cardiac muscle, based on Huxley's model: Simulation of active state and force-velocity relation. *Journal of Biomechanics*, 5(1), 107–117. doi:10.1016/0021-9290(72)90023-1
- World Health Organization. (2020). Global health estimates for 2020: deaths by cause, age, sex, by country and by region, 2000-2019. *WHO*.
- Wu, L., Germans, T., Güçlü, A., Heymans, M. W., Allaart, C. P., & van Rossum, A. C. (2014). Feature tracking compared with tissue tagging measurements of segmental strain by cardiovascular magnetic resonance. *Journal of Cardiovascular Magnetic Resonance : Official Journal of the Society for Cardiovascular Magnetic Resonance*, 16(1), 10. doi:10.1186/1532-429X-16-10
- Wymer, D. T., Patel, K. P., Burke, W. F. 3rd, & Bhatia, V. K. (2020). Phase-Contrast MRI: Physics, Techniques, and Clinical Applications. *Radiographics : A Review Publication of the Radiological Society of North America, Inc*, 40(1), 122–140. doi:10.1148/rg.2020190039
- Xu, C., Pham, D. L., & Prince, J. L. (2000). Image segmentation using deformable models. *Handbook of Medical Imaging*, 2(20), 0.
- Yeon, S. B., Reichek, N., Tallant, B. A., Lima, J. A., Calhoun, L. P., Clark, N. R., Hoffman, E. A., Ho, K. K., & Axel, L. (2001). Validation of in vivo myocardial strain measurement by magnetic resonance tagging with sonomicrometry. *Journal of the American College of Cardiology*, 38(2), 555–561. doi:10.1016/s0735-1097(01)01397-3
- Yip, G., Abraham, T., Belohlavek, M., & Khandheria, B. K. (2003). Clinical Applications of Strain Rate Imaging. In *Journal of the American Society of Echocardiography*. doi:10.1067/j.echo.2003.09.004
- Yoganathan, A. P., He, Z., & Casey Jones, S. (2004). Fluid mechanics of heart valves. *Annual*

- Review of Biomedical Engineering*, 6, 331–362. doi:10.1146/annurev.bioeng.6.040803.140111
- Young, A. A. (1999). Model tags: Direct three-dimensional tracking of heart wall motion from tagged magnetic resonance images. *Medical Image Analysis*. doi:10.1016/S1361-8415(99)80029-2
- Young, A. A., Axel, L., Dougherty, L., Bogen, D. K., & Parenteau, C. S. (1993). Validation of tagging with MR imaging to estimate material deformation. *Radiology*. doi:10.1148/radiology.188.1.8511281
- Young, A. A., Dokos, S., Powell, K. A., Sturm, B., McCulloch, A. D., Starling, R. C., McCarthy, P. M., & White, R. D. (2001). Regional heterogeneity of function in nonischemic dilated cardiomyopathy. *Cardiovascular Research*. doi:10.1016/S0008-6363(00)00248-0
- Young, A. A., Kramer, C. M., Ferrari, V. A., Axel, L., & Reichek, N. (1994). Three-dimensional left ventricular deformation in hypertrophic cardiomyopathy. *Circulation*, 90(2), 854–867. doi:10.1161/01.CIR.90.2.854
- Young, A. A., LeGrice, I. J., Young, M. A., & Smaill, B. H. (1998). Extended confocal microscopy of myocardial laminae and collagen network. *Journal of Microscopy*. doi:10.1046/j.1365-2818.1998.00414.x
- Young, A. A., Li, B., Kirton, R. S., & Cowan, B. R. (2012). Generalized spatiotemporal myocardial strain analysis for DENSE and SPAMM imaging. *Magnetic Resonance in Medicine*, 67(6), 1590–1599. doi:10.1002/mrm.23142
- Youssef, A., Ibrahim, E. S. H., Korosoglou, G., Abraham, M. R., Weiss, R. G., & Osman, N. F. (2008). Strain-encoding cardiovascular magnetic resonance for assessment of right-ventricular regional function. *Journal of Cardiovascular Magnetic Resonance*. doi:10.1186/1532-429X-10-33
- Zerhouni, E. A., Parish, D. M., Rogers, W. J., Yang, A., & Shapiro, E. P. (1988). Human heart: tagging with MR imaging--a method for noninvasive assessment of myocardial motion. *Radiology*, 169(1), 59–63. doi:10.1148/radiology.169.1.3420283
- Zou, H., Xi, C., Zhao, X., Koh, A. S., Gao, F., Su, Y., Tan, R.-S., Allen, J., Lee, L. C., Genet, M., & Zhong, L. (2018). Quantification of Biventricular Strains in Heart Failure With Preserved Ejection Fraction Patient Using Hyperelastic Warping Method. *Frontiers in Physiology*, 9, 1295. doi:10.3389/fphys.2018.01295

List of Publications

Journal Publications

Stimm, J., Buoso, S., **Berberoğlu, E.**, Kozerke, S., Genet, M., & Stoeck, C. T. (2021). A 3D personalized cardiac myocyte aggregate orientation model using MRI data-driven low-rank basis functions. *Medical Image Analysis*, 71, 102064. doi:10.1016/j.media.2021.102064.

Castellanos, D. A., Škardová, K., Bhattaru, A., **Berberoglu, E.**, Greil, G., Tandon, A., Dillenbeck, J., Burkhardt, B., Hussain, T., Genet, M., & Chabiniok, R. (2021). Left Ventricular Torsion Obtained Using Equilibrated Warping in Patients with Repaired Tetralogy of Fallot. *Pediatric Cardiology*, 42(6), 1275–1283. doi:10.1007/s00246-021-02608-y.

Berberoğlu, E., Stoeck, C. T., Moireau, P., Kozerke, S., & Genet, M. (2021). In-silico study of accuracy and precision of left-ventricular strain quantification from 3D tagged MRI. *PloS One*, 16(11), e0258965. doi:10.1371/journal.pone.0258965.

Conference Proceedings

Berberoğlu, E., Stoeck, C., Moireau, P., Kozerke, S., & Genet, M. (2019). Validation of Finite Element Image Registration-based Cardiac Strain Estimation from Magnetic Resonance Images. *PAMM*. doi:10.1002/pamm.201900418.

Acknowledgements

First and foremost, I would like to express my sincere gratitude to my supervisors, Prof. Sebastian Kozerke and Prof. Martin Genet who offered me the opportunity to pursue my PhD on such a fascinating project in an internationally renowned laboratory. I would like to thank Sebastian for his guidance and trust on me during this journey. I really appreciate our scientific discussions that reshaped how I approach the problems. A big thanks to Martin, for our scientific discussions and his endless support when I was lost in details. I am grateful for the freedom he gave me during my research, but showing me how to be disciplined at the same.

I also warmly thank Prof. Julius Guccione who kindly agreed to attend my PhD defense and provided many valuable inputs.

I would like to thank Christian Stoeck who spent time reading my work and followed my thesis during these five years. In addition to his friendship, I am grateful for his valuable inputs for this thesis.

This thesis is based on a joint project between ETH Zürich and École Polytechnique, Paris, that gave me the chance to collaborate with people not only from ETH, but also from team MEDISIM. I would like to thank Dominique Chapelle and Philippe Moireau for their support and offering me a workplace in their laboratory.

I would like to thank all my colleagues from ETH and team MEDISIM. Thank you for listening to my complaints and encouraging me to overcome all the difficulties. I specifically thank Pietro for his valuable friendship and being a great office mate. Thanks to Bannay and Andreas, for our funny discussions and Stefano, for the coffee-breaks. Nicole, my dear friend, thank you so much for listening to me and encouraging me during the times of sorrow. I have to say that I am already missing our trips together. Federica, Maria, and Cecile, thank you so much for your friendship. I really appreciate the moments we spent together in Paris.

Furthermore, I thank all my friends who always supported me. Special thanks go to my family for their unconditional love. This thesis wouldn't be possible without their support.

Curriculum Vitae

Personal Information

Name: Ezgi Berberoğlu
Date of birth: 23 August 1987
Nationality: Turkish

Education

2017 – 2022 PhD candidate
Institute for Biomedical Engineering
ETH Zürich, Zürich/Switzerland

2011 – 2014 MSc in Civil Engineering
The Graduate School of Natural and Applied Sciences
Middle East Technical University Ankara, Turkey
Thesis: “Computational Modeling of Cardiac Dysfunctions”

2008 – 2012 BSc in Computer Engineering (Double major)
Middle East Technical University, Ankara/Turkey

2006 – 2011 BSc in Civil Engineering
Middle East Technical University Ankara, Turkey

Work and Research Experience

2017 – 2022 Doctoral Student at the Cardiovascular Magnetic Resonance Group,
University and ETH Zürich

2014 – 2017 Software Engineer
Kardiosis Cardiologic Diagnostic Systems Ltd.

Ankara/Turkey

2014

Project Engineer (funded by TÜBİTAK - 5130011)

Middle East Technical University, Ankara/Turkey

2011 – 2013
tion

Project Assistant (funded by EU FP7 - People Marie Curie Carrier Integra-
Grant)

Middle East Technical University, Ankara/Turkey